Dissertation zur Erlangung des Doktorgrades
der Fakultät für Chemie und Pharmazie
der Ludwig–Maximilians–Universität München

# Photocatalysis with Carbon Nitrides for Hydrogen Evolution

Brian Tuffy

aus

Castlebar, Irland

2016

*in memory of my grandmother, Bridie Tuffy*

# Acknowledgements

First I offer my sincere thanks to Bettina for supervising me over the past few years. For her guidance, understanding, courage and optimism, I am truly grateful. To the photocatalysis group, my friends Filip, Katharina, Vince and Hongji. Thank you for making my time here so meaningful, insightful and enjoyable. For their abundance of help and friendship, thanks to the rest of the group here in Stuttgart: Tanya, Pirmin, Anna, Ralf, Judith, Freddy, Vijay, Dan and Leslie. To the most excellent technicians, whom we rely on so much. Thank you Vio Duppel, Roland Eger, Claudi Kamella, Willie Hölle and Marie-Luise Schreiber. I also want to thank Prof. Jürgen Köhler and Xiuping Gao for providing me with samples and helpful discussions.

A big thank you to our group in Munich. Leo, Hendrik, Kerstin, Claudia, Katalin, Albi, Linus and especially to those who were there with me from the start: Ida, Erik, Sebastian, Anna, Chris, Stephan W. and Stephan H.

To our former post docs who have shown us the way forward. Dr. Olalla Sánches-Sobrado, Dr. Alexander Kuhn and Dr. Cheng Li, thanks for your leadership.

I want to thank my collaborators, especially the group of Prof. Jürgen Senker including Maria Mesch for their help with NMR measurements. Many thanks to Dr. Maximilian Berr for helping me with my first photocatalysis experiments. To Prof. Dr. Lukas Schmidt-Mende for giving me a start in his lab. A special thanks to Severin Habisreutinger and Dr. Jacek Stolarczyk for their insightful discussions, ideas and engagement.

A big thanks to the CeNS family at LMU, especially Marilena Pinto, Susanne Hennig and all the others who I met over the many workshops and outings. I must also thank the IDK-NBT program for giving me the opportunity to come to Germany. A very special thanks to the other international students; Kamilla, Kasia, Farzad and most especially to Sushi for making our apartment a wonderful place to live.

Most importantly, I thank my family. To my brothers Seamus and Liam, and my sister Marie, thank you for being there for me. Dearest Dad and Mam, thank you for your support, guidance and encouragement. Your choices have allowed me great opportunities and for that I am forever grateful. To Andonia, my love. Thank you for your unconditional support and inspiration.

Go raibh míle maith agaibh — a thousand thanks to you all

# Acknowledgements

# Contents

# Table of Contents

# Abstract

Photocatalysis is a highly desirable solution to the challenges of energy supply and environmental pollution with the potential to offer clean renewable energy, atmospheric $CO_2$ reduction and pollution remediation. This green chemistry approach uses sunlight to break and form covalent bonds, mimicking the mechanisms of photosynthesis. This is a materials design challenge and the discovery of the best photocatalysts is the key to success.

Carbon nitrides offer a new approach because of their light-element structure, diversity and ease of synthesis when compared to conventional metal photocatalysts. Carbon nitrides are inexpensive, abundant, highly stable and functional compounds that show interesting chemical properties because they are bordering organic and inorganic chemistry. The explosion of interest in carbon nitrides is fuelled by their high performance as photocatalysts for hydrogen evolution.

This thesis presents the first photocatalytic hydrogen evolution results from the triazine-based carbon nitride poly(triazine imide), which is the first structurally characterised 2D carbon nitride composed of triazine building units. The doped triazine carbon nitride shows a six times greater activity for hydrogen production compared to heptazine-based *melon* under visible light.

Separately from triazine-based compounds, the crystallinity, optical properties and photocatalysis of heptazine-based carbon nitrides synthesised at long calcination times were investigated. From this, we present a new carbon nitride called *white melon*, which is a surprising candidate for the hydrogen evolution reaction. It has the highest crystallinity degree of the air-synthesised carbon nitrides due to its in-plane order and decreased stacking distance. The emergence of molecular-like absorption peaks in the UV demonstrate its increased structural purity and order. Despite poor absorption of visible light, *white melon* evolves six times more hydrogen compared to the benchmark *melon* under solar illumination conditions. Distinctively, white melon easily forms a stable colloid in water, unlike its less condensed counterparts. It is chemically identical to conventional polymeric "*g-CN melon*" yet its morphology and optical properties are markedly different. This work demonstrates the significance of the reaction conditions, such as calcination time, and adds new perspectives to morphology engineering of carbon nitrides.

isometric pattern inspired by melon, every grid vertex is a nitrogen position
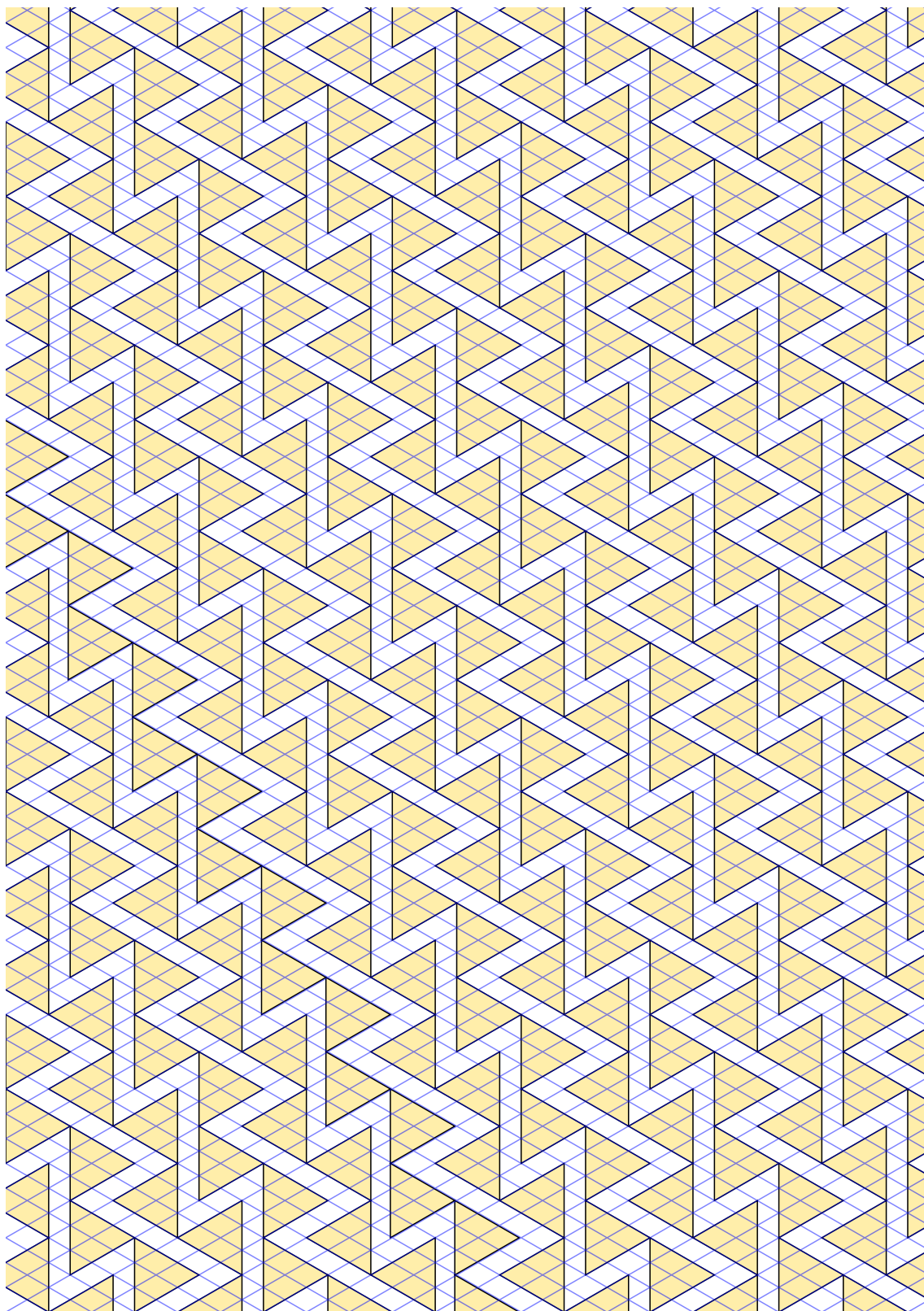
# Chapter 1

# Introduction

## 1. Introduction

Humanity is facing the ultimate challenge because of climate change. Global warming is leading to a chaotic climate and a mass extinction event.[1] Because of this, humanity must adapt, not just to renewable energy, but directly to solar energy. Although a multitude of power technologies should be developed for the future, in the long term, solar technologies such as photovoltaics and photocatalysis are superior because they directly convert energy from the primary source, our sun.[2] In answer to the disadvantages of moderate efficiency, high cost and energy storage issues, solar energy shows the most rapid scientific development.[3,4] It is this scientific development that will drive the transition from an oil economy to a solar economy.

The sun is the primary energy source, emitting at a stunning $3.846{\times}10^{26}$ W.[5] The total solar irradiance at the top of the atmosphere (AM0) is $1.361{\times}10^3$ W m$^{-2}$ as recorded for the solar activity minimum in 2008.[6] At the surface, it averages $1.000{\times}10^3$ W m$^{-2}$ for clear skies in mid latitudes (AM1.5).[7] Averaging over the full year gives a more realistic irradiance of 183 W m$^{-2}$ over land. These values are complemented by the solar spectrum and the irradiance distribution map, given in Figure 1.1. Using current photovoltaic devices, we could convert this to $2.05{\times}10^{25}$ J yr$^{-1}$ of usable energy.[8] Comparing this to the world's primary energy consumption of $4.5{\times}10^{20}$ J yr$^{-1}$ in 2013,[9] it is clear that there is more than enough solar energy to meet demands. Today, 80 % of world energy generation is based on fossil fuels.[9,10] If that is to change, further technologies and scientific developments are needed to ease the transition to solar-based energy.

Photocatalysis (PC) is a broad topic with great promise for the future. In these early stages, efforts are primarily focused on the water splitting reaction with light but $CO_2$ reduction is becoming the new goal to reach. Photocatalysis is a rapidly expanding scientific field with exponentially increasing publications for the past decade. In theory, it can provide wide ranging solutions such as energy generation,[11] pollution remediation[12] and $CO_2$ reduction.[13,14] The challenge lies in the design of new materials and a further understanding of the fundamental principles. These principles are outlined for the photocatalytic hydrogen evolution from water, given in Section 1.3.

**(a)** **Terrestrial Solar Spectrum (Air Mass 1.5 Global 37° Tilted Surface)**
**Data Source: American Society for Testing and Materials (ASTM)**

**(b)** **Yearly Sum of Global Horizontal Irradiation**

Source: www.meteonorm.com; uncertainty 8 %
Period: 1991 - 2010; grid cell size 0.125°

March 2014
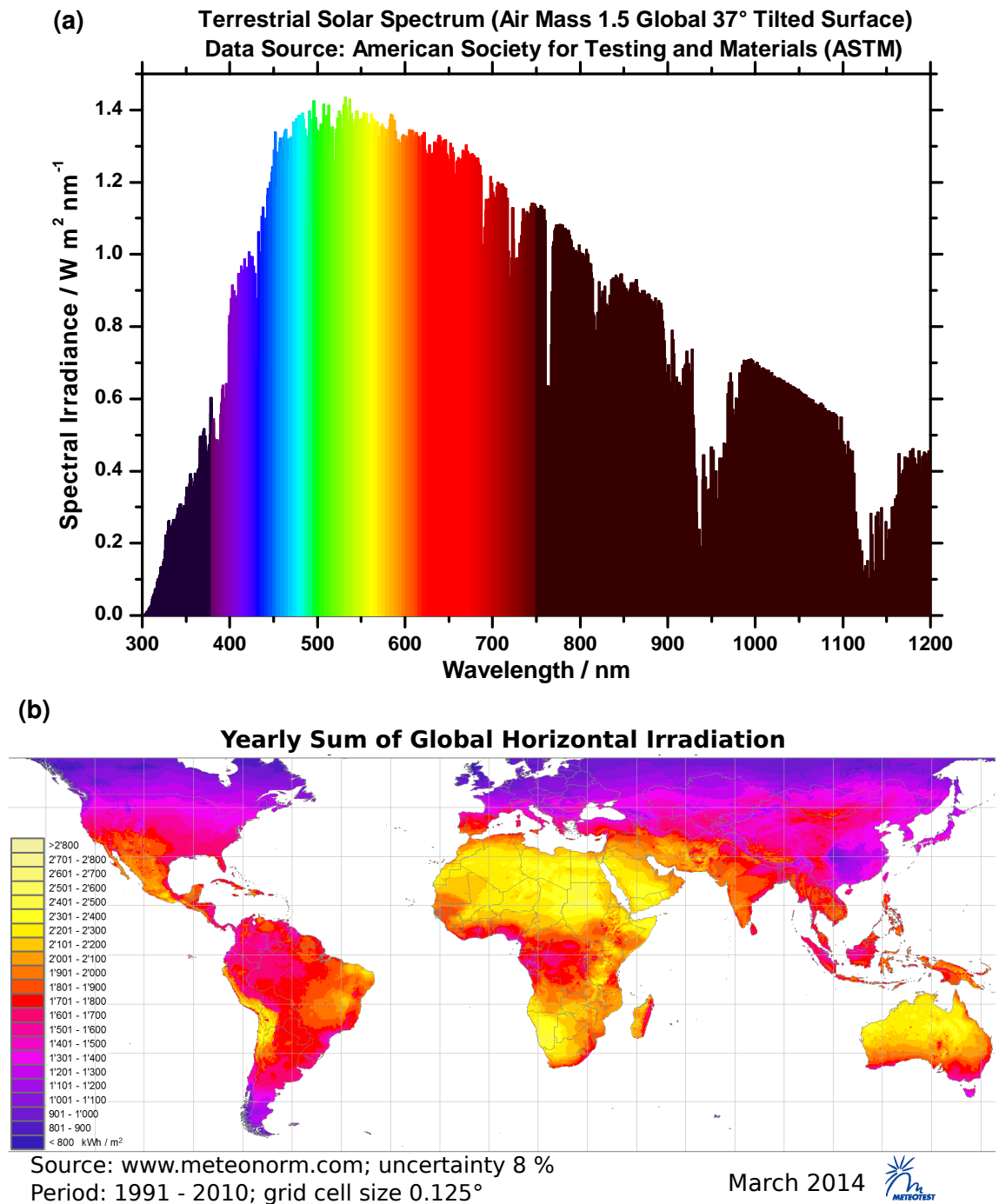
Figure 1.1: **(a)** Solar spectrum at ground level, AM1.5 global with superimposed visible region. Data source: American Society for Testing and Materials (ASTM). **(b)** World map of solar irradiation 1991 to 2010. Adapted from: Meteonorm.com.

## 1.1  Overview of Publications

The growth of photocatalysis stems from the established fields of electrochemistry and photochemistry. As early as 1906, the effect of light on galvanic cells was noted[15] which led to the field of photoelectrochemistry (PEC) in the 70s and 80s. The first mention of photocatalysis is credited to J. Plotnikow in the "Textbook of Photochemistry" in 1910.[16] For further details, the historical perspective by Serpone et al. is recommended.[17]

It is interesting to note the growth of photocatalysis as a topic which has recently expanded rapidly. Figure 1.2 examines the number of publications per year for the terms *photocatalysis* **(a)** and *carbon nitrides* **(b)**. As mentioned, the term photocatalysis already existed in its original form for over a hundred years. During the rapid development of photoelectrochemistry after the 1973 oil crisis, the field of photocatalysis regained interest. From 1996, publications have expanded exponentially with a new motivation. This new interest is primarily to answer the challenges of climate change, namely clean energy production and pollution control.

As can be seen from the inset of Figure 1.2**(a)**, the majority of publications are from east Asia. Two points are noted: firstly, Japan is considered a photocatalysis hub since the publication of the Fujishima and Honda discovery in 1972;[18] secondly, China has the greatest need for photocatalysis considering its fast development, high energy demands and high pollution levels.

The material class of *carbon nitrides* (CNs) which will be discussed in Section 1.2 show two phases of publication activity instead of one. Historically, carbon nitrides belong to the earliest polymeric materials since Liebig's *melon* in 1834.[19] However, the recent trend is characterised by the 1999 peak in interest which was due to the prediction of "Low Compressibility Solids", enticing interest in synthesising a material harder than diamond.[20] From 2010 on, carbon nitrides have rapidly regained interest as an alternative semiconductor photocatalyst material, which is the main focus of this thesis.
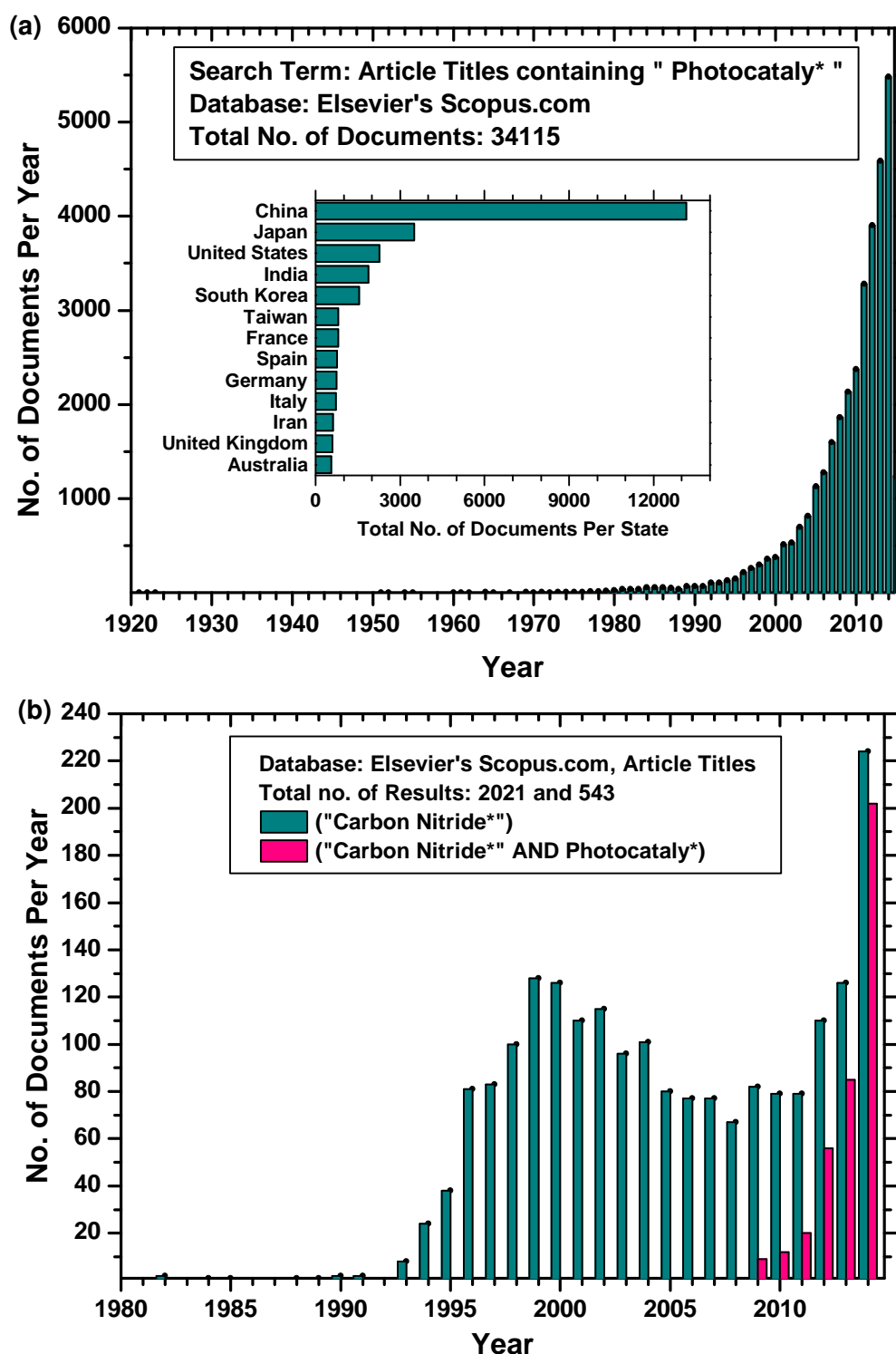
Figure 1.2: Topic survey graphs demonstrate the surge of interest in photocatalysis and the renewed interest in carbon nitrides. The top inset figure shows how 44 % of the publications are from China in 2014. The search terms "photocataly*" and "carbon nitride*" were used with Elsevier's Scopus database with the search restricted to journal article titles before 1st January 2015.

## 1.2   Carbon Nitrides

Carbon nitrides are light-element materials consisting simply of carbon, nitrogen and hydrogen atoms. They are identified by their alternating $\pi$-conjugated C and N backbone and their ring structures composed of triazine or tri-s-triazine (heptazine) units. These ring structures have two forms, the first is the *triazine* structure with melamine as a building block and the second is the tri-s-triazine or *heptazine* structure with melem as the building block. Highly condensed CNs have exceptional chemical stability and are insoluble in most solvents.[21] They also exhibit high thermal stability ($> 500$ °C) and are band gap tunable semiconductors which makes them desirable for many applications. CNs are easily synthesised by heating precursors such as urea, dicyandiamide (DCD) or melamine. However, the properties of the resulting powders depend greatly on the synthesis conditions and can yield a variety of CN species with varying degrees of crystallinity, defects, carbonisation, band gap, absorption and specific surface area etc.

CNs lie at the interface of organic and inorganic materials—although they align more with organic materials in terms of their molecular structure—and are often compared to graphite. The term g-$C_3N_4$ meaning graphitic carbon nitride is commonly found in the literature under different forms. However, this nomenclature is misleading for two reasons. The first is that graphite or more specifically graphene is a 2D carbon. The second is that hydrogen content is ignored. In reality, g-CN type heptazine carbon nitrides form under similar synthesis conditions as Liebig's melon with matching chemical analysis. In 2007 Lotsch et al.[22] proved the structure of melon to be a 1D polymer with in-plane hydrogen bonding explaining the quasi-2D nature of the material (See Figure 1.3). Furthermore, full hydrogen removal during synthesis—as is required for $C_3N_4$—has not been convincingly demonstrated thus far in heptazine-based systems and so hydrogen content must be considered.

### 1.2.1   Thermal Condensation Reactions

The synthesis of carbon nitrides (CNs) occurs through condensation reactions (commonly referred to as dehydration synthesis) although in this case, ammonia is lost instead of water. This is common in polymers and is known as condensation polymerization or *polycondensation.*

**Polycondensation**

The international union of pure and applied chemistry (IUPAC) defines polycondensation as:

> "A polymerization in which the growth of polymer chains proceeds by
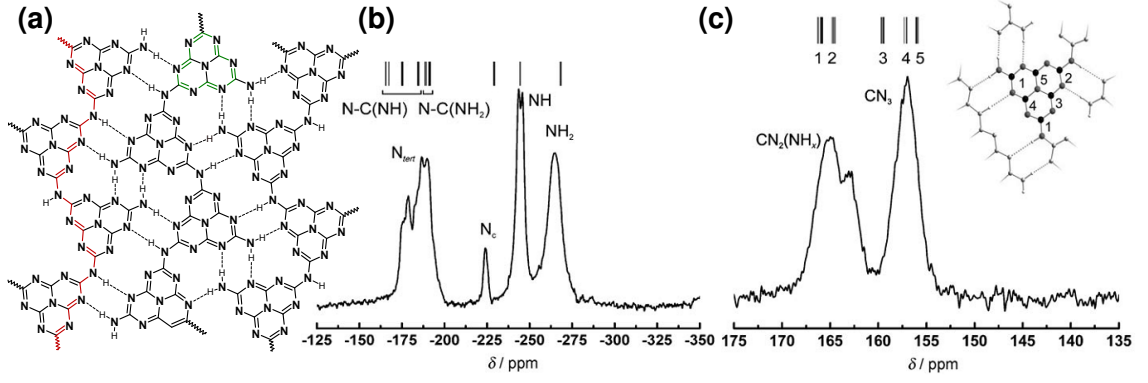
Figure 1.3: **(a)** Melon chemical structure with hydrogen bonding, highlighting the polymer chain backbone (red) and π-conjugation of the heptazine ring (green). **(b)** $^{15}$N and **(c)** $^{13}$C CP-MAS solid-state NMR spectra of melon. The signal assignments according to ab initio calculations of the chemical shift values for the DFT-optimized cell (see inset) are indicated on top of the experimental spectra. (b) and (c) from Lotsch et al.[22]

condensation reactions between molecules of all degrees of polymerization.

$$P_x + P_y \rightarrow P_{x+y} + L \qquad x, y \in \mathbb{N} \qquad (1.1)$$

where $P_x$ and $P_y$ denote chains of degree of polymerization $x$ and $y$ respectively and $L$ is a low-molar-mass by-product. The degree of polymerisation $(x, y)$ is the number of monomeric units in a macromolecule or oligomer molecule, a block or a chain.[23]"

As an example, if we label melamine as the monomeric unit in carbon nitrides, we can write Equation 1.1 above as Equation 1.2 where $x$ and $y$ are = 1. This is the polycondensation of melamine to melam which continues to higher degrees of polycondensation to form melon.[24–26] See Figure 1.4 as an example.

$$C_3H_6N_6 + C_3H_6N_6 \rightarrow C_6H_9N_{11} + NH_3 \qquad (1.2)$$
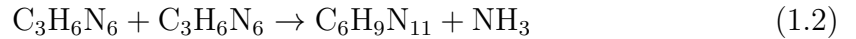
However, this strict definition excludes the direct conversion of melamine to melem, which has been proposed to involve a series of intramolecular ring opening, condensation and addition reactions.[24,25,27]
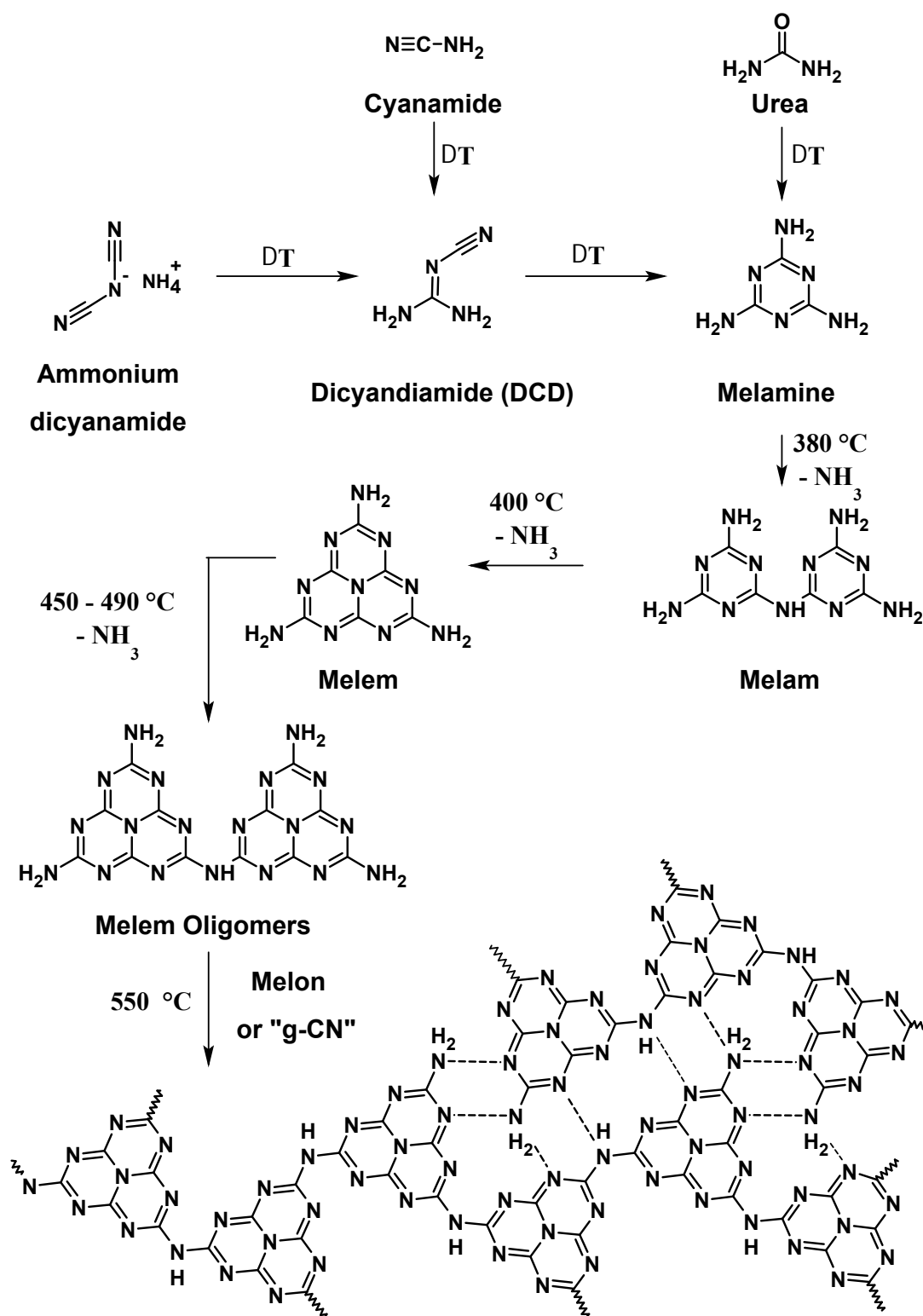
Figure 1.4: Condensation pathway of carbon nitride precursors to highly condensed melon.[24–26] The reaction occurs step-wise at elevated temperatures with the evolution of NH₃ gas. Note that it is not necessarily a linear path as there are multiple side-products and mixed phases such as melamine and melem adducts.[28]

# 1.3   Photocatalysis

Photocatalysis (PC) is a broad term covering a range of topics such as: photolysis of water, photodegradation of pollution, artificial photosynthesis, photochemical synthesis, $CO_2$ reduction, and environmental remediation. Applications include: hydrogen evolution from water, air purification, water purification, dye degradation, photodynamic therapy, green chemistry synthesis, and solar fuel conversion.[29–34]

IUPAC defines the term photocatalysis as:

> "Change in the rate of a chemical reaction or its initiation under the action of ultraviolet, visible or infrared radiation in the presence of a substance—the photocatalyst—that absorbs light and is involved in the chemical transformation of the reaction partners"

In this thesis, we focus on water splitting since it is the thermodynamically most favourable reaction and has great importance.

**Water Splitting**

Water splitting is a term used to describe the process of breaking $O-H$ bonds and thus separating water into its constituent gases, oxygen and hydrogen.

$$H_2O(l) + 2h^+ \rightarrow \frac{1}{2}O_2(g) + 2H^+(aq) \tag{1.3}$$

$$2\,H^+(aq) + 2e^- \rightarrow H_2(g) \tag{1.4}$$

$$H_2O \rightarrow \frac{1}{2}O_2 + H_2 \qquad \Delta G = 237\ kJ\ mol^{-1} = 1.23\ eV \tag{1.5}$$
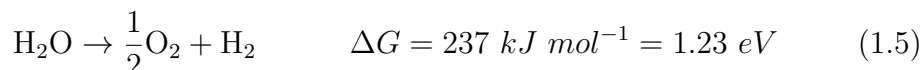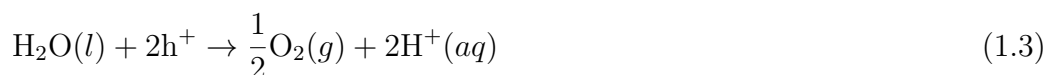
where $\Delta G$ is the Gibbs free energy. In this redox process, the water splitting half-reactions are given first with the full reaction in Equation 1.5.

Conventionally, water splitting is achieved by applying a sufficient electrical potential in *electrolysis* of water. Hydrogen is collected at the cathode and oxygen is collected at the anode. Alternatively, *thermolysis* of water can be achieved at the harsh conditions of temperatures above 2200 °C. In photocatalytic water splitting, energy is supplied by light to a photocatalyst. As can be seen above, excitons with 1.23 eV of energy or illumination with IR radiation is thermodynamically enough to initiate photocatalytic water splitting. However, an over-potential inherent to the photocatalyst (e.g. > 2.2 eV for CNs) must also be overcome for the reaction to proceed at room temperature.

Although full water splitting with hydrogen and oxygen in the ratio of 2:1 is the eventual goal, it is instructive to examine each half-reaction separately. This is because, unlike electrolysis where gas evolution happens on separate electrodes, a

photocatalyst evolves both gases on the same particle. Thus, the recombination rate is high. By using a sacrificial electron donor/acceptor, one half of the reaction is blocked, allowing the other half to proceed without recombination. The higher gas evolution efficiencies by this method allow further understanding of the photocatalysts. One alternative method to allow the evolution of both gases on a photocatalyst particle is to separate them in time. This can be achieved by using the sono-photocatalytic method for example.[35] The hydrogen evolution reaction (HER) is the preferred half-reaction to study. This is outlined in more detail below.

Photocatalytic hydrogen evolution can be separated into five main steps: (1) absorption, (2) excitation, (3) charge transport, (4) redox reactions and (5) product formation (See Figure 1.5).

### 1.3.1  Band Gap Engineering

Band gap engineering is the term given to modify a photocatalyst's energy level positions, thus tuning its conduction band (CB), valence band (VB), Fermi level ($E_{FS}$) and band gap. Band gap tuning is an important part of the material design challenge in photocatalytic research. Tuning the band gap alters the electronic and optical properties, attempting to enhance visible light absorption and photocatalytic performance. It is achieved by copolymerisation, elemental doping, or varying the synthesis conditions.

In Figure 1.6, the valence band and conduction band positions are given for (a) a range of inorganic semiconductors and for (b) carbon nitrides. As can be seen, CNs conduction and valence band positions lie above and below the positions required for water splitting and their electronic properties can be easily tuned to meet the requirements.
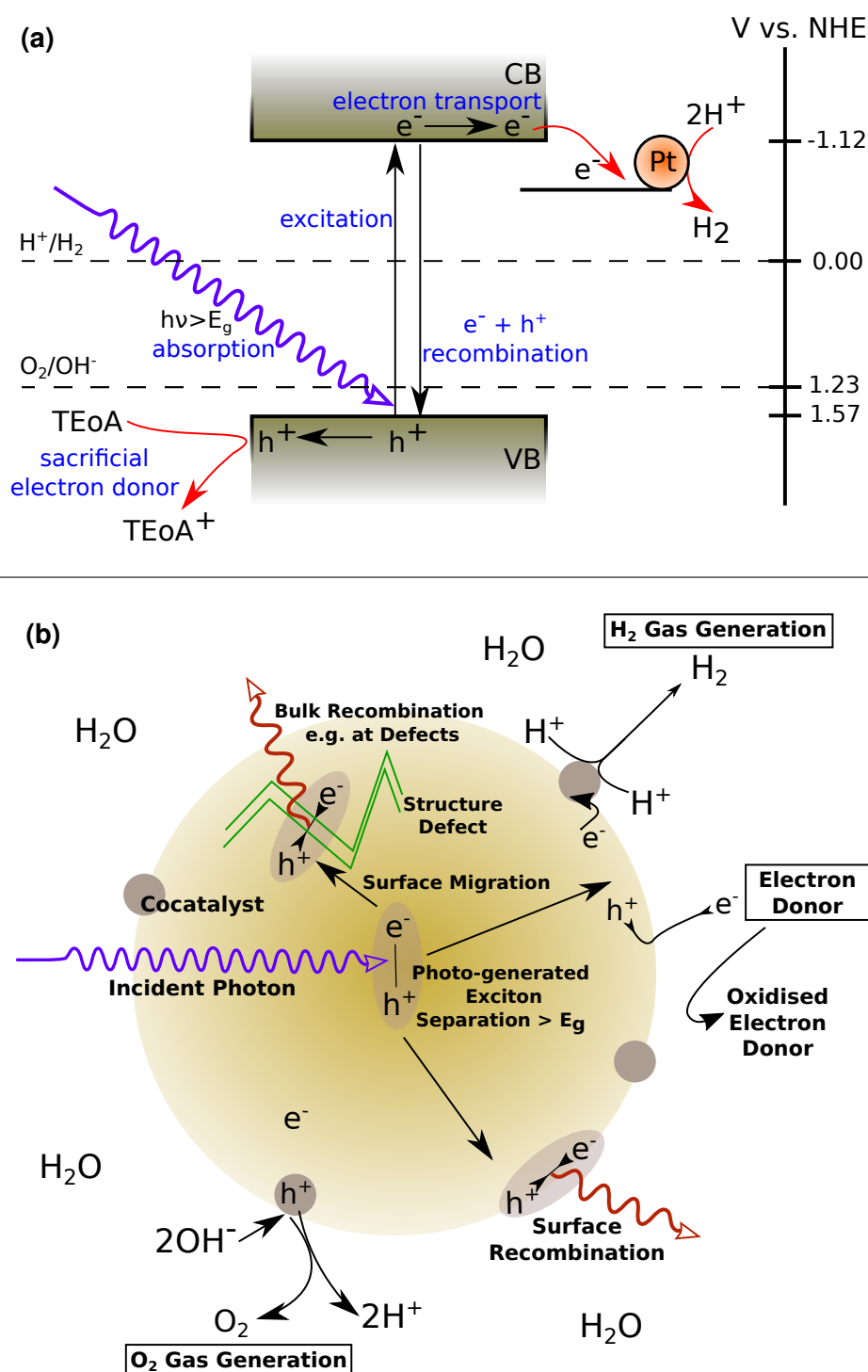
Figure 1.5: **(a)** Working principle of the photocatalytic hydrogen evolution half-reaction with TEoA electron donor and Pt cocatalyst. CB and VB potentials taken from DFT calculations for 'g-C$_3$N$_4$'.[36] **(b)** Scheme of photocatalysis processes on a hypothetical spherical particle with excitons created by light. Charge migration, charge recombination and redox reactions are shown for water splitting.

**(a)**



**(b)**
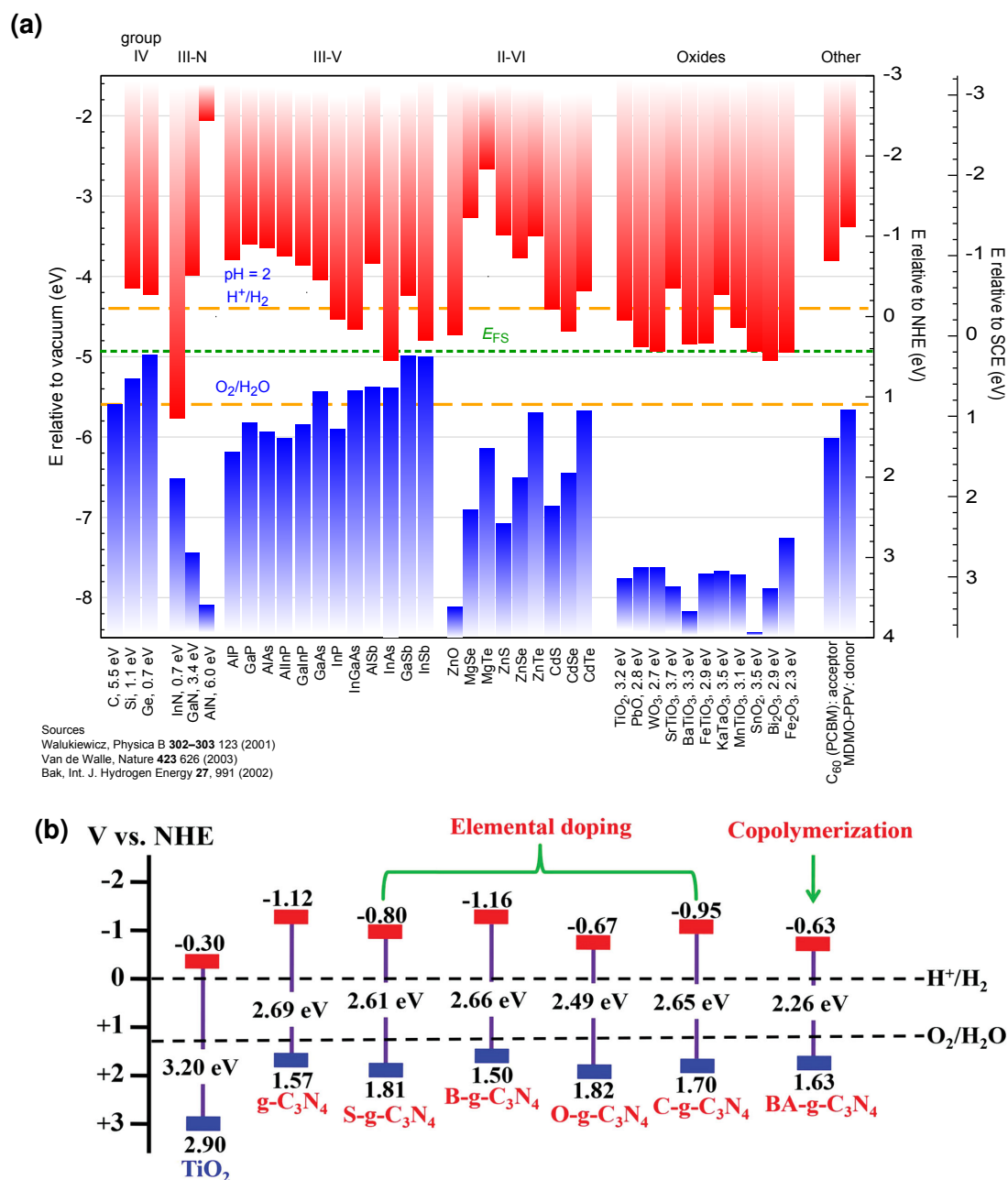


Figure 1.6: **(a)** Conduction and valence band positions for various semiconductors. $E_{FS}$ is the Fermi stabilisation energy. Source: National Renewable Energy Laboratory (NREL), USA. **(b)** Band gaps of different carbon nitrides compared to $TiO_2$. Source: Cao et al.[37]

## 1.4    Motivations and Aims of the Thesis

The motivation for this project originates from identifying carbon nitrides as a new generation of light-element, abundant and functional photocatalysts. Carbon nitrides demonstrated hydrogen evolution from water using visible light in the seminal paper by Xinchen Wang et al.[36] Considering our group's experience with carbon nitrides, and the vast potential of CN photocatalysts, the work began.

The main aims of this thesis and the necessary technical steps are listed below:

1. Develop and screen a variety of semiconductor photocatalysts for their potential for the hydrogen evolution reaction.

2. Selection and installation of a versatile gas chromatograph for hydrogen and hydrocarbon detection and the installation of the Hiden mass spectrometer for real-time gas analysis.

3. Establish the light sources, reactors power meters etc. and the procedures for the photocatalysis lab.

4. Investigate the photoactivity of melem oligomers etc, synthesised by Dr. Hongji Wang.

5. Investigate a range of metal-oxide semiconductors for $O_2$ evolution.

6. Investigate the photoactivity of PTI synthesised by Katharina Schwinghammer.

7. Investigate the photoactivity of heptazine carbon nitrides at long calcination times.

8. Determine the synthesis mechanisms and properties of the material named *white melon.*

# Chapter 2

# Theory of Optical Methods

In this chapter, the optical methods such as absorption and diffuse reflectance spectroscopy and light scattering are introduced. The theory behind the calculation of photonic efficiency and the theory behind the estimation of the optical band gap from diffuse reflectance are outlined.

## 2.1   Definition of Photonic Efficiency

*Photonic efficiency* (PE) is the term recommended by IUPAC for the over-used quantity formerly quoted as quantum efficiency. The term 'photonic' replaces apparent or incident light efficiency. This is in contrast to internal or absorbed light efficiency which does use the term 'quantum'. The term 'yield' is reserved for calculations involving monochromatic radiation whereas 'efficiency' is now recommended for illumination within a wavelength range, as is the case in this work. To sum up, by following the recommendations of IUPAC, the term *photonic efficiency* $\xi$ is used to try to compare various photocatalysts independent of parameters such as light intensity and reactor geometry, although this is not so straight forward as we will see below. Below are the essential equations adapted from IUPAC and current literature:[38]

> **Photonic efficiency, $\xi$:** Ratio of the rate of the photoreaction measured for a specified time interval (usually the initial conditions) to the rate of incident photons within a defined wavelength interval inside the irradiation window of the reactor.[38]

The equation for photonic efficiency as defined by IUPAC is:

$$\xi = \frac{\frac{dn}{dt}}{\int_{\lambda 1}^{\lambda 2} q_{np\lambda}^{0} \, d\lambda} \tag{2.1}$$

where $n$ is chemical amount.* The 0 superscript in $q_p^0$ infers incident photon flux before adsorption.

Spectral photon flux $q_{np\lambda}$ in units of $s^{-1} \, m^{-1}$ is:

$$q_{np\lambda} = \frac{dq_p}{d\lambda} \tag{2.2}$$

Photon flux $q_p$ is a photon quantity. In reality, we measure a radiometric quantity called the radiant power. This is in effect the photon flux over a wavelength range (i.e. the wavelength-dependent photon flux) and is given by the integral below.

$$q_p = \frac{1}{hc} \int_{\lambda 1}^{\lambda 2} P(\lambda) \, \lambda \, d\lambda \tag{2.3}$$

---

*number of entities divided by Avogadro constant

where $P(\lambda)$ is the radiant power in units of $J\,s^{-1}$ or Watts:

$$P(\lambda) = \frac{dW}{dt} \tag{2.4}$$

where W is the radiant energy over the wavelength range in Joules:

$$W = \int_{\lambda} W_{\lambda}\,d\lambda \tag{2.5}$$

The calculation of photonic efficiency is an essential parameter to compare photocatalyst materials independent of light intensity, spectral range, amount of catalyst, illumination time etc. Determining the concentration of evolved hydrogen relates the calibrated ppm value obtained from the GC and uses the assumptions of the ideal gas law for hydrogen to estimate the molar hydrogen amount. Alternatively, a reference value for the density of hydrogen at normal temperature and pressure conditions ($0.083764$ kg m$^3$ at NTP)[39] can be used and essentially both methods agree to within an error of $\pm$ 0.0002 µmol h$^{-1}$. The estimation of the photon rate is more difficult due to the complication of photon energy varying with frequency of light and the measured photon rate is an average over the spectral range. A simplified but effective first estimation is to assume monochromatic light centred on the spectral range used. However, this neglects the higher energy photons contributing more to the total power.

Measuring the spectral response of the light filter used in the calculation is useful for determining which photons are contributing and at what frequency and this can be measured with a calibrated irradiance spectrometer.

## 2.2  Calculation of Photonic Efficiency

Photonic efficiency calculations were progressively established with reference to published recommendations,[38,40–43] and increased certainty of the experimental parameters.

Two calculations for converting $H_2$ concentrations to molar concentrations were cross-checked. Firstly, the density of $H_2$ gas at NTP[44] and secondly using the ideal gas law. The latter was chosen as the default method as it is derived from the gas constant and the reaction temperature is included. Essentially, both methods were compared to show that they give similar results with an error of $< 1\,\%$.

The most challenging parameter to consider is the µmol photons per hour. Three methods were used for this calculation, giving slightly different results with decreasing certainty but with better assumptions of the experimental parameters. The three methods relate to calculating the number of photons being illuminated.

The difficulty lies in calculating the number of photons in a given total energy measured. If each incident photon has a single energy, we simply divide the total power by the photon energy to get the total number of photons. However, in my experiments, a range of photon energies is used depending on the transmitted spectrum. UV photons have much more energy than red light photons and will contribute more to the total power. We can calculate the energy for each photon in the range and then take this into account but now we assume that each photon contributes equally. This is what the second method (square wavelength response) uses. Finally, we want to quantitatively consider which photon energies contribute. We can also obtain this data from the spectral response of the incident light or transmission spectrum of the filter used.

**Central-photon**  The photonic yield[†] is calculated by assuming all photons have a single energy and dividing by the total energy measured by the power meter. This assumes monochromatic light.

**Square wavelength response**  The illumination range (and thus photon energies) is considered but with a square spectral response, meaning that every contributing photon energy is assumed to contribute equally. This method assumes a filter with a perfectly square spectral response.

**Spectral response**  The true spectral response of the incident light or filter is considered. The drawback is that this must be measured quantitatively with a spectrometer calibrated for irradiance measurements and at the correct distances i.e. measure the actual spectral irradiance of the lamp or filter at the sample position. From this, the accurate spectral response is determined.

---

[†]the term yield is used for monochromatic light [IUPAC]

The equation for the calculation of photonic efficiency is given in the following relation:

$$\xi\,(\%) = \frac{M_{H_2} \times 2}{M_{Photons}} \times 100 \tag{2.6}$$

$$M_{H_2} = \frac{\frac{C_{H_2}}{t_i} \times V}{R_g T} \tag{2.7}$$

where $\xi$ is the symbol for photonic efficiency, $M_{H_2}$ is the molar hydrogen evolution rate in $\mu\text{Mol}\,\text{h}^{-1}$, $C_{H_2}$ is the concentration of hydrogen in ppm, $t_i$ is illumination time in hours, $V$ is headspace volume of the reactor (e.g. 210 mL), $R_g$ is the gas constant (e.g. 8.3144621 $\text{J}\,\text{Mol}^{-1}\,\text{K}^{-1}$)[45] and $T$ is the reaction temperature (e.g. 298 K). Calculating the molar photon rate $M_{Photons}$ requires further explanation. Below, the rate for a single photon of energy $\frac{hc}{\lambda}$ is:

$$P(\lambda) = P \times A_i \tag{2.8}$$

$$q_{p\lambda} = \frac{P(\lambda)}{\left(\frac{hc}{\lambda}\right)} \tag{2.9}$$

$$M_{Photons} = \frac{\left(\frac{q_{p\lambda}}{t_i}\right)}{N_a} \times 10^6 \tag{2.10}$$

$P(\lambda)$, as we have seen in the IUPAC definition above, is the radiant power, whereas $P$ is the measured power of incident light in units of $\text{W}\,\text{cm}^{-2}$. $A_i$ is the illumination area of the catalyst suspension in $\text{cm}^2$, $q_{p\lambda}$ is the radiometric photon flux as above, $t_i$ is illumination time in hours and finally $N_a$ is the Avogadro constant.

In the above expression, all photons have the same energy corresponding to the chosen wavelength. This is the commonly used method in photocatalysis where a monochromatic source is assumed. In reality, even for a narrow band-pass filter, a range of photon energies contribute with high-energy blue photons contributing more energy than green photons. The above expression for $q_{p\lambda}$ must then be modified to include the integral of all photon energies $q_p$, which is given in Equation 2.3. Practically, this integral can be measured using a calibrated spectrometer if the irradiance spectrum of the incident light at the sample distance is recorded. In summary, for a monochromatic light source such as a laser, the photonic efficiency calculation is straight forward but lasers are rarely used due to their small spot-size. For a xenon lamp with filtered output light, the calculation of the molar photon rate requires further careful consideration.

## 2.3 UV-Vis Absorption Spectroscopy

Arnold Beckmann and Howard Cary pioneered the first commercially available UV-Vis spectrometers in the 1940s.[46] A UV-Vis instrument compares the intensity of incident and transmitted light $I$ and $I_0$ to give the transmittance $T$. The transmittance of light is defined as the ratio of the incident and transmitted radiant flux. The transmittance is also related to the reflectance $R$ and absorptance $A$ by Equation 2.12. Note that we use 'absorptance' which excludes scattering, photoluminescence, refractive index gradients and energy transfer effects etc. *Absorptance* is the term used for the energy absorbed by the material, it is often confused with *absorbance (Abs)* which is a measure of the energy that passed through the material.[47,48] When $A \leq 1$, $A \approx Abs$.

$$T = \frac{I}{I_0} \tag{2.11}$$

$$T = 1 - R - A \tag{2.12}$$

$$T = 10^{-Abs} \tag{2.13}$$

If reflection, scattering and other effects are negated—as they are in solutions—the absorption of that solution can be obtained ($Abs = 1 - T$). This is the conventional absorbance measurement that a UV-Vis spectrometer is known for.

According to Johann Lambert, absorption is proportional to the thickness of a sample ($Abs \propto l$).[49] According to August Beer, absorption is proportional to the concentration of a sample ($Abs \propto c$).[50] Combining, we get the well-known Beer-Lambert law.

$$Abs = \epsilon c l = \alpha l \tag{2.14}$$

$$Abs = \log \frac{I_0}{I} = -\log T \tag{2.15}$$

Where $\epsilon$ is the molar absorptivity coefficient, $c$ is concentration and $l$ is path length. $\alpha$ is the absorption coefficient also called the attenuation coefficient.

Above, we record the transmitted light to get the absorbance with the aim of extracting the absorption properties but can we get information from reflected light?

# 2.4 Diffuse Reflectance and Band Gap Estimation

A UV-Vis spectrometer normally used for determining the absorbance of solutions can be used in reflectance mode to estimate the optical band gap of potential photocatalysts. The diffuse reflectance method uses the diffuse reflectance accessory (DRA). The main component is a sphere made of an optically white standard reflectance material (e.g. $BaSO_4$). Powders were prepared between two quartz discs and placed at the edge of the sphere. Diffuse light is collected by the detector after multiple diffuse reflections inside the sphere. Spectra were measured in diffuse reflectance mode and band gaps were estimated using a modified Kubelka-Munk analysis method as described below.
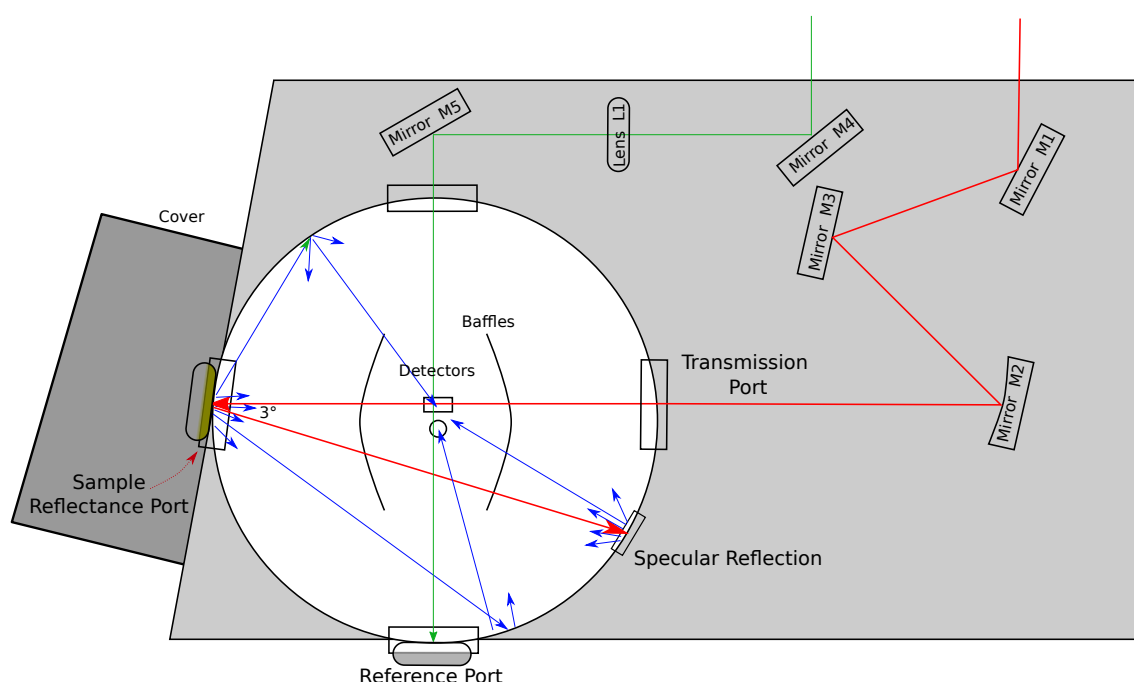


Figure 2.1: Topdown plan of the UV-Vis diffuse reflectance accessory. The diagram shows the 3° hemispherical diffuse reflectance of a powder sample.

## 2.4.1 Kubelka-Munk Theory

This theory is popular because of the simple relations it provides. It is rather limited and caution must be taken to apply it correctly and to be aware of its limitations.[51] Practically speaking, metallic samples should not be used because of their highly specular reflections. Dark coloured samples such as grey or brown are also unsuitable for Kubelka-Munk theory due to their poor reflection and lack of distinct absorption edge. Intensely coloured samples suffer from poor reflectance and should only be applied when diluted with white standard powder. The theory has the following assumptions:

- Incident light is diffuse and monochromatic

- No specular reflections but an isotropic distribution

- Particles randomly distributed (optically rough)

- Particle size much smaller than sample thickness

- More than half of the light is reflected and none is transmitted

- No photoluminescence losses

- Absorption edges are linear

The Kubelka Munk function (F(R)) is given below. It is a function of reflectance and is related to absorbance with the following relation:

$$F(R_\infty) = \frac{(1 - R_\infty)^2}{2R_\infty} = \frac{k}{s} \tag{2.16}$$

Where $R_\infty$ is diffuse reflectance, $k$ is the absorption coefficient and $s$ is the scattering coefficient. In reality, we do not measure the absolute reflectance but a relative reflectance to the white standard $R\%$. Where $R_\infty \equiv \frac{R_{sample}}{R_{standard}} = R\%$.

### 2.4.2 Optical Band Gap Estimation

One of the most crucial parameters of a photocatalyst is the band structure, especially the absolute positions of the conduction band (CB) bottom and the valence band (VB) top, respectfully. It is important to evaluate these positions relative to the redox potentials involved to order to gauge whether a photocatalytic reaction will proceed. These values are difficult to accurately determine but if one is known, the other can be calculated by using the band gap value. This is useful as the optical band gap can be estimated easily using a spectrometer.

Tauc et al. proposed the following equation relating absorption coefficient $\alpha$ to the band gap $E_g$:[52,53]

$$(h\nu \cdot \alpha) \propto (h\nu - E_g)^{1/n} \tag{2.17}$$

$$(h\nu \cdot \alpha)^n \propto (h\nu - E_g) \tag{2.18}$$

where $h$ is Planck's constant, $\nu$ is frequency of light, $\alpha$ is the absorption coefficient and $E_g$ is the optical band gap. The exponent $n$ depends on the type of optical transition of the semiconductor as derived from quantum perturbation theory.

For example, since carbon nitride is claimed to be an indirect semiconductor,[54] we plot for $n = \frac{1}{2}$ (indirect allowed transitions).

Table 2.1: Tauc exponents for semiconductor optical transitions.[55]

| Tauc exponent (n) | Transition |
|---|---|
| 2 | direct (allowed) |
| 2/3 | direct (forbidden) |
| 1/2 | indirect (allowed) |
| 1/3 | indirect (forbidden) |

Note that for our diffuse reflectance measurements the function is $F(R_\infty)$ not $\alpha$ as above. In solution, the scattering coefficient is wavelength-dependent (i.e. Rayleigh type scattering with a $\lambda^{-4}$ dependence). However, in a solid powder with no solvent interaction it is predominantly wavelength-independent. If we assume that the scattering coefficient is independent of wavelength, we can replace $\alpha$ in the relation above with $F(R_\infty)$. So finally, with $C =$ a constant, we substitute and rearrange the Tauc model above to get:

$$(h\nu \cdot F(R))^n \propto (h\nu - E_g) \tag{2.19}$$

$$(h\nu \cdot F(R))^n = C(h\nu - E_g) \tag{2.20}$$

$$(h\nu \cdot F(R))^n = Ch\nu - CE_g \tag{2.21}$$

This is Tauc's expression in a linear form as applied for diffuse reflectance. If we plot our diffuse reflectance data as $(h\nu \cdot F(R))^n$ vs. $h\nu$, it is possible to extract the band gap $E_g$ from the linear region of the plot. This graph is referred to as a Tauc plot and an example is given in Section 5.14 on page 110. To determine the band gap, we apply a linear fit to the absorption edge. Caution must be taken when choosing the range of the linear fit, It is recommended that the derivative of the Tauc plot be taken to unambiguously determine the range as described on page 112. This is recommend for three reasons: (1) The Tauc expression only applies to linear data, some absorption edges may have a wavelength-dependence which makes them nonlinear. (2) The exact range is determined by where the absorption edge deviates from a linear form as clearly seen in the derivative. (3) An absorption edge is often made of multiple linear regions which require separate linear plots.

A good linear fitting of the Tauc plot corresponds to Equation 2.21. Accordingly, the slope is the constant $C$ and the y-axis intercept is $CE_g$. Therefore the band gap is determined by dividing the intercept by the slope. Alternatively, setting the Tauc function to zero, $(h\nu \cdot F(R))^n = 0$, the equation simplifies to $E_g = h\nu$. Thus, the band gap is the baseline intercept. This is the preferred method as the band gap can

be easily determined by eye from the Tauc plot.

$$E_g = h\nu - \frac{(h\nu \cdot F(R))^n}{C} \tag{2.22}$$

Note that the baseline intercept will not correspond to the x-axis intercept, especially if non-zero reflectance is observed at longer wavelengths of $F(R)$. To improve the accuracy of the band gap estimation, it is recommended to ensure that the $F(R)$ reflectance minimum is zero (usually at longer wavelengths) or that a baseline is applied. It is possible to vertically translate the data to ensure that the reflectance minimum is zero but this once again relies on the assumption that the scattering in the powder is wavelength-independent. In fact, a slope in the reflectance at longer wavelengths (inside the band gap) is a sign that the reflectance has a wavelength-dependence and may not be suitable for analysis.[48]

As we have just seen, the Kubelka-Munk theory relies heavily on the scattering coefficient $s$. Another highly recommended step to improve accuracy (although it is rarely performed for practical reasons), is to dilute the sample powder with the white standard reference material powder. This is especially recommended for highly absorbing coloured samples. Diluting the sample with the white standard will increase the overall reflectance. This serves to strengthen the validity of the Kubelka-Munk theory and so results in more reliable band gap estimations.[48,56]

## 2.5   Introduction to Light Scattering

Light scattering is the redirection of electromagnetic radiation by interaction with matter. It depends on the particle size, refractive indicies of particle and media and the wavelength of light. To distinguish different scattering behaviours, we can assume the *scattering size parameter* $x = \frac{2\pi r}{\lambda}$, where $r$ is the radius of a spherical particle and $\lambda$ is the wavelength of light, then we can identify three light scattering regimes.[57] We can say that the *Rayleigh scattering regime* applies when the wavelength of light is much smaller than the particle size or when $0.002 \leq x \leq 0.2$, and the *Mie regime* applies when the particle size is of the order or larger than the wavelength, or when $0.2 \leq x \leq 2000$. At large particle sizes, $x >> 1$, scattering is governed by geometric optics.[48,58]

The wavelength dependence is one of the distinguishing parameters of scattering with a strong dependence at small particle sizes. This dependence ranges form $\lambda^{-4}$ (Rayleigh regime) to $\lambda^{-1}$ (Mie regime) for larger particles. It is this strong wavelength dependence that results in the characteristic blue tinge of light given off by a highly scattering medium. Another characteristic parameter is that Rayleigh scattering occurs equally in the forward and back scattering directions but as the particle size increases, the intensity of forward-scattered light dominates.

John Tyndall, an Irish-born physicist was the first to document the scattering of light from which the name of the Tyndall effect is given. Tyndall was the first to prove the greenhouse effect by showing the infrared absorbing power of the atmospheric gases and especially of water vapour. During these studies, Tyndall acquired particle-free air samples. It was from these investigations that Tyndall published his work on light scattering.[58,59] This work was later built upon by Rayleigh and much later by Lorenz, Mie, and Debye.

# Chapter 3

# Equipment Setup and Gas Measurements

In this chapter, the procedures and equipment used for photocatalysis, gas chromatography (GC) and mass spectrometry (MS) are outlined. Diagrams of the xenon lamps with optics, plumbing diagrams for the GC and operation modes of the mass spectrometer are provided.

## 3.1    Photocatalysis Equipment Layout

In Figure 3.1 a photo of the PC laboratory and the layout of the equipment is shown. In the centre, the anodised aluminium light-box shields the xenon lamps from the outside when in use. It contains three xenon lamps with stirring plates, reactor clamps and cooling water lines. To the right is the gas chromatograph which is the main detector for evolved gases.

The following sections provide in-depth descriptions of the xenon lamps, reactors, gas chromatograph and the mass spectrometer.
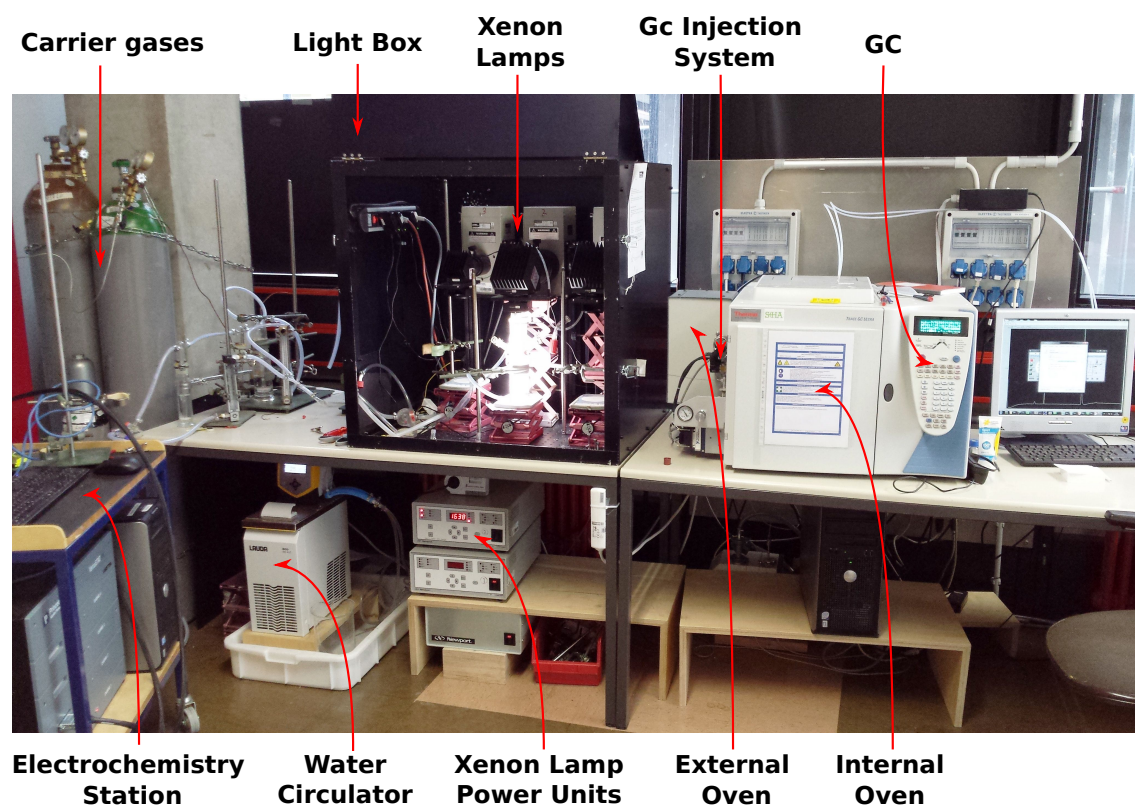


Figure 3.1: Layout of the photocatalysis setup: The light-box in the centre contains three xenon lamps fixed to an optics plate. A reactor under illumination is seen under the central lamp. A hole in the side of the light box allows the GC injection line to connect directly to the reactors. Power cables and cooling water tubes are accessed through the back of the light box. SPF50 sunscreen is also available to the right of the GC!

## 3.2 Xenon Lamps and Light Sources

Initially inexpensive light sources such as fluorescent bulbs and handheld UV mercury vapour lamps were used to illuminate photocatalyst samples. Eventually, research grade xenon lamps were obtained with appropriate filters and optics. A 300 W ozone free xenon lamp fitted with a water filter and a beam turning assembly were used to selectively illuminate visible, UV or a specified wavelength range. This section outlines the lamp setup, the resulting intensity and spectral profiles.

### 3.2.1 Basic Light Sources

Many light irradiation sources were tested, high power xenon lamps, handheld Hg-vapour lamps, fluorescent Hg-vapour tubes and even the Suebian summer sun!

**Hg-vapour tubes:** Handheld UV lamps are common in the lab for testing fluorescence and curing polymers. A Konrad Benda UV lamp was used for illuminating photocatalysts with UV light. (Selectable radiation centred at 254 and/or 365 nm with $2 \times 6$ W power rating).

**Fluorescent tubes:** The long fluorescent tubes (Osram Biolux®) are useful for illuminating up to eight samples at the same time and (provided samples are positioned correctly) with the same lighting conditions, (see Figure 3.2 **(a)**). This is advantageous for quickly obtaining trends, comparing similar photocatalysts and optimising experimental parameters. The main disadvantage of this light source is the low light intensity (18 W power rating). Because of this, experiments suffer from low gas evolution rates.

The Biolux fluorescent tubes were designed to mimic sunlight in a terrarium. They transmit UV light which is otherwise blocked in a conventional fluorescent tube. This means these fluorescent tubes give a closer approximation to natural sunlight, and so proved a useful illumination source for screening photocatalysts (see Figure 3.2 **b**).

The previous two commercial light sources provided a useful start to probe the photoactivity of samples. However, they lack the reliability, dependability and available technical data of research grade sources. Because of this, high power xenon lamps were chosen as detailed in the following section and illustrated in Figure 3.3.
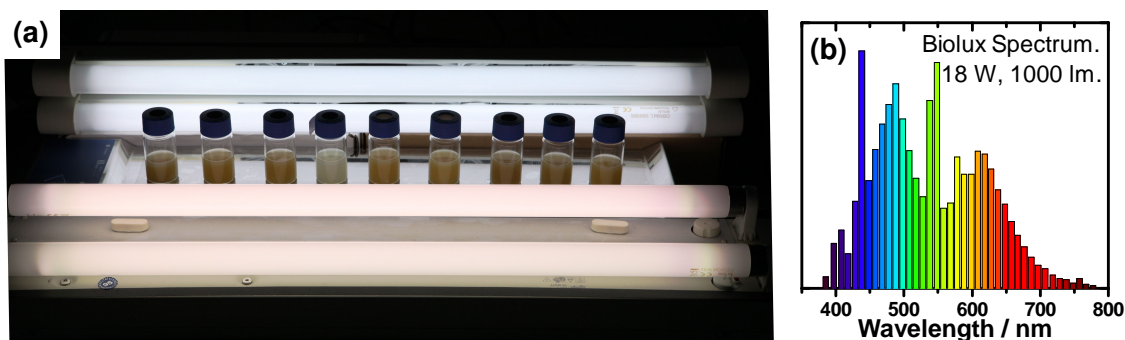
Figure 3.2: **(a)** Illumination of samples with fluorescent tubes which mimic natural sunlight. Biolux® tubes are in the background and conventional fluorescent tubes are in the foreground. **(b)** Spectrum of Biolux tubes showing extra UV emission.

## 3.2.2 Xenon Lamp Components and Setup

The components and accessories for the xenon lamp are important to consider as they affect the eventual spectral response and intensity.

**Xenon bulb** The xenon bulb is the core of the xenon lamp. It is 25 atm. of xenon gas in a quartz glass envelope with tungsten cathode and anode filaments. The filament can slowly deposit on the inside of the quartz envelope with use over time, decreasing the light intensity and weakening the glass wall. Because of this, typical bulb lifetimes are $\approx 1000$ h.

**Rear reflection mirror** Normally only a small angle of the xenon light is output. This mirror captures the back-reflected light and adds it to the output beam, Thus there are now two intense spots in the focused output beam (see Figure 3.4**(b)**). The mirror adds $\approx 30\,\%$ to the intensity of the light.

**Condensing lens** This lens system allows focusing of the output beam to allow collimated light at the output. It also serves as a way to adjust the intensity by changing the spot size.

**Water filter** The water filter is an anodised aluminium liquid container with quartz windows at each end. Shining the beam through the water filter removes IR radiation by absorption. The IR radiation is unnecessary for our applications and is also a fire hazard due to its heating effect. Although water has a high heat capacity, a cooling jacket is also provided to remove heat from the system. Removing heat from the lamp is also beneficial for the bulb lifetime, as this reduces operation at high temperatures. The transmission spectrum of the water filter is given in Figure 3.6**(a)**.
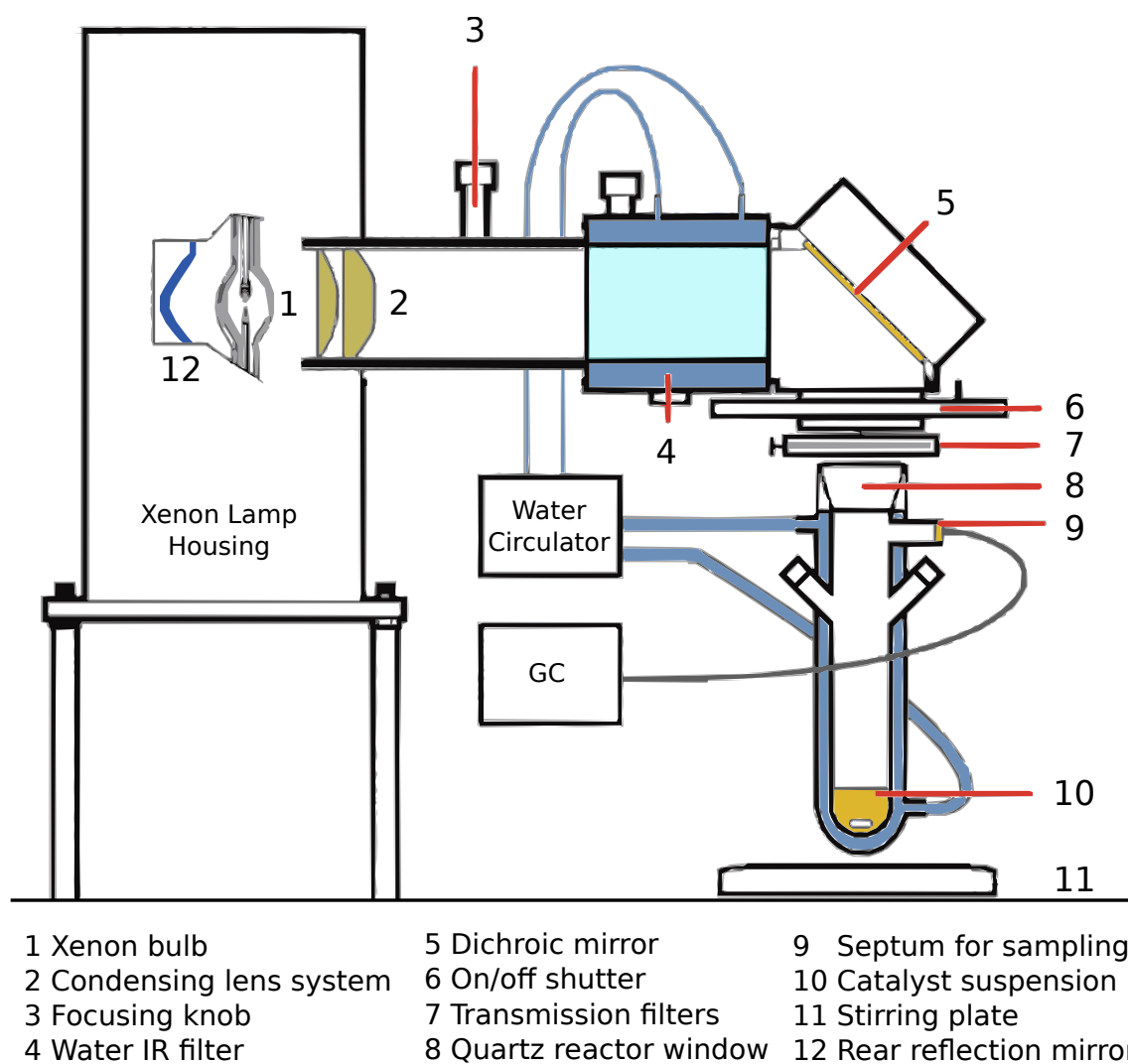
Figure 3.3: Cross-section diagram of xenon lamp setup showing xenon lamp housing, condensing lens, water filter, beam turning dichroic mirror, manual on/off shutter and the reactor.

**Beam turning mirror assembly** The beam turning assembly reflects the output beam by 90°. The assembly can then be rotated to allow top- or side-illumination. It also allows for dichroic mirrors instead of full reflection mirrors. These dichroic mirrors have distinct advantages over other transmission type filters as outlined next.

**Dichroic mirrors** Dichroic mirrors reflect part of the spectrum and absorb or transmit the rest. This can be useful for choosing visible or UV illumination conditions. Although the optical coatings are vulnerable to scratches, they have a high reflection in the selected range and are ideal for broadband sources. More details are listed in Table 3.1 and the reflectance spectra of the dichroics are provided in Figure 3.6**(b)**.

**Transmission light filters.** Transmission filters are convenient for shaping the output spectrum and selecting narrow bands of the spectrum. Since they absorb untransmitted light, they can easily break if not used in conjunction with other filters. Details of the transmission filters are also given in Table 3.1.

### 3.2.3 Light Intensity on the Suspension

The central aspect of photocatalysis is the irradiation of light to activate the photocatalyst. It is therefore imperative to understand the illumination of samples under investigation. The light intensity of a point source decreases with an inverse square relation with increasing distance. For a non-point source such as a xenon bulb, the relationship holds true for distances greater than five times the filament's spark-gap distance (i.e. > 2 mm). Put simply, a small change in distance results in a large change in light intensity. For a photocatalysis experiment, the distance between the lamp and catalyst suspension must be kept constant if the same intensity of light is to be reproduced.

The light intensity impinging on the photocatalyst is an essential measurement and greatly affects the photonic efficiency as discussed in Section 2.1. Care must be taken to measure this quantity accurately and consistently.

Two beam intensity configurations were chosen in these experiments, the first to maximise light intensity and the second to provide a uniform intensity distribution over the spotsize. Firstly, to optimize light intensity–and thus hydrogen production–the xenon lamp condensing lens was focused. This gave the highest intensity ($\approx 2.6$ W at the sample) but most extreme intensity distribution (an image of the xenon filaments with two bright spots 3.4**(b)**). The lamp image was then brought slightly out of focus to blur the image. This gave an uneven intensity gradient from the centre outwards but with high intensity light.
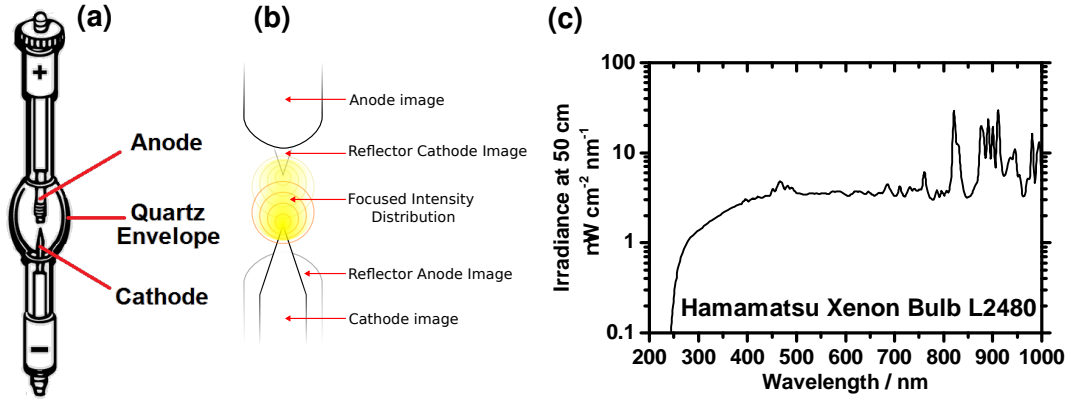
Figure 3.4: **(a)** Diagram of the xenon bulb. **(b)** Resulting focused image of the xenon bulb and reflector image. **(c)** Spectral irradiance of the Hamamatsu xenon bulb.

Secondly, to achieve a more uniform intensity distribution at the expense of high intensity, the xenon lamp was unfocused using the condensing lens system. This allowed a tuning of the intensity without changing the operating power of the lamp. This was the method of choice, for example, when using the AM1.5G conditions to achieve 1 sun illumination with a good intensity distribution. AM1.5G is short notation for air mass coefficient where 1.5 denotes one and a half atmospheres and G denotes global conditions at mid latitudes.

### 3.2.4 Light Intensity Meters

Initially a PM3 (Coherent Optics) power meter was used. Then the S310C thermopile (Thorlabs) power meter was used in all experiments of this work (see Appendix A.2 for specifications). The advantage of this unit is its ease of use, speed and functionality. Moreover, it has a flat spectral response across the whole UV-Vis region (see Figure 3.5). The main disadvantage is its large size since it could not be placed inside the reactor. Another point to note is that the measurements are temperature sensitive and although this effect is corrected with an internal temperature sensor, care must be taken. An alternative power meter for measurements inside the reactors is a Si photodiode (Si227-66BR, Hamamatsu). The disadvantage is that the measured voltage must be calibrated and corrected to the sensor spectral response and its small size makes it difficult to fix perpendicular to the incident light.
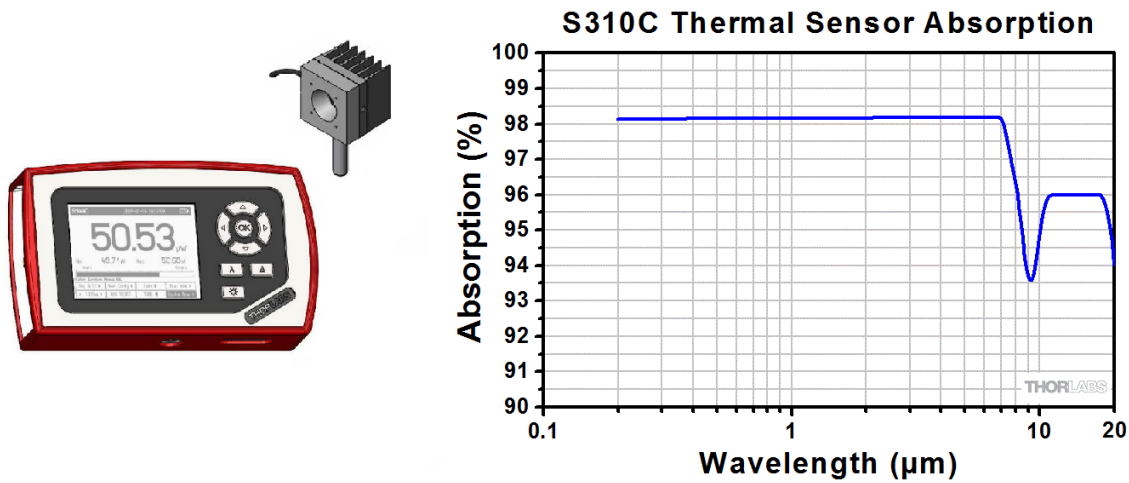


Figure 3.5: Light intensity meter with sensor head and absorption response of the thermal surface absorber coating. Images source: Thorlabs.

### 3.2.5 Spectral Ranges and Filters

The main advantage of using xenon lamps over solar simulators is their versatility. Various spectral ranges could be chosen using the optical filters and mirrors. Primarily, samples were illuminated with visible light or UV light using the dichroic mirrors (spectra shown in Figure 3.6**(b)**). The spectral output could also be shaped with a range of other filters. For example, the spectra of 40 nm bandpass filters are shown in Figure 3.7 on page 37. Details of these and other filters are provided in Table 3.1 below.

Figure 3.6**(c)** shows the measured spectra of the final output beam of the xenon lamps under various illumination conditions. Mainly, we can see the difference between the full arc reflection, AM1.5 conditions and visible light. A UV bandpass filter is also shown for comparison. The spectra resemble the profile of the xenon irradiance spectra as seen in Figure 3.6**(c)**. Many of the characteristic xenon lamp peaks match. However, we can see that much of the IR radiation has been reduced by the water filter above 900 nm.

Table 3.1: Bandpass & longpass light filters with their measured spectral ranges, transmissions and central wavelengths. Spectral ranges are the filters' wavelength range above 5 % transmission.

| Filter Name | Spectral range (nm) [†] | Wavelength Peak (nm) | FWHM (nm) | Transmission $T_{paek}(\%)$ |
|---|---|---|---|---|
| Dichroic UV | 300–460 | – | – | 97* |
| Dichroic Visible | 420–750 | – | – | 98* |
| Full Arc/Reflection | 300–850 | – | – | 93* |
| Visible (GG420) | 420–850 | – | – | 87 |
| UV Filter (UG1) | 332–396 | 373 | 30 | 83 |
| Blue Filter (BPF70) | 409–506 | 455 | 56 | 68 |
| BP400 | 380–430 | 402 | 43 | 42 |
| BP450 | 430–472 | 460 | 35 | 65 |
| BP500 | 477–528 | 500 | 39 | 77 |
| BP550 | 524–580 | 553 | 40 | 70 |
| BP600 | 575–632 | 600 | 45 | 76 |
| BP650 | 628–676 | 652 | 38 | 72 |
| BP700 | 675–730 | 698 | 41 | 75 |
| BP750 | 724–780 | 750 | 44 | 79 |
| BP800 | 780–820 | 800 | 40 | 75 |

---

[†]defined as wavelength range above 5 % transmission.

*These values are reflection ($R_{peak}$ %) for the mirrors
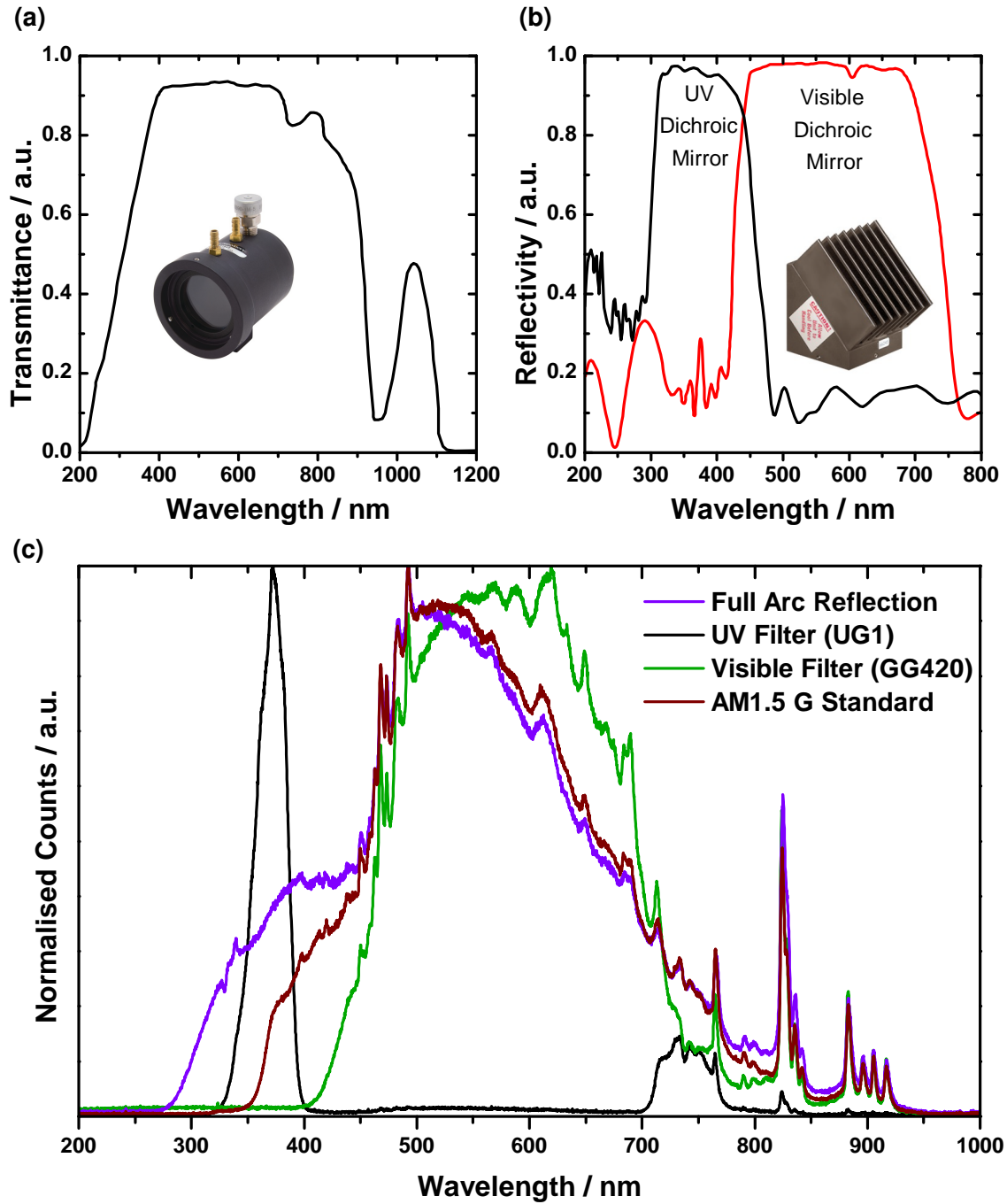
Figure 3.6: Xenon lamp spectral ranges: **(a)** Transmittance of the water filter containing deionised water. **(b)** Reflectance of the visible and UV dichroic mirrors. **(c)** Measured spectra of the final output beam using transmission filters in UV (Bandpass FSQ-1UG), visible (Longpass FSQ GG420), full arc and AM1.5 conditions.
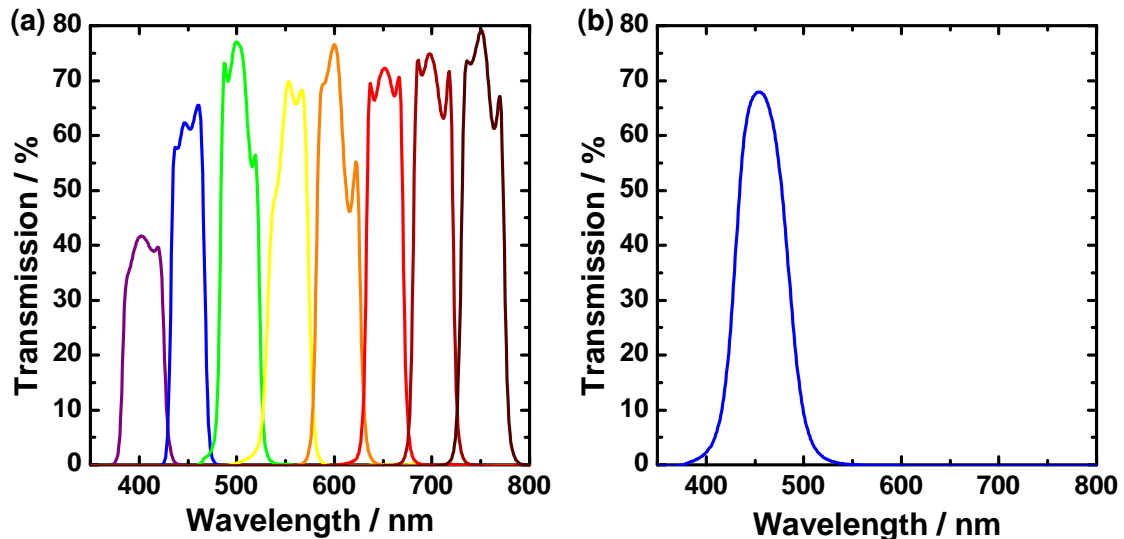
Figure 3.7: **(a)** Transmission spectra for a series of filters used for wavelength-dependent measurements. Full width at half maximum (FWHM) of 40 nm. **(b)** Transmission filter in the blue region used for photonic efficiency calculations. Gaussian profile with a central wavelength at 454 nm and a FWHM of 56 nm.

### 3.2.6 Programmed Lamp Timers

A series of computer programs "Tuffy Timer 2000" were programmed to provide an automatic timer for the lamps (Figure 3.8). Interfacing the power units with the computer provided the advantage of automatically controlling the ignition and quenching of the xenon lamps at set times. This ensured exact running times and safe lamp operation overnight and proved to be valuable in the lab by allowing more experiments to be run.

The programs also record run times etc. to a log called "Xenon_Log.txt" for future reference. The programs have two main functions: (1) digital communication with the power units through the RS232 serial port and (2) timing functions to set and count the running time, delay time, end time, error codes etc. The source code and other details of the program are given in the appendix (page 168).
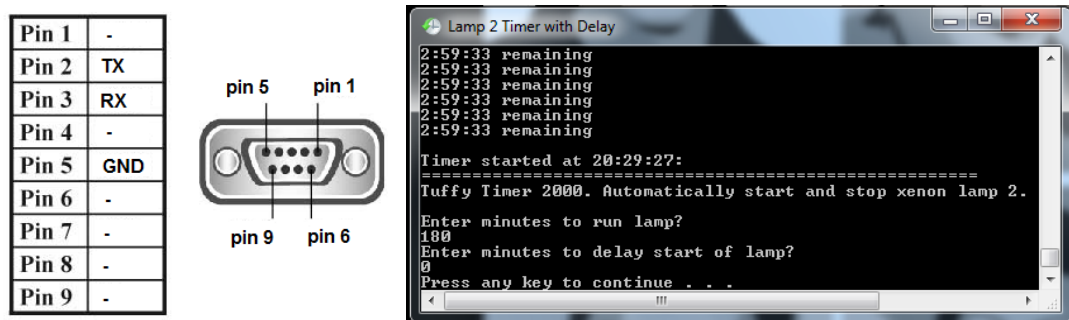


Figure 3.8: Pin-out assignment for the RS232 port and screenshot of the timer program which automatically starts and stops the xenon lamp.

## 3.3   Reactors for Photocatalysis

The *gas-tight, lots-of-light, right-height* reactor and its geometry are important to consider. Initially, 24 mL vials from Chromacol with silicone septa coated with Teflon® (PTFE) on one side, were used as gas-tight reactors. Currently, 230 mL purpose-made quartz glass reactors with water cooling jackets are used as the main photocatalysis reactors. The PTFE coating on the septa ensures the reactors are gas-tight to $H_2$. The glass transmission is also considered to ensure that enough UV light reaches the sample. As shown in Figure 3.9 the borosilicate glass of the 24 mL vial measures 86 % transmission at 365 nm, the main emission line of a Hg-vapour lamp. For the larger reactor, a quartz window is used for superior UV transmission. Both reactors used in this work are described below.

**24 mL Vial:**   The advantages of these vials are their low cost, ease of use and high sample throughput. The major drawbacks are the small headspace volume, ill-defined illumination window,* heating and occasional air leaks through the septa. Air leaks are now eliminated by inverting the vials during illumination so that the suspension itself acts as a barrier to the septum. Inversion also means top-down illumination through the base of the reactor and this gives a well-defined illumination area. During illumination, the vial gets hot. However, a cooling-fan can circulate air to the vial to maintain the operating temperature at $\approx 70$ °C.

**230 mL Reactor:**   Upgrading from vials, larger purpose-made glass reactors are now used. A quartz window, water cooling and gas-tight connections are included. The quartz window ensures excellent UV transmission, the water cooling provides exact temperature control with the use of an external water circulator (Lauda Eco) and the ground-joints provide gas-tight connections for evacuating and purging. Thus, issues with air leaks have been resolved. Table 3.2 compares key details of both reactor types.

Table 3.2: Comparison of vial and reactor typical dimensions and transmission.

|  | Volume (mL) | Headspace (mL) | Inner Diam. (cm) | Light Direction | Transmission at 366 nm (%) |
|---|---|---|---|---|---|
| **Vial:** | 24 | 14 | 2.50 | Side/Bottom | 86 |
| **Reactor:** | 230 | 210 | 2.15 | Top | 92 |

---

*Side illumination on the curved surface of the vial gave ambiguous illumination conditions.
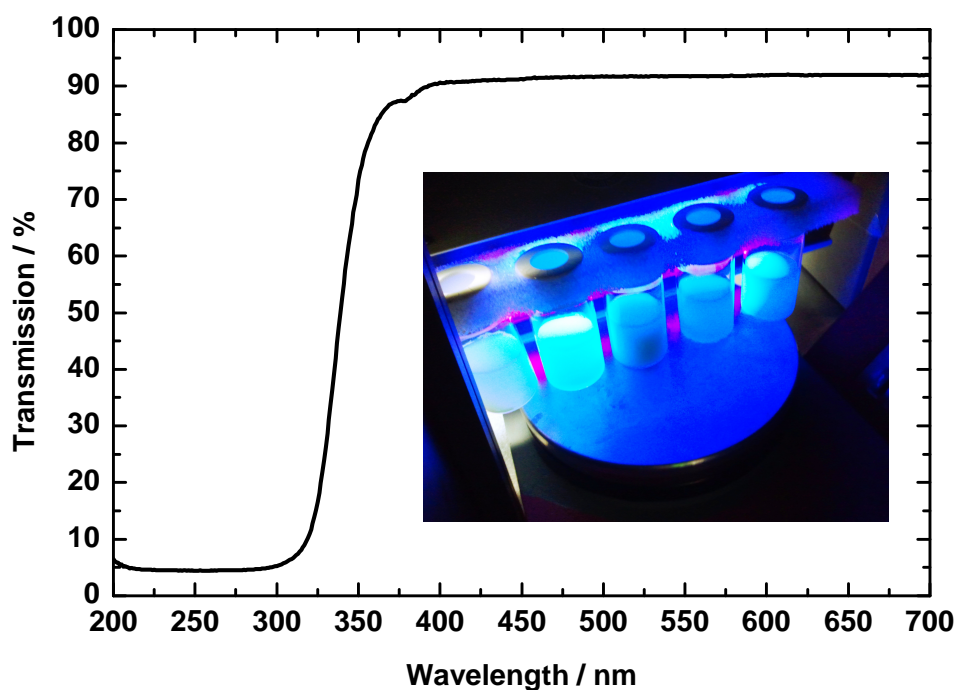
Figure 3.9: Transmission spectrum of borosilicate glass vials used in early photocatalytic experiments. The transmission at 365 nm is 86 % and above 400 nm is > 91 %. The image inset shows carbon nitride samples under UV illumination with a Hg-vapour lamp.
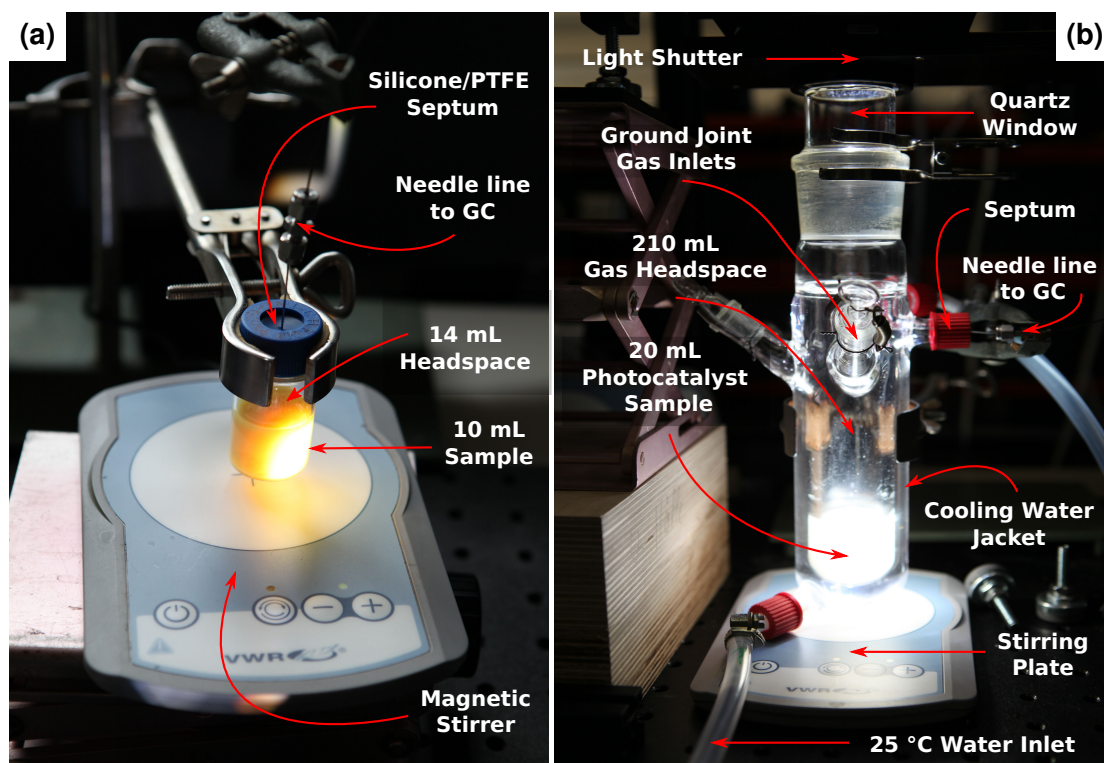


Figure 3.10: Two types of reactor used for photocatalyst measurements. **(a)** 24 mL borosilicate glass vial with gas-tight silicone/PTFE septum. **(b)** Custom glass reactor with quartz window and water cooling.

Figure 3.10(a) is the 24 mL blue capped vial during side illumination. The GC inlet needle is piercing the septum at the top. The sample is under constant stirring using a PTFE magnetic bead and stirring plate. The 10 mL suspension gives a gas headspace of 14 mL.

In Figure 3.10(b) is the custom designed 230 mL reactor with quartz window seen at the top. The septum and GC injection needle are seen to the right of the reactor. The cooling water jacket surrounds the inner volume which contains the sample. Here, 20 mL of sample gives a gas headspace of 210 mL.

## 3.4   Gas Chromatography

For chromatography in general, mixtures of compounds are separated so that they may be identified or quantified. A sample compound (known as the *mobile phase*) flows over a fixed compound (known as the *stationary phase*). Ideally, there is an interaction but no reaction between these phases. The degree of interaction is compound-dependent and reduces the flow of the mobile phase. The sample is often mixed with an inert carrier compound with a fixed flow rate.[60,61]

The origin of chromatography is credited to botanist Mikhail Tswett in 1901, albeit unrecognised for 10 years. He experimented on the selective adsorption of chlorophylls and other pigments by using various solvents. His simple column of calcium carbonate successfully separated the pigment colours for the purpose of separation.[62] He concluded:

> "We see thus that the laws of mechanical affinity may be used for the most complete physical separation of the substances soluble in certain fluids."

Importantly, he wrote the basic concepts of chromatography which still hold true today, namely, the concepts of the stationary and mobile phases and the selective interaction of the "adsorbant" (column material) as he called it. From this work, the techniques of compound separation and purification have expanded into the many chromatography forms we have today e.g. thin layer chromatography (TLC), high pressure liquid chromatography (HPLC) and finally gas chromatography (GC), used in this thesis.

## 3.4.1 Fundamental Gas Chromatography Concepts

A prototypical GC setup is illustrated below (Figure 3.11). The sample is typically a gas or liquid in small amounts mixed with a carrier gas. These are introduced at the injector (conventionally by a gas-tight syringe through a septum.) The mobile phase is then transferred through the column at a fixed flow rate, often at elevated temperatures. In the column, sample components elute at different rates. These rates are determined by component and column properties such as sample boiling point, polarity, electric charge, size of the molecules, column length and material etc. The separated components finally arrive at the detector at different times. The plot of signal detection over time is called a chromatogram and the time to a given peak maximum is called the retention time.
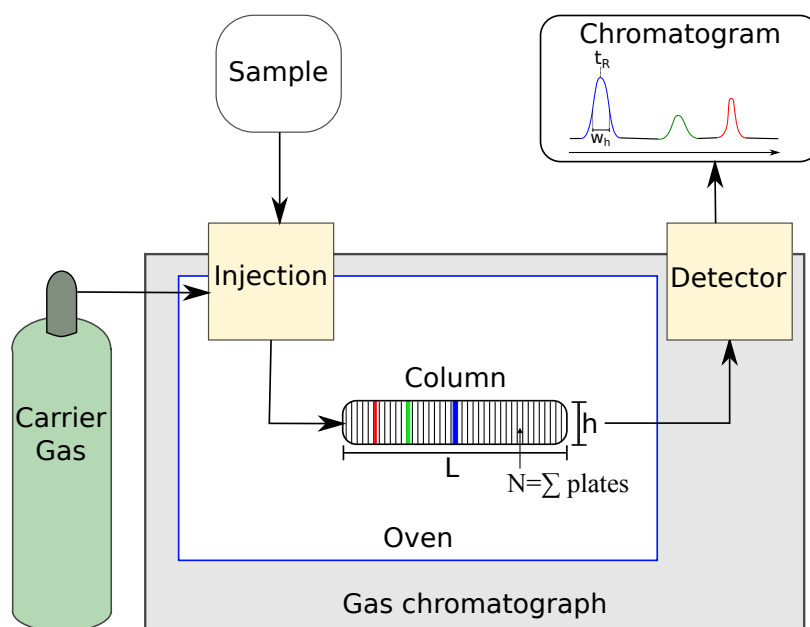


Figure 3.11: Simplified gas chromatograph scheme showing the plate model.

**Theoretical Plate Model**

This model provides insights into the processes of compound separation happening in the primary GC component, the column. The model states that the column is quantised by *theoretical plates* which separately equilibrate between the stationary and mobile phases. The number of plates $N$ and the theoretical plate height $h$ give us information on the separating power of the column and thus its efficiency. The number of theoretical plates of a column (also known as the column efficiency) can be evaluated by examining a peak from its chromatogram with the following relations:

$$N = 5.545 \left( \frac{t_R}{w_h} \right)^2 \tag{3.1}$$

$$h_p = L/N \tag{3.2}$$

Where $N$ is the number of theoretical plates in a column at a fixed temperature, $t_R$ is the retention time of that peak and $w_h$ is the peak width at half the height.[63][†]Columns with higher plate numbers (i.e. 50000) are more efficient and will have a narrower peak width at a given retention time. An alternative measure of column efficiency is the *height equivalent to a theoretical plate* (HETP) denoted as $h_p$ which considers the column length $L$ with the relation 3.2 given above.

As we have seen, this simple model outlines the basics of compound separation in chromatography. However, its assumption that equilibration between the stationary and mobile phases is instantaneous does not explain the resulting peak shape. A more contemporary model known as *rate theory* considers the time for a compound to elute. For now, the basic concepts of gas chromatography have been outlined above.

### 3.4.2   Gas Chromatography Setup

Gas chromatography is the best method for quantifying hydrogen gas. A custom setup by S&H Analytik which allows flexibility, online analysis and unknown gas determination was established. This was based on a Thermo Fischer Trace Ultra GC with both helium and argon carrier gases and a thermal conductivity detector (TCD). This system was customised with an online injection system for precise control of gas injection directly from the reactor as outlined in Section 3.4.5.

### 3.4.3   Gas Chromatograph Components

Figure 3.12 illustrates the layout and setup of the customised GC. The principle components are the three main columns and the two switching valves. There are also two heating zones, one external oven which houses the stripper column (Poropak Q) and the main heating oven of the GC which houses the other two columns. The reason that ovens are included is that compounds elute faster at higher temperatures. There is a customised injection system instead of a conventional injection port which is connected directly to the sample reactor. Argon is the main carrier gas although helium can also be used for increased sensitivity of hydrocarbons and oxygen.

---

[†]In Equation 3.1, $5.545 = 8\ln 2$ which assumes a Gaussian peak profile. This can be replaced with 16 if $w_h$ is replaced with $w_b$ which is the peak width at base.
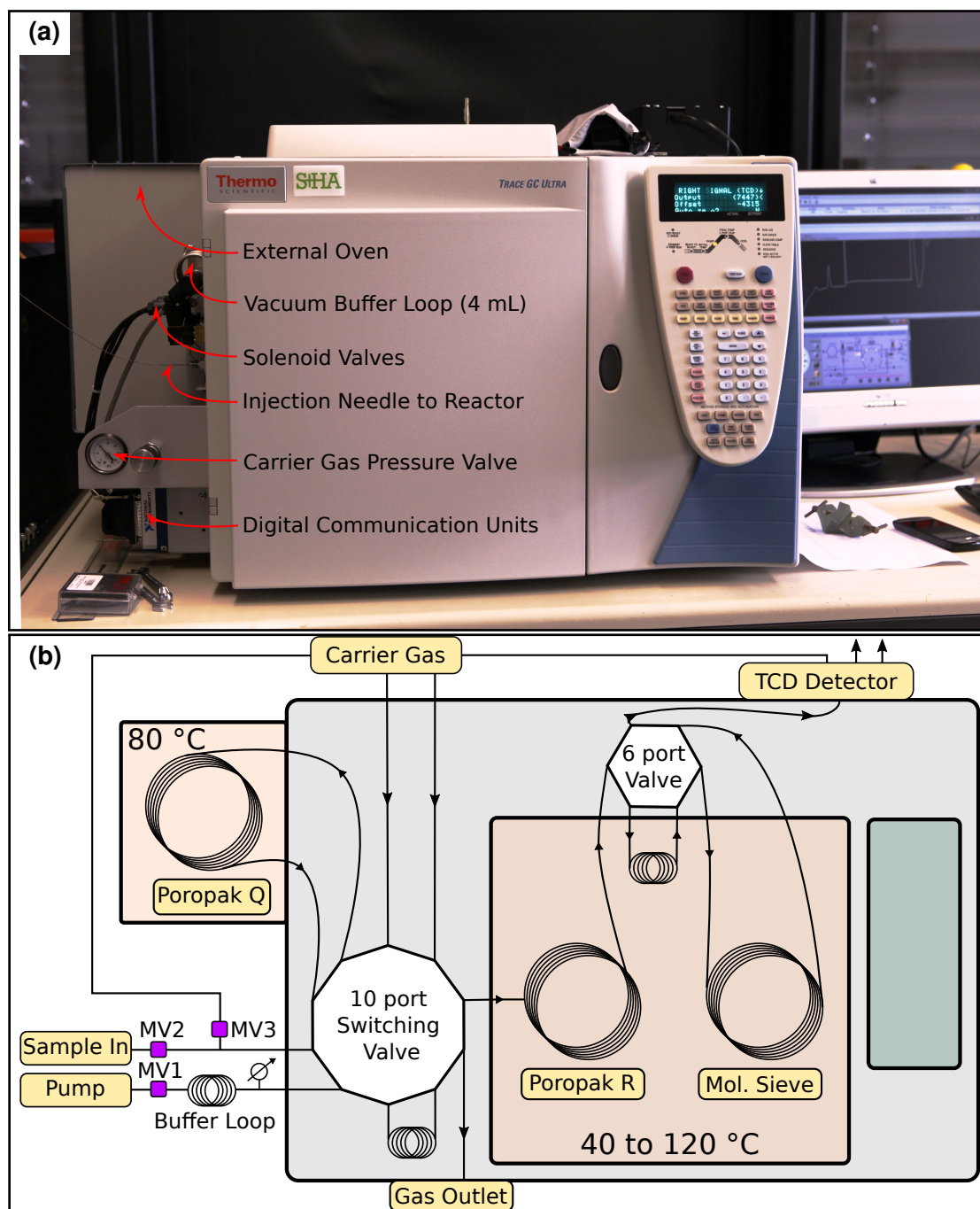
Figure 3.12: GC injection system and components layout. **(a)** Photo of the GC showing the custom injection system to the left side. **(b)** Component layout showing columns, switching valves and heating zones.

**Injection:** The injection system is located in the left foreground of Figure 3.12. It has a gas volume of $\approx 6.5$ mL. This is made up of the buffer loop and the sample loop which is inside the GC. It is interconnected by the sample line, vacuum line and the carrier gas line; all computer controlled by solenoid valves which are coloured purple in the figure (MV1, MV2 and MV3).

**Sample Loop:** This 2 mL loop holds the sample during injection.

**Sampling Valve:** The 10-port sampling valve controls the flow of gas in the GC. The switching behaviour and flow of gas is explained below and in Figure 3.13.

**External Oven:** The external oven houses the stripper column at a constant temperature of 80 °C so that water may evaporate easily.

**Stripper Column (S1):** The Poropak Q packed column strips $H_2O$ from the main GC channel as water would block the Poropak R column.

**Internal Oven:** The internal variable temperature oven houses the main packed column (Poropak R) and the molecular sieve column.

**Hydrocarbons Column (S2):** The Poropak R packed column is the main column for separating hydrocarbons.

**Switching Valve:** Consequently, the gas flow enters the 6-port switching valve. This valve operates a Y-junction, controlling whether to send gas to the molecular sieve column or bypass it through a capillary loop (R1) to protect the molecular sieve from being blocked (by nitrous oxide for example).

**Mol. Sieve (S3):** The molecular sieve column (5 Å sieve) is the most important for measuring $H_2$ as it separates the $H_2$, $O_2$ and $N_2$ components.

**Bypass Loop (R1):** This loop serves to bypass the Mol. sieve column for protection against larger compounds.

**Detector:** Finally the separated gas components enter the TCD detector for measurement and are then exhausted.

### 3.4.4   Gas Chromatograph Column Diagrams

Figure 3.13 shows the operating modes of the GC and the flow of gas through the columns. This is important to understand how the GC works and what its capabilities are. In **(a)**, the *Injection System* is highlighted in blue. This includes the buffer loop and sample loop inside the GC and the three solenoid valves, MV1, MV2 and MV3. Highlighted in yellow is the *Standby mode.* This is the default operating mode of the GC. In **(b)**, the *Sampling Mode* is highlighted. Sample is taken from the sample loop through the columns. Notice that the flow of gas through column S1 (Poropak Q) is reversed. This mode is the measuring mode which happens in the first 1.7 min of the GC method.

### 3.4.5   Online Gas Dosing System

At first, conventional gas-tight syringes were used to sample the evolved $H_2$ or $O_2$ from the reactions. These, although effective, were prone to contamination from air leaks or from previous measurements, even with extensive flushing with GC carrier gas. Also, directly interfacing the reactor to the GC inlet would greatly improve the sampling time and performance.

Because of these reasons, our GC was customised with an online dosing system. The system allows for exact volume injection independent of the reactor pressure (although the reactor is maintained at atmospheric conditions). It also allows back-purging from the injection system to the reactor with argon carrier gas. This ensures that the reactor pressure is maintained for each measurement.
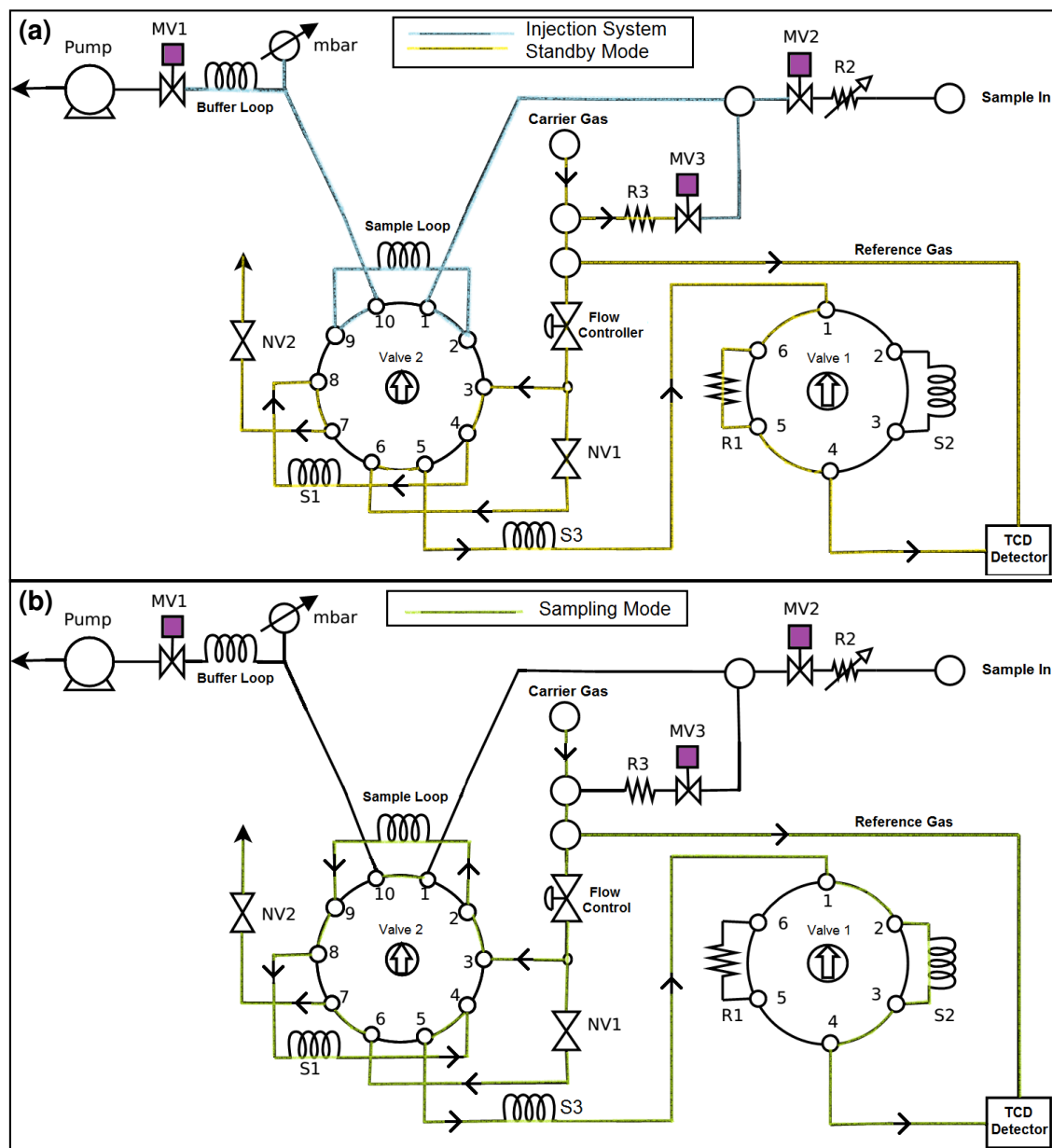
Figure 3.13: GC component and gas flow diagram. **(a)** Injection System (blue) and *Standby mode* (yellow) and **(b)** *Sampling mode* (green). Note that the gas flow in column S1 is reversed during sampling. A more detailed diagram is in the Appendix A.2.

### 3.4.6   Thermal Conductivity Detector

There are a range of detectors available for GC measurements, the most common are flame ionisation (FID) and thermal conductivity (TCD). The FID gives good performance for hydrocarbons and organic gases such as $CH_4$ and alcohols etc. There are two operation modes of the TCD itself: constant temperature or constant voltage mode. For constant temperature, the temperature is set and the voltage difference is measured. Our TCD measures the thermal conductivity of a gas from a filament under constant voltage and compares it to the conductivity of the carrier gas as reference. The key to this technique is the difference in conductivity between the carrier gas and sample gas. To maximise the sensitivity for $H_2$ detection, a carrier gas with a low thermal conductivity is chosen, i.e. argon. As can be seen from the Table 3.14, argon is a poor thermal conductor and hydrogen is a good thermal conductor, this difference enhances the sensitivity for $H_2$ detection.

Although constant voltage mode gives the best sensitivity, it lowers the lifetime of the detector (since it must operate at a higher temperature, 300 °C). Also, not only is the detector sensitive to conductivity contrast between the reference and sample, but also simply to pressure changes between the two cells.



| Gas | Thermal Conductivity at 20 °C (W mK$^{-1}$) |
| --- | --- |
| Hydrogen | 0.1720 |
| Helium | 0.1380 |
| Oxygen | 0.0238 |
| Nitrogen | 0.0234 |
| Carbon oxide | 0.0232 |
| Ammonia | 0.0220 |
| Argon | 0.0160 |
| Carbon dioxide | 0.0146 |
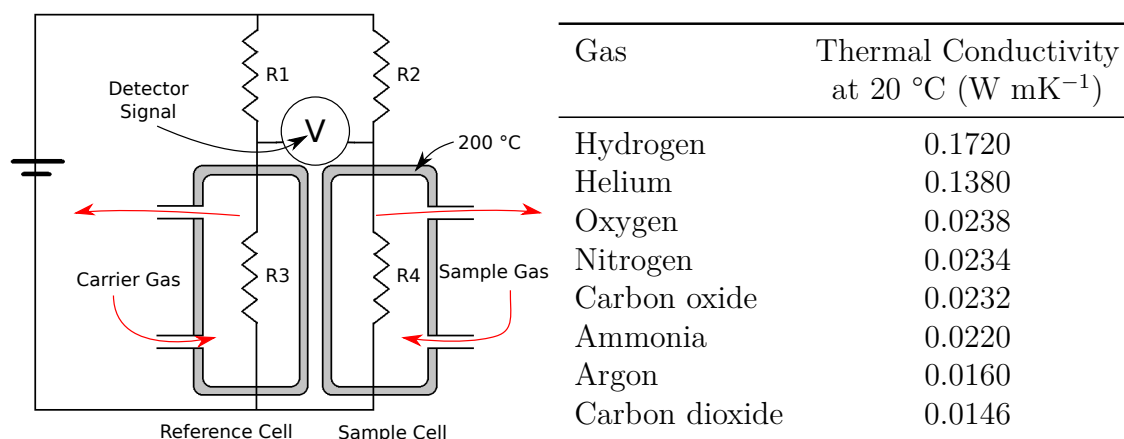
Figure 3.14: Operating principle of the thermal conductivity detector with a resistor bridge comparing the sample and reference gas cells. The thermal conductivity of common gases at 20 °C is given in the table.[64]

### 3.4.7 Chromatograms and Timing Events in the GC

Figure 3.15 shows a chromatogram for a sample of He and $H_2$ in air using argon as the carrier gas. Not all peaks correspond to a sample detection as some correspond to pressure changes from valve switches. The table lists the events and retention times for this measurement.
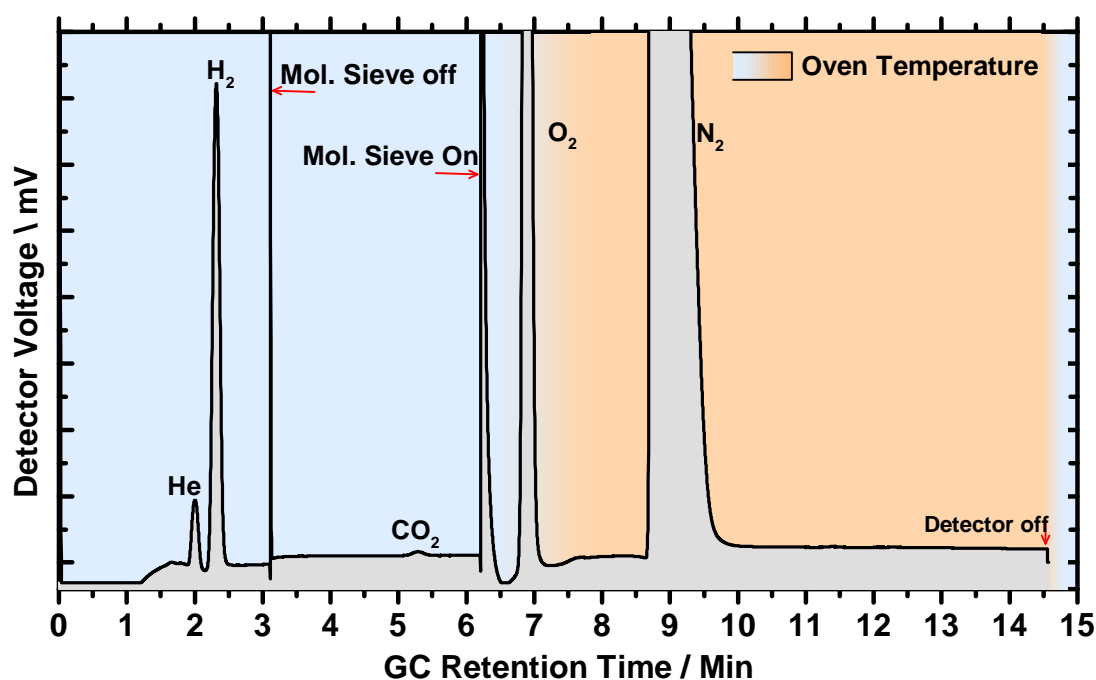


| GC Time (Min) | GC event or gas detection as seen in chromatogram |
|---|---|
| Preprun | TCD is "zeroed" to 1000 mV |
| 0.0 | Valve 2 set to Sampling Mode for 1.7 min |
| 0.0 | Valve 1 switched to Mol. sieve to separate $H_2$ and He |
| 1.7 | Valve 2 reset to standby mode. $H_2O$ back-purged to protect Poropak R |
| 1.9 | He detected |
| 2.3 | $H_2$ detected |
| 3.1 | Valve 1 set to bypass-loop to protect Mol. sieve |
| 5.3 | $CO_2$ detected |
| 6.2 | Valve 1 set to Mol. sieve to separate $O_2$ and $N_2$ |
| 6.2 | Oven ramp start |
| 6.9 | $O_2$ detected |
| 8.4 | $N_2$ detected |
| 9.8 | GC cools down and resets |

Figure 3.15: GC chromatogram of a sample of He and $H_2$ in air using argon carrier gas with a table of GC timing events and gas retention times.

# 3.5  Mass Spectrometry for Gas Analysis

Mass spectrometry (MS) is a powerful technique for analysing and identifying gas species and complements the quantitative capabilities of a GC. The equations below demonstrate a molecule M undergoing ionisation and secondly, fragmentation into components A and B. These are the two main processes which 'crack' a gas species into a number of mass-charge signals known as a cracking pattern.

$$e^- + M^{\bullet\bullet} \longrightarrow 2\,e^- + M^{\bullet+} \tag{3.3}$$

$$M^{\bullet+} \longrightarrow A^+ + B^{\bullet} \tag{3.4}$$

## 3.5.1  Cracking Patterns

Each gas has its own distinct mass spectrum. Take for example, the mass spectrum of $CO_2$ shown in Figure 3.16. This relatively simple gas has at least seven different signals and many more at higher resolution. This is due to a combination of ionisation, fragmentation and isotope species. This gives a highly distinctive fingerprint signal pattern called a cracking pattern. The challenge is that for a mixed or unknown sample, many signals overlap and it is not easy to distinguish each gas. Primarily, mass spectra are deconvoluted by knowledge of the signal ratios.
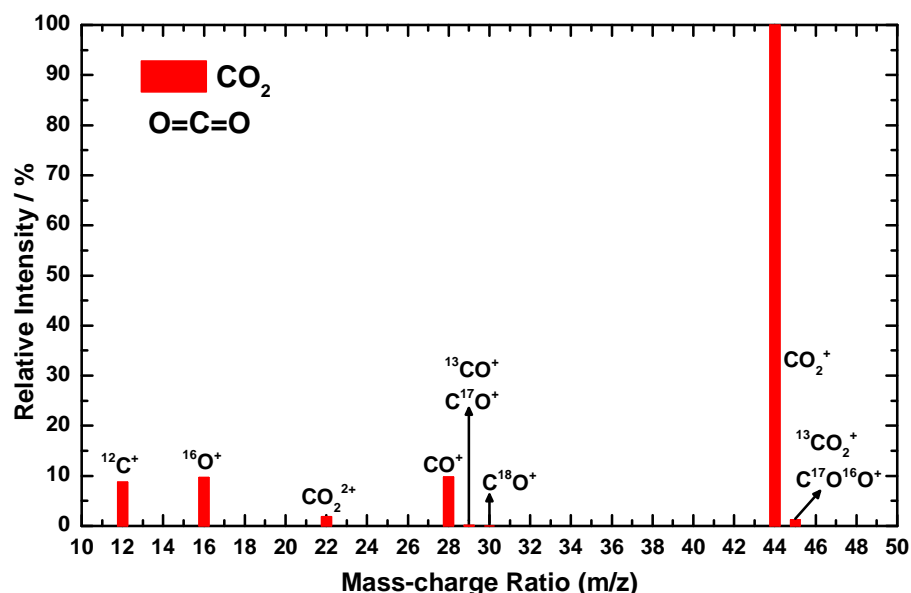


Figure 3.16: Mass spectrum of $CO_2$ gas showing its cracking pattern. This demonstrates how fragmentation, doubly charged ions and isotopic species give a varied mass spectrum for even simple molecular species. Data Source, NIST Mass Spectral Library.

## 3.5.2 Soft Ionisation Technique

As already mentioned, a simple molecule can have many $m/z$ signals. If a mixture of gases is used, the signal only becomes more complex with many signals contributing to different species. The soft ionisation technique is one method to help identify compounds by lowering the ionisation threshold of one of the species, thus reducing or eliminating its contribution to the mass spectrum.

The technique is best described by example. The measurement of $H_2$ in experimental conditions is complicated by the fragmentation signal of water vapour to $H^+$. Unfortunately, water vapour also contributes to the $m/z = 1$ signal and we cannot quantify the hydrogen.

In Figure 3.17(a), the ionisation energy profile of $H_2O^+$ at $m/z = 18$ is shown. We see that for the default operating voltage of 70 V, a high signal is obtained. Figure 3.17(b) compares the ionisation energy $m/z = 18$ and the fragmentation energy $m/z = 1$. We can see that it takes 14.3 eV to ionise water vapour and 17.6 eV to fragment it to $H^+$. Knowing that the ionisation of $H_2$ gas occurs at 15.4 V (see Table 3.3), we can set the operating voltage between 15.4 and 17.6 V, and so finally we will not get a fragmentation of water vapour to $H^+$ but we will see the signal from $H_2$ albeit reduced in intensity.

Besides deconvolution of the cracking patterns of known compounds, the soft ionisation technique is useful to reduce the complexity of mass spectra and so valuable quantitive and qualitive data can be extracted.
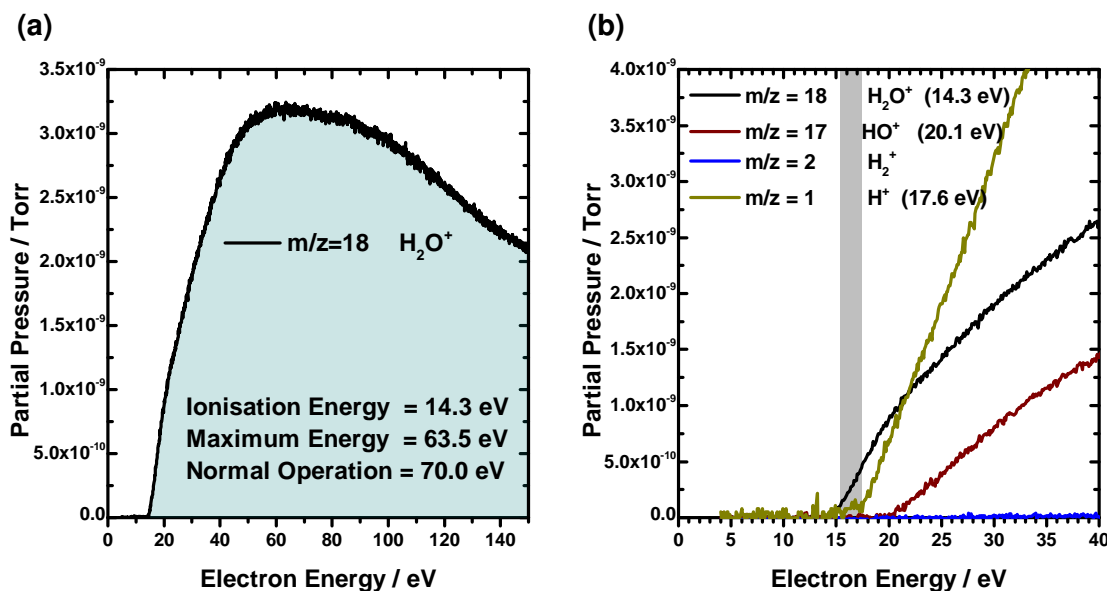


Figure 3.17: **(a)** Measured ionisation profile of $H_2O$ with ionisation energy of 14.3 V and maximum ionisation density at 63.5 V. **(b)** Comparison of ionisation energy ($m/z = 18$) and fragmentation energy of $H_2O$ to $H^+$ ($m/z = 1$).

Table 3.3: Ionisation energies of common gases which can be used to distinguish gases. Source data from Hiden Analytical technical notes.

| Gas | Formula | Ionisation Energy (eV) |
|---|---|---|
| Hydrogen | $H_2$ | 15.425 |
| Nitrogen | $N_2$ | 15.58 |
| Oxygen | $O_2$ | 12.07 |
| Argon | $Ar$ | 15.76 |
| Carbon monoxide | $CO$ | 14.01 |
| Carbon dioxide | $CO_2$ | 13.77 |
| Ammonia | $NH_3$ | 10.07 |
| Nitric oxide | $NO$ | 09.26 |
| Methane | $CH_4$ | 12.61 |
| Ethanol | $C_2H_5OH$ | 10.83 |
| Acetic acid | $CH_3COOH$ | 10.65 |
| Acetone | $CH_3COCH_3$ | 09.70 |
| Methanol | $CH_3OH$ | 10.85 |
| Formic acid | $HCOOH$ | 11.33 |
| Formaldehyde | $HCHO$ | 10.88 |
| Water | $H_2O$ | 14.30 |

### 3.5.3 Hiden MS Components

A gas phase mass spectrometer from Hiden Analytical was purchased to further expand the gas analysis capability. This allowed the analysis of real-time gas evolution and reaction dynamics to be investigated. A measurement response time of 500 µs and a flexible inlet provided a powerful and versatile gas analysis technique. The following sections list the principle components of the Hiden MS as illustrated in Figure 3.18.
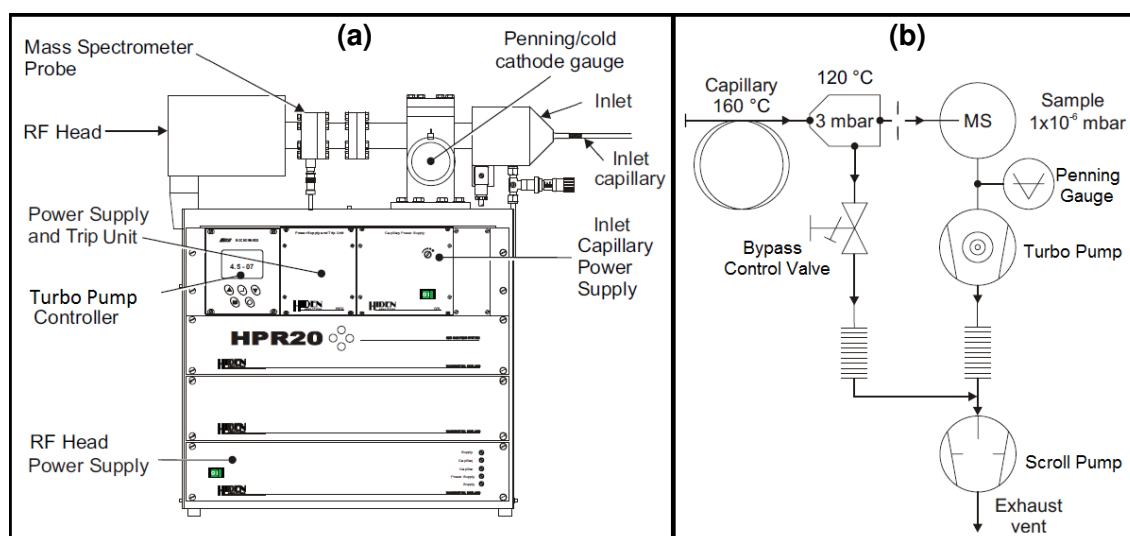


Figure 3.18: Hiden HPR-20 with capillary inlet for real-time gas analysis. **(a)** Front panel and **(b)** vacuum diagrams. Images adapted from Hiden Analytical.

**RF Head and Power Supply**

The main power supply controls the RF Head. This supplies radio frequency (RF) and direct current (DC) to the quadrupole mass filter.

**Inlets**

There are two inlets available; the silica capillary and the PDMS membrane. These are discussed further on page 56. Both inlets can be fitted with a computer controlled solenoid shut-off valve.

The **capillary** is the default inlet. It is a 1.8 m long flexible gas tubing with standard end-connections. It is heated to typically 160 °C to stop gas condensation. It is a low-flow capillary inlet with a gas consumption rate of only 4 mL min$^{-1}$. It is suitable for sampling 0.1 bar to 2.0 bar of pressure.

The **PDMS membrane** probe inlet is a gas permeable polymer membrane surrounding stainless steel tubing under vacuum. This probe can be placed directly into liquids to sample dissolved gas species.

**Ion Source**

The ion source generates ions of the sample by bombardment with a high energy electron beam. The electron beam is generated between the filament and source at voltages such as $-70$ V and $+3$ V respectively. If the ions are generated only by electron bombardment, this is called electron impact ionisation (EI). Another method especially useful for samples that are difficult to ionise involves introducing a reagent gas to the sample such as ammonia. Ammonia is easily ionised and these ammonium ions can then ionise the sample gas. This is termed chemical ionisation (CI).

The generated ions are extracted by focusing magnetic or electric fields and enter the analyser or mass filter. This is normally done by a focusing plate or ion accelerator plate which is typically at $+90$ V, and located at the opening to the analyser. This also serves to repel electrons from entering the analyser if an electron trap is not included. Figure 3.19 is a diagram of the Hiden MS ion source.

**Hiden ion source:** The ion source contains the filaments and ion source cage, which create the positive ions by electron impact and send them to the mass filter. Filaments are oxide coated iridium typically at $-70$ V. The cage is at $+3$ V. The positive charge focusing plate is at $+90$ V.
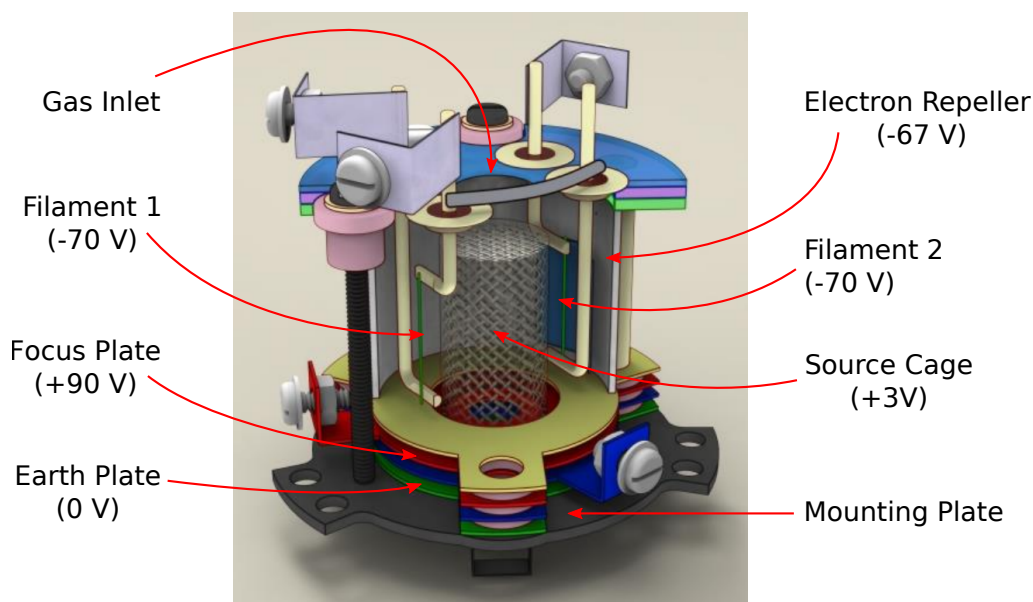


Figure 3.19: Cross-section of the ion source of the Hiden mass spectrometer. Positive ions are generated by electron impact between the filament and source cage. Ions are attracted to the focusing plate and enter the quadrupole mass filter. Image adapted from Hiden Analytical.

### Mass Filter

The mass filter analyser separates the ions by their mass to charge ratio ($m/z$). It alters the speed and trajectory of ions by applying an electromagnetic field. Lighter ions are deflected more, and the same is true for doubly ionised species. Thus, only selected ions pass to the detectors and this selection is scanned over the desired mass-charge range.

**Hiden Quadrupole Mass Filter:** The 125 mm single filter quadrupole (HAL 201) selectively passes the various charged particles to the detectors. Mass range: 1 to 200 u. Partial pressure detection limit down to $1 \times 10^{-14}$ Torr.[‡]

Four poles 15 cm to 20 cm long with an alternating DC and RF applied voltages. This gives rise to a cylindrically symmetrical electric field. Ions pass along the poles and oscillate with the quadrupolar field. Eventually most ions collide with one of the poles. Only ions of the selected ($m/z$) will reach the detector as they are in resonance with the oscillating field. The chamber is maintained at high vacuum to stop ions colliding with gas molecules.[65,66]

A diagram of a quadrupole is given in Figure 3.20 which shows the pole arrangement and path of ions.[65]
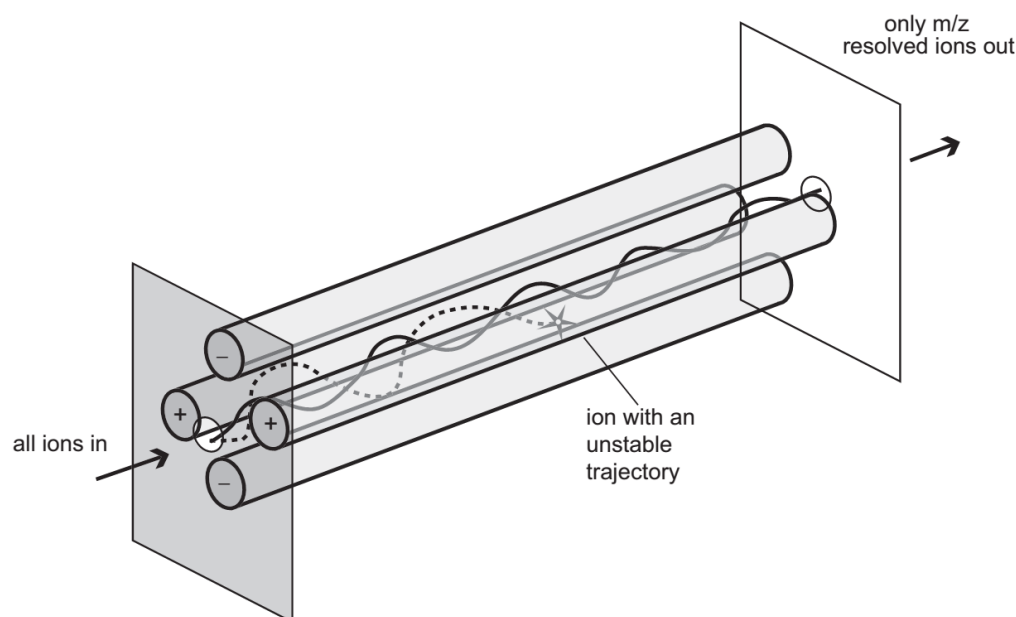


Figure 3.20: Operating principle of a quadrupole mass filter. Image source: Linge et al.[66]

---

[‡] 1 Torr = $\frac{1}{760}$ atm. $= \frac{101325}{760}$ Pa $\approx 1$ mmHg

**Detectors**

MS detectors are usually simple electron-multiplier type detectors. Other detector types can be array detectors which are multichannel detectors capable of simultaneously measuring up to 15 $m/z$ ratios. For the Hiden MS, there are two detectors that we use; the Faraday and SEM (Secondary electron multiplier).

One of the simplest and most common detector is the **Faraday cup**. The Faraday detector cup can create a charge equivalent to $1 \times 10^{-4}$ A Torr$^{-1}$ for nitrogen gas. The advantage over the SEM detector is that the Faraday cup can comfortably operate over the full partial pressure range. The minimum detection limit is $1 \times 10^{-11}$ Torr of partial pressure.

The **SEM** generates a secondary electron cascade when impacted by an ion. A gain of 1000 is achieved with an applied voltage. The applied voltage is dependent on the operating lifetime of the detector (currently 900 V). The SEM lifetime depends on the total ion current and because of this, the SEM is not recommended at higher partial pressures. The advantage over the Faraday detector is the increased sensitivity at low partial pressure with a minimum detection limit of $1 \times 10^{-14}$ Torr.

## 3.5.4 MS Configurations

The following is a list of configurations experimented with for the Hiden MS: More details for each are given in the following sections.

- Reactor headspace gas analysis (Capillary inlet)

- Reactor liquid gas analysis (Membrane probe inlet)

- GC exhaust gases (GCMS-like)

- Furnace gases during carbon nitride synthesis (TGA-MS-like)

- Isotope labelled samples

**Reactor Headspace Gas Analysis**

This is the default mode of operation where the capillary inlet is connected to the reactor in a continuous flow mode. Although our photocatalytic reactors are designed for batch reactions, the low flow rate (4 mL min$^{-1}$) of the MS is useful to analyse our samples over short time frames. It is recommended that the capillary inlet is attached with a T-connector with one end open to atmosphere. This ensures no fluctuations in pressure and thus a stable baseline.

### Reactor Liquid Gas Analysis

An alternative inlet accessory for the Hiden MS is the HPR-40 which allows the measurement of evolved gases directly in the photocatalytic suspension. This is done using a PDMS membrane which has selective permeability to gases as can be seen in Figure 3.21 and Table A.5 in the Appendix. From this, we can directly measure $H_2$ as it is evolved during a reaction and examine dissolved gas concentrations of $CO_2$ and $O_2$ for example. Measurements involving the detection of dissolved gases including $H_2$ evolution are given in Section 4.4.
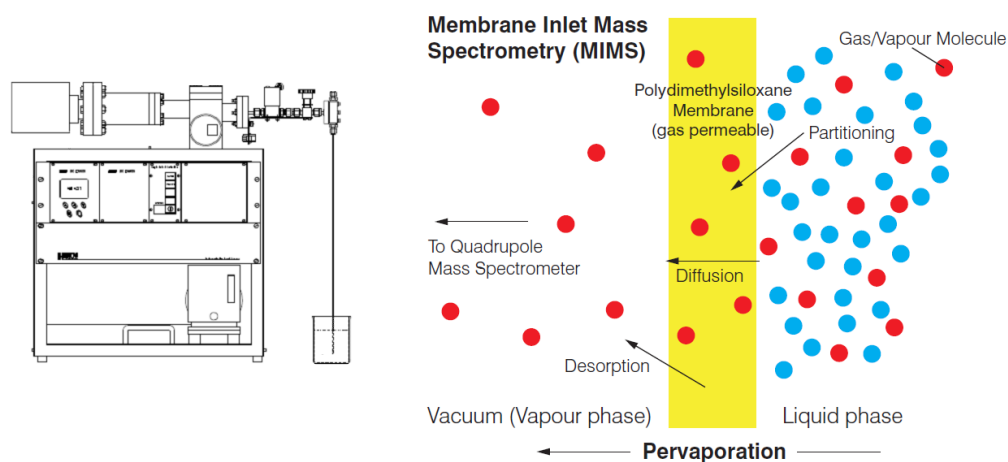


Figure 3.21: The Hiden HPR-40 for gas measurements in liquids. This inlet uses a PDMS membrane which is semipermeable to gases giving real time analysis of dissolved and evolved gases. Images from Hiden Analytical.

### GC Exhaust gases (GCMS-like)

An improvised experiment to confirm the presence of $CO_2$ detected in a GC chromatogram proved useful in a GCMS-type mode of operation. A small signal appearing at the approximate retention time for $CO_2$ was detected but could not be exclusively assigned to $CO_2$. By coupling the TCD sample exhaust of the GC to the MS capillary inlet, the exclusive presence of $CO_2$ was confirmed using a mass-scan. The GC and MS were manually started at the same time and taking into consideration the time for each mass-scan to complete and the delay of $\approx 1$ s between GC and MS detection, a mass scan profile for each peak in the chromatogram could be obtained and sample identification confirmed. An example of this setup is used in Figure 3.22 of the following section.

Although informative, this mode of operation is unreliable as the MS and GC do not share an interface to account for the timing events and analysis must also be done separately.

**Furnace Gases during Carbon Nitride Synthesis (TGA-MS-like)**

The synthesis of carbon nitrides in furnaces at high temperatures is well known to evolve gases such as $NH_3$, $HCN$, $H_2N_2$ etc. Much of what is known about the evolved gases comes from thermogravimetric analysis (TGA),[25,67,68] and TGA-MS experiments.[69–71] In those experiments, evolved gases are evaluated as the temperature increases whereas in our experiments gases are evaluated with temperature and time, thus giving insights into the kinetics of the condensation process.

The MS capillary inlet was attached to stainless steel tubing which was inserted into the back of a muffle furnace. This allowed the identification of evolved gases but focused more on the time evolution of these gases at a fixed temperature. Examples of these experiments are given in Figure 5.3.

### 3.5.5 Isotope Labelling

One powerful MS technique available is the use of isotope labelling to follow the reaction pathways. This will be crucial for $CO_2$ reduction experiments in the future. A simple demonstration of this method involved running a photocatalytic experiment in $D_2O$. Will the evolved gas contain deuterium? A highly active carbon nitride nanosheet photocatalyst was used in conditions that are known to evolve $H_2$ (TEoA as electron donor and Pt cocatalyst). Although the GC could quantify the evolved gas, it could not distinguish $H_2$ and $D_2$. The Hiden MS coupled to the TCD exhaust in the GCMS-like mode was used to analyse the gas in the photocatalytic deuterium oxide splitting experiment.

As can be seen in Figure 3.22, gas is detected in the GC at the expected retention time of 2.3 min, corresponding to 7534 ppm. To identify the gas, the MS scans $m/z = 4$ and $m/z = 2$ (unfortunately, $m/z = 3$ corresponding to $HD^+$ was not monitored). At the expected retention time, both signals increase. The $m/z = 4$ signal can only be assigned to $D_2^+$ as He is separated in the GC at an earlier retention time. $m/z = 2$ corresponds to $D^+$ or possibly to $H_2^+$. The same experiment carried out in deionised $H_2O$ does not result in a signal at $m/z = 4$. This experiment confirms the presence of photocatalytic deuterium evolution. It proves that the origin of at least some portion of the evolved gas stems from the liquid deuterium oxide.
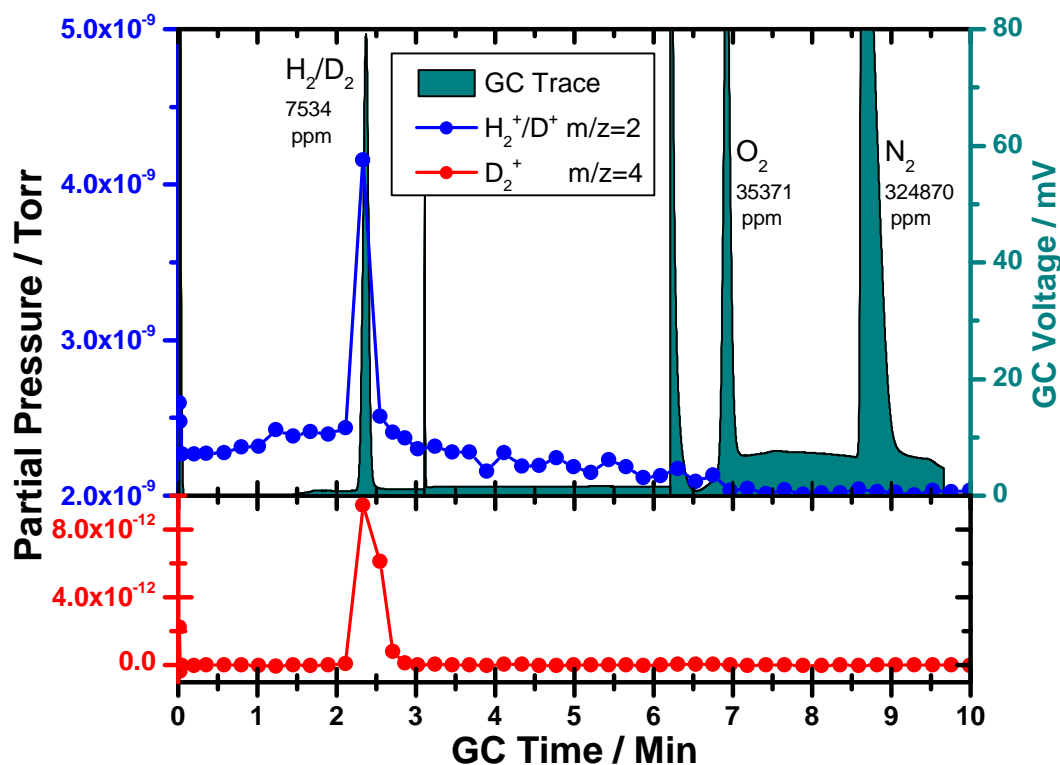


Figure 3.22: Demonstration of photocatalytic heavy water reduction. The evolution of $D_2$ is confirmed by MS coupled to the GC.

### 3.5.6 Quantitative Data from the Hiden MS

Although the experiments with the Hiden real-time MS were not calibrated for quantitative results, it is possible to get quantitative gas concentrations under certain conditions. The simplest method is to have a single sample gas in a single carrier gas. Hence, the measured partial pressure directly relates to the gas concentration. Practically, multiple gases are present either as impurity amounts, unknown gases or air leaks. In a sample of multiple gases, it is required that all gases are known and calibrated with a series of calibration gases. Furthermore, the detection parameters used during the calibration must also be used in the measurements and the pressure of the measured sample must also remain constant. Additionally, each sample gas must be uniquely distinguished in the overall mass spectrum. This is problematic as certain mass-charge ratios will have contributions from different gases. To address this problem, specialised software for quantitative measurements is used (QGA pro). This uses a library of cracking patterns with known mass-charge peak ratios. Using this, multi-gas samples can be deconvoluted to some extent. In the following graphs, quantitative measurements of hydrogen and humidity are demonstrated by example.

In Figure 3.23**(a, b)**, sodium borohydride $NaBH_4$ reducing agent was added to water in a 24 mL vial to produce $H_2$ gas in large quantities. The Hiden inlet probe was inserted into vials of increasing amounts of reducing agent and the gas concentrations were measured from the height of the signals. Figure 3.23**(b)** confirms a linear hydrogen concentration dependence with increasing amount of $NaBH_4$.

In Figure 3.23**(c)**, photocatalytic hydrogen production was measured from melon synthesised at 450 °C for 16 h.[72] The conditions included full spectrum illumination with TEoA as electron donor and photoreduced Pt as cocatalyst. A hydrogen concentration of 500 ppm was obtained and this was later confirmed with GC measurements. The water vapour trace showed the change in humidity when the inlet was placed in the vial, for example at 01:30 when the inlet was placed into a control vial with no $H_2$.

The unique advantage of the MS unit is the ability to monitor evolution rates over time and examples of this are presented on page .
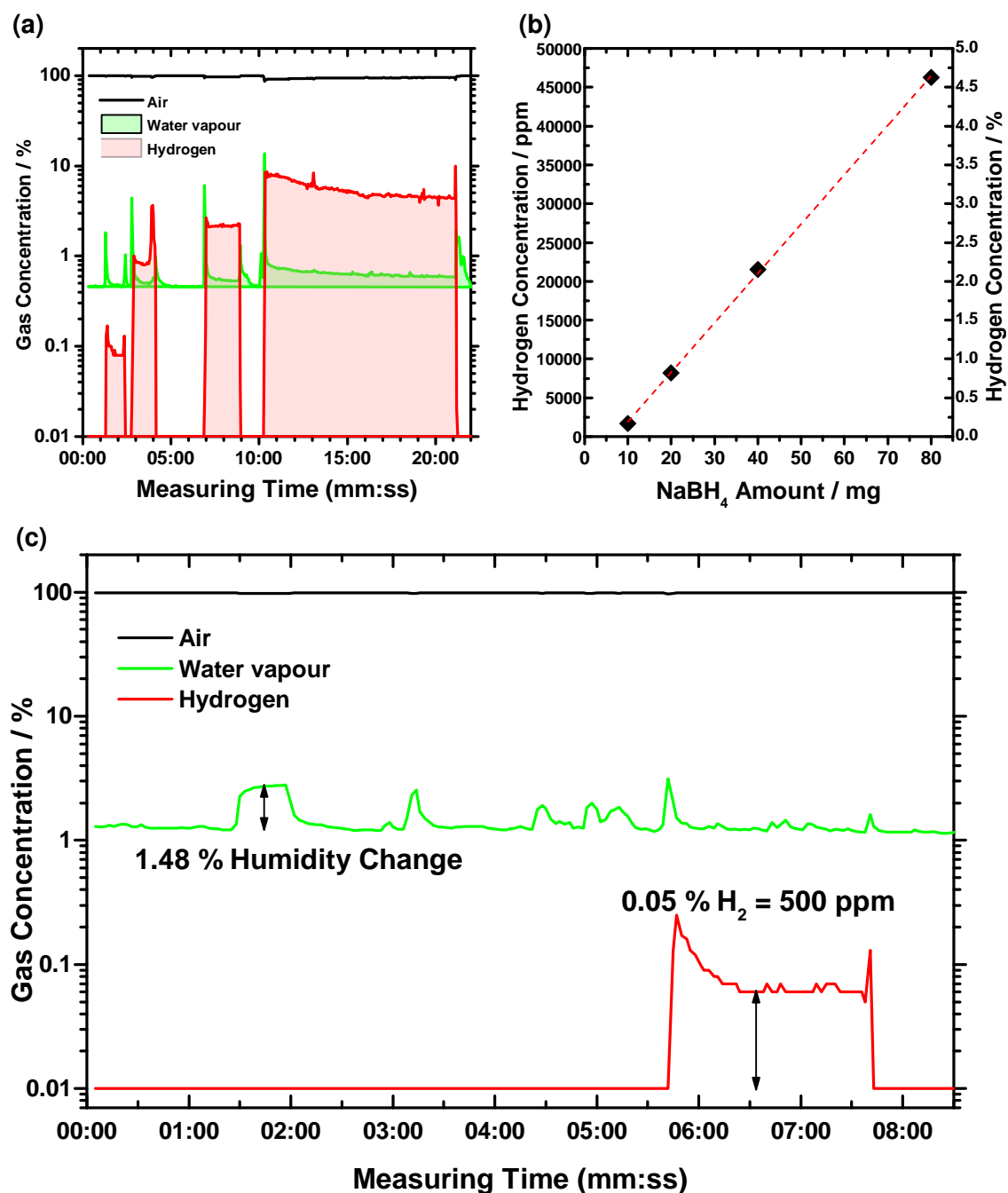
Figure 3.23: Quantitative MS analysis of $H_2$ evolution. The time profiles show the response when inserting the inlet from air to the gas sample. **(a)** Time profile of 10 mg, 20 mg, 40 mg and 80 mg NaBH$_4$ reducing agent in water. **(b)** NaBH$_4$ concentration dependence of $H_2$ evolution and **(c)** $H_2$ quantification of melon with TEoA and Pt in air.

# Chapter 4

# Triazine Carbon Nitrides — Doped Poly(Triazine Imide)

*Chemical synthesis and characterisation in this chapter was carried out by Katharina Schwinghammer (University of Munich and Max Planck Institute, Stuttgart) and this data will also be published as part of her PhD thesis.*

*Solid state nuclear magnetic resonance (NMR) measurements were carried out by Maria B. Mesch (University of Bayreuth), Charlotte Martineau and Francis Taulelle (Tectospin, Institut Lavoisier de Versailles, France) and this will also be published as part of the PhD thesis of Maria B. Mesch.*

This chapter focuses on triazine-based carbon nitrides as photocatalysts, specifically poly(triazine imide) (PTI). Firstly, the publication is presented as it is published in Angewandte Chemie. Secondly, I provide some further results with regards to photocatalysis. I will also draw attention to the data comparing crystalline and amorphous PTI samples.

# 4.1 Triazine Photocatalysis Paper

# Triazine-based Carbon Nitrides for Visible-Light Driven Hydrogen Evolution

Katharina Schwinghammer, Brian Tuffy, Maria B. Mesch, Eva Wirnhier, Charlotte Martineau, Francis Taulelle, Wolfgang Schnick, Jürgen Senker and Bettina V. Lotsch

**Abstract:** A new dimension: The doping of amorphous poly(triazine imide) (PTI) through ionothermal copolymerization of dicyandiamide with 4-amino-2,6 dihydroxy pyrimidine (4AP) results in triazine-based carbon nitrides with increased photoactivity for water splitting compared to crystalline poly(triazine imide) (PTI/ $Li^+Cl^-$) and melon-type carbon nitrides. This family of carbon nitride semiconductors has potential as low-cost, environmentally clean photocatalysts for solar fuel production.

The development of catalysts that enable the direct conversion of solar energy into chemical energy has been defined as one of the major challenges of modern materials chemistry. Hydrogen generated by photochemical water splitting has been identified as a promising energy carrier that offers a high energy density while being environmentally clean.[1] Nevertheless, to realize a light-driven hydrogen-based economy, the exploration of new materials for highly efficient, stable, economically viable, and environmentally friendly photocatalysts is required.

To date, numerous inorganic semiconductors have been developed for water splitting, most of them being transition metal compounds containing heavy metals such as La, Bi, Ta, or Nb, which impede scalability, increase cost, and add complexity.[2] Recently, attention has been attracted to a new class of metal-free photocatalysts, comprising polymeric melon-type carbon nitrides (CNs) based on imide-bridged heptazine units (see Figure 4.1 **(a)**).[3] CNs are readily accessible, lightweight, stable, and low-cost compounds that offer an attractive alternative to metal rich catalysts while still maintaining efficient photoactivity.[4] Thermal condensation of CNs forms a wide variety of chemical species that differ substantially with respect to their degree of condensation, hydrogen content, crystallinity, and morphology.[5,6] The chemical modification of CNs by molecular "dopants" has resulted in a number of CN materials with improved photocatalytic activity.[7] Although the evidence is largely empirical, the property enhancement presumably originates from subtle modifications of the parent structures by incorporation of heteroatoms as well as structural defects, to give rise to enhanced absorption in the visible light range and a more complete exploitation of the solar energy spectrum.

In contrast to all known CN photocatalysts, which are composed of heptazine building blocks, poly(triazine imide) (PTI/Li$^+$Cl$^-$) is the only structurally characterized 2D CN network featuring imide-linked triazine units (see Figure 4.1 **(b)**).[8,9] Owing to its high level of crystallinity, PTI/Li$^+$Cl$^-$ lends itself as an excellent model system to study photocatalytic activity towards water splitting as a function of the number of building blocks, the composition, and the degree of structural perfection of the system. Herein, we present a new generation of CN photocatalysts based on triazine building blocks and demonstrate their enhanced photocatalytic activity in comparison to heptazine-based CNs. Moreover, we show that their performance can be amplified by small-molecule doping, thus rendering them the most active nonmetal photocatalysts for the hydrogen evolution reaction that have been reported to date.

As a starting point, we synthesized crystalline PTI/Li$^+$Cl$^-$ as a model structure for triazine-based CNs in a two-step ionothermal synthesis according to the procedure of Wirnhier et al.[8,9] To study the effect of crystallinity on the photocatalytic activity, we also synthesized an amorphous variant of PTI (aPTI), through a one-step ionothermal

X = NH, O or OH
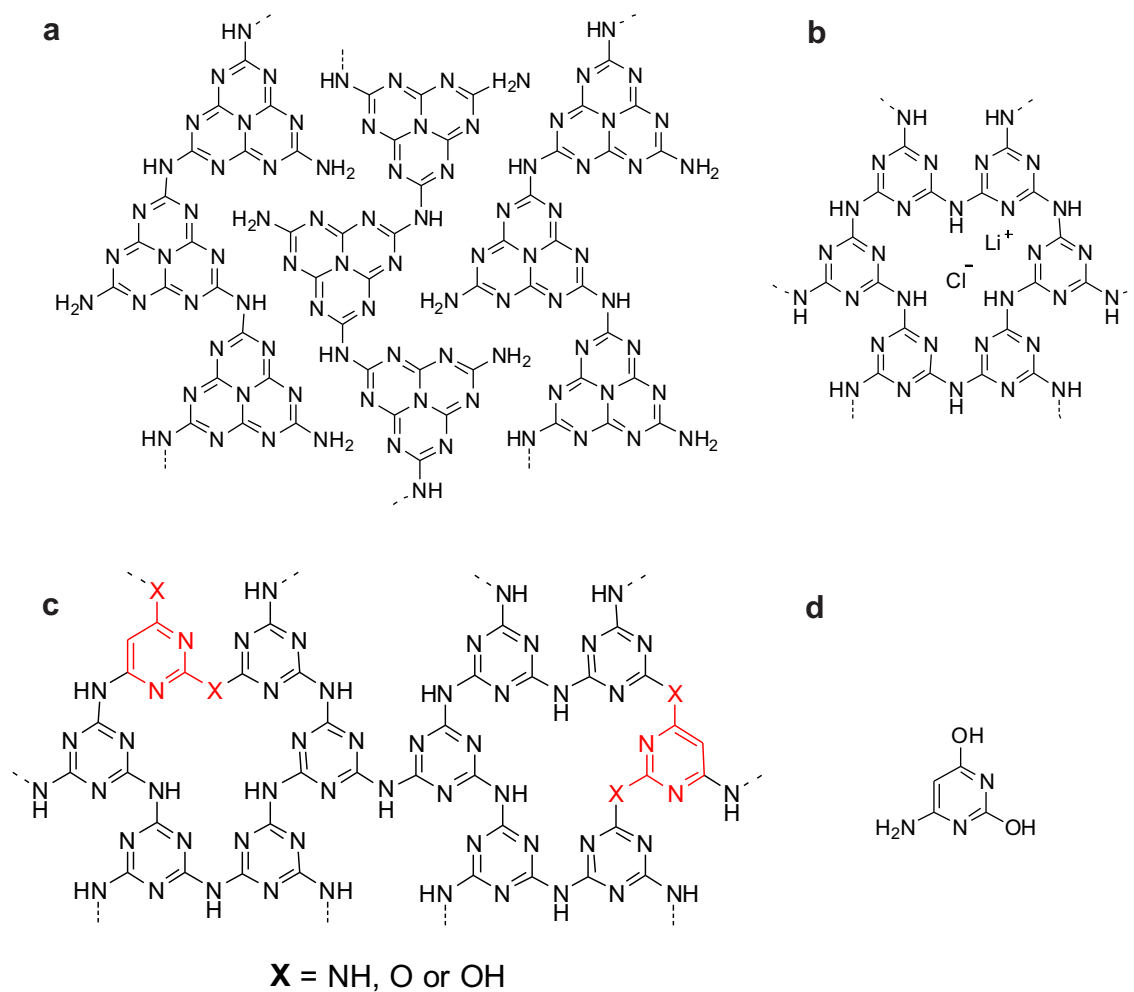
Figure 4.1: Chemical structures of **(a)** melon, **(b)** PTI/ Li$^+$Cl$^-$ (idealized structure), **(c)** aPTI_4AP$_{16\%}$ (proposed structure), and **(d)** the dopant 4AP.

synthesis involving a LiCl/KCl salt melt. We used 4-amino-2,6-dihydroxypyrimidine (4AP; Figure 4.1 **(d)**) as the dopant because of its structural similarity to melamine and higher carbon and oxygen content. The photocatalytic activity of the as-prepared CNs was compared with that of crystalline PTI/Li$^+$Cl$^-$ and of heptazine-based raw melon (see the Supporting Information).

The XRD patterns of the aPTI samples confirm their amorphous character by the absence of sharp reflections (see the Supporting Information, Figure S1), which are present in the XRD patterns of crystalline PTI/Li$^+$Cl$^-$. However, the FTIR spectra of the synthesized aPTI CNs are still largely similar to that of PTI/Li$^+$Cl$^{-[8]}$ (Figure 4.2 **(d)** and Figures S2–5 in the Supporting Information), as they contain a band at 810 cm$^{-1}$ (ring sextant out of plane bending) and a fingerprint region between 1200 and 1620 cm$^{-1}$ that is dominated by $\bar{\nu}$(C$-$NH$-$C) and $\bar{\nu}$(C=N) stretching vibrations.[5,10] Doping with 4AP gives rise to less well-defined IR bands, thereby indicating a decrease in the structural order. In addition, in the spectra of 16 % and 32 % doped PTI there is a band at 914 cm$^{-1}$ that can be assigned to aromatic C$-$H bending vibrations of the dopant (see the Supporting Information, Figure S5). Interestingly, the bands at 2160 cm$^{-1}$, 1730 cm$^{-1}$, and around 1200 cm$^{-1}$, which are seen in the spectrum of aPTI and partially in those of the doped samples, point to the presence of terminal nitrile groups as well as oxygen containing functionalities, such as C=O and C$-$O.

Elemental analysis (EA) indicates the atomic ratio C/N = 0.68 for PTI/Li$^+$Cl$^-$, whereas the C/N ratios of the aPTI samples are slightly increased for those synthesized at elevated temperatures, indicating either a higher degree of condensation or an increase of oxygen incorporation (see the Supporting Information, Table S1). Notably, the amount of Li and Cl is lower in doped and nondoped aPTI than in crystalline PTI/Li$^+$Cl$^-$, whereas the oxygen content is significantly higher, consistent with the IR results. This finding is worth noting as the amount of carbon and oxygen atoms in CNs is likely to play an essential role in the activity of CN photocatalysts.[11] By increasing the amount of 4AP incorporated in the doped PTI from 2 % to 64 % the C/N ratio increases from 0.69 to 1.13, respectively (see the Supporting Information, Table S2). In summary, the EA and IR results suggest that both carbon and oxygen atoms are incorporated into the amorphous materials, most likely through replacement of one of the ring or bridging nitrogen atoms, as proposed in Figure 4.1 **(c)**.

The $^{13}$C and $^{15}$N cross-polarization magic-angle spinning (CP–MAS) NMR spectra (Figure 4.2 **(a)** and **(c)**) for aPTI doped with 16 % 4AP and synthesized at 550 °C (aPTI_4AP$_{16\%}$) provide additional information about the structural composition of the material derived from copolymerization with 4AP. Both spectra are similar to those of PTI/Li$^+$Cl$^-$ (see the Supporting Information, Figure S6),[8,9] albeit with
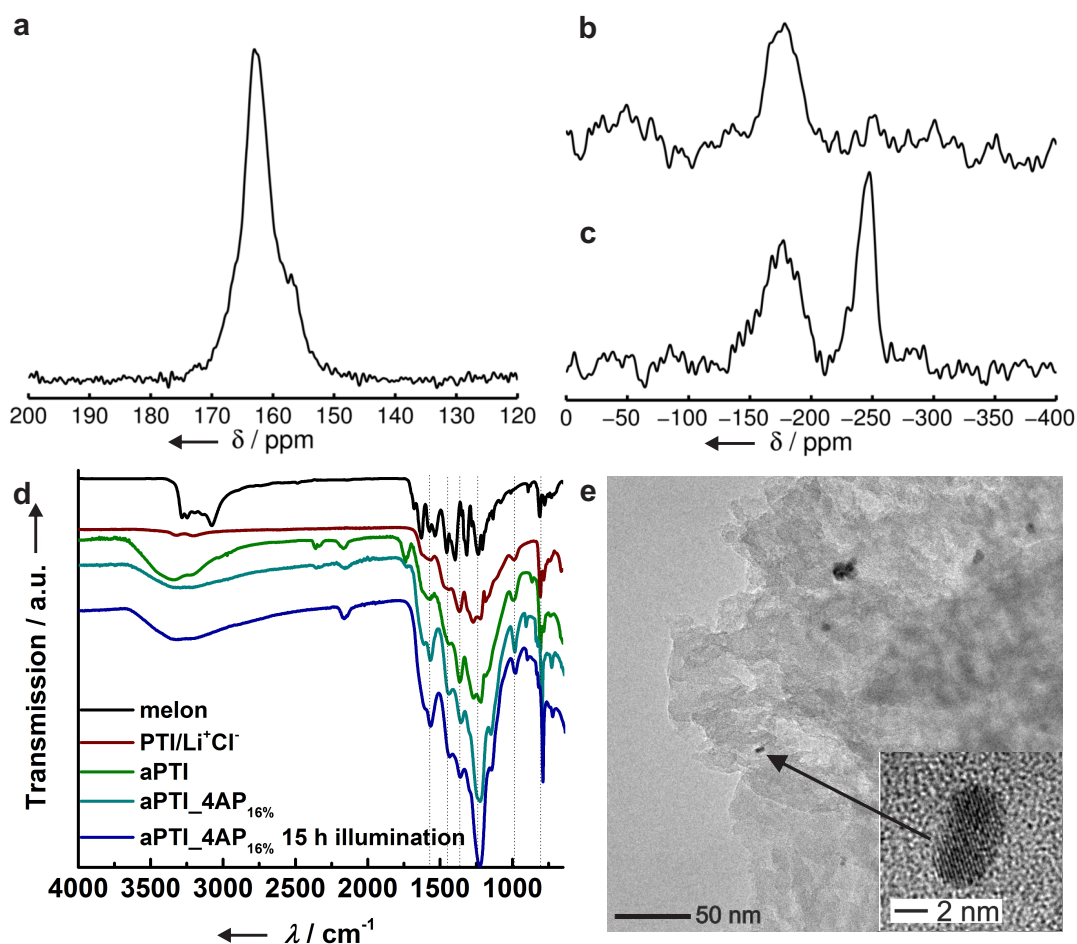
Figure 4.2: **(a)** $^{13}$C CP-MAS NMR spectrum (10 kHz), **(b)** $^{15}$N CPPI MAS NMR spectrum (6 kHz, inversion time = 400 µs) and **(c)** $^{15}$N CP-MAS NMR spectrum (10 kHz) of aPTI_4AP$_{16\%}$. **(d)** FTIR spectra of aPTI_4AP$_{16\%}$ synthesized at 550 °C before and after 15 h illumination, compared to crystalline PTI/Li$^+$Cl$^-$, aPTI$_{500\,°C}$, and melon. **(e)** A typical image of 2.3 wt% Pt-loaded aPTI_4AP$_{8\%}$ after illumination for 3 h under visible light ($\lambda > 420$ nm) and at higher magnification (inset).

significantly increased line width (full width at half maximum (FWHM)) of 1.5 kHz compared to 600 Hz owing to the less ordered character of the materials (see the Supporting Information, Figure S1). The $^{15}$N CP–MAS spectrum shows two broad signal groups centered around $-175$ and $-245$ ppm. The former group is typical for tertiary ring nitrogen atoms ($N_{tert}$; from the outer ring nitrogen atoms of heptazine or triazine rings), whereas the latter is characteristic of bridging NH groups. A weak signal around $-280$ ppm indicates that only a small amount of terminal NH$_2$ groups is present, hence a melon-type structure seems very unlikely. However, to further corroborate this hypothesis and identify the type of heterocycle formed under the conditions used—triazine versus heptazine—we recorded a $^{15}$N cross polarization polarization inversion (CPPI)[12] NMR spectrum of aPTI_4AP$_{16\%}$ (Figure 4.2 **(b)**) with an inversion time of 400 µs. Under such conditions, resonances of the NH groups are reduced to zero intensity whereas signals of NH$_2$ units will be inverted. In contrast, the $^{15}$N signals of tertiary nitrogen atoms are expected to remain largely unaffected. Hence, the unique signal for the central nitrogen atom, $N_c$, of a heptazine ring between $-220$ and $-240$ ppm can unequivocally be identified.[5] The absence of any signals in the $^{15}$N CPPI spectrum (Figure 4.2 **(b)**) in the region between $-200$ and $-300$ ppm therefore strongly suggests the absence of heptazine units within the detection limit of roughly 10 to 15 %. The markedly different intensity ratios in the $^{13}$C CP-MAS spectrum of aPTI_4AP$_{16\%}$ (Figure 4.2 **(a)**) compared to those in the $^{13}$C CP-MAS spectrum of PTI/Li$^+$Cl$^-$, and the broad asymmetric high-field flank of the signal between $-140$ and $-170$ ppm in the $^{15}$N CP-MAS spectrum (Figure 4.2 **(c)**) may indicate partial incorporation of pyrimidine into the PTI framework during copolymerization, which is not observed for PTI/Li$^+$Cl$^-$.[8,9]
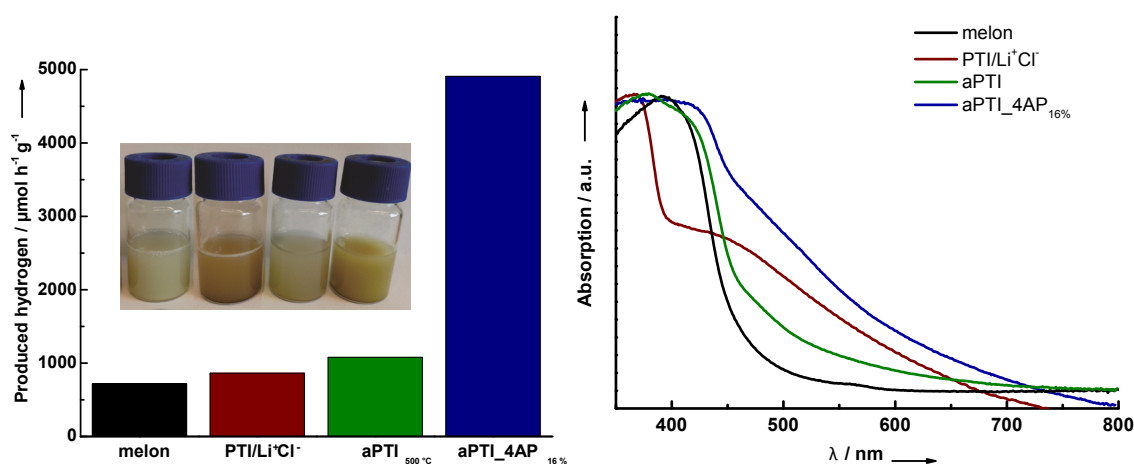


Figure 4.3: Photocatalytic activity towards hydrogen production **(a)**. UV/Vis spectra **(b)** and color of the water/TEoA suspensions (inset in (a)) of aPTI_4AP$_{16\%}$ synthesized at 550 °C compared to crystalline PTI/Li$^+$Cl$^-$, aPTI synthesized at 500 °C, and melon.

The brown color of crystalline $PTI/Li^+Cl^-$ indicates substantial absorption in the visible range of the spectrum. More specifically, the material absorbs largely in the UV region, yet additional absorption takes place in the blue part of the visible region and there is a gradual decrease in absorption toward longer wavelengths (Figure 4.3 and Figure S7 in the Supporting Information). The absorption spectra of aPTI synthesized at 400 to 600 °C show bands that are comparable to those in the spectrum of melon, thus rendering the color of the materials similar to that of melon (see the Supporting Information, Figures S7 and S10). When the reaction temperature is increased, the color of aPTI changes from cream (400 °C) to yellow (500 °C), suggesting enhanced absorption in the visible region. The absorption of $aPTI_{500\,°C}$, which is synthesized at a reaction temperature of 500 °C, is strongly red-shifted compared to that of crystalline $PTI/Li^+Cl^-$, thereby representing further improvement in the visible-light absorption (see the Supporting Information, Figure S7 (1)). With increasing amounts of dopant the color of the 4AP-doped CNs gets darker, changing from yellow (2 %) to red-brown (64 %); this color change correlates well with the red-shift observed in the absorption spectra (see the Supporting Information, Figure S8).

The inherent 2D architecture of crystalline $PTI/Li^+Cl^-$ gives rise to an expanded $\pi$-electron system, lower band gap, and enhanced absorption as compared to the 1D polymer melon, and thus renders $PTI/Li^+Cl^-$ a promising photocatalyst that may even outperform the heptazine-based semiconductors. In fact, hydrogen production of 864 µmol h$^{-1}$ g$^{-1}$ (ca. 15 % error) was measured for crystalline $PTI/Li^+Cl^-$ in the presence of a Pt cocatalyst and triethanolamine (TEoA) as sacrificial electron donor; this result equates to an enhancement of approximately 20 % compared to synthesized raw melon (see the Experimental Section; 722 µmol h$^{-1}$ g$^{-1}$) and is comparable to "g-C$_3$N$_4$" synthesized at 600 °C (synthesis according to Zhang et al.;[7a] 844 µmol h$^{-1}$ g$^{-1}$). The photocatalytic activity of the amorphous CNs synthesized in an open system in the temperature range 400 to 600 °C showed that the highest activity was achieved for the CN synthesized at a reaction temperature of 500 °C (1080 µmol h$^{-1}$ g$^{-1}$); this activity corresponds to an approximately 50 % enhancement compared to that of raw melon (see Table 4.1).

Table 4.1: Physicochemical properties and photocatalytic activity of different Pt\CN$_x$ species for the hydrogen evolution reaction driven by visible light.

| Catalyst | Surface Area (m$^2$ g$^{-1}$) | C/N Molar Ratio | H$_2$ Evolution Rate (µmol h$^{-1}$ g$^{-1}$) | Quantum Efficiency (%) |
|---|---|---|---|---|
| PTI/Li$^+$Cl$^-$ | 37 | 0.68 | 864 | 0.60 |
| Melon | 18 | 0.62 | 722 | 0.50 |
| aPTI$_{500\,°C}$ | 122 | 0.69 | 1080 | 0.75 |
| aPTI_4AP$_{16\%}$ | 60 | 0.82 | 4907 | 3.40 |

Although the above results show a moderate improvement of the photocatalytic activity of PTI derived materials compared to melon-based ones, when PTI is doped with 4AP the increase in the photoactivity of PTI is a function of the doping level and synthesis temperature. By increasing the temperature from 400 to 600 °C, an optimum photocatalytic activity was measured for the material synthesized at 550 °C (see the Supporting Information, Figure S13). When the content of 4AP was increased from 2 to 64 %, the highest photocatalytic activity of 4907 $\mu$mol h$^{-1}$ g$^{-1}$ (3.4 % quantum efficiency) was detected for 16 % doped aPTI, synthesized at 550 °C (aPTI_4AP$_{16\%}$; Figure S14 in the Supporting Information and Table 1). In essence, the photocatalytic activity of PTI/Li$^+$Cl$^-$ can be enhanced by 5 to 6 times upon doping with 4AP in a simple one-pot reaction. 4AP doping of crystalline PTI/Li$^+$Cl$^-$ leads to no apparent photocatalytic activity. Also, as a control experiment, pure 4AP was shown to be photocatalytically inactive by itself and under ionothermal or thermal treatment. Water oxidation experiments in which O$_2$ evolution was measured, carried out in the presence of a Co$_3$O$_4$ cocatalyst, did not yield substantial amounts of oxygen, thus suggesting that either water oxidation is thermodynamically unfeasible or that the reaction conditions need to be further optimized.

A typical TEM micrograph shows that the surface morphology of doped aPTI is layered and platelet-like (Figure 4.2 **(d)** and S11 in the Supporting Information). The crystallite size and composition of the platinum nanoparticles deposited on the carbon nitride catalyst in situ were studied by TEM and EDX. The results reveal that the photoinduced reduction of the cocatalyst results in well-dispersed nanoparticles roughly 5 nm in diameter.

N$_2$ sorption measurements allow us to quantify the impact of the surface area (SA) of the catalysts on the photocatalytic activity. In Table 4.1, the measured specific Brunauer-Emmett-Teller (BET) SAs indicate a weak correlation between SA and activity, but the increased photoactivity in the doped species cannot be rationalized by an increased SA alone.

As seen in Figure 4.3, the aPTI_4AP$_{16\%}$ photocatalyst yields an orange-brown suspension and its diffuse reflectance spectrum spans across the visible region. It is therefore instructive to examine the wavelength-specific hydrogen production to determine which wavelengths actively contribute to the H$_2$ evolution.

In the wavelength dependence graph (Figure 4.7**(b)**, the absorption is overlaid with the wavelength-specific hydrogen evolution. The hydrogen production rate falls off at 450 to 500 nm, thus indicating that the majority of photons contributing to the hydrogen production are at $\lambda < 500$ nm. It is suggested that the active absorption follows the band edge observed between 430 and 440 nm. This band is similar to that seen for the other PTI compounds although red-shifted by the 4AP doping. The broad absorption profile suggests the existence of intra band gap electronic states at

various energies, which could arise from the incorporated 4AP (see the Supporting Information, Figure S4 and S5).

However, as Figure 4.7(b) infers, not all electronic states—especially those associated with absorption at longer wavelengths—contribute to the hydrogen evolution but may rather act as traps and quenching sites for excitons. We therefore envision that through active control of the number and position of defects in the material, photocatalysts with further enhanced activity can rationally be designed. Nevertheless, the increased visible-light activity up to approximately 500 nm in doped PTI results in a significant improvement over its undoped or crystalline counterparts and is a contributing factor to its high photoactivity.

In conclusion, we have reported a new family of 2D triazine-based carbon nitrides that shows substantial visible light-induced hydrogen production from water, and in this regard rivals the benchmark heptazine-derived photocatalysts. With external quantum efficiencies as high as 3.4 %, the amorphous carbon- and oxygen-enriched poly(triazine imide) species not only outperform melon-type photocatalysts, but also crystalline PTI by 5 to 6 times. Consistent with previous results,[13] we have demonstrated that a rather low level of structural definition and the introduction of defects up to a certain doping level (16 % for 4-amino-2,6dihydroxypyrimidine) tend to enhance the photoactivity of the catalysts. We believe that the diverse range of available organic and inorganic dopants will allow the rational design of a broad set of triazine-based CN polymers with controlled functions, thus opening new avenues for the development of light-harvesting semiconductors. The easily adjustable structural and electronic properties of CN polymers render them particularly versatile for solar energy applications.

## 4.1.1 Paper Bibliography

[1] X. Chen, S. Shen, L. Guo, S. S. Mao, *Chem. Rev.* **2010**, 110, 6503 – 6570.

[2] H. Tong, S. Ouyang, Y. Bi, N. Umezawa, M. Oshikiri, J. Ye, *Adv. Mater.* **2012**, 24, 229 – 251.

[3] **a)** X. Wang, K. Maeda, A. Thomas, K. Takanabe, G. Xing, J. M. Carlsson, K. Domen, M. Antonietti, *Nat. Mater.* **2009**, 8, 76 – 80.
**b)** E. Kroke, M. Schwarz, E. HorathBordon, P. Kroll, B. Noll, A. D. Norman, New *J. Chem.* **2002**, 26, 508 – 512.

[4] **a)** Y. Wang, X. Wang, M. Antonietti, Angew. Chem. 2012, 124, 70 – 92; *Angew. Chem. Int. Ed.* **2012**, 51, 68 – 89.
**b)** Y. Zheng, J. Liu, J. Liang, M. Jaroniec, S. Z. Qiao, *Energy Environ. Sci.* **2012**, 5, 6717 – 6731.

[5] **a)** B. V. Lotsch, M. Döblinger, J. Sehnert, L. Seyfarth, J. Senker, O. Oeckler, W. Schnick, *Chem. Eur. J.* **2007**, 13, 4969 – 4980.
**b)** L. Seyfarth, J. Seyfarth, B. V. Lotsch, W. Schnick, J. Senker, *Phys. Chem. Chem. Phys.* **2010**, 12, 2227 – 2237.
**c)** B. Jürgens, E. Irran, J. Senker, P. Kroll, H. Müller, W. Schnick, *J. Am. Chem. Soc.* **2003**, 125, 10288 – 10300.

[6] **a)** D. Mitoraj, H. Kisch, *Chem. Eur. J.* **2010**, 16, 261 – 269.
**b)** E. Kroke, M. Schwarz, *Coord. Chem. Rev.* **2004**, 248, 493 – 532.
**c)** G. Goglio, D. Foy, G. Demazeau, *Mater. Sci. Eng. R* **2008**, 58, 195 – 227.
**d)** X. Li, J. Zhang, L. Shen, Y. Ma, W.Lei, Q. Cui, G. Zou,
*Appl. Phys. A* **2009**, 94, 387 – 392.

[7] **a)** J. Zhang, X. Chen, K. Takanabe, K. Maeda, K. Domen, J. D. Epping, X. Fu, M. Antonietti, X.Wang, *Angew. Chem.* **2010**, 122, 451 – 454;
*Angew. Chem. Int. Ed.* **2010**, 49, 441 – 444.
**b)** Q. Li, B. Yue, H. Iwai, T. Kako, J.Ye, *J. Phys. Chem.* C **2010**, 114, 4100 – 4105.
**c)** Y. Zhang, A. Thomas, M. Antonietti, X. Wang, *J. Am. Chem. Soc.* **2009**, 131, 50 – 51.
**d)** H. Yan, Y. Huang, *Chem. Commun.* **2011**, 47, 4168 – 4170.

[8] E. Wirnhier, M. Döblinger, D. Gunzelmann, J. Senker, B. V. Lotsch, W. Schnick, *Chem. Eur. J.* **2011**, 17, 3213 – 3221.

[9] M. J. Bojdys, J.-O. Müller,M. Antonietti, A. Thomas, *Chem. Eur. J.* **2008**, 14, 8177 – 8.

[10] **a)** B. V. Lotsch, W. Schnick, *Chem. Mater.* **2006**, 18, 1891 – 1900.
**b)** A. I. Finkel'shtein, *Opt. Spektrosk.* **1959**, 6, 33.
**c)** M. Takimoto, *Kogyo Kagaku Zasshi* **1961**, 64, 1452 – 1454.

**d)** M. Takimoto, *Nippon Kagaku Zasshi* **1964**, 85, 159 – 168.

**e)** D. A. Long, *J. Raman Spectrosc.* **2004**, 35, 905 – 905.

**f)** B. V. Lotsch, W.Schnick, *Chem. Eur. J.* **2007**, 13, 4956 – 4968.

[11] **a)** P. Niu, G. Liu, H. M. Cheng, *J. Phys. Chem. C* **2012**, 116, 11013 – 11018.

**b)** A. Thomas, A. Fischer, F. Goettmann, M. Antonietti, J.-O. Müller, R. Schlçgl, J. M. Carlsson, *J. Mater. Chem.* **2008**, 18, 4893 – 4908.

**c)** A. V. Semencha, L. N. Blinov, *Glass Phys. Chem.* **2010**, 36, 199 – 208.

**d)** X. Q. Gong, A. Selloni, M. Batzill, U. Diebold, *Nat. Mater.* **2006**, 5, 665 – 670.

**e)** M. K.Nowotny, L. R. Sheppard, T. Bak, J. Nowotny, *J. Phys. Chem. C* **2008**, 112, 5275 – 5300.

[12] **a)** X. Wu, K. W. Zilm, *J. Magn. Reson. Ser. A* **1993**, 102, 205 – 213.

**b)** C. Gervais, F. Babonneau, J. Maquet, C. Bonhomme, D. Massiot, E. Framery, M. Vaultier, *Magn. Reson. Chem.* **1998**, 36, 407 – 414.

[13] **a)** X. Chen, L. Liu, P. Y. Yu, S. S. Mao, *Science* **2011**, 331, 746 – 750.

**b)** M. Alvaro, E. Carbonell, V. Fornés, H. García, *Chem. Phys. Chem.* **2006**, 7, 200 – 205.

**c)** G. Zhang, J. Zhang, M. Zhang, X. Wang, *J. Mater. Chem.* **2012**, 22, 8083 – 8091.

[14] While this paper was in review, complementary data on the photocatalytic water splitting of crystalline PTI were published: Y. Ham, K. Maeda, D. Cha, K. Takanabe, K. Domen, *Chem. Asian J.* **2013**, 8, 218 – 224.

## 4.1.2   Supplementary Information

**Experimental Section:**

**Photocatalysis:** 1 mg mL$^{-1}$ aqueous solutions of carbon nitride catalyst were prepared and dispersed with an ultrasonic bath for 30  min. Triethanolamine (TEoA) was used as a sacrificial electron donor and $H_2PtCl_6$ (8 wt% in $H_2O$) was used as the Pt cocatalyst precursor which was photo-reduced during the reaction. Suspensions with 10 vol% TEoA and 6 µL $H_2PtCl_6$ (2.3 wt% Pt) were illuminated in 24 mL glass vials in an argon atmosphere with silicone/PTFE septa. Samples were side-illuminated with a 300 W Xenon lamp with a water filter and dichroic mirror blocking wavelengths < 420 nm. The evolved gas was measured by gas chromatography with an online injection system and using a thermal conductivity detector with argon as carrier gas.

**Synthesis of PTI/Li$^+$Cl$^-$ according to Wirnhier et al.**[S1−2]
Dicyandiamide (0.20 g, 2.38 mmol) and an eutectic mixture of lithium chloride (59.2 mol%,

0.90 g, 21.33 mmol) and potassium chloride (40.8 mol%, 1.01 g, 14.70 mmol) were ground together in a glovebox. The reaction mixture was transferred into a dried thick-walled silica glass tube ($\oslash$ ext. 15 mm, $\oslash$ int. 11 mm). The tube was placed in a horizontal tube furnace and heated under atmospheric argon pressure at 6 °C min$^{-1}$ to 400 °C. This temperature was held for 12 h and afterwards the sample was cooled to room temperature at 20 °C min$^{-1}$. After this procedure, the tube was evacuated and sealed at a length of 120 mm. In a second step the ampoule was placed in a vertical tube furnace and heated at 1 °C min$^{-1}$ to 600 °C at which the sample was held for 24 h. After cooling down to room temperature the ampoule was broken and the sample was isolated and washed with boiling water to remove residual salt. The resulting material PTI/Li$^+$Cl$^-$ was obtained as a brown powder (80 mg, 50 %)*.

**Synthesis of aPTI using a modified procedure reported by Wirnhier et al.**[S1−2]
Dicyandiamide (1.00 g, 11.90 mmol) and an eutectic mixture of lithium chloride (59.2 mol% 2.26 g, 53.56 mmol) and potassium chloride (40.8 mol%, 2.74 g, 39.88 mmol) were ground together in a glovebox. The reaction mixture was transferred in open porcelain crucibles which were heated either in an argon-purged tube- or muffel furnace at 12 °C min$^{-1}$ to 400 to 600 °C. The temperature was held for 6 h and afterwards the samples were cooled down to room temperature. The samples were isolated and washed with boiling water to remove residual salts. The resulting materials yielded beige (0.70 g, 88 %) to yellow colored powders (0.30 g, 38 %)[1].

**Synthesis of doped amorphous PTI using a modified procedure reported by Wirnhier et al.**[S1−2]
Dicyandiamide (0.50 g, 5.95 mmol), an eutectic mixture of lithium chloride (59.2 mol%) and potasiumchloride (40.8 mol%) and 4AP as doping agent (2, 8, 16, 32 or 64%) were ground and transferred in open porcelain crucibles, which were heated in a muffel furnace at 12 °C min$^{-1}$ to 400 to 600 °C for 6 h. The syntheses yielded yellow (0.30 g, 75 %) to dark orange colored products (0.16 g, 40 %)[1].

**Synthesis of raw melon according to Sattler et al.**[S3]
A porcelain crucible was loaded with melamine (20 g) and covered with a porcelain lid. The crucible was placed in a muffle furnace and maintained at 490 °C for 4 days. The product was ground to a powder and homogenized after the first day.

**Synthesis of "g-C$_3$N$_4$" according to Zhang et al.**[S4]
A porcelain crucible was loaded with dicyandiamide and heated in a muffle furnace at 600 °C for 4 h. The synthesis yielded a yellow colored powder.

---

*Yields in percentage are based on crystalline PTI and can be considered as an approximate value.

## Methods:

**X-ray powder diffraction:** X-ray powder diffraction experiments were carried out on a Huber G670 diffractometer in Guinier geometry using Ge(111) monochromatised Cu-K$\alpha_1$-radiation ($\lambda = 1.54051$ Å). The specimen was ground in a mortar and evenly spread between two chemplex foils (Breitländer GmbH).

**IR-spectroscopy:** FTIR spectra were recorded on a Perkin Elmer Spektrum BX II spectrometer with an attenuated total reflectance unit. NMR-spectroscopy.

**NMR:** The $^{13}$C and $^{15}$N MAS NMR spectra were recorded at ambient temperature on an Avance 500 solid-state NMR spectrometer (Bruker) with an external magnetic field of 11.7 T, operating at frequencies of 500.1 MHz, 125.7 MHz and 50.7 MHz for $^{1}$H, $^{13}$C and $^{15}$N, respectively. The sample was contained in a 4 mm $ZrO_2$ rotor which was mounted in a standard double resonance MAS probe (Bruker). The $^{13}$C and $^{15}$N chemical shifts were referenced relative to TMS and nitromethane.

The $^{1}$H$^{15}$N and $^{1}$H$^{13}$C cross-polarization (CP) MAS spectra were recorded at a spinning speed of 10 kHz using a ramped-amplitude (RAMP) CP pulse on $^{1}$H, centered on the n = +1 Hartmann-Hahn condition, with a nutation frequency $\nu_{nut}$ of 55 kHz ($^{15}$N) and 40 kHz ($^{13}$C). During a contact time of 7 ms the $^{1}$H RF field was linearly varied about 20 %.

The $^{15}$N cross polarization combined with polarization inversion (CPPI) NMR spectrum was recorded at a spinning frequency of 6 kHz using a contact time of 7 ms and an inversion time of 400 µs. Constant amplitude CP pulses were applied on $^{15}$N ($\nu_{nut}$ = 55 kHz) and $^{1}$H ($\nu_{nut}$ = 50 kHz).

In all $^{15}$N NMR experiments, a flip-back (FB)[S5] pulse was applied on $^{1}$H after the acquisition of the FID, so that the recycle delay becomes less dependent of the $^{1}$H T$_1$ relaxation time. $^{1}$H continuous wave (CW) decoupling (ca. 70 kHz RF field) was applied during the acquisition of the $^{15}$N signal. The recycle delay was set to 1.5 s. About 47500 and 121000 transients were accumulated for the CP and CPPI experiments, respectively.

**Diffuse reflectance measurements:** Optical diffuse reflectance spectra were collected at room temperature with a UV/VIS diffuse reflectance spectrometer (Varian, Cary 500). Powders were prepared between two quartz discs at the edge of the integrating sphere with $BaSO_4$ as the optical standard. Absorption spectra were calculated from the reflectance data with the Kubelka-Munk function.

**TEM:** HRTEM was performed with a Philips CM 30 ST microscope (LaB$_6$ cathode, 300 kV, CS = 1.15 mm). Images were recorded with a CCD camera (Gatan) and Digital Micrograph 3.6.1 (Gatan) was used as evaluation software. Chemical analyses (EDX) were performed with a Si/Li detector (Thermo Fisher, Noran System Seven).

**Adsorption measurements:** Nitrogen adsorption measurements were performed at 77 K with an Autosorb iQ instrument (Quantachrome Instruments, Boynton Beach, Florida, USA). Samples were outgassed in vacuum at 300 °C for 12 h. For BET calculations

pressure ranges were chosen with the help of the BET Assistant in the ASiQwin software (version 2.0). In accordance with the ISO recommendations multipoint BET tags equal or below the maximum in $V \cdot (1 - P/P_0)$ were chosen.

**Quantum efficiency:** The quantum efficiency was calculated according to $QE\% = ((2 \times H)/P) \times (100/1)$, where $H$ = number of evolved $H_2$ molecules and $P$ = incident number of photons on the sample. The incident light was measured with a thermopile power meter with a constant efficiency response across the visible spectrum. Wavelength specific hydrogen evolution was measured with 40 nm FWHM light filters (Thorlabs) and with the same incident light and filter transmission efficiency for each filter.

**Elemental analysis:** Elemental analysis of the elements C, H, N and S is accomplished by high temperature digestion coupled with dynamic gas components separation. The samples are burned explosively at 1150 °C in a highly oxygenated helium atmosphere. The combustion products are $CO_2$, $H_2O$, $H_2$, NO, $NO_2$, $SO_2$ and $SO_3$. The detection of the gases is done by a thermal conductivity measurement cell. The accuracy is 0.30 %. Measurements were done on an Elementar vario EL. The determination of oxygen was done under inert conditions at high temperature (1200 to 1400 °C).

[S1] E. Wirnhier, M. Döblinger, D. Gunzelmann, J. Senker, B. V. Lotsch, W. Schnick, *Chem. Eur. J.* **2011**, 17, 3213 – 3221.

[S2] M. J. Bojdys, J.-O. Müller, M. Antonietti, A. Thomas, *Chem. Eur. J.* **2008**, 14, 8177 – 8182.

[S3] A. Sattler, Doctoral Thesis, University of Munich (LMU), **2010**.

[S4] J. Zhang, X. Chen, K. Takanabe, K. Maeda, K. Domen, J. D. Epping, X. Fu, M. Antonietti, X. Wang, *Angew. Chem. Int. Ed.* **2010**, 49, 441 – 444.

[S5] **(a)** J. Tegenfeldt, U. Haeberlen, *J. Magn. Reson.* **1979**, 36, 453 – 57
**(b)** K. Saito, C. Martineau, G. Fink, F. Taulelle, *Solid State Nucl. Mag.* **2011**, 40, 66-71.

Figures S1 to S11 are not shown here and are available in the Supporting Information of the publication. Figures S12 to S15 are given below.
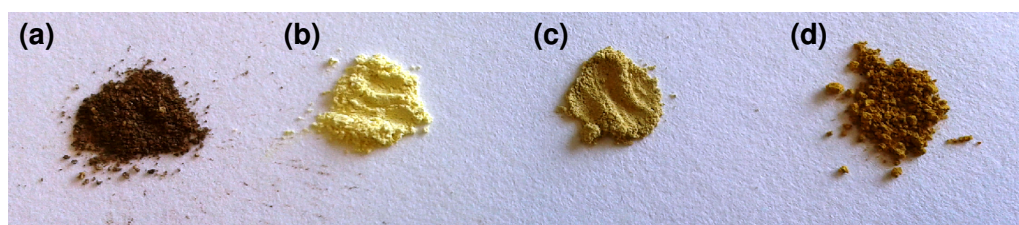


Figure 4.4: Picture of the photocatalyst powders: **(a)** Crystalline PTI, **(b)** melon 96 h at 490 °C, **(c)** amorphous PTI and **(d)** 4AP doped amorphous PTI.
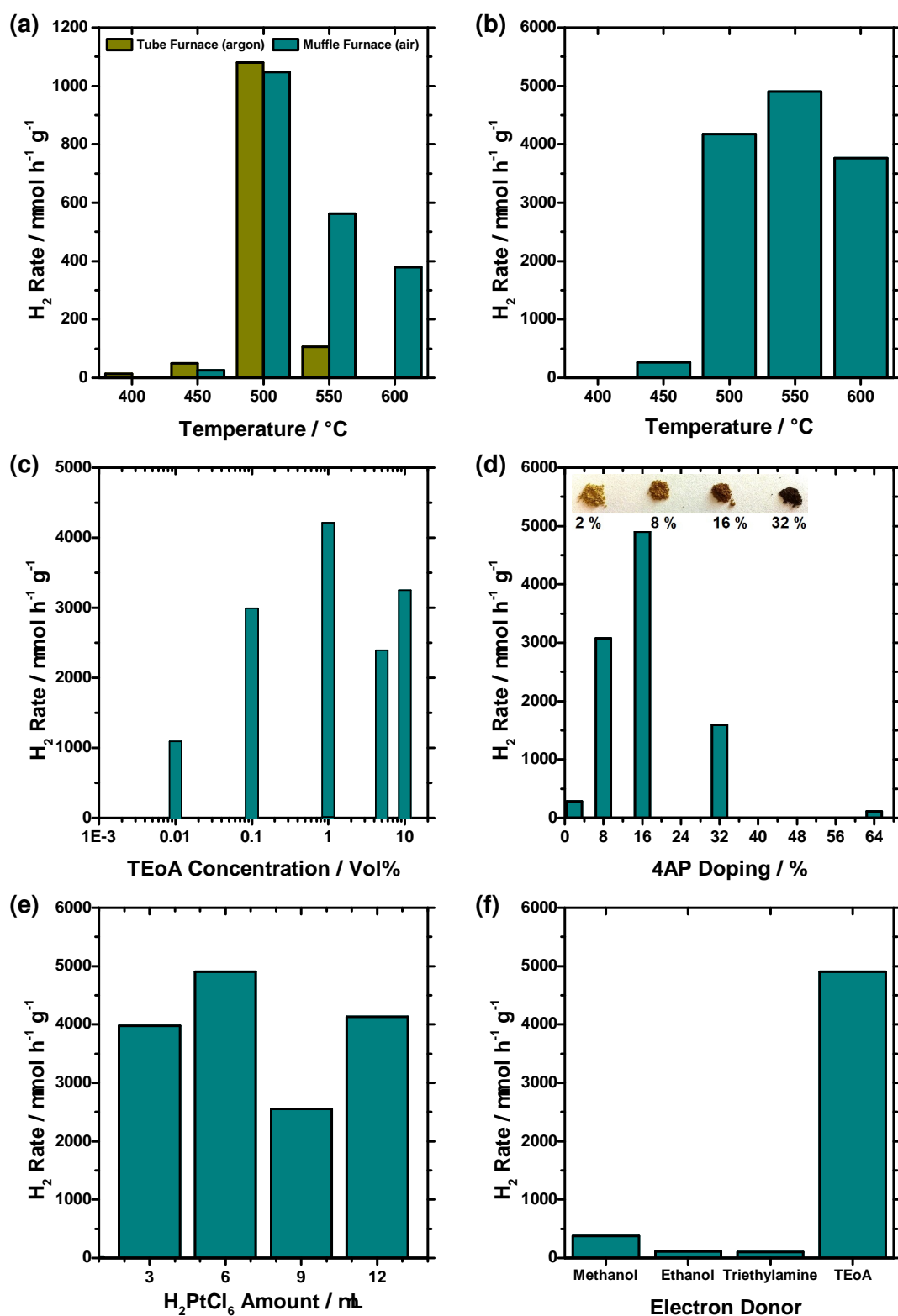
Figure 4.5: Optimisation experiments for $H_2$ generation: **(a)** Comparison of synthesis temperatures in air (muffle furnace) and in argon (tube furnace) for the *undoped* amorphous PTI. **(b)** Synthesis temperatures for the 16 % *doped* PTI. **(c)** TEoA amount for doped PTI (10 vol% was used in experiments). **(d)** Amount of 4AP doping calculated as (2, 8, 16, 32 and 64) % C-content with photos of the powders shown in the inset. **(e)** Cocatalyst amount optimisation and **(f)** hydrogen evolution rate as a function of the electron donor used.

## 4.2   Stability of 4AP-doped PTI

The chemical stability of a photocatalyst is important to consider so that it can continuously produce its product. Although fouling and regeneration of catalysts is common after an extended working time, the stability of these non-metal catalysts must be established. An ideal photocatalyst should produce product at a constant rate before physical limitations such as saturation of the reactor or depletion of electron donor are reached. There are many factors which will eventually degrade the performance of a photocatalyst. These can be categorised by structural changes of the reactants, aggregation and morphological changes, absorption changes, active site fouling etc. Of most importance at this stage, is the chemical stability of the photocatalyst itself.

$H_2$ generation from the degradation of photocatalysts or other by-products in the reaction is common and must be separated from true photo-generated hydrogen. A first step is to show that the photocatalyst produces more hydrogen than is theoretically available in the photocatalyst + electron donor + cocatalyst. This demonstrates that at least some of the $H_2$ is catalytically reduced from water. The 4AP doped PTI reaction conditions produced more than ten times the $H_2$ amount that is available chemically, so we confirm that it is catalytically active. We also show the $H_2$ is continuously produced for more than 32 h.

However, as can be seen in the stability curve (Figure 4.6), the rate decreases significantly in the first six hours. The effect of sonication, TEoA and Pt cocatalyst amount were firstly investigated and then, attention was directed to colour changes in the suspension.

Firstly, it is worth noting the high hydrogen production rate given in units of $\mathrm{mmol\,g^{-1}}$ instead of the usual $\mathrm{\mu mol\,g^{-1}}$. For this reason, the reactor was evacuated and argon purged after 3 h intervals. The hydrogen evolution rate after 1 h of illumination is marked with the red line in the figure. In Figure 4.6, the hydrogen production rate decreases for the first 12 h. This initial activity decrease could be attributed to factors such as blocking of active sites, particle aggregation, increased back-reaction and decreasing electron donor concentration. As can be seen from the figure, the rate stabilises to $3\ \mathrm{mmol\,g^{-1}}$ after 12 h illumination.

Three attempts to recover the hydrogen production rate were then taken. Firstly, to assess if particle aggregation, or cocatalyst aggregation might be the cause of the decreased activity, the suspension was ultrasonicated for 30 min. Although the initial rate is not restored, ultrasonication resulted in a $0.25\ \mathrm{\mu mol\,g^{-1}}$ increase in the rate suggesting that it has a beneficial effect. It is again worth noting that the added energy introduced during sonication produces $H_2$ from cavitation but this is removed from the reaction vessel during the argon purging steps. Besides aggregation
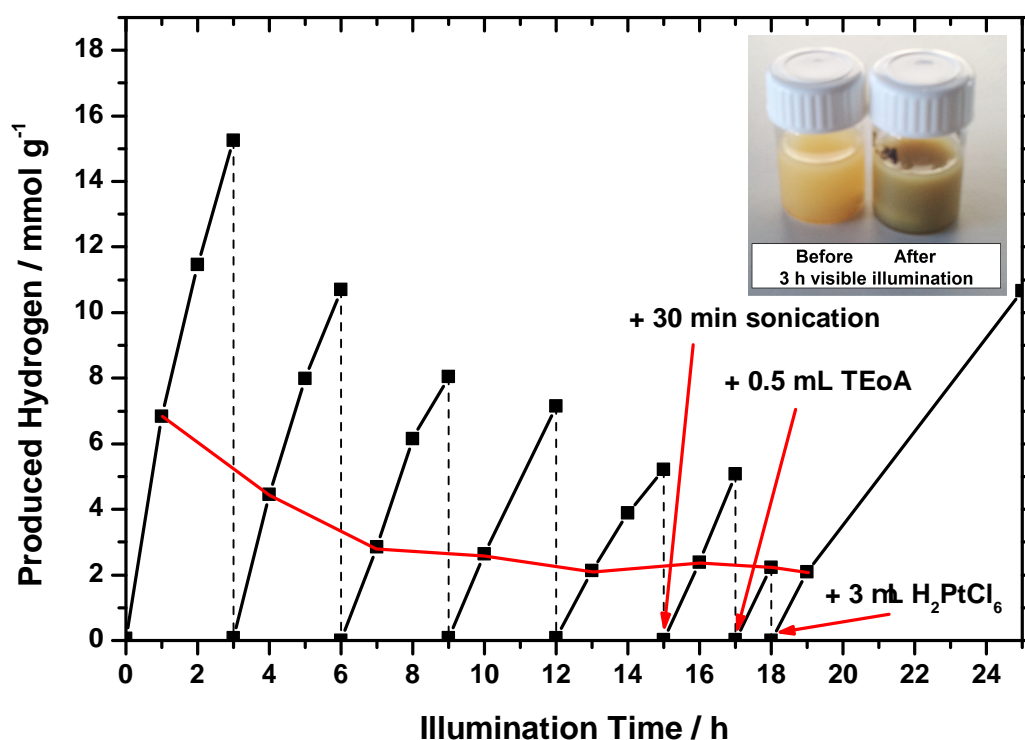
Figure 4.6: Stability of $H_2$ generation from 4AP doped aPTI. Photo of suspension colour change inset.

effects, sonication may simply open up new active sites that were previously blocked. Secondly, extra sacrificial electron donor was added to promote the removal of positive holes. This has proven to be effective at enhancing the rate with other photocatalytic experiments although usually after illumination times greater than 24 h. The convention of using 10 vol% electron donor is a concentration excess and the reducing power of TEoA should be maintained in the first 24 h of a reaction. As shown, addition of TEoA resulted in an insignificant change in the reaction rate. Thirdly, an additional 3 µL of cocatalyst precursor was added which also resulted in an insignificant change in the rate. Therefore, these attempts to restore the initial hydrogen evolution rate were unsuccessful. In summary, although the $H_2$ initially decreases, it reaches a stable rate of 3 mmol$\,$g$^{-1}$ which is maintained for a further 20 h illumination time. The initial decrease is not attributed to aggregation effects or depletion of electron donor or cocatalyst. Newly synthesised batches of doped PTI showed the same behaviour although with varying hydrogen evolution rates. Washing and Soxhlet-extraction of the powder also showed similar results. FTIR spectra of the doped PTI powder were identical before and after photocatalysis which suggests there were no detectable chemical structure changes.

Concerning stability, it was further observed that reaction suspensions got darker after 2 h illumination, changing from yellow to a yellow-green colour as shown in

the inset of Figure 4.6. Note that the suspension remained photocatalytically active, albeit at the lower hydrogen evolution rate of 3 mmol g$^{-1}$.

Importantly, the colour change is reversible as a yellow-orange colour could be restored by shaking the suspension by hand for 10 s although the original yellow colour could not be fully restored. Additional tests such as performing the reaction in the dark or illuminating TEoA or doped PTI by themselves did not show the green colour change. The dark yellow-green colour was only observed in aqueous suspensions of the doped PTI + TEoA + illumination. The photoreduced Pt precursor was not necessary to produce the colour change. $^1$H solution NMR of TEoA showed no changes when illuminated with full spectrum light. Oxidised TEoA in other photocatalytic reactions—although it may become irreversibly darker—did not show this reversible green colour change either.

In conclusion, It is proposed that this colour change is the reason for the decreasing reaction rate previously discussed and that the origin is a light activated interaction between 4AP doped aPTI and TEoA that produces an as yet unknown green intermediate that competes with the photocatalyst for absorption of light. It is still unclear if this interaction is intrinsic to the 4AP doped aPTI photocatalyst or if it is a result of the environment of the high H$_2$ evolution rates that it yields. The reversible colour change is reminiscent of the photobleaching effect as briefly discussed for methylene blue dye but a more plausible explanation is the formation of stable charge-transfer complex.[73,74]

# 4.3 Wavelength Dependence of Gas Evolution

In this section, the wavelength specific $H_2$ generation spectra (referred to as action-spectra) of amorphous PTI **(a)** and 4AP doped amorphous PTI **(b)** synthesised at 500 °C are explained further. Both samples were illuminated under the same conditions using bandpass filters for 1 h illumination time. Interestingly, the undoped aPTI produces four times more hydrogen than the doped PTI at 400 nm. Between 450 nm and 550 nm the rates are relatively equal for both samples. For 600 nm light, hydrogen is produced only in the doped aPTI sample. These results suggest that undoped PTI may outperform doped PTI if 400 nm light is included, for example in full spectrum or AM solar conditions. The publication uses $> 420$ nm illumination, excluding the 400 nm photons and prioritising the 550 nm to 600 nm visible light photons.

Overall, the wavelength specific hydrogen production follows the absorption spectra for both materials. The visible light enhancement effect is confirmed for the doped aPTI as hydrogen is produced using the yellow transmitting 600 nm filter. Finally, these results propose that undoped amorphous PTI should be revisited for photocatalytic hydrogen production, especially for standard AM1.5 conditions.
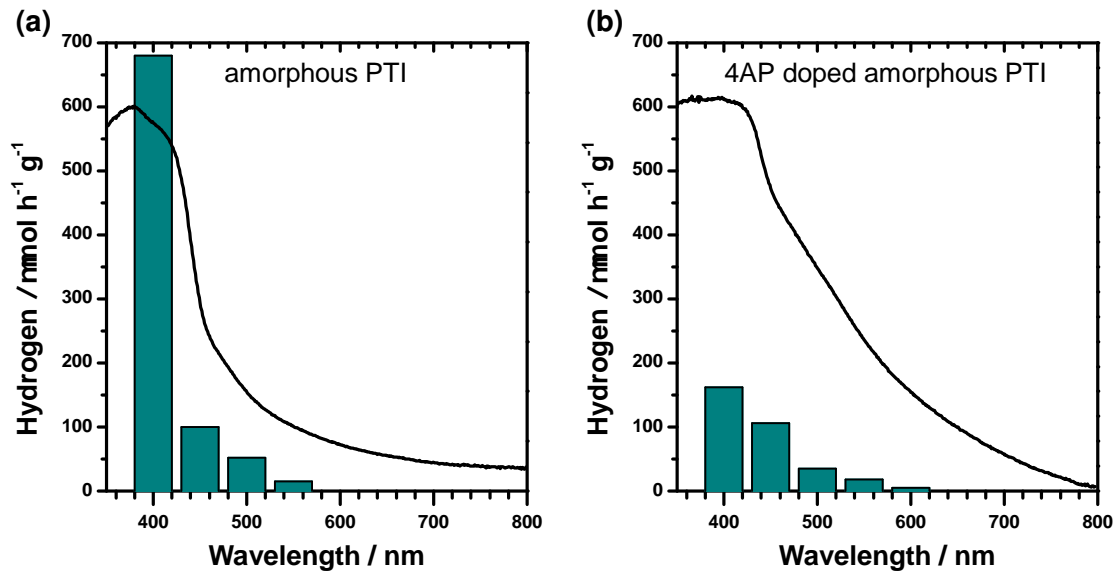


Figure 4.7: Wavelength-dependent $H_2$ generation of **(a)** undoped amorphous PTI and **(b)** 4AP doped amorphous PTI. Transmission filters were used to select the wavelengths (40 nm FWHM).

## 4.4 Gas Evolution in the Suspension using the Hiden MS Liquid Probe

As described in Section 3.5.4, it is possible to measure dissolved gases directly in the water/PTI/TEoA suspension rather than the headspace. Using the liquid probe of the Hiden mass spectrometer (PDMS membrane that is semi permeable to gases), we can investigate gas evolution as it is produced and also investigate dissolved gas species in the water/TEoA suspension. In this setup, the probe is submerged in an open-air beaker of the photocatalyst suspension and illuminated from the side with a xenon lamp. Standard conditions were chosen: 10 mg catalyst, 9 mL $H_2O$, 1 mL TEoA and 6 µL $H_2PtCl_6$ cocatalyst precursor.

In Figure 4.8, the $H_2(\mathbf{a})$ signal for *crystalline* PTI (cPTI) is monitored. Firstly, the detector settling time takes $\approx$ 1 h. At time 01:12, the xenon lamp is turned on and the signal instantly increases. The response time of the detector is $\approx$ 600 $\mu$s so these are practically real-time responses. As shown by the blue fitting, there is a linear (Y=mX+C) increase in the $H_2$ signal for 15 min. Then the signal begins to plateau exponentially (Y=$A_0$e$^{-kX}$+C) as marked by the red fitting. At 02:39 measuring time, the lamp is switched off and the signal decreases exponentially as marked by the green fitting.

The linear increase in the signal is expected for an increasing concentration of $H_2$ and this shows that the rate of $H_2$ evolution is constant over this 15 min time interval. There was no lag in hydrogen evolution detected when the lamp was switched on. The second exponential fitting describes the limit of the $H_2$ concentration in the suspension. This may be due to saturation of the suspension, loss of $H_2$ at the liquid surface or limited permeability of the probe membrane. Consequently, the $H_2$ signal reaches a plateau. At 02:39 the xenon lamp is switched off and the signal exponentially decays as marked by the green fitting. Interestingly, the decay rates are similar for both exponential fittings (e.g. 0.011). This is expected for an instantaneous halt to hydrogen generation when the light is turned off, as observed for the start of the reaction. The fitting equations are given below for reference.

$$f_1 = +2.540 \times 10^{+1}(x) - 8.446 \tag{4.1}$$

$$f_2 = -1.041 \times 10^{-5}(e^{(\frac{-x}{0.011})}) + 1.782 \times 10^{-7} \tag{4.2}$$

$$f_3 = +1.760 \times 10^{-3}(e^{(\frac{-x}{0.011})}) + 8.488 \times 10^{-8} \tag{4.3}$$

$$f_4 = +1.502 \times 10^{-5}(x) - 9.191 \times 10^{-7} \tag{4.4}$$

$$f_5 = -8.945 \times 10^{-7}(x) - 6.206 \times 10^{-7} \tag{4.5}$$
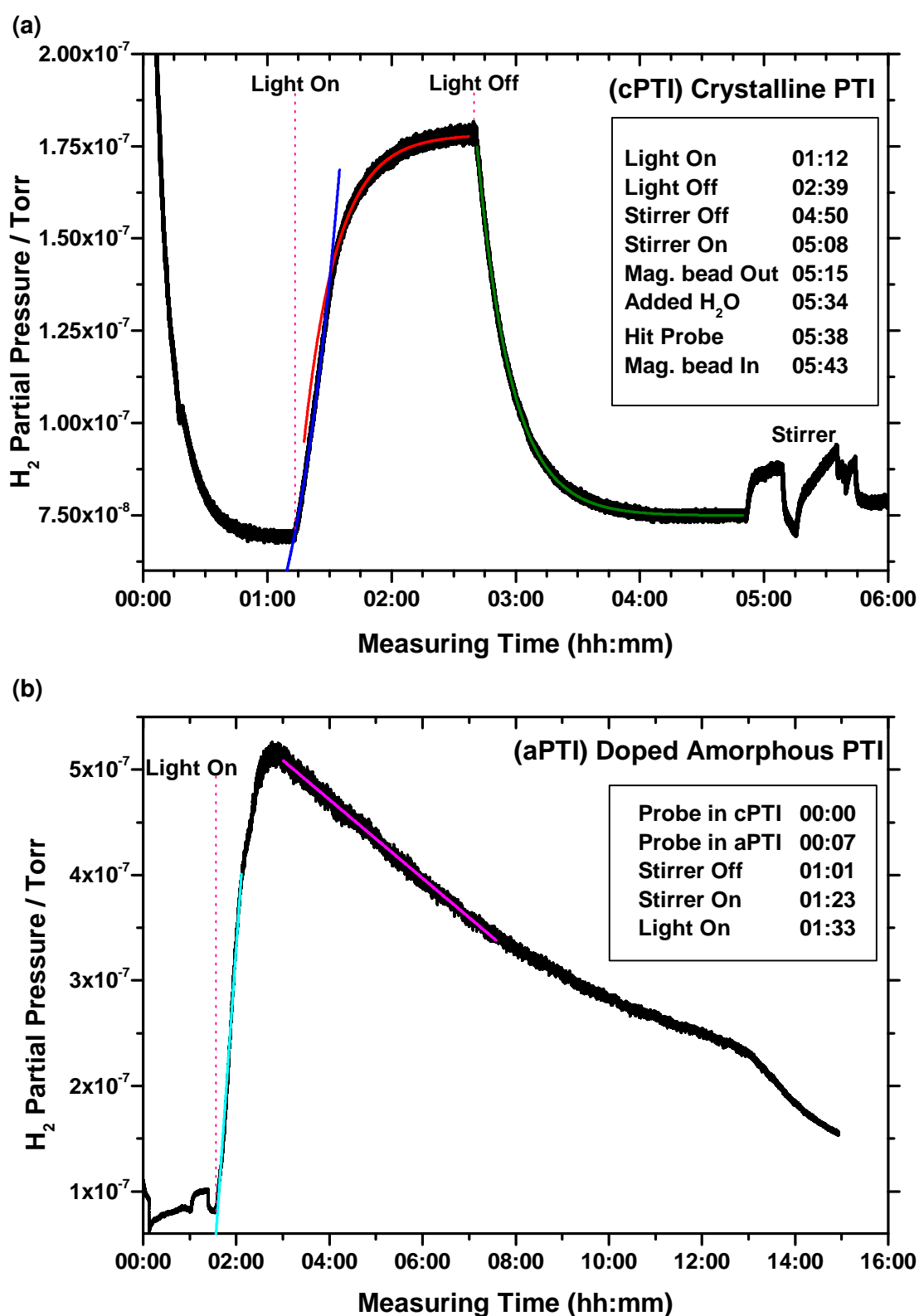
Figure 4.8: Real-time $H_2$ evolution measured directly in the photocatalytic suspension with side illumination from a xenon lamp in an open-air beaker. **(a)** Crystalline PTI with linear ($f_1$ blue), asymptotic growth ($f_2$ red) and exponential decay ($f_3$ green) fittings. **(b)** Doped amorphous PTI with linear fittings ($f_4$ cyan and $f_5$ magenta).

The smaller signals observed at 04:50 and after were control tests to see what else could recreate the $H_2$ signal. These included stopping the stirrer, topping up water in the beaker and tapping the probe head. Evidently, the same magnitude of signal was not recreated but it was observed that stirring the suspension did affect the signal. Stopping the stirrer or similarly removing the magnetic bead (with stirrer on) resulted in an increased signal from background. This is expected as still suspensions would lower the rate of gas loss from the surface of the suspension.

Figure 4.8**(b)** is a similar plot for the doped amorphous PTI. Illumination with the xenon lamp starts at 01:33 and a linear increase in the $H_2$ signal is again observed (marked in $f_4$ cyan). In contrast to crystalline PTI, the doped PTI signal does not plateau but reaches a maximum after 1 h 15 min and then begins to decrease for the rest of the measurement. The light remains on until the measurement ends.

The reason for the decrease is attributed to the colour change previously discussed in Section 4.2. The rate of $H_2$ evolution decreases linearly for 4 h 30 min (marked in $f_5$ magenta). Since the loss behaviour is more linear than exponential, this is further evidence that the cause is a decreasing reaction rate. The rate appears to recover slightly (09:00 to 13:00) but at 13:00 the rate decreases further for an unknown reason. Comparing graphs (a) and (b), it is clear that doped PTI produces significantly more $H_2$ and at a higher rate but suffers from the poisoning effect discussed.

These experiments demonstrated the detection of photocatalytic hydrogen gas, taken directly from the liquid phase. We are able to detect the product in real time and qualitatively evaluate their kinetics.

# Chapter 5

# White Melon

In this chapter the synthesis, crystallinity and hydrogen evolving capacity of carbon nitrides synthesised at ultra long calcination times (ULT) are discussed, especially focusing on a new melon-like material which shows interesting optical and photocatalytic properties. The step from bulk carbon nitride to nanoscale particles presents a range of new properties to investigate and has seen great interest recently.[75-79] Apart from the expected higher surface area, new properties have emerged, such as the formation of a stable suspension in water, light scattering and, most interestingly, increased crystallinity. This work presents a carbon nitride nanosheet material which unexpectedly shows enhanced photocatalytic activity. In general, this work also offers new insights into carbon nitride calcination and the importance of reaction conditions and provides a facile route to crystalline melon by open air synthesis.

Two synthesis methods are compared, namely *Ultra Long Time* (ULT) melon and *Recalcined* melon. Both methods are carried out in an open air system at ambient pressure. Of these samples, some show a remarkable transformation in their properties and are named *white melon* due to their distinctive change in colour.

**Ultra long time Melon**

Ultra long time (ULT) melon is a series of melon carbon nitrides synthesised in air at 510 °C for 200 h, 300 h, 400 h and 500 h (see Section 5.1.3 for synthesis details). In a one-step synthesis method, CN precursors are calcined for extremely long times compared to conventional bulk synthesis (e.g. 500 h compared to 48 h calcination). The effects of long calcination times, without significant sublimation or carbonisation were investigated. The 500 h ULT melon was distinctive and named *white melon.*

**Recalcination**

The recalcination method was later developed to reduce the synthesis time whilst maintaining the properties of ULT melon. It involves grinding of a CN sample in a mortar after calcination and then recalcining the sample a second time, (see Section 5.1.4 for synthesis details).

In 2012, Niu et. al[78] claimed the production of CN nanosheets by thermal oxidation etching in air. Their method involved grinding the synthesised carbon nitride in air (named 'bulk g-$C_3N_4$') and recalcining the sample to obtain nanosheets.

In summary, their method involves heating DCD at 550 °C for 4 h, then grinding in a mortar and recalcining at 500 °C for 2 h. Our *recalcined melon* method involves heating melamine at 510 °C for 24 h. Then grinding in a mortar and recalcining at 510 °C for +12 h to +48 h. The synthesis conditions are different but the recalcining step is common to both. We assume that the intermediate step of grinding the

sample to a powder in air is the important step to obtain the product, otherwise the nanosheets do not form until 500 h as in ULT melon. We used the recalcination step to compare to the ULT samples and to significantly reduce the calcination time.

**White Melon**

White melon refers to the +24 h, +36 h and +48 h recalcined samples and the 500 h ULT sample. However, since the majority of analysis was carried out on 500 h melon, references to white melon infer the 500 h melon, unless otherwise stated.

Figure 5.1 presents photos of white melon. In **(a)**, a series of white melon powders are shown. In **(b)**, the raw product from a crucible is shown with white melon at the top and unreacted yellow melon at the bottom. The gradient of reacted and unreacted melon is instructive to understand the synthesis mechanism. The unreacted melon remains yellow at the bottom of the crucible, this led to the hypothesis that oxygen in the air plays a role in white melon formation.
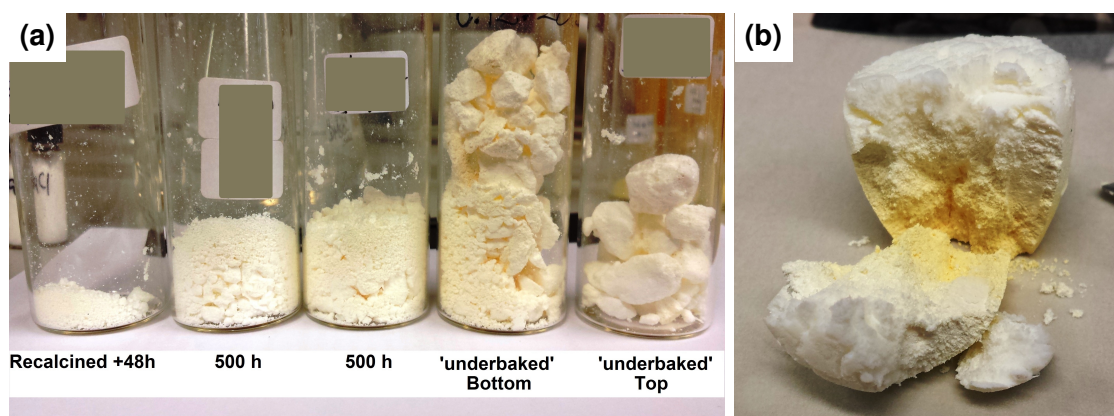


Figure 5.1: Photos of white melon, **(a)** a series of white melon powders comparing recalcined melon, two identical batches of 500 h melon and the 'underbaked' white melon from (b). **(b)** 'underbaked' white melon. 10 g melamine, 60 h at 510 °C, 14 wt% yield (≈130 vol% yield), see Figure 5.3 for MS synthesis profile.

## 5.1 Synthesis of Melon-type Carbon Nitrides

Carbon nitride materials (CNs) were primarily synthesised in our lab while other photocatalyst candidates such as the metal oxides were obtained through collaborations. Heptazine carbon nitride synthesis was initially carried out by Dr. Hongji Wang and triazine CNs such as Poly(triazine imide) (PTI) were synthesised by Katharina Schwinghammer. For chemical supplier, purity etc. see Table A.1.

### 5.1.1 Synthesis Conditions

Carbon nitrides have been synthesised in 'open' and 'closed systems', the former meaning open or partially open to the air and the latter sealed in a quartz ampule. It is known that highly crystalline species are best synthesised in closed systems due to the autogenous ammonia atmosphere which promotes crystallisation during synthesis owing to the microscopic reversibility under autogeneous ammonia backpressure.[22,80] The amount of material, furnace time and the synthesis temperature are the three main parameters to control the synthesis products. Highly condensed species are produced at elevated temperatures and at longer reaction times. Although furnace temperature is the most important parameter, it can be constructive to keep this parameter fixed and 'fine-tune' the resulting properties by the secondary parameter of calcination time. As we will see in later discussions, the longer calcination time may also distinguish key properties such as condensation degree, crystallinity and carbonisation.

### 5.1.2 Melon 48 h Reference Sample

Amorphous melon was synthesised as a reference CN according to Sattler et al.[81]

1. 10 g of melamine powder was placed in a ceramic crucible with a lid.

2. Crucible was placed in the centre of a muffle furnace at room temperature in static air.

3. Temperature was set to 510 °C at a heating rate of 5 °C min$^{-1}$ for 48 h.

4. Product was allowed to cool to room temperature for 24 h (yield: 43 wt%).

5. Product was then ground in a mortar and stored in a glass vial.

### 5.1.3 Ultra Long Time (ULT) Calcination – 200 h to 500 h Melon

Powders were synthesised by calcining melamine in a muffle furnace at 510 °C for 200 h to 500 h. The melamine was placed in a ceramic crucible with a lid on top and underwent a thermal polycondensation reaction from melamine to melon.

1. 30 g of melamine powder was placed in a ceramic crucible with a lid.

2. Crucible was placed in the centre of a muffle furnace at 26 °C in static air.

3. Temperature was set to 510 °C at a heating rate of 5 °C min$^{-1}$ for 200 h, 300 h, 400 h and 500 h separately.

4. Product was allowed to cool to room temperature over 24 h
   (yield = 14 wt% for 500 h sample).

5. Product was then ground in a mortar and stored in a glass vial.

The 200 h to 400 h products appeared similar to amorphous melon although coarse in texture. The 500 h sample is remarkably different in appearance. It is white in colour and its texture is soft like a foam. At the end of the synthesis, its volume expanded greater than the initial starting material volume in the crucible (Yield ≈ 130 vol%, 14 wt%). To get an estimate of its density, the volume and mass of the 500 h sample was measured (without compacting) with the density estimated at $530 \pm 90$ kg m$^{-3}$, a remarkably low density similar to cork or lithium metal at room temperature.

### 5.1.4 Recalcined Melon

Recalcined melon was synthesised based on the method from Niu et al.[78] described below, but modified by time and temperature for comparison with ULT melon. In a two-step reaction in air, melon is formed at 510 °C for 72 h, then further ground in a mortar and recalcined in the oven for +12 h to +48 h. The notation of '+48 h recalcined melon' infers additional 48 h calcination after 72 h calcination of melamine.

**Melon 72 h Reference:**

1. 10 g of melamine powder was placed in a ceramic crucible with a lid.

2. Crucible was placed in the centre of a muffle furnace at room temperature in static air.

3. Temperature was set to 510 °C at a heating rate of 5 °C min$^{-1}$ for 72 h.

4. Product was allowed to cool to room temperature (yield = 40 wt%).

5. The yellow product was ground in a mortar and stored in a glass vial.

**+12 h to +48 h Recalcined Melon:**

1. The 72 h reference melon was taken as starting material.

2. It was further ground in a mortar to a fine powder and placed in a ceramic crucible with a lid in air.

3. Temperature was set to 510 °C at a heating rate of $5\,°\mathrm{C\,min^{-1}}$ for 12 h, 24 h, 36 h and 48 h separately.

4. Products were allowed to cool to room temperature
(yields: 72, 29, 12 and 2.6 wt% respectively).

5. The pale yellow products were ground in a mortar and stored in glass vials.

## 5.2 Preparation of Carbon Nitride Suspensions

Since CNs are insoluble in water, they form suspensions when the ground photocatalyst powder is added. Photocatalytic suspensions are composed of four main parts: water, photocatalyst, cocatalyst and electron donor or acceptor.

Typically, 10 mL to 20 mL suspensions were chosen because the amount of photocatalyst under investigation was often limited. This was at the expense of hydrogen production performance. A relatively high photocatalyst concentration is needed to ensure adequate absorption of light. Carbon nitride suspensions were opaque at concentrations above $0.4\ \mathrm{mg\,mL^{-1}}$ and so a typical concentration of $1\ \mathrm{mg\,mL^{-1}}$ was chosen. Amounts of cocatalyst were chosen to correspond to a certain wt% in the range 0.5 to 3.0 wt%. This amount was optimised where possible but was primarily 2.4 wt%. A typical suspension preparation is presented below:

1. 10 mg of ground photocatalyst was added to 9 mL deionised $H_2O$ in a vial.

2. Suspension was ultrasonicated for 30 min.

3. Suspension was added to the clean reactor with a magnetic stirring bead.

4. 6 µL of $H_2PtCl_6$ corresponding to 2.4 wt% cocatalyst was added.

5. 1 mL TEoA was slowly added with the suspension under vigorous stirring.

6. Reactor was sealed and exposed to 4 cycles of evacuation and argon purging to remove residual air.

# 5.3 Mass Spectrometry During Synthesis

To further understand the origin of white melon and the condensation mechanisms of CNs in general, mass spectrometry was employed to identify the evolved gases over time. Although numerous thermo-gravimetric and mass spectrometry (TGA-MS) studies have been carried out on carbon nitrides,[30,69–71] no temporal analysis of evolved gases is available. Studies over time are interesting considering the long calcination times involved. Our experiments agree with published reports with $NH_3$, $CO_2$, $HCN$ and $C_2N_2$ species identified. However, the identification of gas species is complicated by the synthesis in air and this is discussed further below. Control experiments show no significant changes in signal over time or with changing oven temperature although unidentified spikes and artefacts are observed.

The identification of gases was first evaluated by running a continuous mass-scan as seen, for example, in Figure 5.2. This identifies which gases are present. Simple molecular gases were the focus of interest, so relatively low mass ranges of 1 to 40 amu were chosen.
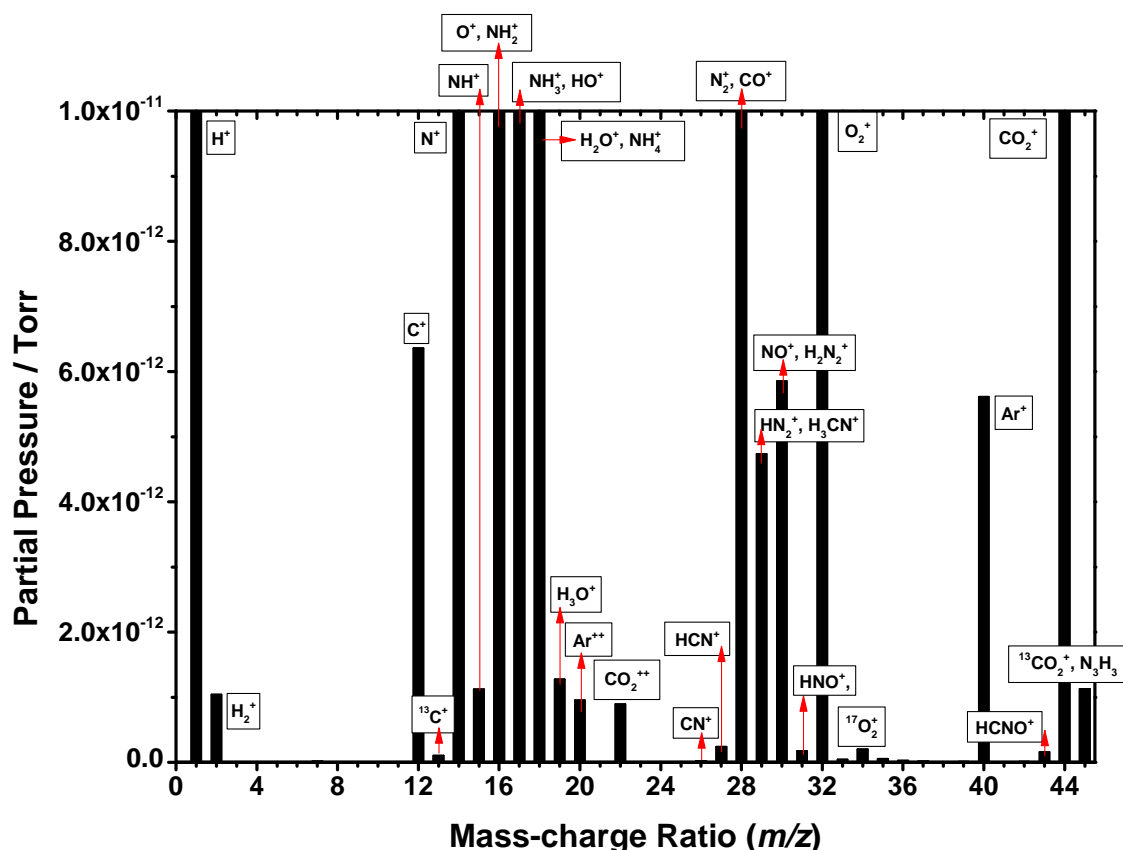


Figure 5.2: Mass-scan 1 to 40 amu with proposed ionisation species.

Table 5.1: Detected mass-charge ratios and possible gas species identified with the use of the NIST Standard Reference Database 69 and Jürgens et. al. [24]

| $m/z$ | Proposed Species | Gas of Origin |
|---|---|---|
| 1 | $H^+$ | Hydrogen |
| 2 | $H_2^+$ | Hydrogen |
| 12 | $C^+$ | Carbon dioxide |
| 13 | $^{13}C^+$ | Carbon dioxide |
| 14 | $N^+$ | Nitrogen, Ammonia |
| 15 | $NH^+$ | Ammonia |
| 16 | $O^+$, $NH_2^+$ | Oxygen, Ammonia |
| 17 | $NH_3^+$, $OH^+$ | Ammonia, Water |
| 18 | $H_2O^+$, $NH_4^+$ | Ammonia, Water |
| 19 | $DHO^+$, $H_3O^+$ | Water |
| 20 | $Ar^{++}$ | Argon |
| 22 | $CO_2^{++}$ | Carbon dioxide |
| 26 | $CN^+$ | Hydrogen cyanide |
| 27 | $HCN^+$ | Hydrogen cyanide |
| 28 | $N_2^+$, $CO^+$, $H_2CN^+$ | Nitrogen, Carbon dioxide, Hydrogen cyanide |
| 29 | $HN_2^+$, $H_3CN^+$ | Nitrogen, Hydrogen cyanide |
| 30 | $NO^+$, $N_2H_2^+$ | Nitric oxide, Diimide |
| 31 | $HNO^+$ | Nitric oxide |
| 32 | $O_2^+$ | Oxygen |
| 33 | $H_2NOH^+$, | Hydroxylamine |
| 34 | $^{17}O_2^+$ | Oxygen |
| 40 | $Ar^+$ | Argon |
| 42 | $H_2NCN^+$ | Cyanamide, |
| 43 | $H_2NCNH^+$, $HCNO^+$ | Cyanamide,[24,82] Cyanic Acid |
| 44 | $CO_2^+$, $N_2O^+$ | Carbon dioxide, Nitrous oxide, Cyanamide |
| 45 | $^{13}CO_2^+$ | Carbon dioxide |
| 52 | $C_2N_2^+$ | Cyanogen |

Figure 5.3 highlights the initial stages of the reaction with the probe positioned close to the CN reactant. Figure 5.4 shows the full reaction profile under the same synthesis conditions with the probe placed further back from the reaction.

In Figure 5.3, starting at 40 °C with a ramp of 5 °C min$^{-1}$, a small increase in the $NH_3$ signal is observed at 00:10 (120 °C). It is possible that this signal is from evaporating $H_2O$ contributing to the $m/z = 17$ signal. There is a gradual increase in $CO_2$ at 00:22 (212 °C). At oven time 00:45 (394 °C), there is a considerable spike in the evolved $NH_3$. This is the main feature of the MS time profile. Evolution of $NH_3$ is expected for this condensation reaction and is well understood.[24,25] Interestingly, there appears to be some dynamic between $NH_3$ evolution and $CO_2$ evolution with $CO_2$ reaching a trough as the $NH_3$ signal peaks. There is a sharp increase in the $CO_2$ signal at 56 min (483 °C). During this highly volatile stage of carbon nitride condensation, a HCN signal is observed at 01:07 at the oven running temperature of 510 °C. HCN evolution continues to increase for 5 min before decreasing rapidly. A weak $C_2N_2$ signal is also observed coinciding with the release of HCN. The sharp increase and decrease of $NH_3$ evolution shows the volatile nature of the condensation process. At the same time that the HCN signal is detected (01:07), the $NH_3$ signal is decreasing rapidly.
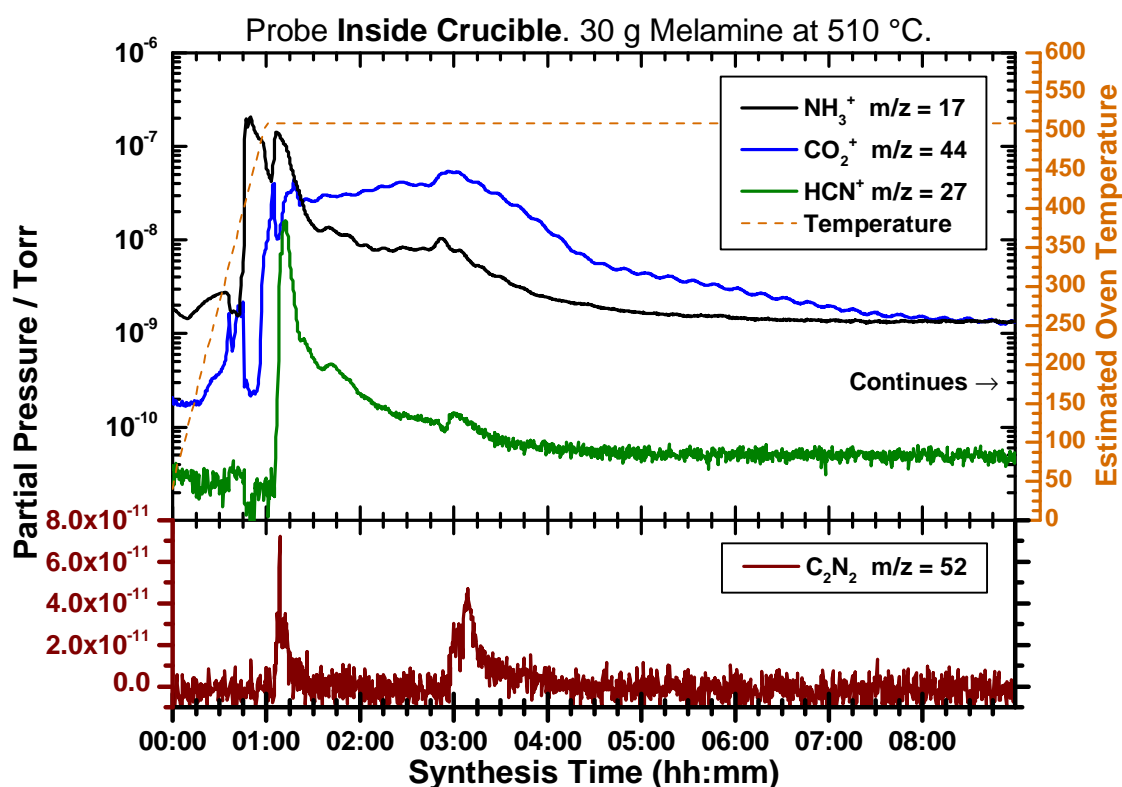


Figure 5.3: DEI MS time profile of evolved gases during the calcination of 30 g melamine *Inside Crucible:*. 70 V source, Faraday detector.

At 01:22 the $CO_2$ signal slowly rises as the other signals slowly decrease. The release of $CO_2$ gradually increases until the oven time of 3 hours (03:00). At this point, all signals show a local maximum with a second release of $C_2N_2$ detected. This could mark a second volatile rally of the reaction. After this point, the $NH_3$, $CO_2$, HCN signals slowly decrease over the long synthesis time. Finally, when the oven is turned off and allowed to cool down (38:00 not shown in figure), signals decrease to their baseline levels within 1 h.

In Figure 5.4, more gases are tracked and the full time profile is shown. This data has been normalised to the argon gas signal which was also tracked in order to remove artefacts from pressure fluctuations (see Figure A.10 for raw data). The same observations mentioned above are observed here. Although we do not observe HCN or $C_2N_2$ since the probe is placed further from the reaction, we now track $O_2$, $H_2O$ and NO. From this experiment, we can now see that the rapid evolution of $NH_3$ at 02:13 coincides with the evolution of NO and $H_2O$ and a decrease in the $O_2$ signal. The consumption of $O_2$ and the evolution of $NH_3$, $CO_2$, $H_2O$ and NO lasts for the entire oven runtime of 60 h. The consumption of $O_2$ stops when the oven is turned off and allowed to cool with the signal of the other gases decreasing slowly over 4 h.
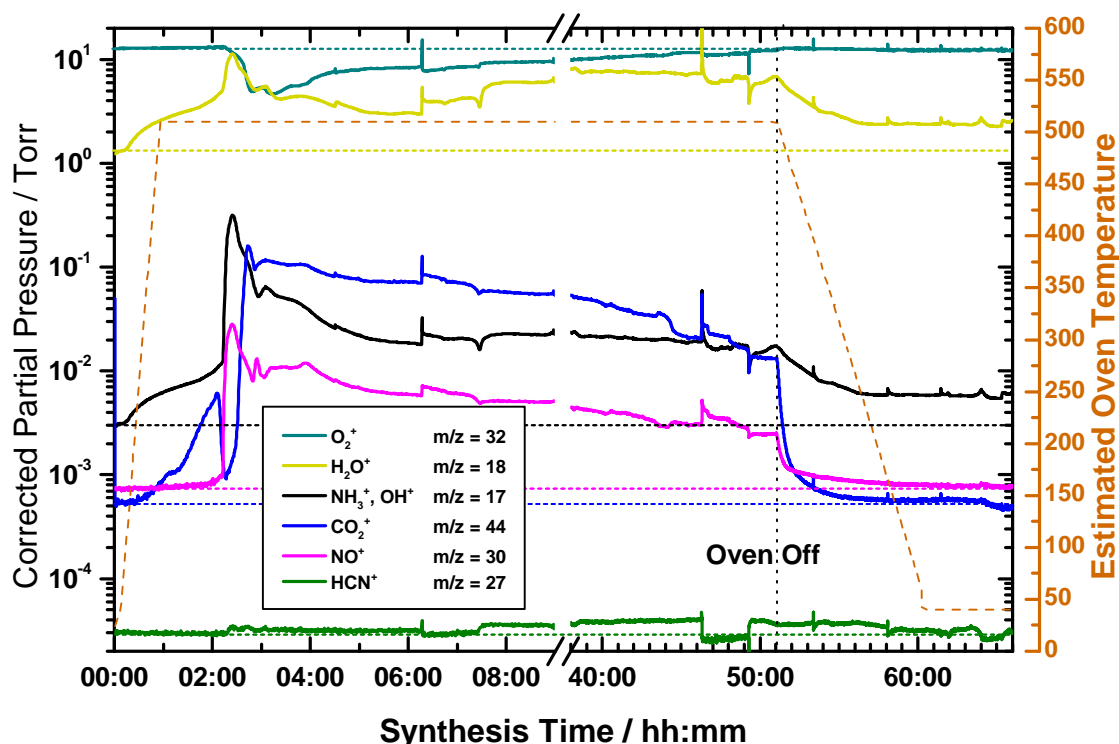


Figure 5.4: Full MS time profile of evolved gases during the calcination of melamine at 510 °C. Data normalised to argon signal (see Appendix A.10 for raw data), 70 V source, Faraday detector.

As mentioned previously, the identification of gas species is complicated by the synthesis in air. Here, some of the key points are discussed. It is clear that $m/z = 17$ is active during the experiment. The possibilities are $OH^+$ and $NH_3^+$. It is accepted that part of this signal is from water vapour ($OH^+$) but this signal deviates from the main water signal ($m/z = 18$) during the experiment. To explain this further, the ratio 18:17 $m/z$ is constant for $H_2O^+$ (i.e. 10.000:2.122, NIST database). These $m/z$ ratios should remain constant if the signal is only from water (as they do at the start and end of the experiment) but they deviate, especially at the peak of the $m/z = 17$ signal (see Figure A.9). This proves an additional species contributes to the $m/z = 17$ signal and we assign this to ammonia as observed by others.[69,71]

The signal at $m/z = 22$ can only be reasonably assigned to doubly charged carbon dioxide $CO_2^{++}$ so the presence of carbon dioxide is confirmed. However, we cannot rule out the possibility that $m/z = 44$ ($CO_2^+$) is also from $N_2O$, especially considering we assume the presence of NO.

$m/z = 30$ is assigned as NO, nitric oxide. The detection of a small signal at $m/z = 31$, consistent with $HNO^+$, supports the assignment to NO. In response, there is no signal at $m/z = 46$ for $NO_2$ which is expected to be present in an oxygen atmosphere, if NO is detected. Thermal NOx formation from $O_2 + N_2$ occurs above 1,100 °C and as this reaction occurs at 510 °C, it is doubtful that this is responsible.[83]

The presence of hydrogen cyanide is clearly proved by the signal at $m/z = 27$ and its corresponding signal at 26 $m/z$. This highly poisonous gas is a reminder of the dangerous synthesis conditions of the reaction.

From the data above, we propose the following reaction which is the thermal oxidation of melamine. Oxygen from the air reacts with condensed melamine and releases water vapour, carbon dioxide and nitric oxide. This is in line with the thermal oxidation hypothesis proposed by Niu et. al.[78]

$$2\,(C_3H_6N_6) + 15\,O_2 \rightarrow 6\,(CO_2) + 12\,NO + 6\,H_2O \qquad (5.1)$$
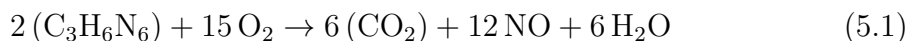
Normally, the condensation of CN does not proceed much further than the first 24 h of the reaction, hence the short synthesis times in the literature. Here, the competing oxidation reaction promotes the continual condensation of CNs over a long period of time, thus enhancing the overall crystallinity.

Although there are many questions related to this new experimental technique for the in-situ study of carbon nitride formation, competing reactions and the added difficulty of assigning gas species such as NO, there is potential for valuable new evidence to determine the mechanisms of CN synthesis in air. We have identified all evolved species, plotted their order of evolution and can also observe the dynamic processes and reactions involved.

## 5.4 IR Vibrational Spectroscopy

Fourier transform infrared (FTIR) spectra of the 200 h to 500 h samples along with the 48 h melon reference are shown in Figure 5.5 with the bands assigned to heptazine carbon nitrides.[22,84]

The out-of-plane breathing vibration of the ring system is detected at 810 cm$^{-1}$. The deformation mode of N$-$H is observed at 890 cm$^{-1}$. The bands in the region 1200 cm$^{-1}$ to 1700 cm$^{-1}$ are commonly assigned to the bridging units C$-$NH$-$C or the central trigonal nitrogen C$-$N($-$C)$-$C. The bands from 3000 cm$^{-1}$ to 3300 cm$^{-1}$ are assigned to adsorbed H$_2$O and also N$-$H stretching, suggesting the presence of NH or NH$_2$ groups as expected.

The samples show all vibrations seen in the amorphous melon reference albeit much sharper. The increasing resolution and sharpness of the vibrations indicates increased order in the material.[85] The sharpness of vibrations increases with calcination time with the exception of the 300 h sample which appears marginally superior to the 400 h sample. There is particularly an increase in the sharpness of the vibrations in the 500 h sample compared to shorter calcined samples (e.g. 1280 cm$^{-1}$, 1010 cm$^{-1}$ and 890 cm$^{-1}$). Overall, spectra are consistent with previous reports in the literature[22,84,86–88] and no significant changes between the 200 h to 500 h samples and the 72 h reference were observed.

Figure 5.6(c) compares the IR of recalcined and ULT melon. There is no noticeable difference between the three synthesis methods. Figure 5.6(d) compares the 48 h and 72 h references and the starting material melamine. Again, no significant differences are observed.
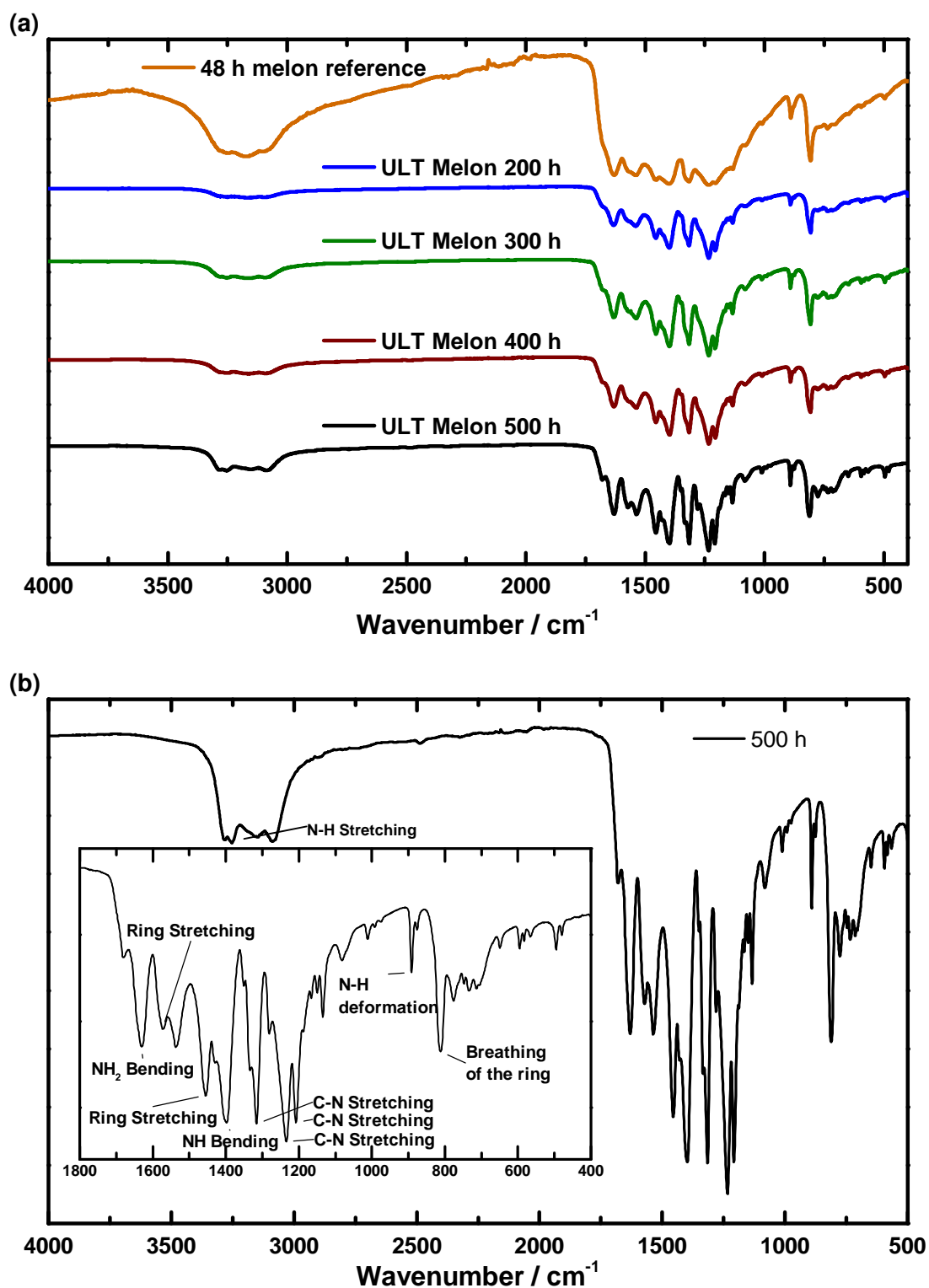
Figure 5.5: **(a)** FTIR of 200 h to 500 h carbon nitrides showing no changes in the vibrational bands with calcination time, except increasing band resolution. **(b)** 500 h melon with main vibrations identified.

**(c)**



**(d)**
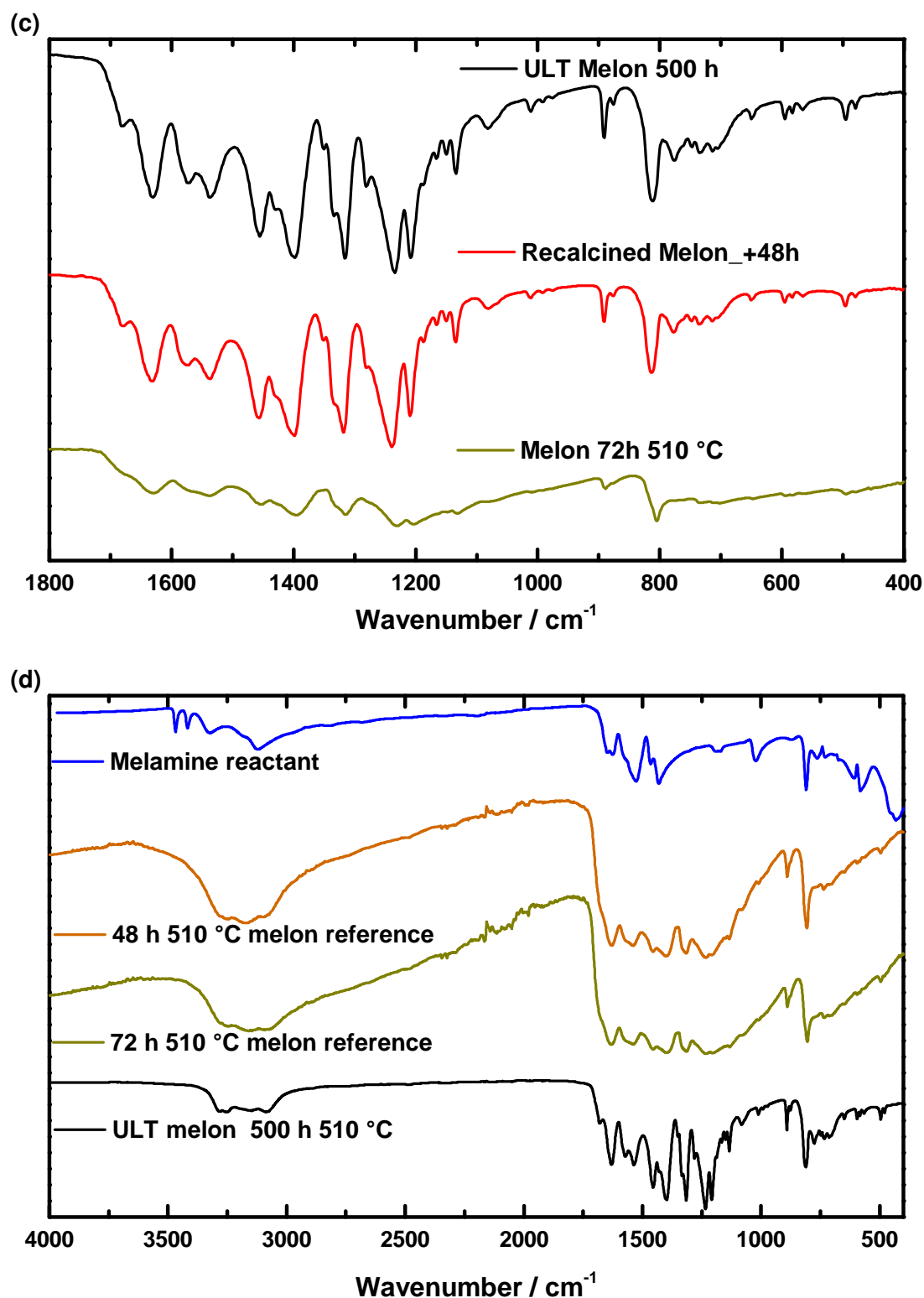


Figure 5.6: FTIR of ULT 500 h vs. recalcined +48 h melon. **(c)** Fingerprint region comparison of 500 h and recalcined +48 h. **(d)** Full comparison with the 72 h melon reference and the melamine reference.

## 5.4.1 IR Spectroscopy of Recalcined Melon

Figure 5.7 compares the recalcined melon samples with a conventional melon sample. Although the bands are more pronounced for the recalcined samples, the positions show no significant difference to bulk melon. This is also similar to the ULT melon which will be presented in the following sections and further detailed.
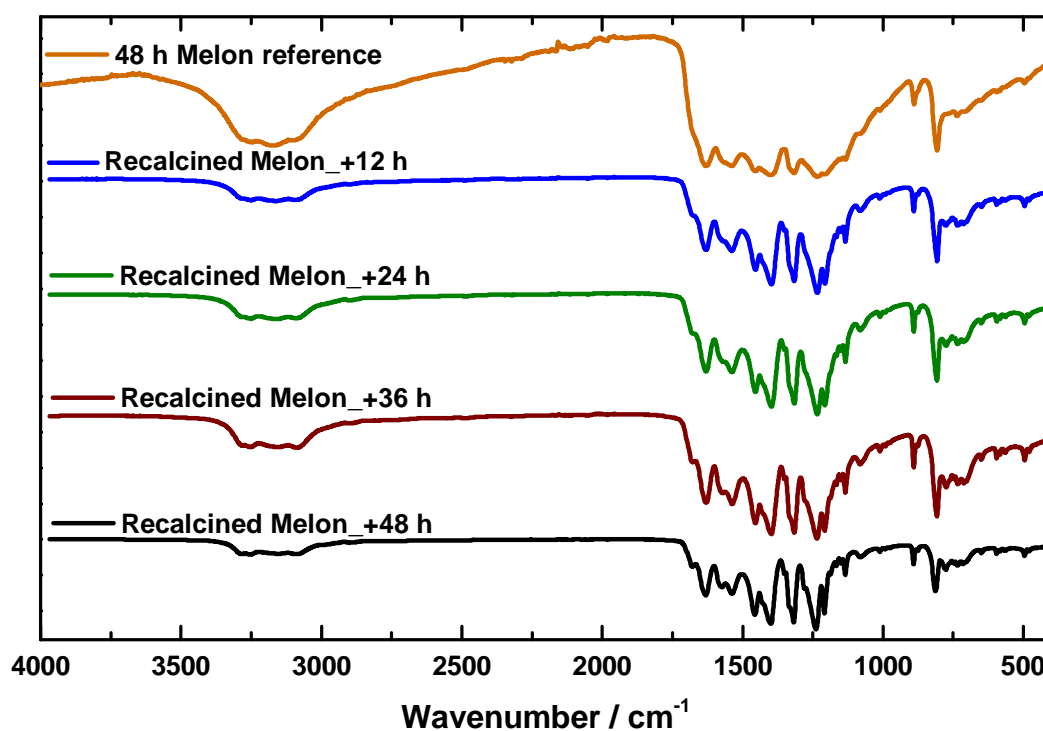


Figure 5.7: FTIR of +12 h to +48 h recalcined melon and the 48 h melon reference.

## 5.5 Elemental Analysis

CHNO elemental analysis (EA) and energy-dispersive X-ray analysis (EDX) were performed to evaluate the chemical composition of the samples. The average empirical formula calculated from EA was $C_{6.00}N_{8.94}H_{3.84}$. As seen in Table 5.2, the samples match the N/C molar ratio to the calculation of crystalline melon $C_6N_9H_3$, N/C molar $= 1.5$.[22,25] According to Komatsu,[84] a condensed triangular melon would give $C_6N_8H_1$, N/C $= 1.33$. Alternatively, an infinitely long linear melon chain approaches the formula $C_6N_9H_3$ giving N/C $= 1.5$. This is in agreement with what is expected for melon as a 1D polymer carbon nitride. EA shows that the oxygen content decreases with calcination time (Figure 5.8) and this is supported by XPS data. EDX measurements were also taken during TEM measurements of the 500 h samples (Appendix Section A.3). As expected, only C and N species were observed.

Table 5.2: CHNO elemental analyses and calculated N\C molar ratios.

| Calcination Time (hours) | N ± 0.05 (wt%) | C ± 0.05 (wt%) | H ± 0.1 (wt%) | O ± 0.1 (wt%) | Sum ± 0.16 (wt%) | N\C ± 0.003 |
|---|---|---|---|---|---|---|
| Melem* | 64.20 | 33.00 | 2.80 | 0.00 | 100 | 1.668 |
| Melon * | 62.70 | 35.80 | 1.50 | 0.00 | 100 | 1.502 |
| Melon[70] | 60.60 | 35.40 | 1.83 | 0.80 | 98.63 | 1.468 |
| 48 | 61.18 | 34.58 | 1.86 | 2.37 | 99.99 | 1.517 |
| 72 | 61.78 | 35.29 | 1.69 | 1.37 | 100.13 | 1.502 |
| 200 | 60.70 | 34.93 | 1.99 | 0.79 | 98.41 | 1.490 |
| 300 | 61.13 | 35.18 | 1.89 | 0.48 | 98.68 | 1.490 |
| 400 | 61.38 | 35.20 | 1.85 | 0.41 | 98.84 | 1.495 |
| 500 | 61.15 | 35.25 | 1.83 | 0.44 | 98.67 | 1.487 |
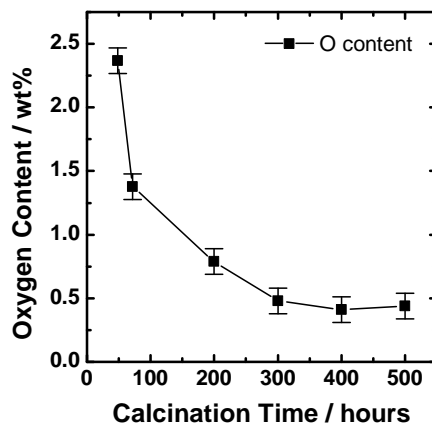


Figure 5.8: Oxygen content dependence on calcination time by elemental analysis.

---

*theoretical values

## 5.6 X-ray Photoelectron Spectroscopy

X-ray photoelectron spectra (XPS) were measured to further elucidate the surface structure of the analysed materials. Figure 5.9 compares the C, N and O spectra of the 48 h to 500 h samples. Due to an insignificant adventitious carbon peak,the single carbon peak was calibrated to 288.2 $\pm$ 0.2 eV.[89–92] Note, this places the adventitious carbon at 285.7 eV. The high resolution C 1s spectra show no changes from 48 h to 500 h with only a single peak corresponding to the sp$^2$ N$=$C($-$N)$-$N group observed. Figure 5.9(b) compares the N 1s spectra for all samples. The 48 h and 500 h signals were further deconvoluted into three components centred at 398.7, 399.9 and 401.1 eV for comparison (Figure 5.10). The main peak at 398.7 eV is assigned to the sp$^2$ hybridised N atoms within the heptazine ring (C$=$N$-$C). The shoulder at 399.9 is assigned to the core nitrogen (C$-$N($-$C)$-$C). The signal at 401 is the bridging group (C$-$NH$-$C).[93] The weak signal at 404 eV is attributed to charging effects.

The oxygen spectra show weak signals at 532.2 eV for all samples. The 300 h sample shows a peak at 535.6 eV which is due to SiO$_2$ contamination (see survey spectra (Figure 5.9 (d)). It is evident from the very low signal intensities that oxygen is not a main constituent in the 48 h to 500 h surface composition. Moreover, in support of the EA results, the O 1s signal appears to decrease with calcination time and is absent in the 500 h sample.

High resolution valence band spectra for the 48 h and 500 h CNs are shown in the Appendix A.12. From this comparison, we can estimate that the difference in HOMO levels is 0.15 eV and coupling this with the band gap information, an estimated band structure is given. However, the positions of the HOMO and LUMO levels are still undetermined.

XPS N/C molar ratios are lower than observed for the bulk material by elemental analysis, as expected for this surface sensitive technique.

Table 5.3: XPS Molar N/C ratios. Relative sensitivity factor (RSF) values of 0.477 and 0.278 for N 1s and C 1s component peaks respectively.

| Calcination Time (hours) | XPS Molar N/C Ratio $\pm$ 0.05 |
|---|---|
| 48 | 1.47 |
| 72 | 1.44 |
| 200 | 1.43 |
| 300 | 1.41 |
| 400 | 1.44 |
| 500 | 1.45 |
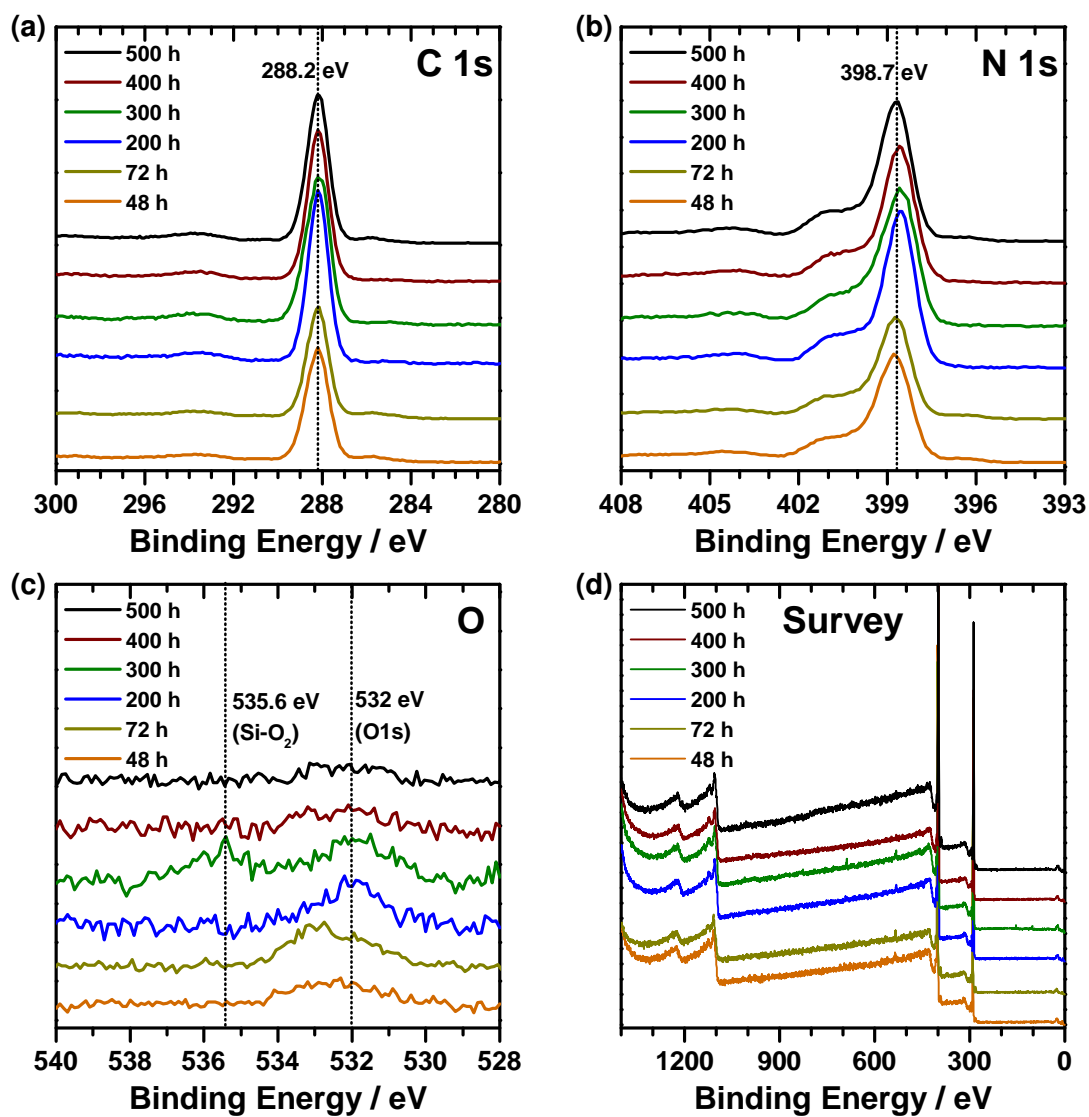
Figure 5.9: XPS spectra for 200 h to 500 h samples. **(a)** C 1s spectra, **(b)** N 1s spectra, **(c)** O 1s spectra and **(d)** survey spectra. Shirley type baseline and Gauss-Lorentz peak fittings used.

| Label | Asigned | Position eV | FWHM eV | R.S.F. | Area | Area Limit | % Conc. |
|---|---|---|---|---|---|---|---|
| 1 | C=N–C | 398.7 | 1.176 | 0.477 | 14825.8 | A | -- |
| 2 | C–N(–C)–C | 399.9 | 1.285 | 0.477 | 2470.57 | A/6 | -- |
| 3 | C–N–Hx | 401.1 | 1.304 | 0.477 | 2470.18 | A/6 | -- |
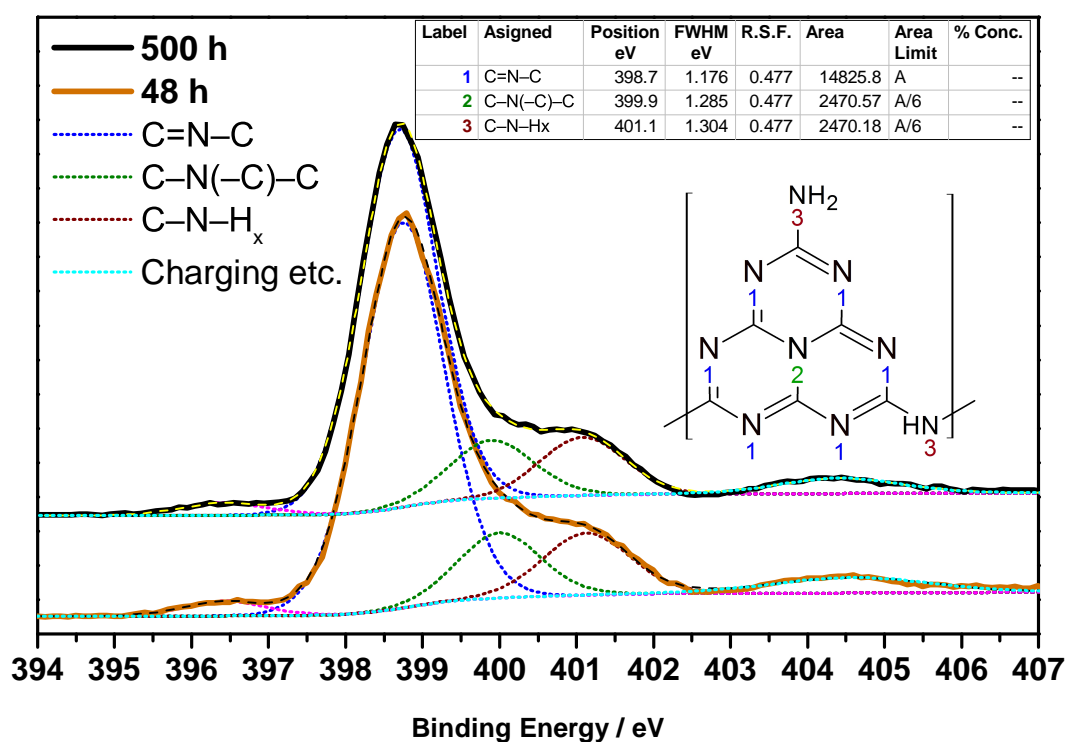
Figure 5.10: XPS spectra for curve fitting of N comparing 500 h and 48 h samples. Shirley type baseline and Gauss-Lorentz peak fittings used.

## 5.7   Powder X-ray Diffraction

Figure 5.11 shows the powder X-ray diffraction (PXRD) patterns. Samples were ground and placed in a 1 mm capillary and transmission XRD spectra were taken from 4° $2\theta$ to 40° $2\theta$ with 0.1 stepsize. The characteristic stacking reflection and the in-plane reflections are observed as expected. The stacking plane for the 72 h melon is observed at 27.67° $2\theta$. The stacking reflection shifts to higher angles with increasing calcination time, to a value of 28.00° $2\theta$ for the 500 h sample. This implies a condensation of the layers of 0.04 Å with increasing calcination time. Comparing the 500 h and the 72 h melon, more in-plane reflections are observed for the 500 h sample. These have been assigned to the Miller indices for crystalline melon as shown in the figure.

As can be seen from Table 5.4, a decreasing FWHM with increasing calcination time suggests increased order in the stacking plane distance. Most importantly, the shift to higher Bragg angle indicates a decrease in the layer distance. This 0.04 Å shift is key to the increased crystallinity of this material.

Table 5.4: PXRD stacking peak parameters for normalised data of 72 h to 500 h ULT samples and recalcined samples.

| Calcination Time (hours) | Stacking Peak FWHM (°$2\theta$) | Position (°$2\theta$) | $d$-spacing $\pm$ 0.005 (Å) |
|---|---|---|---|
| 12 h[70] | 1.16 | 27.60 | 3.23 |
| 48 h | 1.20 | 27.68 | 3.22 |
| 72 h | 0.94 | 27.67 | 3.22 |
| 200 h | 0.88 | 27.73 | 3.21 |
| 300 h | 0.71 | 27.80 | 3.21 |
| 400 h | 0.71 | 27.86 | 3.20 |
| 500 h | 0.60 | 28.00 | 3.18 |
| Recalcained +12 h | 0.81 | 27.85 | 3.20 |
| Recalcained +24 h | 0.75 | 27.93 | 3.19 |
| Recalcained +36 h | 0.81 | 28.00 | 3.18 |
| Recalcained +48 h | 0.62 | 28.03 | 3.18 |

For completeness, the crystallite size calculated by the Scherrer formula for 500 h melon is 17 nm and for the +48 h recalcined is 15 nm (Scherrer constant = 0.94, peak broadening correction of 0.075° $2\theta$), although it is doubtful that this method can be applied reasonably due to stacking faults, grain boundaries and strain effects in the material.

Figure 5.11: Powder XRD pattern comparisons from 4° 2θ to 40° 2θ. (a) 72 h to 500 h. (b) Comparison of ULT 500 h melon, recalcined +48 h and 72 h melon reference with identified Miller indices shown.

## 5.8 Nuclear Magnetic Resonance

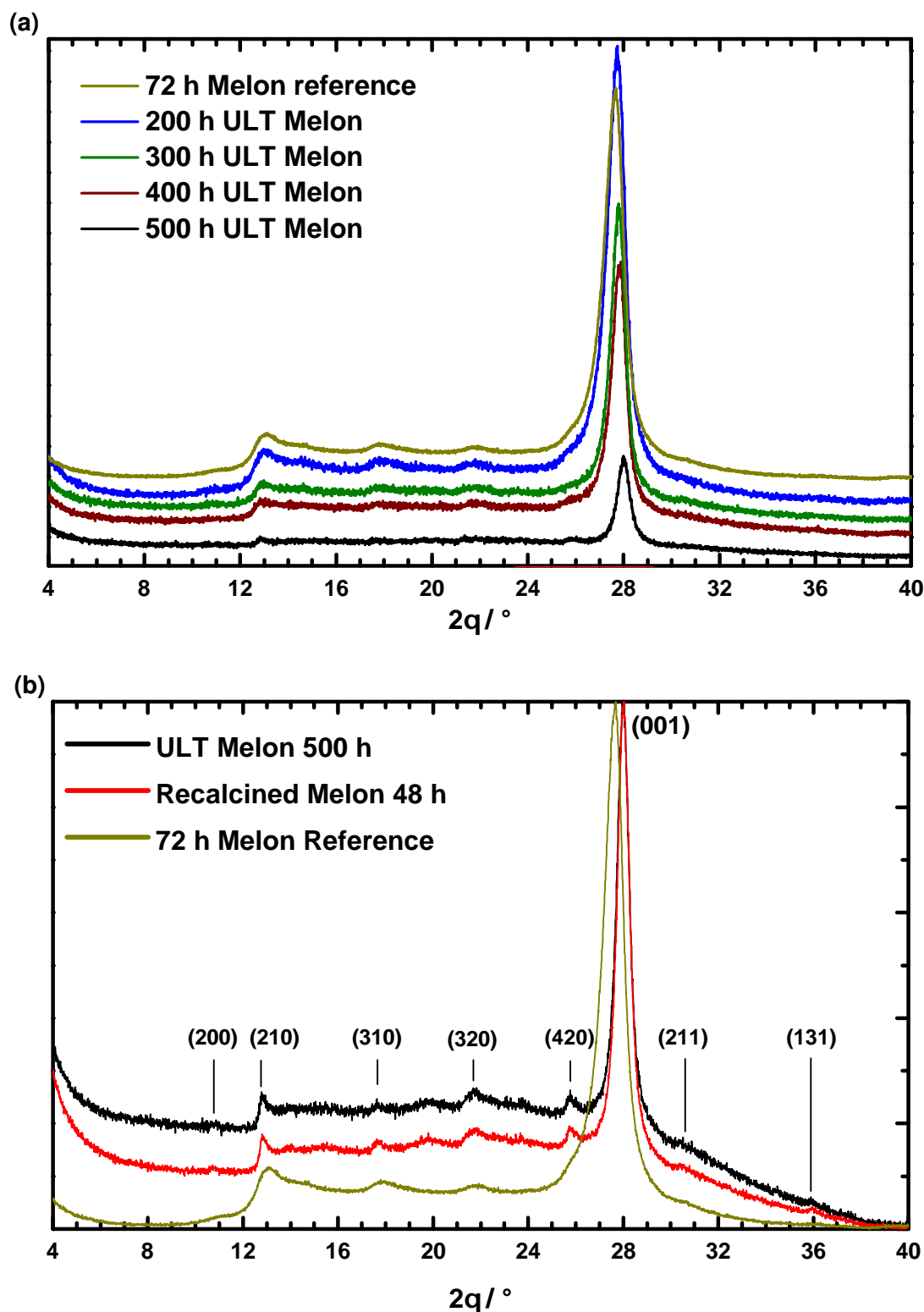Solid state nuclear magnetic resonance (ssNMR) was measured by Maria Mesch in collaboration with the group of Prof. Jürgen Senker at Universität Bayreuth. Figure 5.12 shows the ssNMR for the 200 h to 500 h samples and the 72 h melon reference. For the $^1$H magic angle spinning (MAS) spectra, the proton assignment is complicated by the overlap of the NH and NH$_2$ signals at 9 ppm. However, the assignment is resolved as discussed in detail below. The signals at 4 ppm and below are attributed to adsorbed H$_2$O.

For $^{13}$C, the spectra show two main peaks. The first at 157 ppm is assigned to the sp$^2$-bonded central carbons in the melon structure (labelled 3). The second at 165 ppm is assigned to the carbons in the NH and NH$_2$ environments. We assign the shoulder visible in the 500 h spectrum to the carbon in the environment of the bridging amine units ($-$C$-$NH$-$, 4) and the main signal at 165 ppm corresponds to the $-$C$-$NH$_2$ carbon environment (5).[22,24]

For $^{15}$N, we assign the $-171$ ppm to $-200$ ppm region to the conjugated nitrogen of the heptazine ring system (6).[22,24] At $-226$ ppm there is the signal from the central nitrogen of the heptazine ring (7). At $-242$ ppm to $-244$ ppm we assign the signal to the bridging amine unit $-$NH$-$ (8) and finally at $-262$ ppm is the $-$NH$_2$ environment (9) as explained below.

A previously published detailed NMR study of crystalline melon provides the best evidence of its chemical structure.[22] Here, we compare the proton environments of the 500 h sample (e) to those of the published crystalline melon (f). $^1$H $^1$H DQ-SQ self-correlation spectra were investigated. As can be seen, no significant changes are observed, proving that both samples share the same proton substructure.

Moreover, we can now confidently assign the $^1$H signals to the NH and NH$_2$ protons. A $^{15}$N $^1$H heteronuclear multiple-quantum correlation (HMQC) map was taken for the $^{15}$N enriched melon sample from the publication. Examining Figure 5.13(a), the $^{15}$N signal for NH$_2$ is at $-262$ ppm, correlating to proton signals at 10.3 ppm and 8.6 ppm. For NH, there is a splitting and the $^{15}$N shifts are $-242$ ppm and $-244$ ppm, correlating to a proton signal at 8.9 ppm. Unfortunately, the overlap of the NH and NH$_2$ proton signals complicates quantitative analysis. Having said that, a deconvolution of the $^1$H spectrum with Pseudo-Voigt profiles is possible.
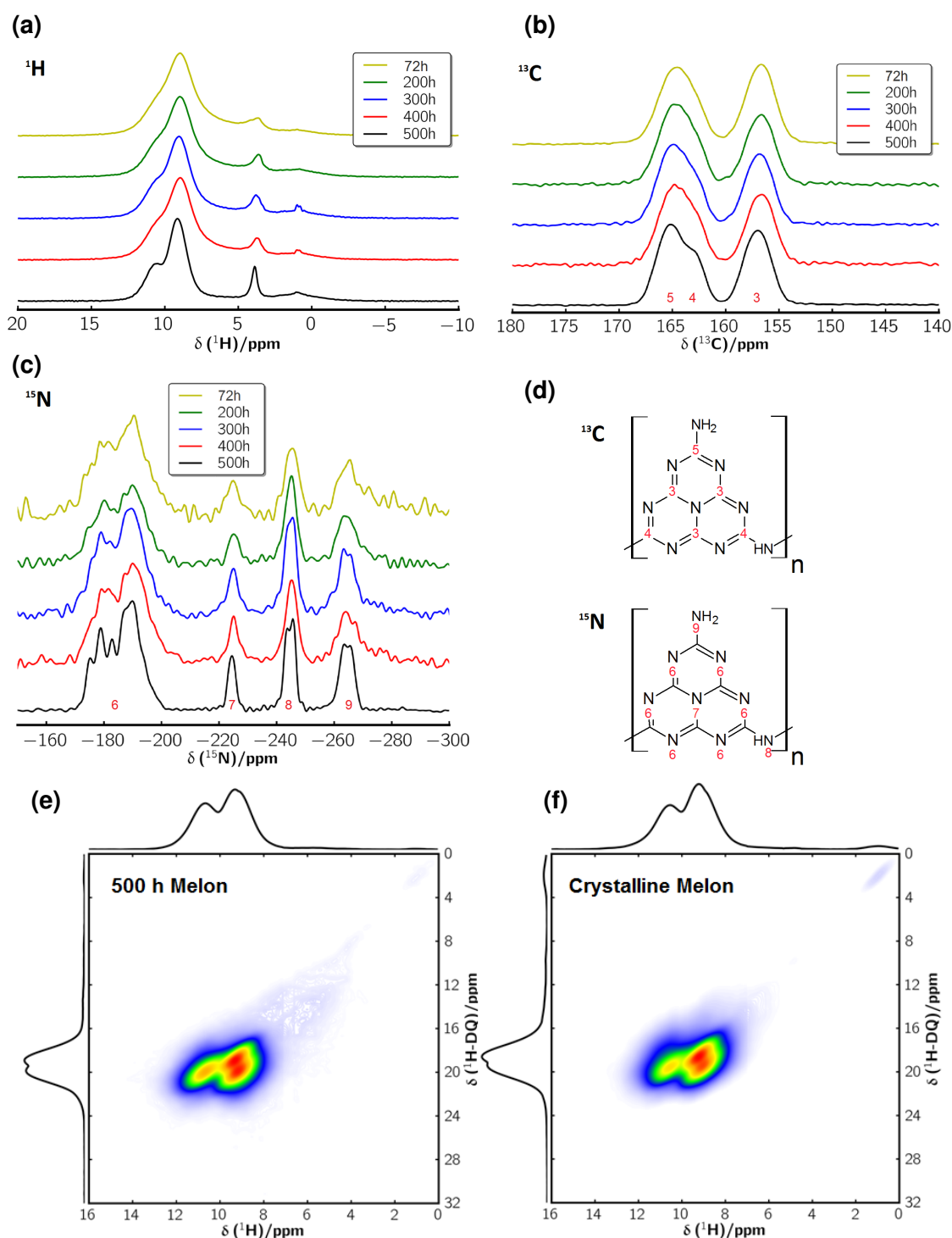
Figure 5.12: ssNMR and cross correlation studies. **(a)** $^1$H CP-MAS spectra, **(b)** $^{13}$C CP-MAS spectra, **(c)** $^{15}$N CP-MAS spectra, **(d)** atomic environment legend for C and N. Finally, $^1$H $^1$H DQ-SQ spectra comparing **(e)** 500 h to **(f)** crystalline melon from Lotsch et al.[22] ($\nu_{rot}$ = 62.5 kHz, B$_0$ = 14.1 T, t$_{mix}$ = 160 µs).

In Figure 5.13(b), the deconvolution of the 500 h melon sample is given and this is compared to the deconvolution of crystalline melon. Two signals belonging to $NH_2$ with the same fitting parameters and one signal for the NH group is assumed. The intensity at 4 ppm and below is fitted with two additional signals although these signals show no correlation with any of the $^{15}N$ signals suggesting it is not part of the CNH structure. These signals are assumed to be from $H_2O$ present in the sample. As the spectra are not well resolved, the absolute integrals strongly depend on the fitting parameters. Therefore, the $NH_2$/NH ratio—which is a measure of the condensation degree—fluctuates for different devolutions. Nevertheless, the $NH_2$/NH ratio is always significantly higher for $^{15}N$ melon (0.96) than for the 500 h sample (0.75). For this comparison, the lower $NH_2$/NH ratio for 500 h melon implies more NH or conversely less $NH_2$ in the sample. This most likely corresponds to longer polymer chains of the 500 h CNH network.

In summary, there are no qualitative changes in NMR signals with increasing calcination time, with the exception of clearly visible increased signal resolution for the 500 h sample. Results for the 500 h sample are thus essentially identical to that of previously published crystalline melon. We prove that both share the same proton environment and that the proton environment contains both NH and $NH_2$ groups. Finally, comparing the $NH_2$/NH ratio, a significantly higher degree of condensation is indicated for the 500 h ultra long calcined sample.
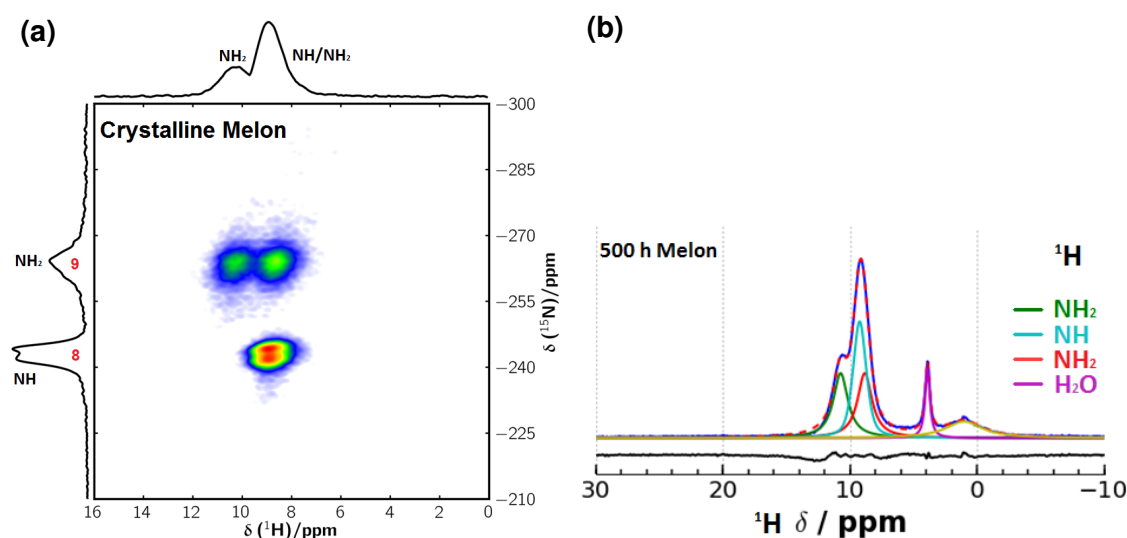


Figure 5.13: **(a)** $^{15}N$ $^{1}H$ (HMQC) spectra of the $^{15}N$ enriched melon from Lotsch et al.[22] and **(b)** the deconvolution of 500 h $^{1}H$ spectra showing the assignment for the NH and $NH_2$ groups.

## 5.9  UV-Vis Diffuse Reflectance and Band Gap

UV-Vis diffuse reflectance spectra for the ULT melon samples are shown in Figure 5.14. The spectra show the main absorbance in the UV region below 400 nm as expected for such pale samples.

Figure 5.14 shows the UV-Vis diffuse reflectance spectra for the 200 h to 500 h powder samples. The main absorbance occurs in the UV region but strangely there is also a low intensity absorbance in the visible at 560 nm which emerges after 48 h of calcination.

Absorbance peaks for the 500 h sample are well defined and occur at 385 nm, 367 nm and a broad absorbance centred at 309 nm. The peak at 385 nm is only visible as a shoulder for the 200 h calcination sample but becomes more pronounced with increasing calcination time. The peak at 367 nm is visible in all spectra. A peak at 342 nm is most prominent in the 200 h calcination sample but decreases for the 300 h sample. At 300 h calcination, the most prominent peak is at 331 nm. The maximum absorption of the 48 h reference melon occurs at 368 nm, whereas the 72 h melon reference peaks at 382 nm with an absorbance edge further in the visible compared to the 200 h to 500 h samples.

Notably, with the emergence of distinct absorbance peaks in the 500 h sample as opposed to broad bands, this once again hints to the increased crystalline order in the 500 h sample. Distinct UV-Vis peaks have so far not been observed in the g-CN melon literature. Also, these peaks do not clearly match with the absorbance spectra of precursor CNs such as melamine, melam or melem.
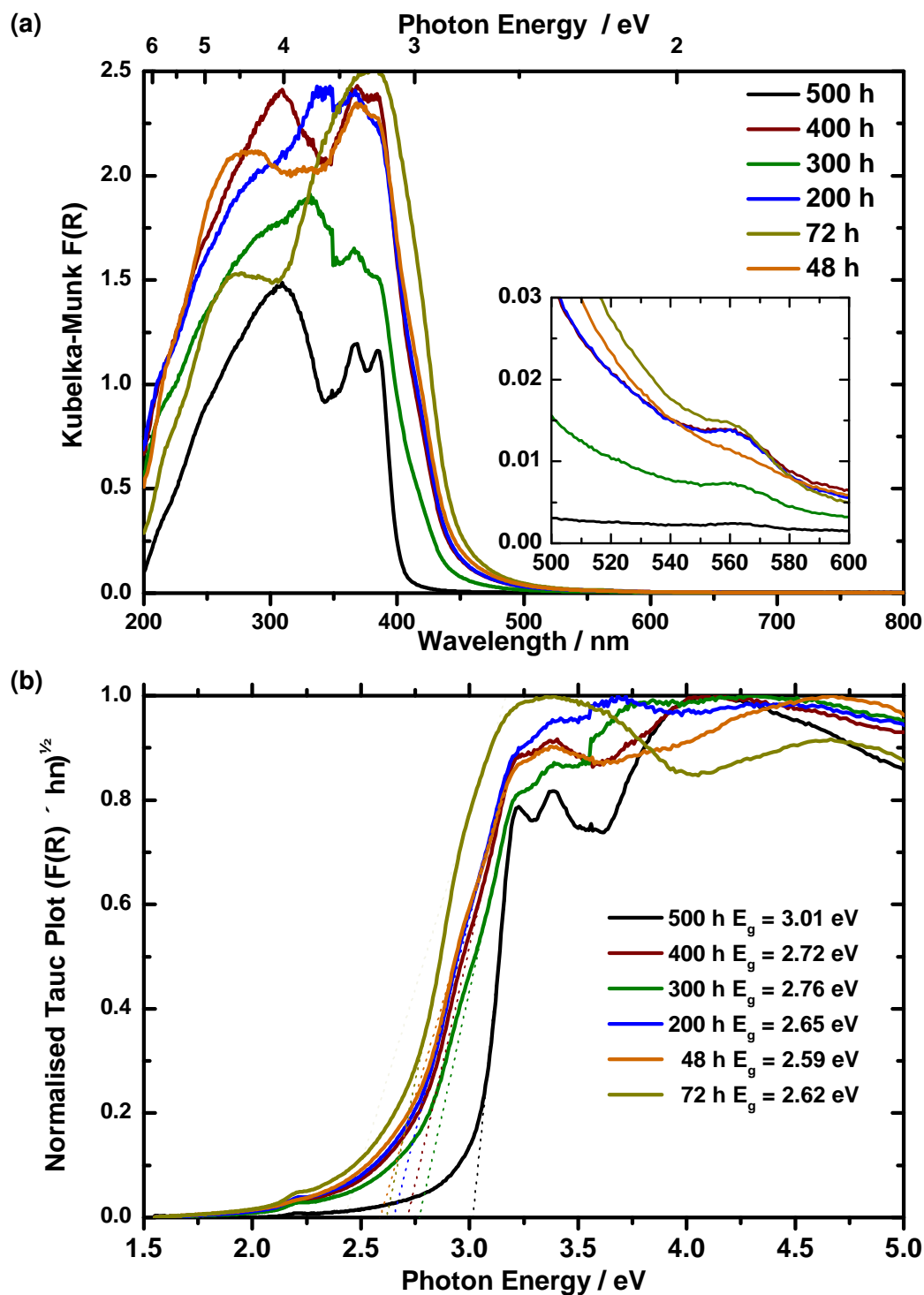
Figure 5.14: **(a)** Diffuse reflectance spectra of ULT Melon from 200 h to 500 h calcination time. **(b)** Tauc plot of ULT melon and the estimated indirect band gap values.

The optical method provides an estimate of the band gap (see Section 2.4.2) which is given from the Tauc plot in Figure 5.14(b). The calculated band gap values for direct and indirect (allowed) transitions for ULT and recalcined melon are provided in Table 5.5. It is still unclear if carbon nitride melon behaves as a direct or indirect semiconductor. The seminal paper by Antonietti's group provide DFT calculations on melon as a direct semiconductor with a calculated band gap of 2.6 eV and an optically estimated band gap of 2.7 eV.[36] As mentioned in Section 2.1, the Tauc plot band gap estimation depends on whether the semiconductor is direct or indirect. Most authors use the Tauc method with exponent $n = \frac{1}{2}$ $((F(r)h\nu)^{\frac{1}{2}})$ which corresponds to an indirect allowed semiconductor transition. Calculations by Wei et al.[94] provide direct and indirect band gap values but these are for the fully condensed g-$C_3N_4$. Recent calculations from Zhang et al. (also for a fully condensed heptazine carbon nitride) report an indirect semiconductor with band gap 2.71 eV although the band dispersion is quite flat.[95] Wu et al.[96] calculated the effect of water on carbon nitride heptazine sheets and saw that the sheets become buckled and, most interestingly, give a direct transition (3.05 eV), whereas the planar sheet was indirect (2.75 eV). Direct transition semiconductors are more favourable for their enhanced absorption rate, but less favourable in terms of charge separation. In Table 5.5, the band gap values for both direct and indirect transitions are given.

Table 5.5: UV-Vis absorbance edge parameters and calculated band gap ($E_g$) values from normalised diffuse reflectance.

| Sample | Abs. Edge Inflexion (nm) | Abs. Onset (nm) | Direct $E_g$ $\pm$ 0.05 (eV) | Indirect $E_g$ $\pm$ 0.05 (eV) |
|---|---|---|---|---|
| 48 h | 398, 425 | 439 | 2.7 | 2.6 |
| 72 h | 405, 426 | 452 | 2.9 | 2.6 |
| 200 h | 395, 423 | 434 | 3.0 | 2.7 |
| 300 h | 393, 423 | 422 | 3.1 | 2.8 |
| 400 h | 393, 419 | 431 | 3.0 | 2.7 |
| 500 h | 393, - | 402 | 3.1 | 3.0 |
| Recalcained +12 h | 399, 422 | 421 | 3.0 | 2.7 |
| Recalcained +24 h | 395, 418 | 411 | 3.1 | 2.9 |
| Recalcained +36 h | 395, - | 406 | 3.1 | 3.0 |
| Recalcained +48 h | 392, - | 407 | 3.1 | 3.0 |

An important parameter to extract and compare from these spectra is the absorption edge and the onset of absorption. At what wavelengths is the sample absorbing light? This is not easy to answer due to different absorption coefficients, light scattering and poorly defined absorption edges but we can give a definition that can compare these spectra mathematically. One possibility is to use the point of inflexion,[97] a point which gives the 'centre' of the absorption edge. Additionally, here we define a point which approximates the onset of absorption or a lower bound to the absorption edge while attempting to exclude scattering. This is the same method used when calculating the optical band gap as discussed in Section 2.4. Defining the onset of absorption as the x-axis intercept of the slope of the linear part of the absorption edge for the normalised data (Figure 5.15(c)), we see that the value for the 200 h calcination sample is 434 nm, at 300 h it is slightly blue-shifted to 422 nm. At 400 h the absorption edge does not move and remains at 431 nm, unexpectedly reverting to a similar value as observed for the 200 h sample. Finally, at 500 h, the edge is blue-shifted once again to 402 nm.

Examining the first derivative of these curves **(d)** and looking closely at the positions of the absorbance edges, two points of inflexion are observed in the 200 h to 400 h samples. The second point of inflexion (as indicated by the minimum) is at 423.5 nm. This indicates a 'second' absorbance edge or inter-band state. What is most interesting is that the 500 h sample does not have the second absorbance edge but rather has a highly linear single absorbance edge. The absorbance state responsible for visible light absorption is absent in the 500 h sample. This explains the whiter colour and the increased band gap.

The derivative curves are also helpful for identifying the linear sections of the absorption edge as indicated by straight lines. With the exception of the 72 h sample, the most linear domain for all samples is from 385 nm to 390 nm. Hence, this region was chosen for optical band gap calculations according to recommendations.[56] Arguably, the 72 h absorbance edge is incorrectly applied in this region but should be further extended to the visible. Accordingly, two linear fittings were applied to the 72 h sample, one matching the other samples (seems to underestimate the band gap) and a second more appropriately matching the second inflexion point in the visible.

Another interesting point is that extending the absorbance to visible light does not include shifting the primary absorbance peak, but involves the emergence of new states in the visible, possibly arising from structural defects. These defects could be from edge states or buckling of the layers, rather than being inherent to the molecular structure of carbon nitride. Another likely possibility is that the band in the visible is due to interlayer interactions between stacked melon strands, which would explain why these bands gradually disappear for increasing calcination time.
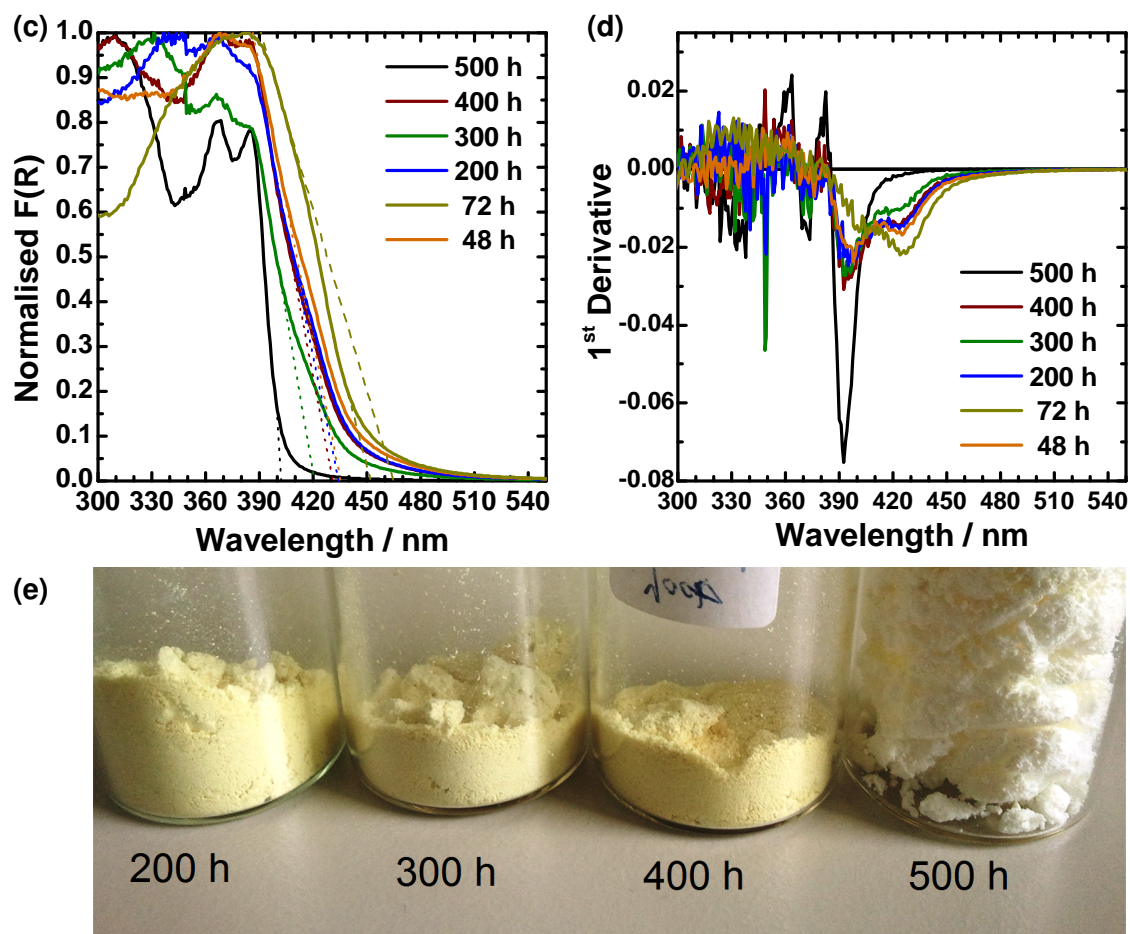
Figure 5.15: **(c)** Normalised Kubelka-Munk spectra with absorbance edge linear fittings (dashed lines) and **(d)** $1^{st}$ derivative for determining absorbance edges and onsets. **(e)** Photo of the 200 h, 300 h, 400 h, and 500 h ULT melon samples. Note the colour change and volume increase of the 500 h sample.

### 5.9.1   UV-Vis of Recalcined Melon

Figure 5.16 shows the diffuse reflectance spectra for the recalcined melon samples along with the 72 h melon starting material. The peaks observed at 367 nm and 385 nm emerge after just +24 h recalcination and match those of the 500 h ULT sample. The absorption edges of recalcined samples are blue-shifted compared to the 72 h and as summarised in Table 5.5, closely match the ULT samples. The +36 h and +48 h absorption onsets match that of 500 h melon. The absence of the visible absorbance inflexion at 424.5 nm for the 500 h sample is also observed for the +36 h and +48 h samples.

Overall, spectra match with the ULT samples and the +36 h and +48 h samples are optically identical to the 500 h ULT sample.
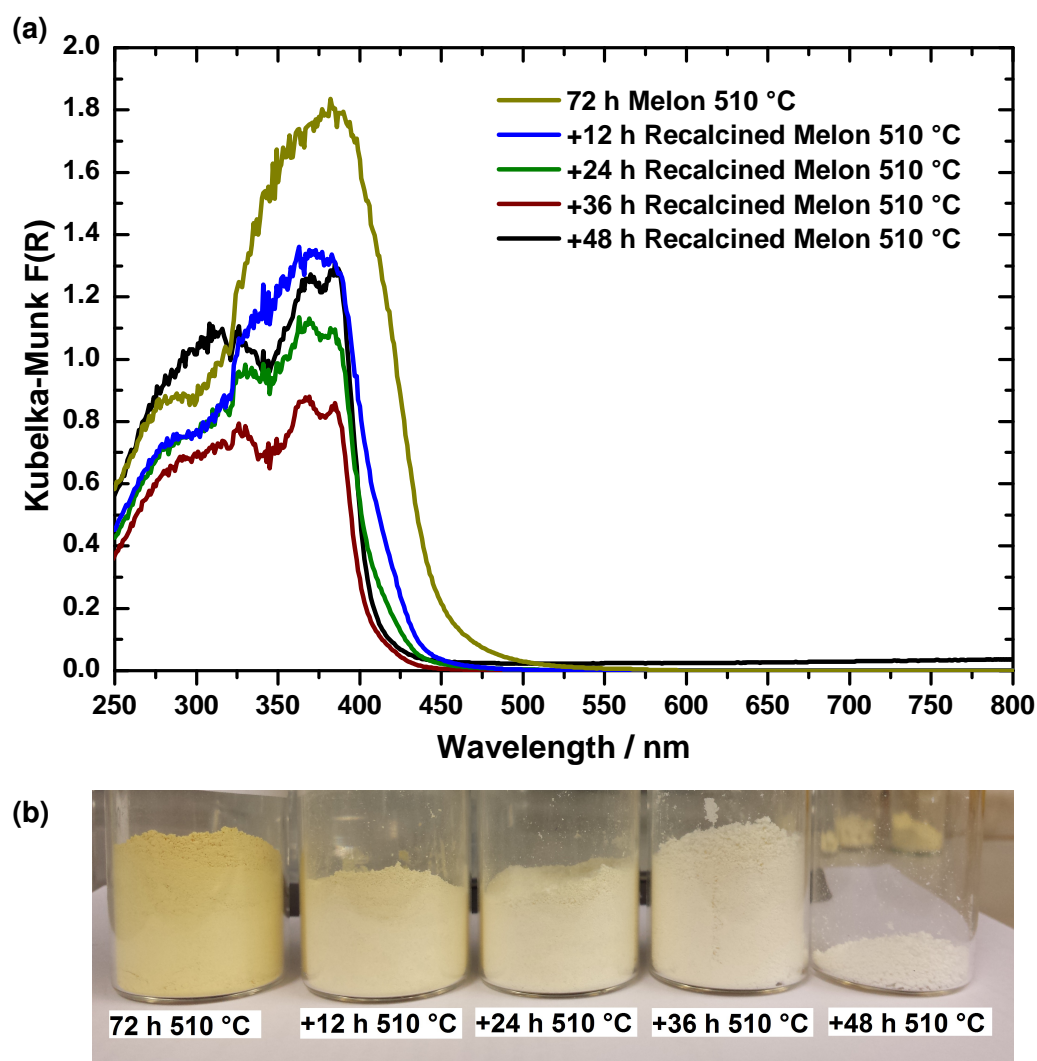


Figure 5.16: **(a)** Diffuse reflectance spectra of recalcined melon samples compared to 72 h melon reference. **(b)** Photos of recalcined melon samples.

**Fluorescence Spectra**

Graph 5.17 compares the UV-Vis absorption and photoluminescence of a dilute suspension of 500 h melon in water. For 280 nm excitation, the absorption intensity maximum for this dilute suspension occurs at 320 nm in agreement with diffuse reflectance measurements of the solid.

The fluorescence maximum peaks in the blue at 437 nm. Interestingly, there is a shoulder fluorescence peak at 394 nm for the colloid. This shoulder becomes prominent at low concentrations but is dominated by the main fluorescence at high concentrations or in the solid. The 437 nm emission can be attributed to one of the main radiative decay pathways for excited states and thus reduces the amount of available excitons for charge transfer and hence, photocatalysis.

A solvent dependent study of the optical properties for the 500 h sample was also carried out. Solvents chosen were deionised water, DMSO, acetonitrile, acetone, methanol, ethanol, THF, toluene and chloroform. The 500 h colloid disperses best in water and DMSO, which testifies to its protic, polar nature and capability to form hydrogen bonds. It also disperses in acetonitrile and acetone although suspensions are less stable and settled after 24 h. From this, UV-Vis absorption and fluorescence spectra were recorded for acetone and DMSO suspensions. None of the optical states were quenched and there were no changes observed in the position of the absorbance or fluorescence peaks of these suspensions. This suggests a weak solvent interaction with the ULT melon surface and implies that the optical transitions observed are part of the core structure.
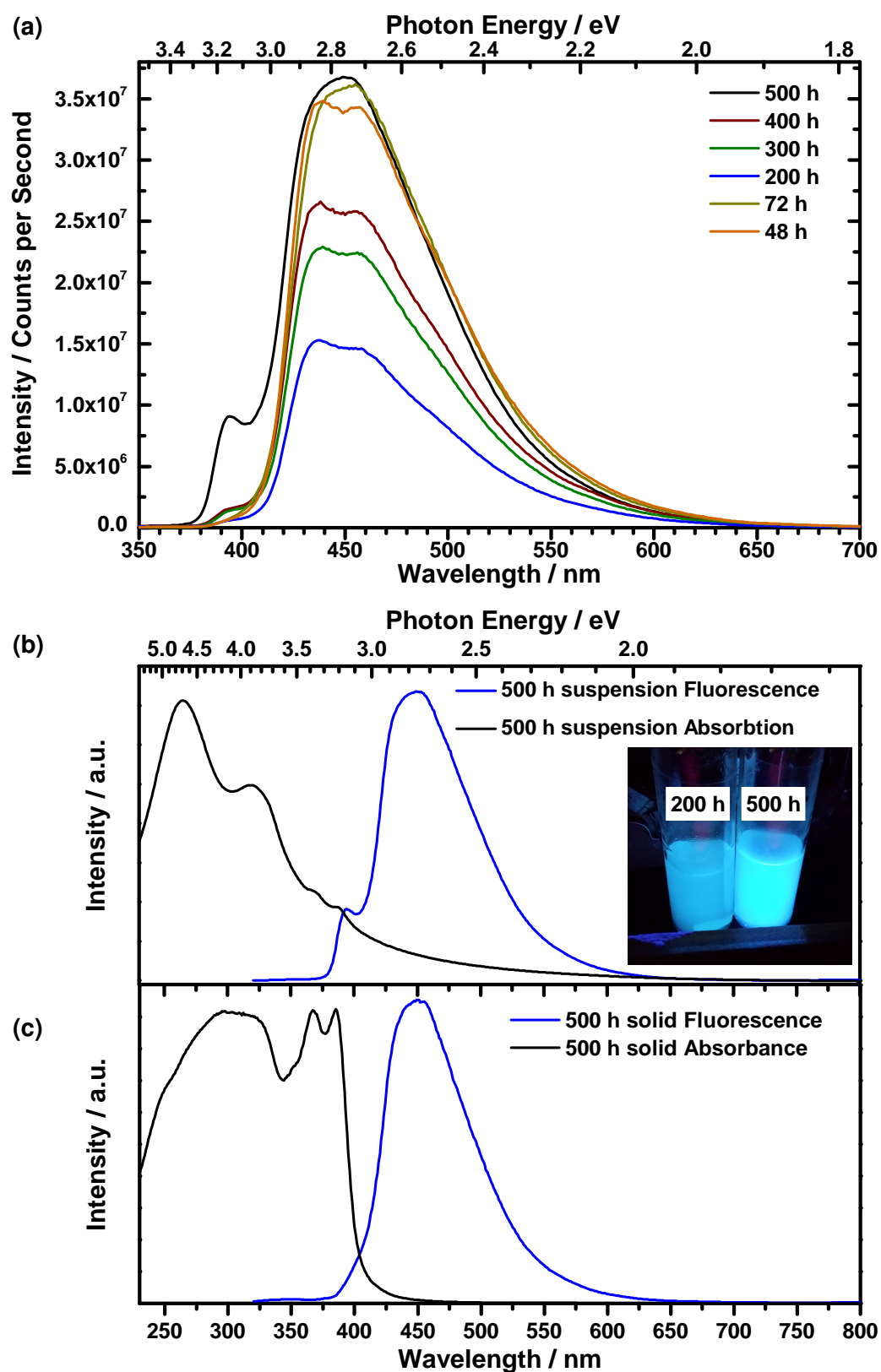
Figure 5.17: **(a)** Fluorescence of 200 h to 500 h colloidal samples $(0.2 \text{ mg mL}^{-1})$. **(b, c)** Comparison of absorbance and fluorescence for 500 h ULT melon in aqueous colloid (b) and solid powder (c).

## 5.9.2 Light Scattering in the Suspension

Unlike the 200 h to 400 h, the 500 h melon sample shows considerable scattering of light in the suspension. This can simply be observed as the Tyndall effect or measured with the UV-Vis spectrometer. What is interesting is that this scattering of blue light broadly coincides with the absorption of the photocatalyst and may enhance absorption through multiple scattering directions, effectively increasing the light penetration depth. This would also explain high photoactivity at low catalyst concentrations as observed in Figure 5.30(a).

**Tyndall effect**

The Tyndall scattering effect is observed when the particle size is of the same order as the wavelength of light. The scattering size parameter $x \approx 1$ (see Section 2.5) and is not necessarily restricted to spherical particles.

The Tyndall scattering effect is a quick and easy test for the presence of dispersed nanomaterials in suspension. A laser is shone through the suspension and if the laser light is scattered, then the particle sizes are in the same order of magnitude as the photon wavelength (in this case, 633 nm from a He-Ne laser pointer). This confirms that the sample is a suspension or colloid and not a solution. Tyndall scattering for the 500 h melon sample is demonstrated in Figure 5.18(a). The laser light is dispersed by the particles in the colloid, thus demonstrating the Tyndall effect. The particle sizes for this sample determined from DLS measurements (yielding a hydrodynamic diameter) are in the range of 50 nm to 500 nm as shown in Section 5.11.

In Figure 5.18(b), the characteristic blue tinge is seen in vial 1 when brightened with sunlight from the left side. Vial 2 has a redder hue since the majority of light must pass through vial 1 and the blue light is already scattered away. The effect is not due to lighting conditions or sample conditions as the samples are the same concentration and from the same batch. Importantly, the effect was also observed when the vials swapped positions, so that vial 2 shows a blue tinge and vial 1 a redder hue. This effect is analogous to the blue sky during the day and a red sky at dusk. However, the blue sky is mainly attributed to Rayleigh scattering from molecular gases, whereas the hue seen in the 500 h sample is attributed to Mie (or more specifically Tyndall) scattering because of the presence of melon nanoparticles.
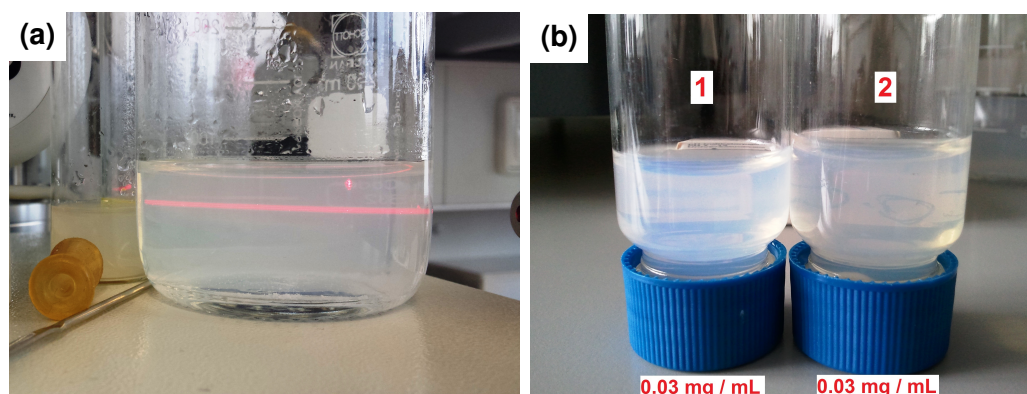
Figure 5.18: **(a)** Tyndall effect of 500 h melon suspension with laser light. **(b)** Vial 1 appears blue due to scattering as it is directly in the light, vial 2 has a redder hue. Both samples are from the same batch (same particle size and concentration) and the scattering effect is the same when samples swap positions.

**Diffuse Transmittance + Direct Trap**

It was attempted to measure these scattering effects experimentally. The intension was to capture the spectrum of the blue light as seen in Figure 5.18**(b)** (Vial 1). Figure 5.19**(a)** shows how scattering in a colloid gives a wavelength-dependent non-zero absorption, even above 500 nm. A power fitting ($y = Ax^b$) is applied to the absorption and confirms that there is a $\lambda^{-4}$ dependence for the colloid. This high inverse lambda dependence is characteristic of small particles such as in Rayleigh scattering.[98] As expected, the fitting diverges from the measured spectrum below 400 nm as the true absorption now dominates.

To fully explain Figure 5.19**(b)** we must first examine the scheme of the spectrometers integrating sphere to understand the configuration used to only measure scattered light. Figure 5.20 shows three configurations for the integrating sphere. Scheme **A** is the default configuration for the *Diffuse Reflectance* of a powdered sample as conventionally used. Scheme **B** illustrates the *Diffuse Transmittance* measurement. This configuration compensates for scattering losses compared to a conventional specular transmission experiment by collecting the scattered light in the integrating sphere. Finally, in an attempt to only measure scattered light (and exclude transmitted light), Scheme **C** which is the *Diffuse Transmission with Direct Trap* was used. This is similar to the conventional diffuse transmission of a suspension, except that instead of placing the white standard at the reflectance port (reflecting it back into the sphere), the port is blocked, so the directly transmitted (or directly forward scattered) light is removed from the system. Hence, only highly scattered light in the forward direction will scatter in the sphere and finally reach the detector. In short, this configuration removes the directly transmitted light and only records scattered light in the forward direction.
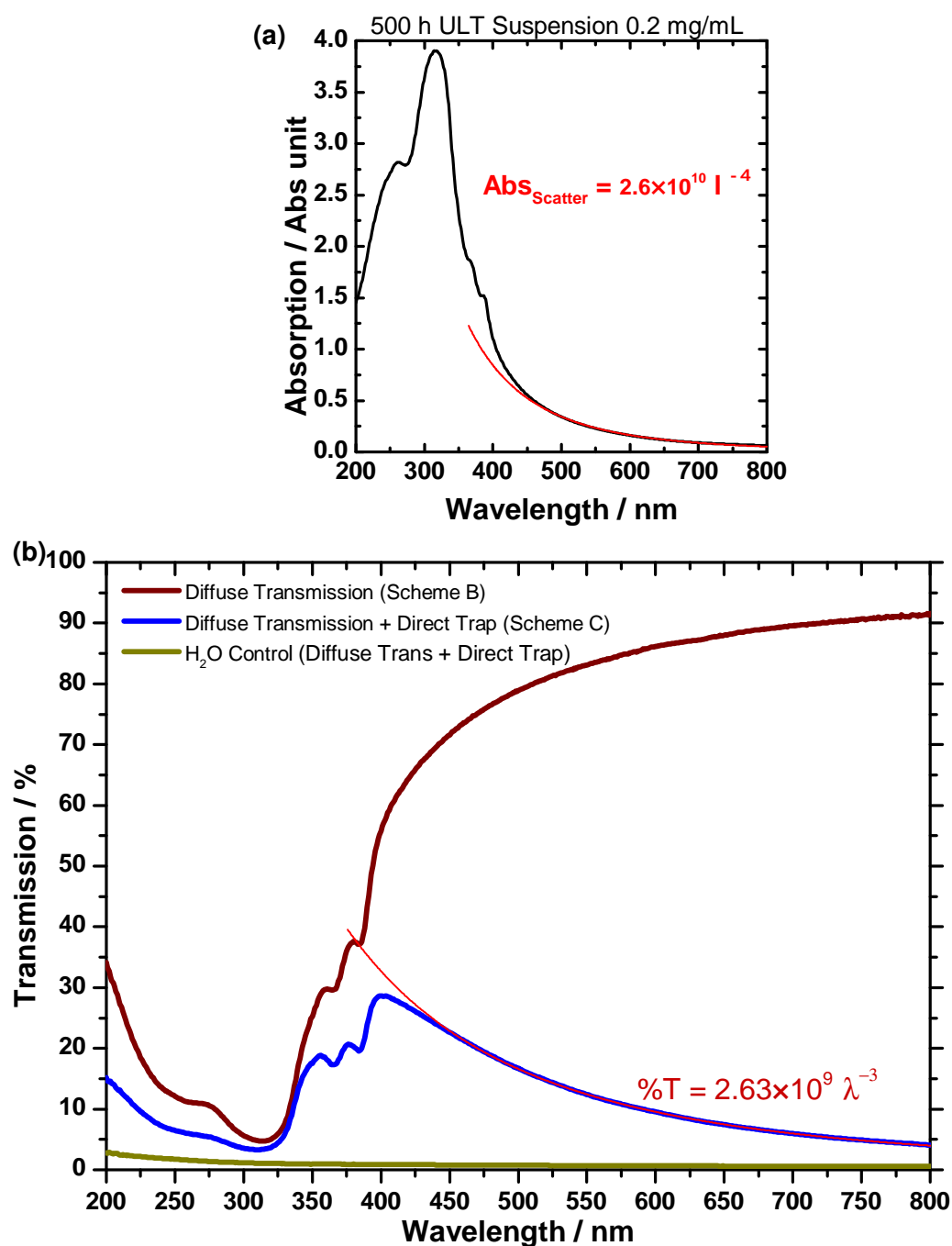
Figure 5.19: Scattered light in 500 h colloid. **(a)** Conventional absorption of a colloid with a $(y = A\lambda^b)$ fitting showing a $\lambda^{-4}$ dependence at higher wavelengths. **(b)** Diffuse transmission of a colloid compared to the diffuse transmission + direct trap to measure the forward scattered light.
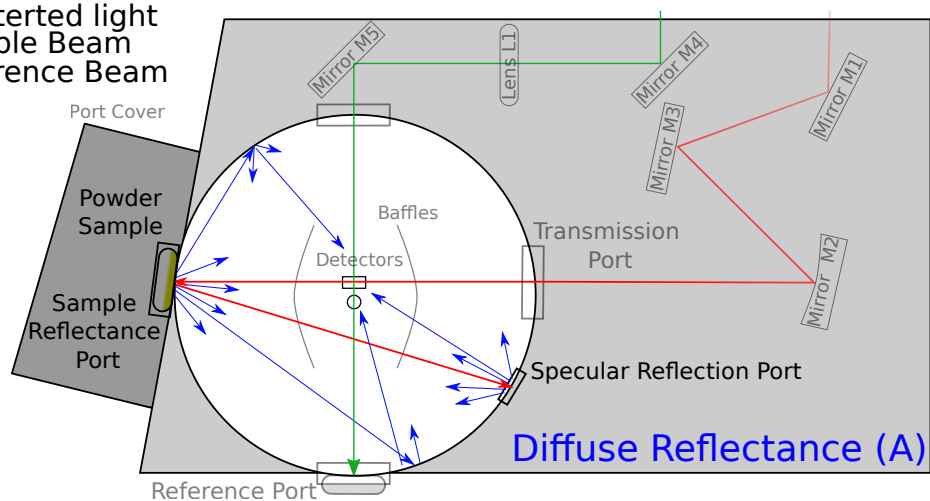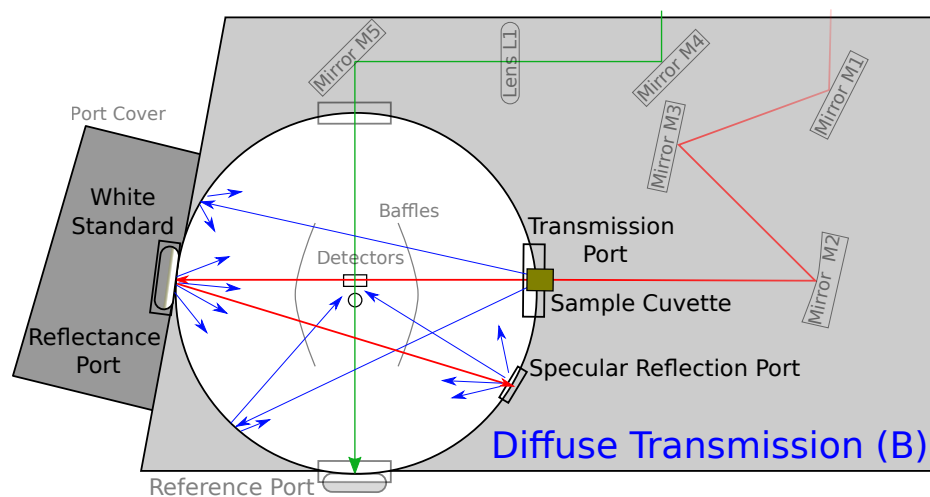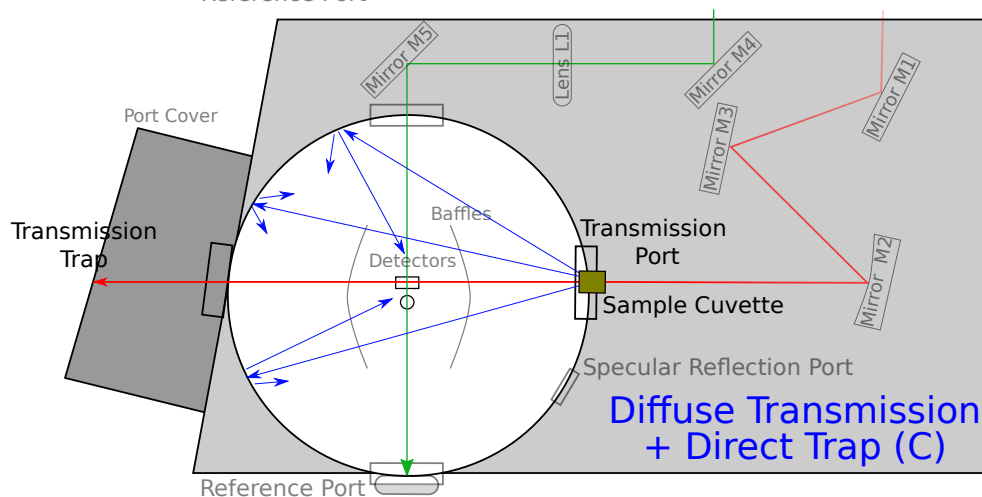
Figure 5.20: Topdown schematic of the UV-Vis diffuse reflectance accessory (DRA). **(A)** Hemispherical diffuse reflectance of a powder sample (default setup), **(B)** diffuse transmission of a suspension and **(C)** diffuse transmission + direct trap setup of a suspension with the directly transmitted component removed in an attempt to measure the spectrum of forward scattered light.

So Figure 5.19**(b)** compares the conventional *Diffuse Transmittance* of a suspension (Scheme **B**) to the *Diffuse Transmittance + Direct Trap* (Scheme **C**) as described above. In other words, this graph compares the diffusely transmitted light to the highly scattered light. Mathematical fittings are also applied to these spectra. For the *Diffuse Transmittance*, the transmission decays exponentially with wavelengths above 450 nm (93 - 484 e$^{\frac{-7\lambda}{1000}}$). For the *Transmittance + Direct Trap*, the spectra have a $\lambda^{-3}$ dependence (2.63 $\times 10^9$ $\lambda^{-3}$).

Although unconventional methods are used, it is proposed that for the *Transmittance + Direct Trap* plot (green), the increasing transmittance from 800 nm to 400 nm is only due to forward scattered light and the spectrum of Tyndall scattering was successfully captured. This scattered light spectrum decreases below 403 nm due to absorption by the melon sample. The transmission maximum at 403 nm corresponds to the blue scattered light observed by eye. To prove these claims, it would be necessary to examine colloids with well defined particle sizes and thus shifts in the scattering peak. It would also be more instructive to capture both forward and back scattered light by placing the cuvette in the centre of the integrating sphere using the provided accessory.

## 5.10 Sorption Isotherms, Pore Size Distributions and Surface Area

Gas sorption analysis was meaured by Dr. Stephan Hug at LMU Munich. Figure 5.21 presents the gas sorption-desorption analysis used to investigate surface area and pore sizes. Figure 5.21**(a)** shows the isotherm for the 500 h sample which resembles a type IV behaviour.[99] From the observed H3-type hysteresis (aggregates of plate-like particles with slit shaped pores), a mesoporous material is suggested. The limited uptake above 0.8 $P/P_0$ represents the filling of the mesopores with capillary condensation as the main mechanism. Some desorption still occurs at relatively low pressures of 0.2 $P/P_0$, suggesting a delayed release of adsorbate. This is associated with phenomena such as swelling of the pores and coupled with this, pore sizes are expected to be of the order of the argon adsorbate size (3.4 Å kinetic diameter[100]). In addition, network and restricted percolation effects may play an important role which are caused by non-uniform particle size distributions. Swelling of the pores can be especially rationalised due to the synthesis conditions, where there is an autogenous pressure of gases during sublimation. Evidence of this swelling can be seen in the SEM images (Figure 5.24**(c)**) as bubble-like formations.

With regard to pore sizes in the range of argon gas, the pore volume distribution supports this (Figure 5.21**(b)**), as it shows micropores with a width of 1.09 nm. A further peak is observed at 2.71 nm width. The total pore volume is calculated as 0.290 $cm^3 g^{-1}$. Overall, the 500 h sample contains some mesopores as seen from the slight hysteresis, but is better characterised by its microporous nature. A slit pore, QSDFT equilibrium model was used, see Appendix A.2 for more detail.

Brunauer-Emmett-Teller (BET) surface areas were calculated for the samples as shown in Table 5.6. The surface areas generally increased with calcination time and with temperature, but sharply increased for the 500 h sample to 134 $m^2 g^{-1}$. This sample shows a nearly four times higher surface area than the initial 200 h sample.

Table 5.6: BET surface area for a range of calcination times and temperatures. (0.12–0.27) P/P$_0$ range on adsorption, see Appendix A.2 for more details.

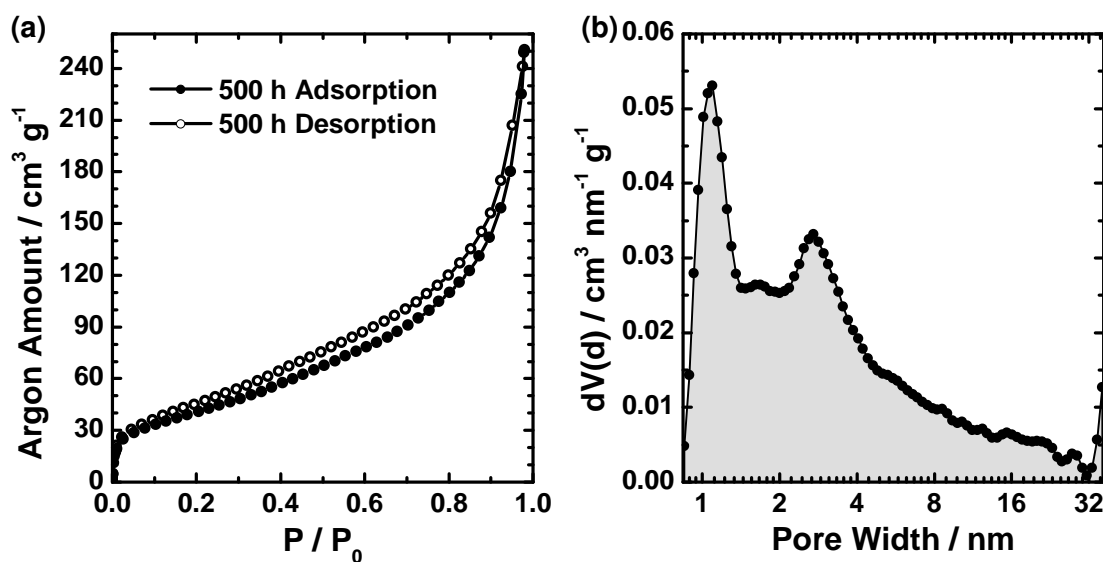| Calcination Time (hours) | Temperature (°C) | BET Area ± 0.5 (m$^2$ g$^{-1}$) |
|---|---|---|
| 160 | 430 | 6.5 |
| 160 | 450 | 10.5 |
| 160 | 470 | 47.3 |
| 160 | 490 | 91.7 |
| 200 | 510 | 34.8 |
| 300 | 510 | 57.7 |
| 400 | 510 | 52.3 |
| 500 | 510 | 134.2 |



Figure 5.21: **(a)** Argon adsorption/desorption isotherm of 500 h calcined melon sample. **(b)** Argon pore size distribution with the total pore volume calculated as 0.290 cm$^3$ g$^{-1}$. Ar at 87 K on carbon (slit pore, QSDFT equilibrium model).

## 5.11  Particle Sizes — Dynamic Light Scattering

The hydrodynamic particle size of the colloids was estimated with dynamic light scattering (DLS). The effects of concentration, sonication time and colloid stability were investigated.

The samples had high polydispersity indices (PDI), defined here as "a dimensionless measure of the broadness of the size distribution calculated from the cumulants fit analysis" and thus required a particle size distribution (PSD) analysis rather than comparing average particle sizes directly. The reliability of DLS for particle size is hindered by the assumption of spherical particles instead of nanosheets for the 500 h sample. Results are also influenced by the polydispersity and aggregation so only colloidally stable suspensions were chosen. The average of 10 measurements was taken per reading and 3 readings were taken separately per sample to increase the accuracy of results. Only results which met the software criteria for good data collection were used and size distributions *by number* were evaluated.

Figure 5.22**(a)** compares the particle size distributions by *volume* and *number* with the raw *intensity* distribution data. For example, if we were interested in the distribution of the overall volume, we would use the volume distribution (red) and see that most of the volume (22.5 %) is distributed in the large 5.56 µm aggregates. However, these may be few in number or even be foreign contaminants. We are interested in the particle size distribution by number (green), the distribution based on the particle count. Note however, that while number distributions highlight the small particle sizes present, they tend to ignore large particle sizes, which are present albeit scarce in number. This is best illustrated in Figure 5.22**(a)** where the size distribution by volume peaks at 5560 nm and the size distribution by number peaks at 68 nm. The table in **(b)** summarises the trend for the main particle diameters as seen in (c) and (d) which are described below.

Figure 5.22**(c)** shows how the particle size changes with concentration. There is a general trend that at lower concentrations, particle sizes are smaller. At the relatively high concentration of $1 \, \text{mg mL}^{-1}$ there is a broad size distribution spanning 78 nm to 1400 nm. Decreasing the concentration to $0.2 \, \text{mg mL}^{-1}$ slightly shifts the distribution to smaller particle sizes from 220 nm to 190 nm. At $0.05 \, \text{mg mL}^{-1}$, the distribution splits into small (122 nm) and large particles (459 nm). Further decreasing the concentration shifts the distribution to smaller sizes and also increases the amount of smaller particle sizes. Hence, going from $0.05 \, \text{mg mL}^{-1}$ to the centrifuged $0.03 \, \text{mg mL}^{-1}$, we go from 18 % of 122 nm particles to 26 % of 72 nm particle diameters. Centrifuging the $0.03 \, \text{mg mL}^{-1}$ sample (10 000 rpm for 10 minutes) did not remove the larger signal (presumably because the large and smaller particle sizes are so similar) but did help remove large aggregates (e.g. 5.56 µm). As before,

the supernatant continued the trend of shifting to smaller particle sizes. These DLS results agree with a recent publication by Panasiuk et al.[101] who also observed a decrease in particle size upon dilution. These results are interesting as they demonstrate how lowering the concentration of the samples can deaggregate the particles—shifting to smaller and less dispersive size distributions—by the interaction of carbon nitride and water.

Figure 5.22 **(d)** shows how ultrasonication time decreases the particle size. We see the expected trend of increased sonication time decreasing the particle size. The unsonicated sample shows two particle sizes peaking at 190 nm and 459 nm. Sonicating the sample breaks the particle sizes above 0.7 µm and slightly shifts the overall distribution to smaller sizes. After 9 h sonication, there is a significant shift to smaller particles (68 nm) although some larger particles remain. Finally, at 12 h sonication there are $< 1\,\%$ of particles above 100 nm with the distribution peaking at 44 nm and the smallest particle size was calculated to be 33 nm diameter.

In summary, lowering the concentration promotes smaller particle sizes and sonicating the colloid breaks the aggregates into smaller pieces. The smallest particle size peak of 44 nm for 12 h sonication at $0.2\,\mathrm{mg\,mL^{-1}}$ is expected to give the best colloids with high surface area and consequently the best colloids for photocatalytic $H_2$ evolution.
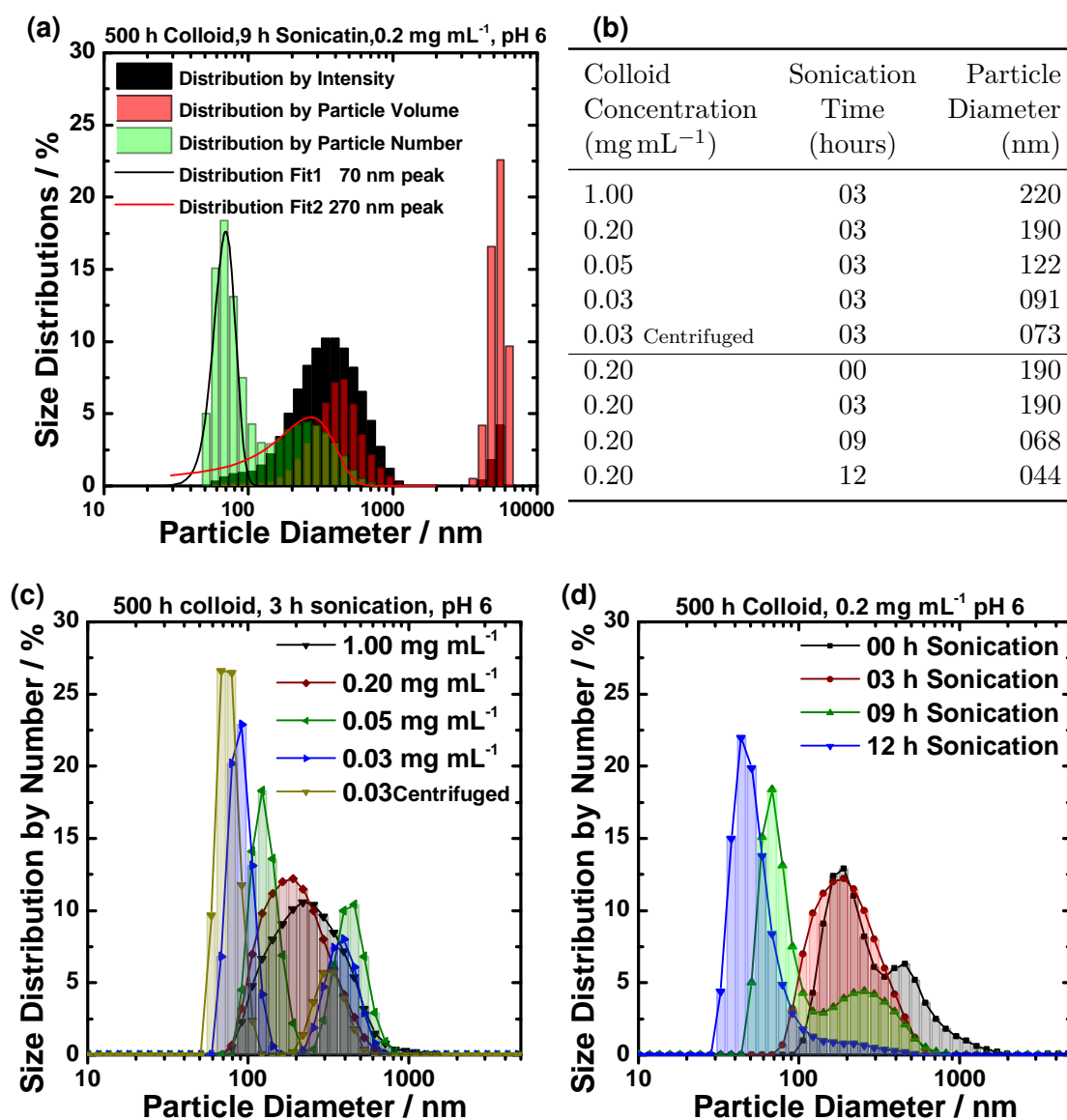
Figure 5.22: Particle size distributions of the 500 h sample by DLS. **(a)** Comparison of volume and number distributions and histogram fittings. **(b)** Table showing the primary peak diameters from (c) and (d). **(c)** Concentration dependence. **(d)** Sonication time dependence.

## 5.12   Zeta-potential

To determine the stability of the colloid, the pH dependent zeta-potential of the ULT samples in deionised water was measured. Fresh samples were ultrasonicated for 15 min. Phosphate pH buffers (0.1 M) were added and pH was measured with a Toledo pH meter. Small amounts of buffer were added to keep the ionic strength low. As shown in Figure 5.23, the colloids are isoelectric at pH 3. This is the pH where colloids have no surface charge and are considered least stable. From pH 4 to pH 7, there is a negative zeta potential with a low value of $-10$ mV. The value decreases further with increasing alkalinity to a value of $-22$ mV at pH 11. This indicates that the colloid is more stable in basic solutions, which is observed empirically, since colloids flocculate at pH 4 and below, but remain stable for months at pH 7 and above. Although the colloids appear to be stable for months, the value of $-10$ mV at pH 7 is considered to be in a state of *incipient instability* ($\pm 10$ mV to $\pm 30$ mV).[102]
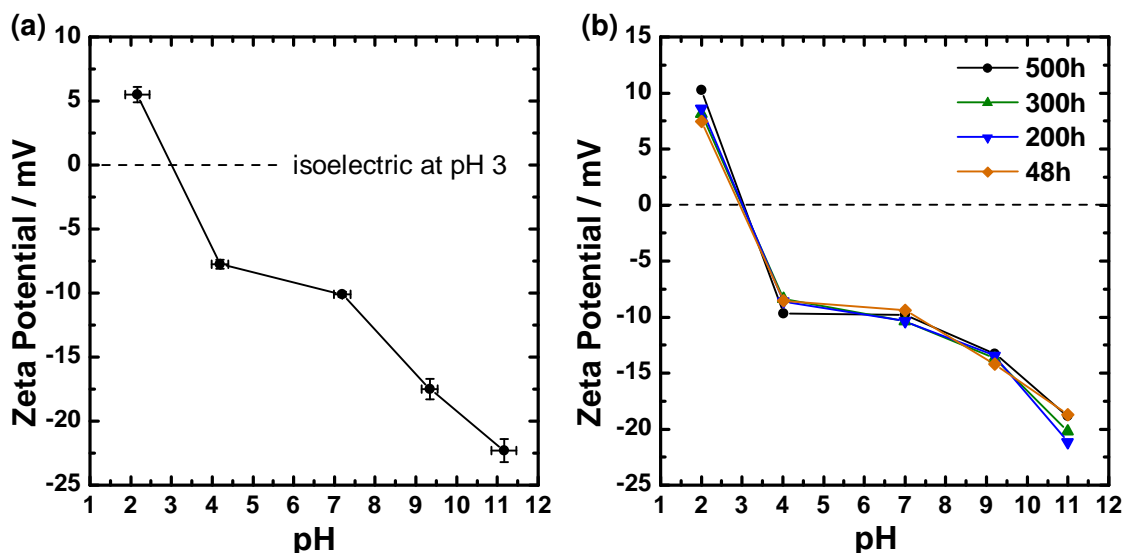


Figure 5.23: Measured zeta-potential by DLS of ULT melon samples. **(a)** 500 h and **(b)** 48 h, 200 h, 300 h and 500 h samples.

## 5.13 Scanning Electron Microscopy

Scanning electron micrographs (SEM) are shown in Figure 5.24. They show powder surfaces containing smaller particle aggregates. The smaller particles are $\approx$ 50 nm in diameter. Interestingly, the 200 h to 400 h samples show semi-hollow structures, which could be due to gas evolution during synthesis. These structures have a flat skin that appears to be composed of small 45 nm $\times$ 45 nm particles that are ubiquitous. There is no preferred morphology for these particles. The inside of the structures is either hollow or contains small particle aggregates. This unstructured material is unlike the surrounding CN and is assumed to represent less condensed compounds such as melem oligomers, melam or even unreacted melamine. While the 200 h to 400 h samples are similar, the 500 h sample shows smaller broken sheets and particles (**d**). This seems to indicate that the 500 h sample could have a higher surface area which corroborates with the BET surface areas (page 123).
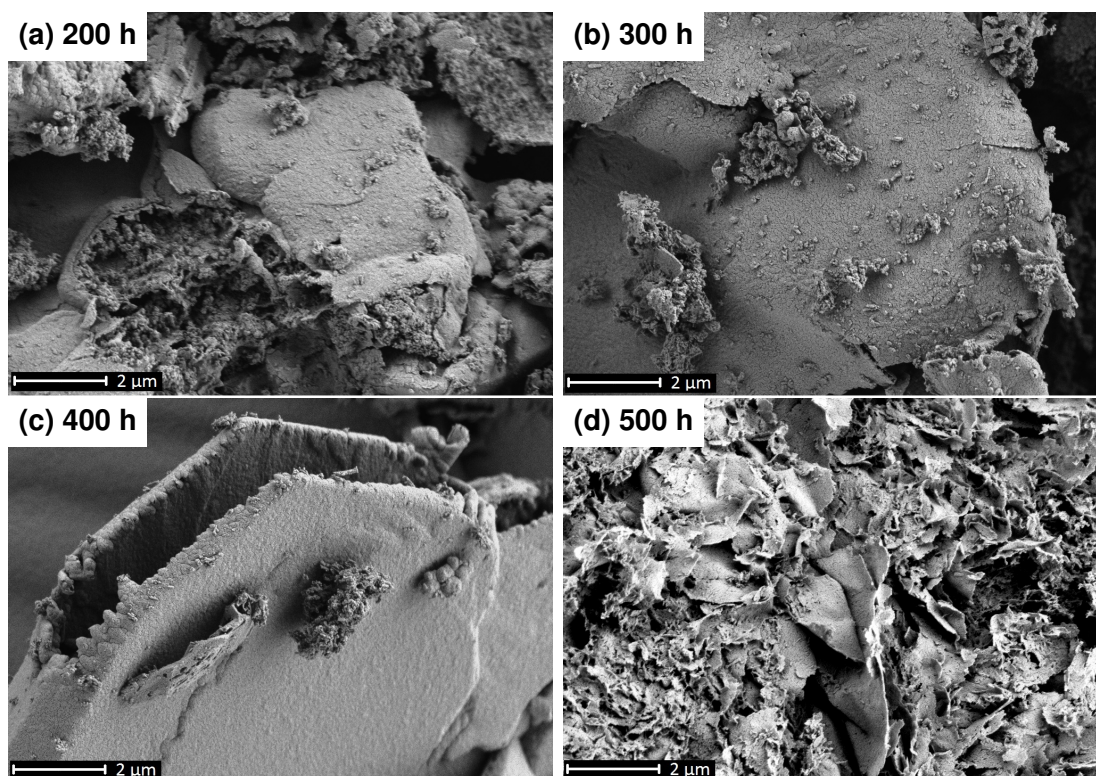


Figure 5.24: SEM images for (**a**) 200 h, (**b**) 300 h, (**c**) 400 h and (**d**) 500 h calcination. (10000$\times$ magnification, 2 µm scalebar).

SEM shows us the varied morphology of carbon nitrides. The 500 h sample is characterised by smaller broken up sheets. These sheets appear to be composed of 45 nm $\times$ 45 nm particles and this size is consistent with the 50 nm particles measured by DLS.

## 5.14 Transmission Electron Microscopy

Transmission electron microscopy (TEM) is one of the most important techniques to directly examine the crystallinity and also to investigate the morphology of the samples. TEM measurements of the 200 h, 300 h and 400 h samples show mostly amorphous melon that is sensitive to the electron beam. The 200 h sample also contained a crystalline phase observed in melem synthesised in an open system.[103]

Figure 5.25 shows transmission electron micrographs for the 500 h sample. The overview **(a)** shows dark areas where the carbon nitride flakes have curled up. The nano-flakes appear loosely connected, forming a sheet with various plane orientations facing up. A sheet of overlapping crystalline nano-flakes is seen in the top left of Figure 5.25**(a)**. A selected area electron diffraction pattern (SAED) was measured for the area marked with an arrow. The diffraction spot pattern proves the high degree of crystallinity of the sample **(b)**. Inset **(b)** is the simulation for the melon [001] zone axis which matches with the measured spot pattern. A high resolution TEM of the nano-flakes is presented in Figure 5.25**(c)** with the fast Fourier transform (FFT) inset. The large nano-flake at the centre of the image measures 30 nm × 50 nm.

A reverse-FFT colour map was calculated from the diffraction spots to identify the various diffraction planes and their orientations **(d)**. From this, we can estimate the nano-flake (*hkl*) planes and grain boundaries and determine if the nanosheets are connected. The diffraction planes in the largest nanosheet are assigned to *d*-spacings of 4.45 and 5.55 Å. These possibly correspond to the melon planes (120) and (420). The flake on the top left of the image represents *d*-spacings of 6.42 and 6.12 Å. These likely correspond to the (210) and (020) planes of crystalline melon. Finally, the reverse-FFT colour map shows that the nano-flakes overlap and do not share grain boundaries.

Table 5.7: Summary of smallest particle dimensions measured by different techniques.

| Measurement | Particle Dimensions (nm) |
| --- | --- |
| SEM | 45 |
| TEM | 40 × 40 |
| AFM | 40 × 40 × 3 |
| DLS | 50 |
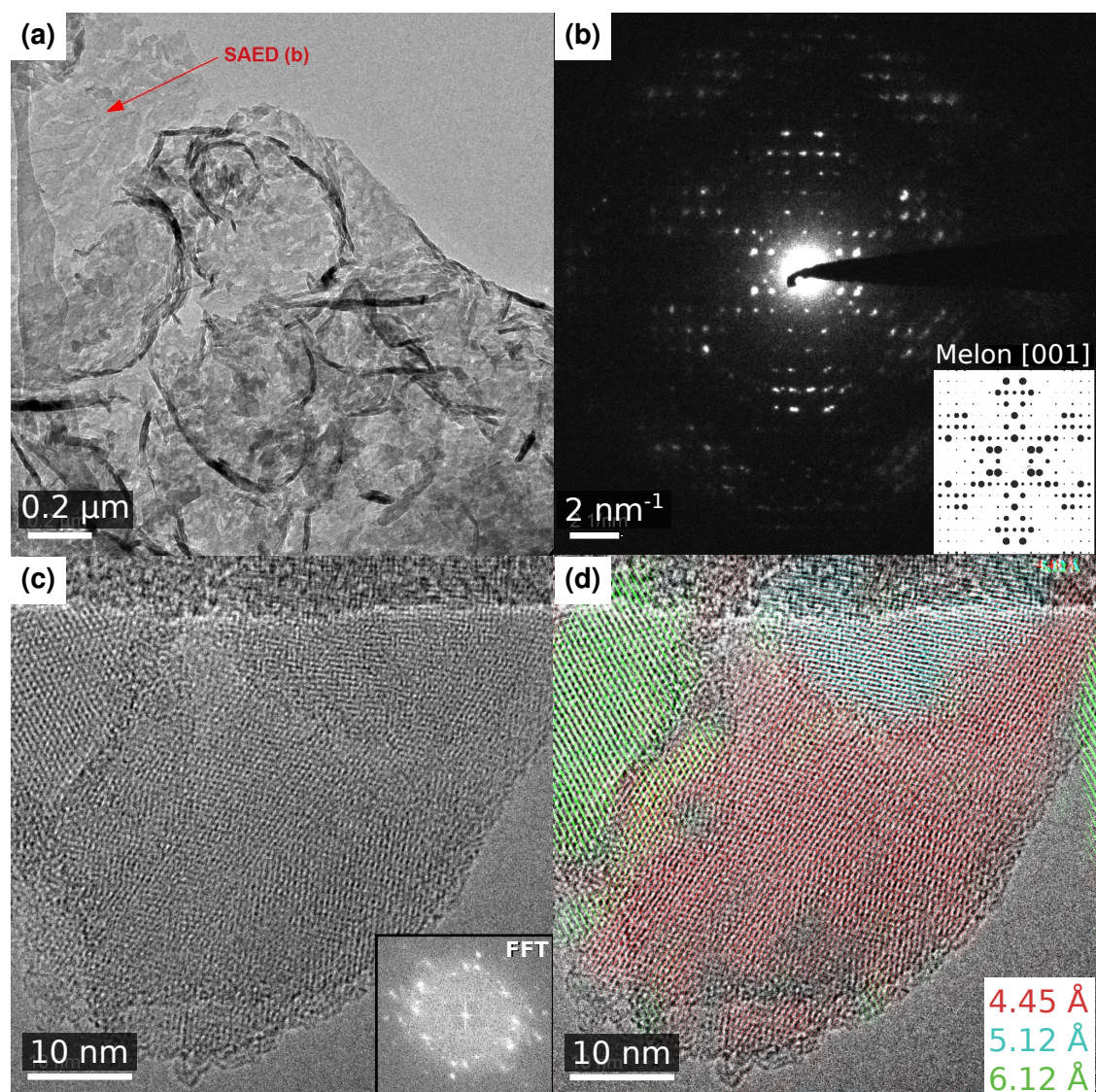
Figure 5.25: HRTEM of 500 h calcined sample with overview **(a)** showing curled-up CN sheets in black areas and flat sheets marked with an arrow. Selected area electron diffraction **(b)** (area marked with red arrow in (a)), matching with the simulated melon [001] zone-axis inset. High resolution CN nano-flake **(c)** with fast Fourier transform inset. A reverse Fourier transform colour-map **(d)** overlaid with nano-flake image highlighting the various diffraction planes.

## 5.15 Atomic Force Microscopy

Figure 5.26 shows the high resolution AFM images and height profiles for the 500 h sample (See page 151 for experimental details). The overview image **(a)** shows a similar morphology to the SEM image (Figure 5.24**(d)**). Height profiles of a sheet at the edge of the aggregates were taken. Profile 1 shows a 500 nm long particle with a height of 10 nm to 20 nm. The top is rough, presumably due to the removed or deposited smaller particles. Profile 2 is the baseline profile for this sheet. It shows roughness that is due to the smaller particles which are randomly distributed throughout.

Figure 5.26**(b)** presents the smaller particles observed in the 500 h colloid. Of these, the smallest have dimensions of 25 nm × 25 nm × 1 nm (profiles 3, 4). Average particle sizes are 40 nm × 40 nm × 3 nm (Profile 1). These particles are not spherical, although no clear height-steps are observed. It is suggested that these 25 nm × 25 nm × 1 nm particles are the building blocks for the larger aggregates and sheets observed. Once again, the small particle sizes are in agreement with TEM (40 nm), SEM (45 nm) and even DLS (50 nm) with AFM giving us the smallest particle sizes observed of 25 nm width and 1 nm height (Profiles 5,6).
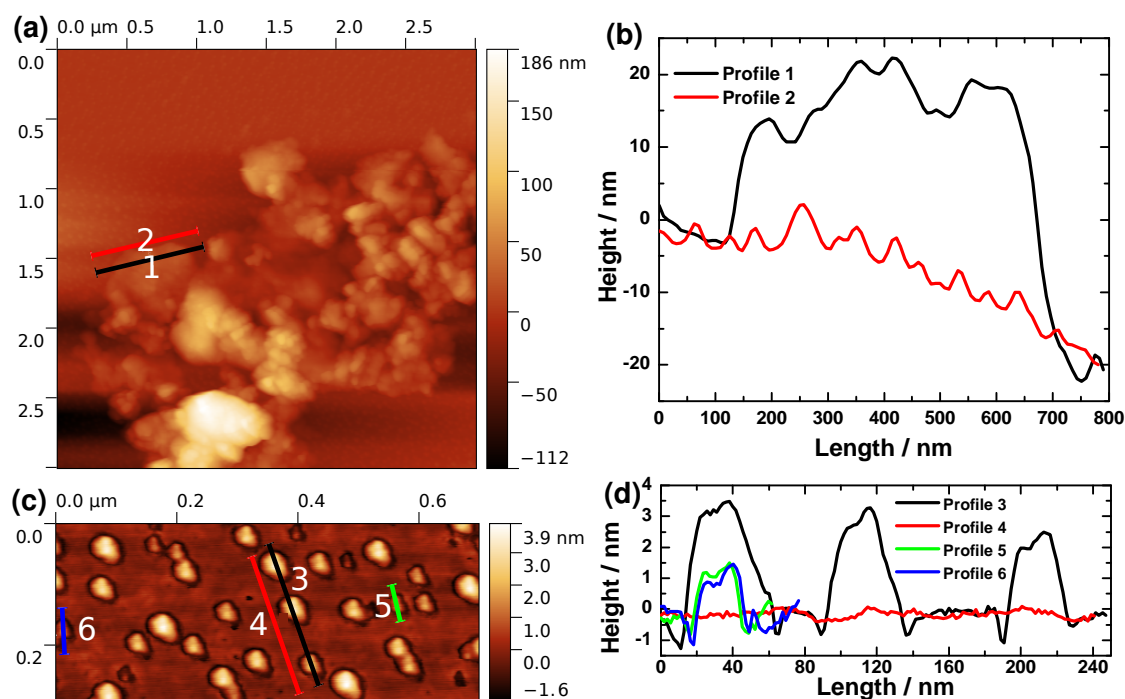


Figure 5.26: AFM of 500 h melon sample on silicon wafer. **(a)** Overview image showing aggregated carbon nitride surrounded by small particles. **(b)** Height profiles from (a). **(c)** Close-up of nanoparticles with average dimensions of 40 nm × 40 nm × 2 nm. **(d)** Height profiles from (c).

## 5.16 Photoactivity
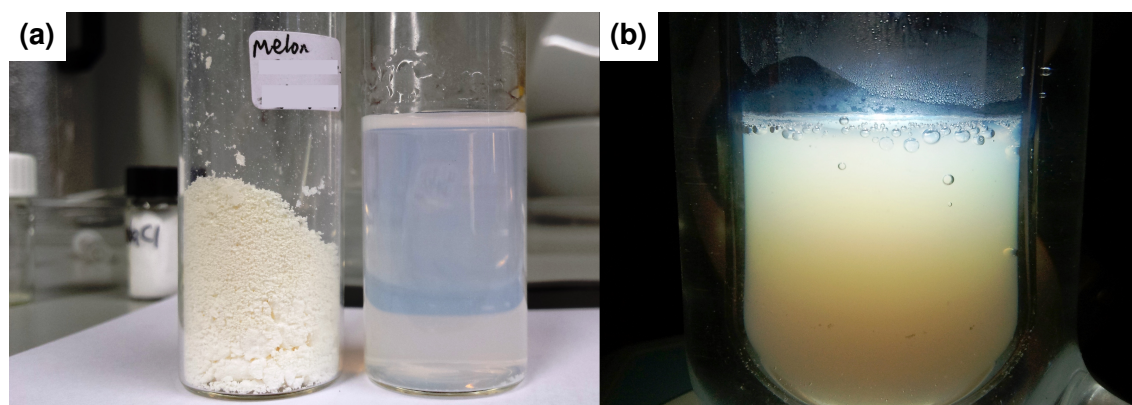


Figure 5.27: Photos of photocatalytic preparations. **(a)** 500 h white melon powder, 510 °C calcination and a 2.5 µg mL$^{-1}$ colloid of white melon after 12 h ultrasonication and **(b)** hydrogen bubbles evolving under illumination with TEoA as electron donor and Pt as cocatalyst.

Figure 5.28 shows photocatalysis results for the hydrogen evolution from water using triethanolamine as sacrificial electron donor and Pt as cocatalyst. Samples are illuminated under standard AM1.5-Global conditions using a transmission filter and adjusting the intensity to 100 mW cm$^{-2}$.

As can be seen in Figure 5.28**(a)**, the 500 h sample produces more H$_2$ compared to the other samples. This is surprising because its lack of visible absorbance would suggest it is unsuitable for visible light photocatalysis. Table 5.8 summarises and compares the hydrogen evolution rates from 5.28**(a)**. The 500 h sample performs best in the initial hour of the reaction with a six times higher production rate compared to the others. However, this rate decreases over time and after 24 h illumination time, all samples show a similar H$_2$ evolution rate of 2 µmol h$^{-1}$.

Since the production rates are not linear, it is informative to look at the rates in more detail. Examining the derivative curve 5.28**(b)**, we see that in the first six hours, the 200, 400 and 500 h samples experience an almost constant decrease in the H$_2$ evolution rate. The 48 h and the 300 h samples are not affected by this rate decrease but show a stable H$_2$ production rate of 4.5 µmol h$^{-1}$. The decreasing derivative rate is 4 µmol h$^{-2}$ for the 500 h sample and 0.2 µmol h$^{-2}$ for the 200 h sample, for the first six hours. Experimental parameters such as stirring, illumination conditions, oxygen, instrumental errors could not account for this rate and it is therefore assumed that it is intrinsic to the samples. However, these suggestions are tentative and it remains unclear why the 48 h and 300 h samples are unaffected. The hydrogen rate appears to stabilise from 6 h to 9 h reaction time for all samples, although there is still a decrease in the rates.
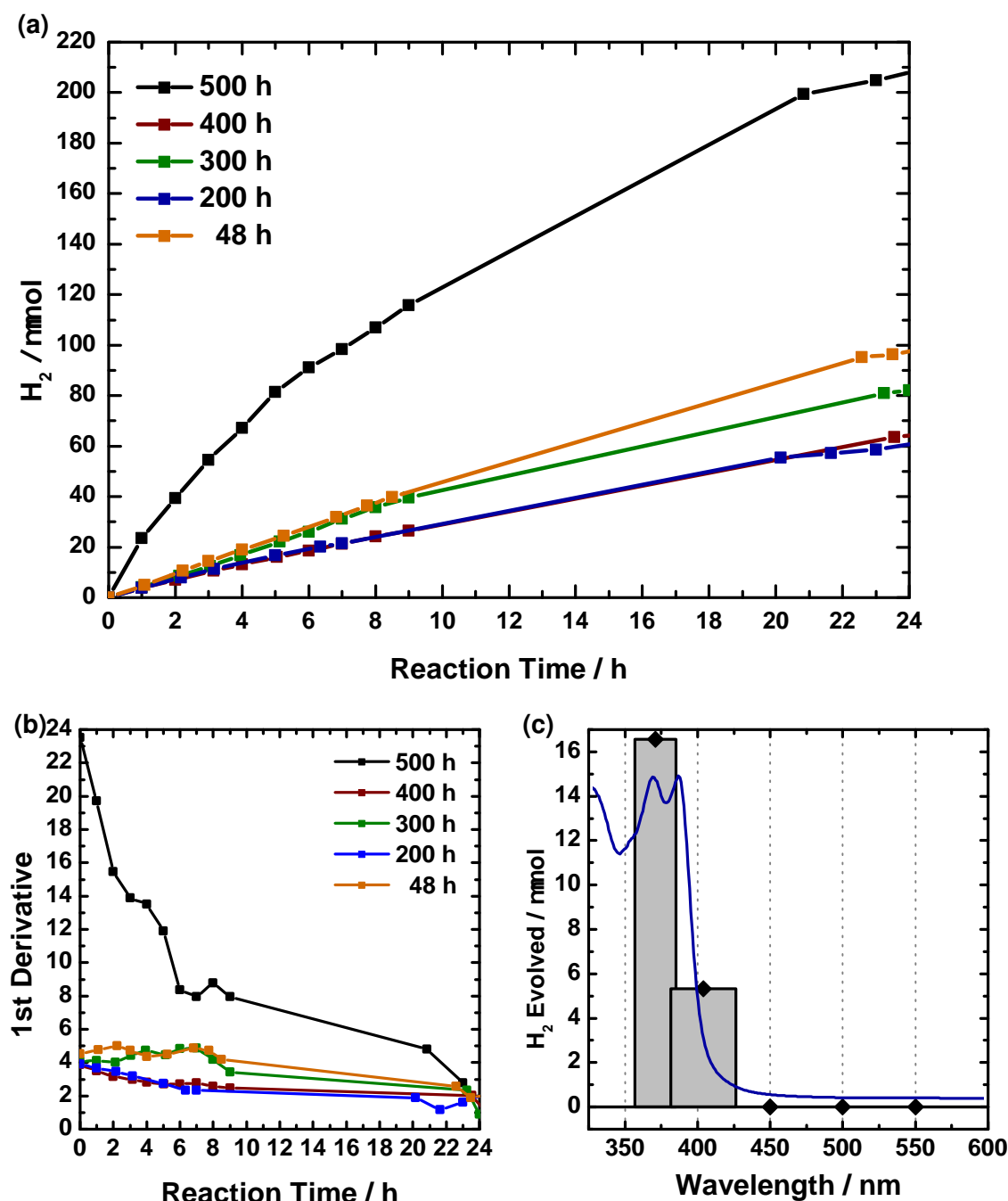
Figure 5.28: **(a)** Hydrogen evolution reaction of 200 h to 500 h calcined samples for 24 h illumination in AM standard conditions. **(b)** First derivative of (a) highlighting the changes in evolution rates. **(c)** Wavelength-dependent hydrogen evolution overlaid with the colloid absorption. Colloids were ultrasonicated for 15 min with 10 vol% TEoA as electron donor and 2.4 wt% photo-reduced Pt. AM1.5G illumination conditions at 100 mW cm$^{-2}$.

If we examine the relationship between BET surface area and $H_2$ evolution, we see that there is a 2.3 times increase in surface area from the 300 h to the 500 h sample. This corresponds to a 4 times increase in the $H_2$ rate.

The wavelength-dependent $H_2$ evolution or *action spectrum* is provided in Figure 5.28(c). The width of the columns represents the transmission width of the filters used. The hydrogen evolution coincides with the absorption spectrum as expected. No $H_2$ is detected between 430 nm to 520 nm. This suggests the 500 h sample is not active under visible light for hydrogen evolution. Hence, the higher evolution rate under AM conditions is surprising since the UV contribution is only $\approx 5\,\%$.
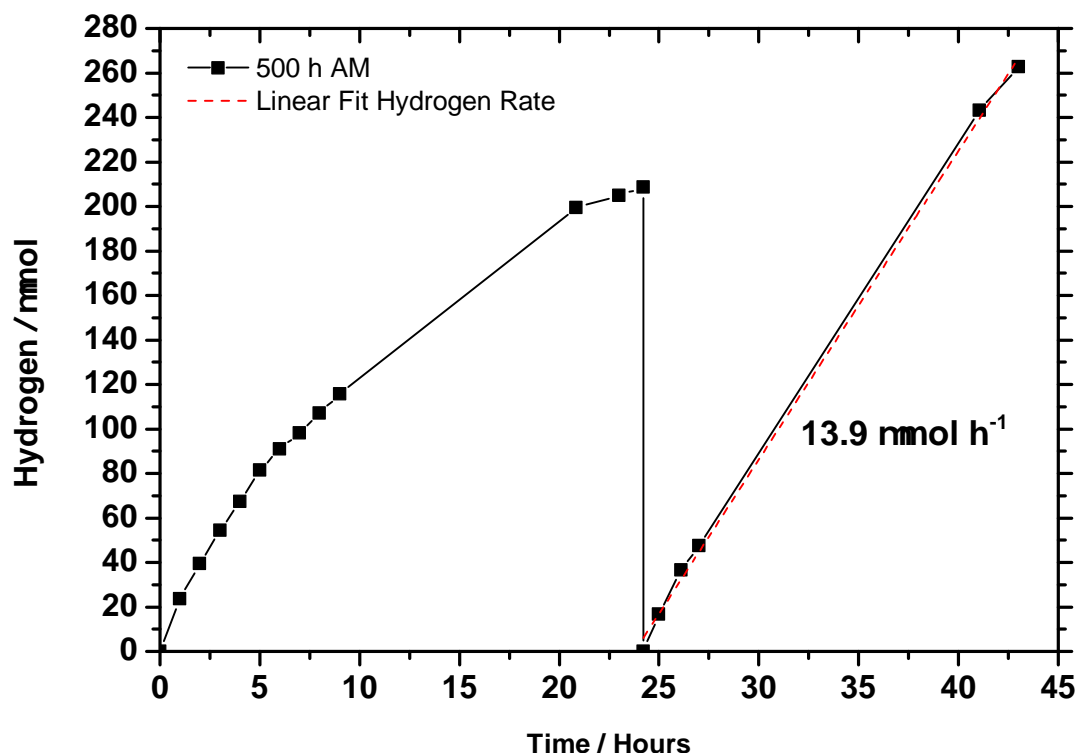


Figure 5.29: Second illumination cycle of 500 h melon showing a stabilised hydrogen evolution rate of 13.9 µmol h$^{-1}$. Argon purging was carried out for the second illumination cycle with no other alterations. AM standard illumination conditions.

Table 5.8: Summary of photocatalytic hydrogen evolution rates from Figure 5.28(a).

| Calcination Time hours | Average $H_2$ Rate µmol h$^{-1}$ | Photonic Efficiency % | $H_2$ Rate per Gram µmol h$^{-1}$ g$^{-1}$ |
|---|---|---|---|
| 500 | 13.90 | 0.83 | 4704 |
| 400 | 2.68 | 0.14 | 774 |
| 300 | 3.42 | 0.14 | 814 |
| 200 | 2.52 | 0.14 | 784 |
| 48 | 4.09 | 0.16 | 904 |

The colloid concentration dependence in Figure 5.30(a) was carried out with full spectrum illumination. At low concentrations, there is a linear increase in hydrogen evolution as expected. At a concentration of $1\,mg\,mL^{-1}$, the rate has already plateaued. Assuming a linear increase in $H_2$ production with increasing concentration and assuming that the $H_2$ production already saturates at $1\,mg\,mL^{-1}$, we estimate the saturation point to be between $\approx 0.2\,mg\,mL^{-1}$ and $0.4\,mg\,mL^{-1}$. For this reason, a concentration of $0.5\,mg\,mL^{-1}$ was chosen for the photocatalysis experiments as recommended.[104]

The hydrogen evolution with full spectrum illumination for the 200 h to 500 h samples is shown in Figure 5.30(b). Again, the 500 h sample out-performs the other samples by nearly four-fold.

Figure 5.30(c) compares the hydrogen evolution of 500 h ULT melon and the +48 h recalcined melon. Both materials show the same hydrogen evolution rate under the same conditions. In Figure 5.30(d), we compare the electron donors TEoA and MeOH. TEoA produced four times more hydrogen compared to MeOH under the same conditions ($> 420$ nm illumination, $745\,mW\,cm^{-2}$, MeOH buffered with phosphate buffer).

Considering these results, white melon samples produce a four-fold increase in hydrogen evolution rates compared to their less calcined counterparts.
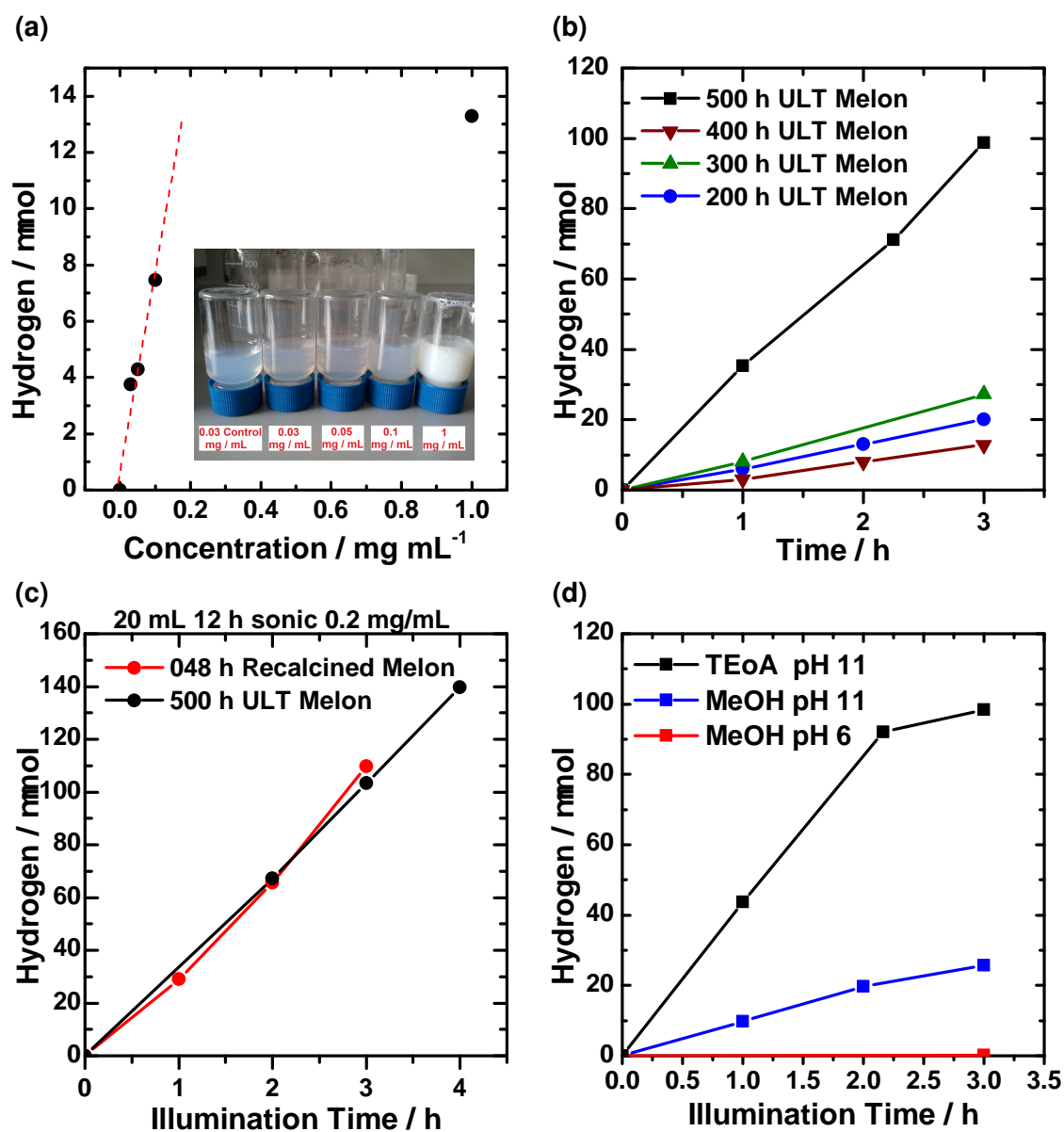
Figure 5.30: **(a)** H$_2$ concentration dependence (full spectrum). **(b)** H$_2$ evolution of 200 h to 500 h samples under full spectrum illumination and **(c)** a comparison of 500 h ULT vs. +48 h recalcined melon. **(d)** TEoA Vs. MeOH as electron donors ($>420$ nm illumination, 745 mW cm$^{-2}$, MeOH buffered with phosphate buffer.

## 5.17   Discussion on White Melon

This chapter has examined the synthesis of carbon nitrides at extended calcination times and discovered an interesting CN material named *white melon*. This white melon shows the same chemical structure of polymeric melon commonly found in the literature as 'g-C$_3$N$_4$' with an in-plane crystal structure as that reported by Lotsch et al.[22] We showed that 500 h white melon is chemically identical to the crystalline melon as proven by FTIR, EA, PXRD and NMR analysis. The defining features of white melon are its increased crystallinity, porous and sheet-like morphology, wider band gap, well-defined optical spectra and colloidal stability. The following sections provide a deeper discussion of the results presented.

**Calcination temperature:**   510 °C was chosen as the reaction temperature because it is high enough for the condensation reaction to proceed yet low enough to reduce sample loss through democposition into volatiles or carbonisation. This can be further understood by observing that 510 °C lies just before sample loss begins in a TGA curve.[70]

**Calcination time:**   Although temperature and atmosphere are more influential on the synthesis of carbon nitrides, the synthesis time was chosen to be studied in this work. The exceptionally long time of 500 h is not considered necessary to form the white melon material. The synthesis time has been successfully reduced to 60 h by scaling down the reaction (from 30 g melamine to 10 g melamine), using smaller crucibles. Although it may seem obvious, it was difficult to obtain the white product at smaller scales since it was obtained just before complete sublimation. There was a narrow time-frame between uncondensed melon and fully subliming the material. The reproducibility of the 500 h calcination time also varied ±48 h possibly due to slight variation in the furnace temperatures. Reducing the synthesis time further was also achieved by the recalcination method discussed below.

As can be seen from the summary graphs on page , there is a trend for calcination times for the PXRD data, surface area and band gaps. However, the data shows that the 400 h sample breaks the calcination time trends for these measurements. It is proposed that the 400 h sample is, in reality, less condensed than the 300 h sample. This is possible if the target temperature of 510 °C was not reached during the synthesis resulting in a slower condensation reaction. Slight variations in temperature can dominate the condensation process in carbon nitrides.

**Evolved gases:**   From the MS study of gas evolution during condensation, there is a vigorous reaction stage within the first 3 h, marked by a pulse of expelled gases. After this stage, there is a continual evolution of gases to the end of synthesis.

$CO_2$ evolution is indicative of an oxidation process and this is supported by the consumption of oxygen over the same time frame. The dip in $CO_2$ evolution is remarkable and may be key to identifying the main reactions involved. The most likely proposal for the dip in $CO_2$ is the reaction with $NH_3$. Loss of carbon through $CO_2$ evolution may be central to the lack of carbonisation in these materials, resulting in the yellow-white colour observed. Also, the loss of oxygen through $CO_2$ and/or NO may be the key to the sustained condensation reaction.

D. J. Martin et. al[71] performed TGA-DSC-MS analysis on urea and also observed $CO_2$ evolution throughout the reaction. They claim that this is due to the presence of oxygen in urea. They also claim the presence of formaldehyde ($CH_2O$) at m/z = 30, whereas we claim this to be NO. Their suggestion is that CO undergoes hydrogenation to form $CH_2O$, thus releasing the N to covalently bind to higher condensation products such as melamine. Martin et al. claimed that the high hydrogen evolution was linked to low proton/H content in their CNs. However, the hydrogen content in their material was high, ranging from 16 – 18 % compared to < 2% in this work. Examining the H-content of our ULT CNs, we see that there is no change in H-content or link to photoactivity.

**Oxygen:**  It is clear that oxygen is consumed throughout the synthesis time, it is also clear that oxygen is not a main constituent of the obtained CNs (impurity levels only). The synthesis conditions were recreated under argon and under argon/oxygen atmospheres, by assembling a tube furnace and gas lines. Unfortunately, due to the limited amount of precursor that could be placed in the quartz tube, attempts to create the ULT or white melon samples only resulted in uncondensed melamine or fully sublimed carbon nitride.

Although the oxygen content of all samples is very low, there is evidence that the O-content from EA decreases with calcination time and this is supported by XPS analysis (see page 100). Assuming oxygen is present as an impurity, it makes sense that the O-content decreases as crystallinity increases, removes defects and increases structural order.

Carbonisation or, put simply, burning of defect sites is often observed at high synthesis temperatures, oxygen atmosphere or carbon doping.[105] Carbonisation leads to browning of the photocatalyst—which may improve absorbance to some degree–but generally destroys the semiconductor band gap. It is interesting that carbonisation is not a problem in the ULT samples, which is again suggestive of oxidative removal of carbon.

**Morphology:**  The morphology of white melon is interesting. During synthesis, the powder transforms from a coarse yellow cake (300 h) to a fluffy white 'foam' (500 h).

Grinding the yellow melon in a mortar requires crunching the particulates. Grinding the white melon is soft with a similar texture to talc powder. In this regard, talc ($Mg_3Si_4O_{10}(OH)_2$), graphite and molybdenum disulfide ($MoS_2$) are also known as dry lubricants. This application derives from the weak bonding between the sheets at the molecular level. From SEM, we see that white melon is composed of broken sheets of CN. These sheets appear to be composed of inter-connected platelets.

It is surprising to note that during the synthesis, the volume of white melon expands considerably ($\approx$ 130 vol%). The less condensed samples show a loss in volume accompanied with the loss of weight, as expected. It is estimated to be eight times less dense than the melon reference by comparing their macroscopic mass and volume measurements and this is supported microscopically by the BET surface area physisorption measurements. The white melon powder also appears to be charged as the particles disperse from each other when disturbed.

**Crystallinity:** White melon shows a high degree of crystallinity, especially since carbon nitrides synthesised in air are amorphous. Evidence of this crystallinity is seen in the selected area diffraction spots in TEM, in-plane reflections in PXRD and increased structural order observed in the IR and NMR spectra. It is understood that this crystallinity increases linearly with calcination time and follows the trend of decreased inter-layer spacing (*d*-spacing) as seen from PXRD and the decreasing FWHM of the normalised *d*-spacing peak (corresponding to increasing Scherrer crystallite size estimation).

**Optical properties:** The 500 h ULT melon and the +36 h and +48 h recalcined samples have been named white melon because of their distinctive appearance. They are in fact yellow-white, or similar to fresh cream in colour. The yellow component is unsurprising, considering that most CNs are yellow. Ironically, white melon may provide the origin of the yellow colour of carbon nitrides. White melon samples show a miniscule absorbance peak at 560 nm. Although small, it marks the edge of the yellow light region (570 nm to 590 nm) which is predominantly reflected. The proposed inter band gap state did not produce measurable amounts of hydrogen when illuminated with a 550 nm transmission filter and so is considered photocatalytically inactive. Furthermore, the photoactivity is not linked to the changing band gap.

Most distinctive is the emergence of peaks in the reflectance and luminescence spectra. Chen et. al.[106] also observes some of the new absorbance and PL peaks which were seen in white melon. In contrast to our white melon, their presumably buckled melon has a strong absorbance in the visible due to a transition at 480 nm which produces an orange photocatalyst. It is suggested that high crystallinity is the property that links these two materials. Their synthesis is simple with a two-stage

oven ramp. The first is at 400 °C for 1.5 h and then to 700 °C for 2 h. This was done in $N_2$ atmosphere instead of air.

Scattering was studied for white melon considering the importance of the colloid. Tyndall scattering was confirmed and an attempt to measure the scattered light showed a 403 nm blue light peak overlapping with the absorption.

**Recalcined melon:**  This material produced by a two-step synthesis, is identical to the 500 h ULT melon by FTIR, EA and PXRD analysis and hydrogen evolution reactions. It also provides more control over the formation of white melon. In the ULT samples, the white melon is only found after 500 h calcination whereas, the recalcined samples show the same characteristics after just +48 h calcination. Recalcined melon shows more control over the optical properties since a gradual emergence of the absorbance peaks emerges from +12 to +48 h recalcination. The +36 h is considered to be similar in properties to the 500 h melon in this regard. The +48 h is 'overbaked' with loss of weight to sublimation/decomposition and there is no change in band gap from +36 h to +48 h.

Since both the ULT and Recalcined synthesis methods yield the same product, it is evident that the long calcination times are not necessary to produce white melon. Air is necessary and the first calcination step is important to precondense the melamine.

**Dispersibility:**  The importance of the colloid formation should not be underestimated. It is remarkably difficult to dissolve or disperse CN materials. White melon easily forms a stable colloid in a one-step synthesis reaction. The specific surface area as measured by BET gas sorption analysis, is not the true surface area of a photocatalyst/water interface during the hydrogen evolution reaction. It is understood that the colloid must have a considerably high contact surface area compared to the less condensed samples because of its ability to easily disperse in water. However, no measurements to quantify dispersibility could be taken. To shed some light on this issue, particle sizes, concentration dependencies and zeta-potential measurements were made. The reason that white melon can disperse so easily is evident in the SEM images. For 500 h melon, the CN microsheets are broken up into smaller platelets. This is more evident in the 500 h sample compared to the less condensed species.

**Photoactivity:**  The enhanced visible light photoactivity of white melon compared to the other samples is a surprise. Firstly, because the low absorbance at short wavelengths should produce much less charge carriers compared to the other samples. The 500 h sample has the lowest absorbance yet the highest photoactivity. This is

contrary to what is expected and suggests the enhanced activity of the 500 h is not dominated by absorbance.

The chemical structure of white melon is identical to the melon references and photoactivity does not increase linearly with crystallinity as was assumed it would. We presume that crystallinity follows the trend for the decreasing FWHM of the normalised *d*-spacing peak, as discussed above and shown in Figure 5.31**(a)** below. However, the photoactivity trend **(c)** is relatively constant until the 500 h sample. This tells us that crystallinity is not the dominant factor in the 500 h samples enhanced photoactivity. As can be seen in the summary graphs, Figure 5.31**(d)**, the specific surface area by the BET method does not follow the trend for photoactivity either. Since it is shown that absorbance, BET surface area and crystallinity do not dominate the trend for photoactivity, it is proposed that another factor might explain the hydrogen evolution trend.

The high dispersibility of the colloid may be the unrecognised parameter with its high effective surface area from the well dispersed and small 40 nm particles. This would enhance the albeit low absorption and it may also enhance absorption through multiple scattering events. This is supported by the fact that white melon is surprisingly active at concentrations as low as 2.5 $\mu g\,mL^{-1}$. In reality, many factors contribute to the hydrogen evolution trend and it is difficult to assign any one parameter as the dominant factor.

Evidently, the photoactivity of white melon is suited to UV illumination. The same hydrogen evolution trend for calcination time was observed in UV, visible and full spectrum illumination.

The experimental conditions of the photocatalytic reactions are also important to consider. TEoA was chosen for the majority of experiments because of its good performance and common usage. However, its use is controversial. Oxidised TEoA has many unknown products which may interfere with the photocatalytic reaction.[107–109] It is also light sensitive and turns from transparent to light-yellow over time. This coloured TEoA absorbs light in the reaction and hampers the calculation of photonic efficiencies. TEoA is highly alkaline at pH 11. Thus, high ionic concentrations of pH buffer would be required to compensate for this.
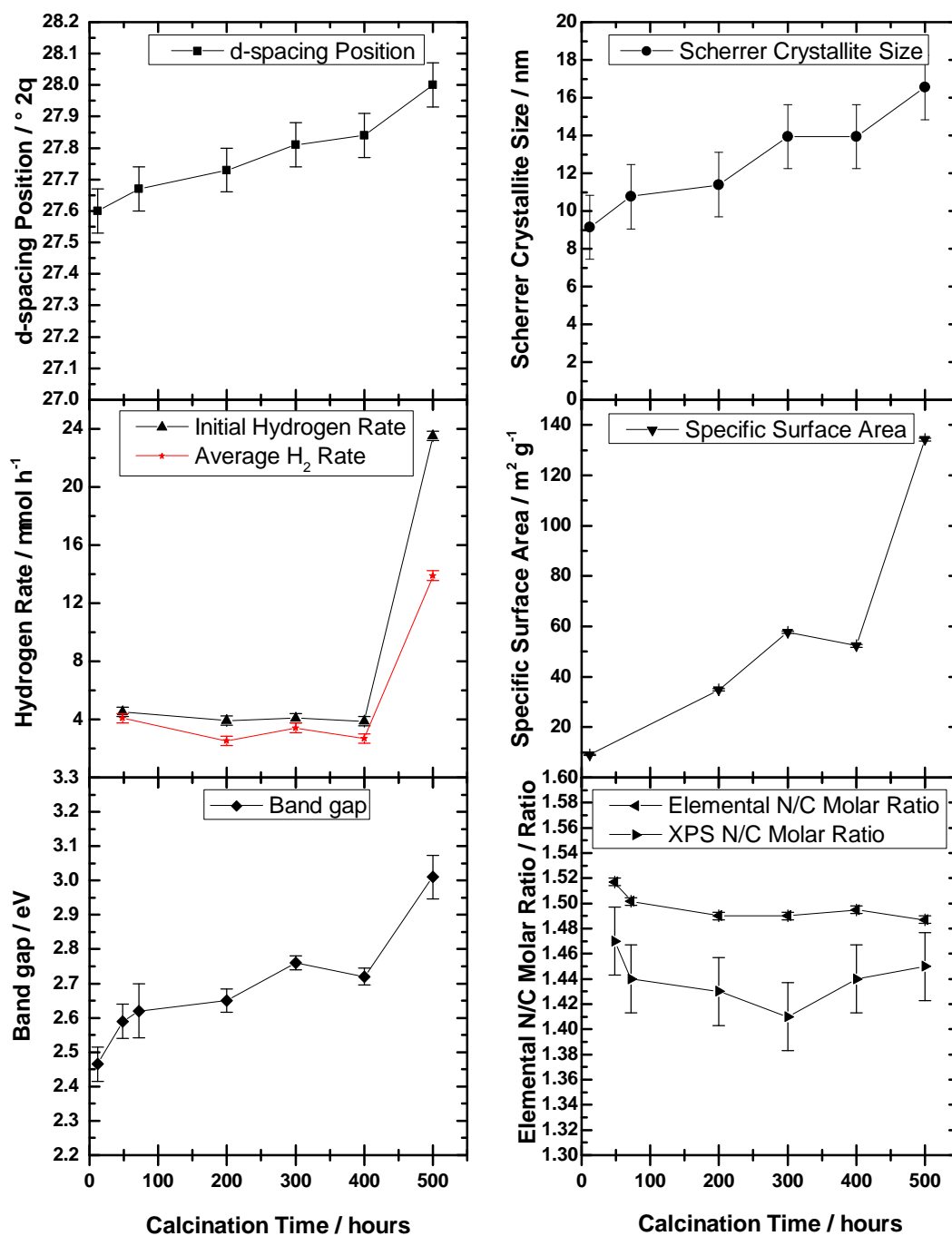
Figure 5.31: Summary graphs of important photocatalyst parameters and their dependence on the calcination time.

## 5.18   Summary of White Melon Chapter

An old carbon nitride has been reinvestigated because of its recent interest as a light-element photocatalyst. White melon carbon nitride has been synthesised from melamine in a half-open crucible in a muffle furnace at 510 °C for 500 h. Initially, the material was only obtained at long calcination times and with large amounts of starting material. Recalcination was shown to produce the same material at much shorter calcination times. White melon is the most crystalline CN synthesised in an open air system. A decreased $d$-spacing of the nanosheet layers and the fluffy texture provide the ability to easily disperse in $H_2O$. White melon shows enhanced photocatalytic performance for water reduction to $H_2$ compared to other CNs synthesised under the same conditions, despite its poor visible light absorption.

# Chapter 6

# Conclusions

In conclusion, this work laid the foundation for photocatalysis research in the Lotsch group, establishing the photocatalysis setup and it explored a range of photocatalytic methods and materials. We have set up a versatile photocatalysis laboratory and made valuable contributions to carbon nitride chemistry and the understanding of photocatalytic systems.

The first five aims of this thesis were to establish the photocatalysis lab, as mentioned in the introduction. This has been successfully achieved as we now have a functional, well-equipped laboratory and have successfully contributed to the field with a number of publications by the photocatalysis subgroup.[70,77,110–113] This work had a broad scope of interest covering many areas of photocatalysis and many material types. The next aims of this thesis involved the investigation of both triazine and heptazine-based carbon nitrides as photocatalysts. Focusing on carbon nitrides, we have made specialised discoveries such as the performance boost of doped PTI and the interesting optical and colloidal properties of white melon.

In the first chapter, a short introduction with an overview of solar energy, photocatalysis and carbon nitrides is given. The second chapter introduces the theory behind the calculation of photonic efficiency and the calculation of the band gaps from diffuse reflectance data.

In the third chapter, the photocatalysis setup is described extensively with the equipment used as well as the procedures and methods. Detailed figures describe the experimental configuration including the light sources, light filters, power meters and gas-tight reactors. The next section details the gas chromatography background theory and setup with the custom built GC, columns, and dosing system. The TCD detector is then explained and finally the resulting chromatogram of the GC and its timing events are listed. Section 3.5 provides the relevant background and experimental information for the MS unit including how it was used in different operating modes. The experimental chapter was given in great detail, not only because this was the first description of the setup, but also because the equipment was chosen with great flexibility and adaptability in mind: for example, the choice of xenon lamps instead of solar simulators, the optional He carrier gas for hydrocarbon analysis by GC or the flexibility and mobility of the MS unit. This flexibility, although sometimes inconvenient, can address the specific challenges otherwise unavailable, allowing creative solutions to difficult problems and providing powerful new techniques. With regards to the procedures and calculations, the best efforts were made to comply with recommendations and standards, although, since there are no widely accepted standards, these procedures are still in active development.

Chapter 4 presents the results of the first photocatalytic tests on triazine carbon nitrides with the accompanying publication. We have demonstrated the first

photocatalytic measurements of triazine-based carbon nitrides. We showed that doping of PTI significantly enhances the photocatalytic activity. We also compared crystalline and amorphous PTI for wavelength specific hydrogen evolution. The long-term stability of this photocatalyst remains a concern and this was discussed in more detail. There have subsequently been many publications on triazine-based CNs and on PTI in particular.[114–116]

Chapter 5 looks at heptazine carbon nitrides, especially focusing on the calcination time and its influence on the structural, colloidal, optical and photocatalytic properties. The synthesis methods for carbon nitride powders are listed at the start of the chapter. Then, the default procedure for preparing photocatalytic suspensions for $H_2$ evolution is outlined. A detailed chemical analysis is provided and the resulting photoactivity of ULT melon is investigated. 'White melon' is an unusual carbon nitride which provides valuable insights into carbon nitride synthesis and the photocatalytic activity of colloids. We see from the discussion that the enhanced $H_2$ evolution does not only depend on the absorption or specific surface area, but is more likely dominated by the environmental conditions created by the CN colloid, high crystallinity degree and the optical properties.

This work has significance for the understanding of carbon nitride chemistry and the formation of CN materials in air. We also provide new perspectives for the key parameters of photocatalytic action, highlighting that high absorbance is not essential for photoactivity and drawing more attention to the particle sizes and dispersibility of the photocatalysts. As the established equipment and procedures form the foundation for the future development of the photocatalysis subgroup, a detailed experimental description is provided in this thesis. This is essential for understanding the measurements, and more importantly, where they can be improved.

The development of photocatalysis is an exciting and rapidly developing research topic that can have profound new applications for energy, the environment, optoelectronics and green chemistry as long as the requirements for the photocatalysts are met. The results from this thesis show that carbon nitrides are light-element photocatalysts that can meet these requirements.

# Appendix A

# Appendix

## A.1   Details of Purchased Chemicals

Purchased chemicals were of a high purity research grade and used without modification. TEoA turned from transparent to light beige colour after 2 to 4 months. TEoA purity: ethanolamine $\leq 0.1$ % (by GC), water $\leq 0.2$ %.

Table A.1: Supplier and chemical details of purchased chemicals.

| Name | Formula | CAS No. | $M_w$ (g Mol$^{-1}$) | Supplier | Purity % |
|---|---|---|---|---|---|
| Chloroplatinic Acid | $H_2PtCl_6$ | 18497-13-7 | 409.81 | Sigma-Aldrich | 99.9 |
| Triethanolamine | $C_6H_{15}NO_3$ | 102-71-6 | 149.19 | Alfa Aesar | 98 |
| Silver Nitrate | $AgNO_3$ | 7761-88-8 | 169.87 | Merck | 99.8 |
| Sodium Persulfate | $Na_2S_2O_8$ | 7775-27-1 | 238.10 | Sigma-Aldrich | 98 |
| Titanium Dioxide | $TiO_2$ | 13463-67-7 | 79.87 | Sigma Aldrich | 99 |
| Methylene Blue | $C_{16}H_{18}N_3SCl$ | 61-73-4 | 319.85 | Sigma Aldrich | – |
| Melamine | $C_3H_6N_6$ | 108-78-1 | 126.12 | Carl Roth | 99 |
| Dicyandiamide | $C_2H_4N_4$ | 461-58-5 | 84.08 | Acros | 99.5 |

## A.2  Equipment Specifications

**Gas-tight GC syringes:** 10 and 1 mL gas-tight syringes from Hamilton, Australia. These were used to inject evolved $H_2$ into the GC before the online system was established.

**Blue vials with PTFE septa for $H_2$ evolution:** Borosilicate glass vials with silicone/PTFE septa from Chromacol, UK (EPA quality), natural silicone with PTFE coating on one side, 3.2 mm thick, 45° shore, hardness A.

**UV Lamp:** Konrad Benda NV-6 KL, $2 \times 6$ W. 254 and/or 365 nm radiation.

**Xenon Lamps:** Newport Corp. (USA): Model: 66985 Xe/Hg(Xe) research source, borosilicate crown, 2.7 inch collimated output, F/0.7, 3 inch accessory series. Xenon bulbs: L2480 from Hamamatsu (Japan) 300 W, guaranteed lifetime 1000 h, arc length 3 mm.

**Si-diode:** Si227-66BR (Hamamatsu) 100 $mW\,cm^{-1}$. 11.6 µA. Reverse voltage: 5.0 V. Spectral response 320 nm to 1000 nm. High UV sensitivity.

**Light intensity meter:** The S310C thermopile-based power meter from Thorlabs (USA) was used to determine the total incident power. The broadband coating ensured a flat spectral response across the UV-Vis range providing wavelength-independent power measurements. The power range was 0.01 W to 10 W and the operating wavelength range was 0.19 µm to 25 µm. The circular aperture size was ⌀ 20 mm and metal fins provided passive cooling for the sensor head.

**FTIR – Fourier Transform Infrared Spectra:** Infrared vibration spectra were recorded on a Perkin Elmer Spektrum BX II spectrometer with an attenuated total reflectance (ATR) unit made of diamond.

**DLS – Dynamic Light Scattering:** Dynamic light scattering using the Zetasizer Nano ZS from Malvern Instruments Ltd. (Worcestershire, UK) was used to estimate particle sizes and particle zeta potential. Plastic cuvettes were used with an equilibrium time of 120 s. An average of three measurement runs consisting of ten measurements each were taken as the result and compared with other samples.

**PXRD – X-ray Powder Diffraction:** X-ray powder diffraction experiments were carried out on a Stoe diffractometer in Debye-Scherrer mode with a linear PSD detector. Ge(111) monochromatised Cu-K$\alpha_1$ radiation ($\lambda = 1.54051$ Å) was used as the radiation source. Samples were ground and placed in a 1 mm outer diameter capillary and transmission XRD spectra were typically taken from 4° $2\theta$ to 40° $2\theta$, 0.1 stepsize.

**Sonication:** Ultrasonication of photocatalyst powders used an Elma S 100H Elmasonic with an ultrasonic frequency of 37 kHz and an ultrasonic RMS power of 150 W. Typical sonication times were 5 to 30 min and samples were sonicated before addition of electron donors or cocatalysts.

**Gas Sorption:** Argon at 87.4 K was used with an Autosorb iQ surface analyzer (Quantachrome Instruments,USA). Samples were outgassed in a vacuum $(10 \times 10^{-7}$ mbar) at 200 °C to 300 °C for 6 h to remove all guest molecules. Pore-size distributions were determined using the calculation model for Ar at 87 K on carbon (slit pore, QSDFT equilibrium model). For BET calculations, pressure ranges of the Argon isotherms were chosen with the help of the BET Assistant in the ASiQwin software. (0.12–0.27) $P/P_0$ range on adsorption.

**EA – CHN and O Elemental Analysis:** Elemental analysis (Elementar vario EL) of the elements C, H, N and O were measured by high temperature digestion coupled with dynamic gas components separation. Samples were burnt explosively at 1150 °C in a highly oxygenated helium atmosphere.

**TEM – Transmission Electron Microscopy:** Philips CM 30 ST with an accelerating voltage of 300 kV. The dissolved sample was deposited on a copper grid, coated with carbon and dried under an IR-lamp.

**SEM – Scanning Electron Microscopy:** Zeiss Merlin microscope with an accelerating voltage of 1.50 kV.

**AFM – Atomic Force Microscopy:** Measurements were performed on a diluted aqueous suspension of nanosheets and allowed to dry on a silicon substrate, using an Asylum MFP3D Stand Alone AFM (Asylum Research, Santa Barbara, CA) using a Si micro cantilever (300 Hz resonant frequency and 26.1 $N\,m^{-1}$ spring constant) operated in tapping mode.

**XPS – X-ray Photoelectron Spectroscopy:** High resolution X-ray photoelectron spectra were recorded with an AXIS Ultra spectrometer with Al, k$\alpha$ radiation (Kratos, UK). Charge compensation was used and the spectra were calibrated with the N-C-N peak at 288.2 eV due to the lack of an adventitious carbon signal. Gauss-Lorentz peak fittings were used in all fittings using the CasaXPS software.

**PL – Photoluminescence:** Fluorescence spectra were recorded with a Fluorolog® 3-22 fitted with double gratings for the excitation and emission. The source was a 450 W xenon lamp and the detector was a photo multiplier tube. Typically, an excitation wavelength of 280 nm with 1 sec integration time over 1 nm

step was used. Powdered samples were collected at a right angle from the incident light. Liquid samples were measured in quartz cuvettes. Calibration was performed by checking the water Raman peak at 397 nm.

**UV-Vis – Diffuse Reflectance:** UV-Vis spectra were recorded on an Agilent Technologies Cary 5000 UV-Vis-NIR spectrophotometer. Diffuse reflectance spectra were collected at room temperature with a 15 cm diameter integrating sphere (DRA 2500). Powders were prepared between two quartz discs and placed at the edge of the sphere. Spectralon® was used as the optically white standard. Band gaps were estimated using a modified Kubelka-Munk method as outlined in Section 2.4.1.

**MS – Real-time Mass Spectrometry:** Gas analysis timelines and bar-scans were recorded with the Hiden HPR-20/40 systems from Hiden Analytical (UK).

**Inlets:** Response time of 500 µs, 1.8 m capillary inlet at 250 °C, low-flow 4 cm$^3$ min$^{-1}$ or PDMS gas permeable membrane for gas analysis in liquids.

**Detector:** Quadrupole mass spectrometer (HAL 8 RC RGA 201), $m/z$ range of 1 to 200 amu with an oxide coated iridium filament. The software packages MASsoft 7 pro and QGA Pro were used in the data collection.

**GC – Gas Chromatography:** Thermo Fischer Trace Ultra GC with custom injection system from S&H Analytik GmbH (Mönchengladbach, Germany). Chromcard software. TCD detector linearity: 10$^6$, Columns: Poropak Q, Poropak R and 5 Å molecular sieve. See Table A.2 for details. Detector block temperature 200 °C, filament voltage 10 V. 25 mL min$^{-1}$ gas flow.

**Optical Spectrometer:** Optical spectra were recorded with an Ocean Optics USB2000+ spectrometer (Ocean Optics, FL, USA). Wavelength range 200 nm to 1100 nm coupled to a SMA 905 single-strand optical fiber.

**NMR – Nuclear Magnetic Resonance:** Solid State NMR was measured in collaboration with the group of Prof. Jürgen Senker at Universität Bayreuth by Maria Mesch. All ssNMR spectra were referenced relative to TMS ($^1$H, $^{13}$C) and nitromethane ($^{15}$N), respectively. $^{13}$C and $^{15}$N cross-polarization (CP) MAS-NMR spectra were recorded at ambient temperature on an AvanceII 300 solid-state NMR spectrometer (Bruker) with an external magnetic field of 7.1 T. The operating frequencies are 300.1 MHz, 75.4 MHz and 30.4 MHz for $^1$H, $^{13}$C and $^{15}$N, respectively. The samples were contained in 4 or 7 mm ZrO$_2$ rotors, which were mounted in a standard triple resonance MAS probe (Bruker) and the spinning speed was set to 5 kHz for $^{15}$N and 10 kHz for $^{13}$C measurements. The $^{15}$N measurements were acquired using a conventional CP

sequence with a contact time of 10 ms. For $^{13}$C measurements a CP sequence with a ramped-amplitude (RAMP) contact pulse[1,2] on $^1$H (the RF field was linearly varied about 50 %) and a contact time of 5 ms was used. During acquisition, broadband proton decoupling was carried out using SPINAL-64[3] with a nutation frequency of about 70 kHz. The recycle delay was set to 2 s.

$^1$H 1D and 2D MAS-NMR spectra were recorded at ambient temperature on an AvanceIII HD 600 solid-state NMR spectrometer (Bruker) with an external magnetic field of 14.1 T, operating at frequencies of 600.1 MHz and 60.8 MHz for $^1$H and $^{15}$N respectively. The samples were contained in 1.3 mm $ZrO_2$ rotors, which were mounted in a standard double resonance MAS probe (Bruker) and the spinning speed was set to 62.5 kHz. 1D measurements were carried out using a conventional Hahn-echo experiment.[4] $^{15}$N-$^1$H HETCOR spectrum was recorded using a D-HMQC pulse sequence.[5] To transfer polarization between the nuclei the supercycled symmetry based SR412 sequence was applied[6]. The t1 evolution was rotor synchronized using a dwell time of 128 µs and a recoupling time of 64 µs was chosen. The 2D $^1$H-$^1$H single-quantum-double-quantum (SQ-DQ) correlation spectra were recorded using a rotor-synchronized symmetry based R-sequence[6,7] R1225 in a excitation-reconversion-$\frac{\pi}{2}$-acquisition scheme. The R-block was implemented using 180° pulses and the phase cycling was performed with the conventional 16-fold phase cycle to select the required coherence pathway 0 ±2 0 −1. Recoupling times of 64 µs and 160 µs were chosen. The power for the R-sequence was optimised on the sample directly.

[1] A. Pines, M. G. Gibby, J. S. Waugh, *J. Chem. Phys.* **1973**, 59, 569–590.

[2] G. Metz, X. Wu, S. O. Smith, *J. Magn. Reson. Ser. A,* **1994**, 110, 219–227.

[3] B. M. Fung, A. K. Khitrin, K. Ermolaev, *J. Magn. Reson.* **2000**, 142, 97–101.

[4] R. S. Hartmann, E. L. Hahn, *Phys. Rev.* **1962**, 128, 2042–2053.

[5] Z. Gan, *J. Magn. Reson.* **2007**, 184, 39–43.

[6] A. Brinkmann, A. P. M. Kentgens, *J. Am. Chem. Soc.* **2006**, 128, 14758–9.

[7] M. H. Levitt, *Encycl. NMR,* **2002**, 9, 165–196.

[8] P. E. Kristiansen, D. J. Mitchell, J. N. S. Evans, *J. Magn. Reson.* **2002**, 157, 253–266.

[9] T. Gullion, *Concepts Magn. Reson.* **1998**, 10, 277–289.

## A.3   GC Technical Details
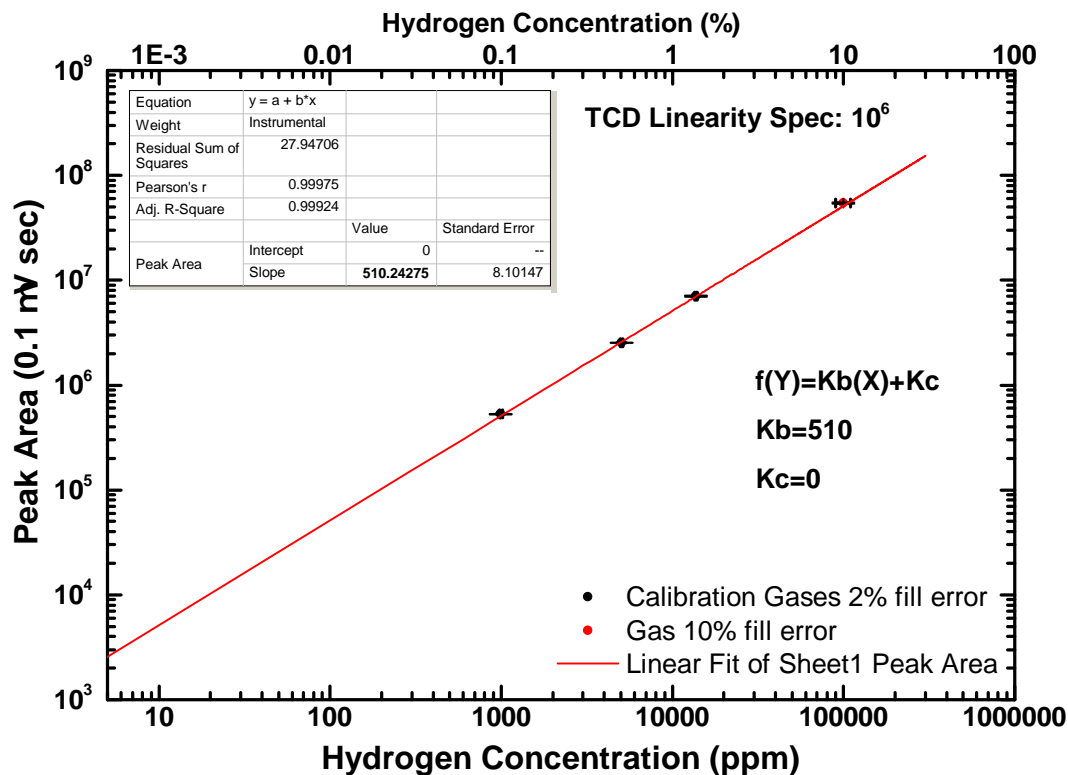


Figure A.1: H$_2$ calibration curve for GC in argon carrier gas.

Table A.2: Separating column specifications for the Trace GC Ultra.

| Name | Diagram Label | Mesh Size* | Outer Diameter (inch) | Length (m) | Comment |
|---|---|---|---|---|---|
| Poropak Q | S1 | 80/50 | 1/8 | 1.0 | Stripper Column |
| Mol. Sieve | S2 | 100/80 | 1/8 | 3.0 | 5 Å Sieve |
| Poropak R | S3 | 80/50 | 1/8 | 2.5 | Packed Column |

---

*Mesh size is the number of openings in one inch of grid, often used in industry. e.g. 80 mesh = 177 μm.
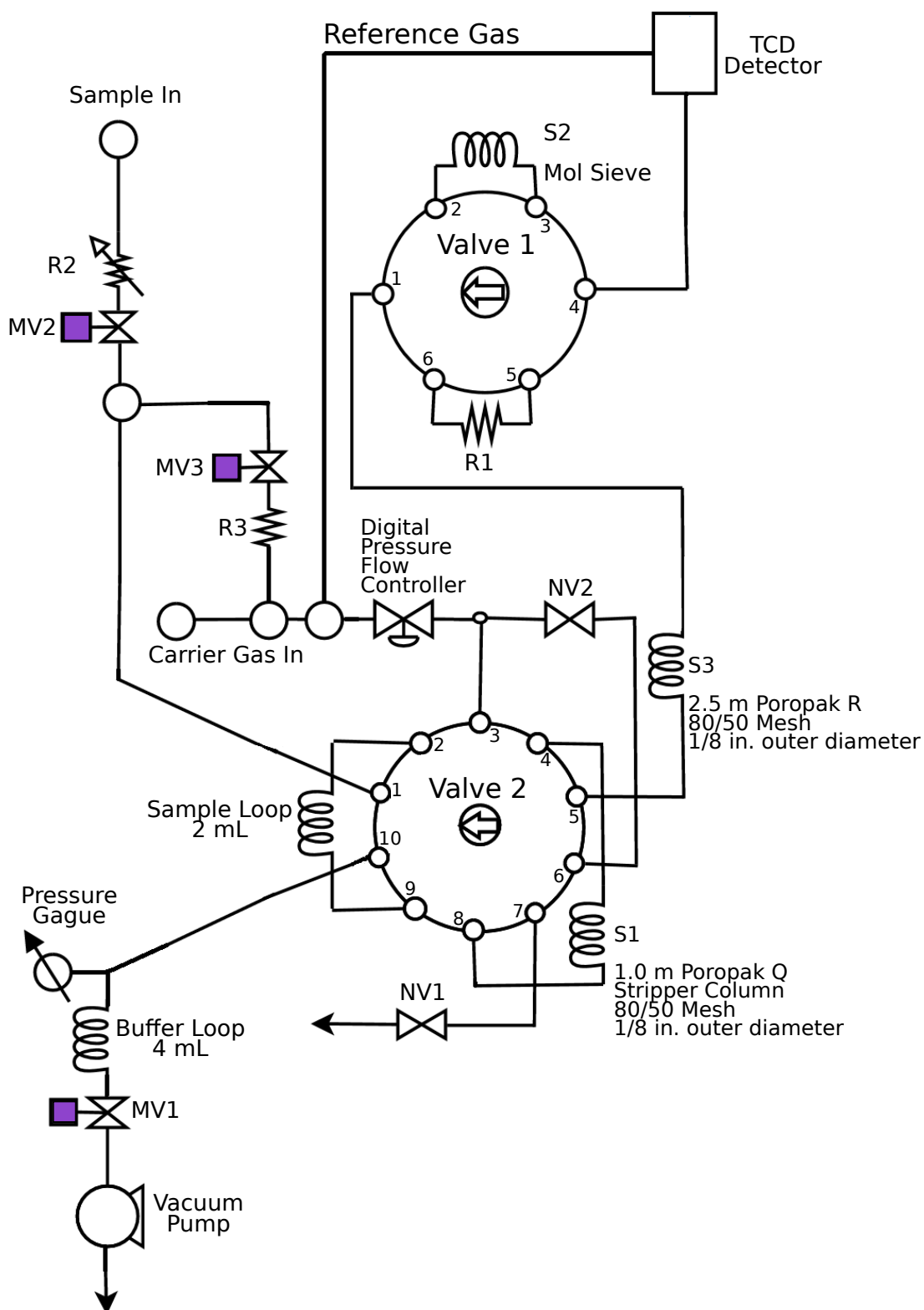
Figure A.2: Detailed GC component diagram adapted from technical notes. See Figure 3.13 for gas flow diagrams.

## A.4 Additional Support Data
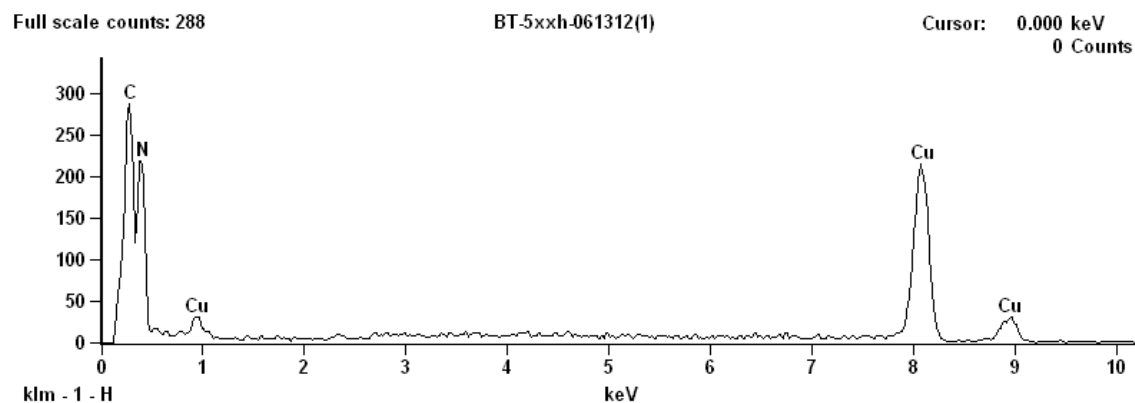


Figure A.3: EDX of 500 h melon on a copper grid substrate.

Table A.3: Summary of experimental parameters by calcination time.

| Calcination Time (hours) | Stacking Peak Position (° $2\theta$) | Stacking Peak Width (FWHM) | Surface Area ($m^2\,g^{-1}$) | Hydrogen Rate ($\mu mol\,h^{-1}$) | N/C Molar (Ratio) | Band Gap (eV) |
|---|---|---|---|---|---|---|
| 12 | 27.68 | 1.16 | 9.0 | 0.60 | 1.468 | 2.6 |
| 48 | 27.68 | 1.20 | - | 4.09 | - | 2.6 |
| 72 | 27.67 | 0.94 | - | - | - | 2.6 |
| 200 | 27.73 | 0.88 | 34.8 | 2.52 | 1.490 | 2.7 |
| 300 | 27.80 | 0.71 | 57.7 | 3.42 | 1.490 | 2.8 |
| 400 | 27.86 | 0.71 | 52.3 | 2.68 | 1.495 | 2.7 |
| 500 | 28.00 | 0.60 | 134.2 | 8.66 | 1.487 | 3.0 |
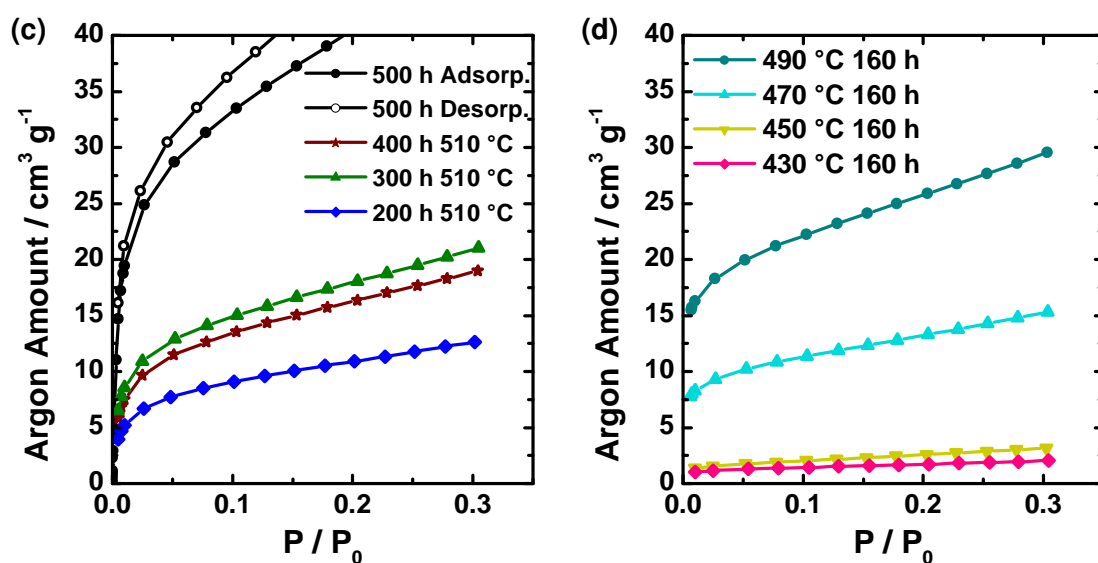
Figure A.4: **(c)** Argon adsorption for 200 h to 500 h samples at 510 °C used for BET calculation and **(d)** comparison with samples synthesised from 430 °C to 490 °C at calcination times of 160 h.
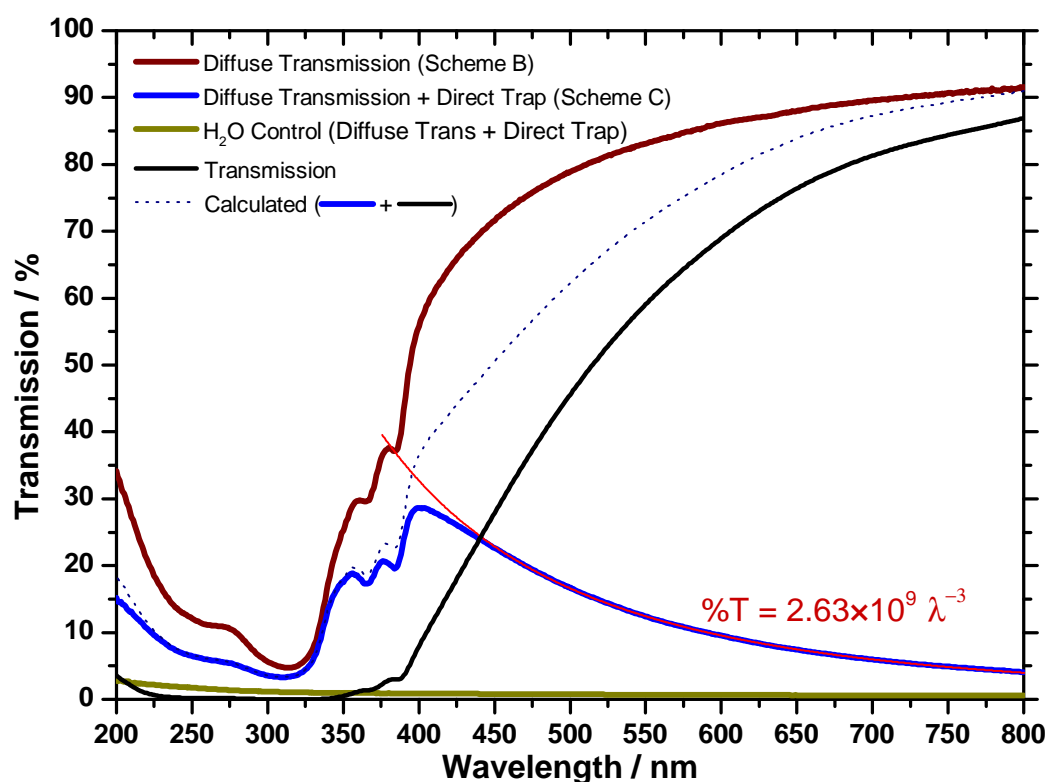


Figure A.5: Support spectra for diffuse transmission measurements. Conventional transmission (black) and the calculated sum of the conventional transmission + (diffuse reflected + direct trap) are added to the previously discussed spectra (See Figure 5.19).

## A.5  The Degradation of Methylene Blue by Light

The degradation and colour change of organic dyes has been a classic indicator of photocatalytic activity which does not require significant investment. The photodegradation of methylene blue is a commonly used technique to screen for photocatalytic activity.[117,118] This approach is attractive due to its simplicity which can be used with the use of a UV-Vis absorption spectrometer. In this section, photocatalytic dye degradation for a CN-oligomer and a cesium titanate/CN hybrid material is demonstrated. More information on these photocatalysts can be found in the thesis of Dr. Hongji Wang.[72]

In Figure A.6, a cesium titanate photocatalyst with TEoA electron donor and the Pt precursor ($H_2PtCl_6$) were added to a methylene blue dye solution ($1.5\times10^{-4}$ M). After stirring in the dark for 72 h, the samples were illuminated with UV light and absorbance spectra were measured at 2 h, 6 h, 8 h, and 10 h illumination. Samples were compared to a control without the catalyst. The results show how the photocatalyst degrades the dye by 75 % of its original absorbance after 10 h whereas the control degrades by 20 %.

These experiments showed the importance of distinguishing clearly between photocatalytic dye degradation and photobleaching of the dye. Although useful as an indicator, dye decolouring experiments are not sufficient to prove photoactivity because of effects such as photobleaching and dye adsorption. Hydrogen evolution experiments are recommended to show true chemical bond breaking with light.
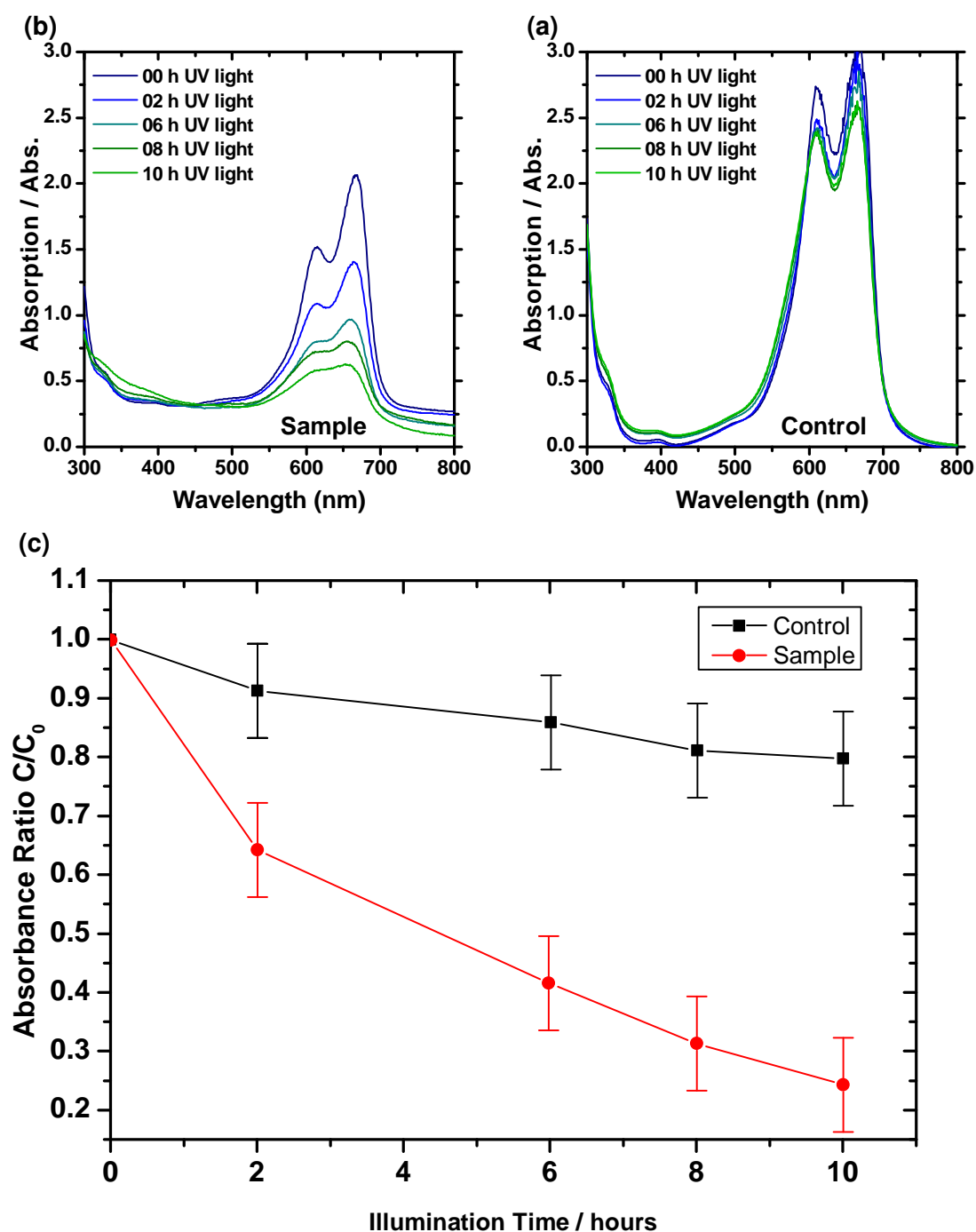
Figure A.6: **(a)** Absorbance spectra showing the photocatalytic degradation of MB dye for 10 h illumination with UV light. **(b)** Absorbance spectra of the control sample without the photocatalyst and **(c)** comparison of the absorbance ratios of the sample and control.

## A.6   Sonolysis of Water to Hydrogen

Ultrasonication of prepared catalyst materials is an essential step to control particle size and thus surface area, sometimes greatly enhancing hydrogen evolution. However, it must be noted that ultrasonication alone readily produces hydrogen gas in a process known as sonolysis.[35,119] Water splitting occurs due to the intense temperatures created during the cavitation of bubbles excited by the ultrasonic waves. Additionally, light may also play a role in a process known as sonoluminescence but . In relation to the main topic of photocatalysis, the effects of hydrogen generation by ultrasound are easily circumvented simply by purging the reactions with inert gas to remove any produced $H_2$. However, it is worth exploring the links between sonolysis and photolysis of water with regard to the catalysts, cocatalysts and acceptor/donor materials used in this work.

In Figure A.7, an overview of hydrogen evolution by sonolysis is given using our best photocatalyst, the 4AP doped amorphous PTI. Experiments were carried out in a glass reactor with argon atmosphere (unless otherwise stated) and covered with a lid to block all light. Readings were taken before sonication to confirm 0 ppm $H_2$. As expected, for 30 min sonication, $H_2$ concentration increases as the power of the 150 W sonic bath is increased. The effect of sonication time is not clear as the $H_2$ concentration decreases unexpectedly after 20 min. It is interesting to note how different materials affect the hydrogen evolution in part (c). Water alone produces 0.032 µmol of $H_2$ gas. The inert silica microspheres gave a similar value suggesting the gas evolution is not a surface nucleation site phenomenon. TEoA electron donor produced 0.160 µmol, although this may not be so surprising, considering that TEoA out-performs other electron donors in photocatalysis. Another electron donor, sodium persulfate ($Na_2S_2O_8$), produced 0.050 µmol. For reference, P25 $TiO_2$ produced 0.187 µmol of $H_2$. The 4AP doped PTI produced the most by far with a value of 0.654 µmol and was enhanced further by the addition of TEoA and Pt to a value of 0.976 µmol of $H_2$ gas. It is interesting to observe that our photocatalyst also performs as a sonocatalyst for hydrogen generation.
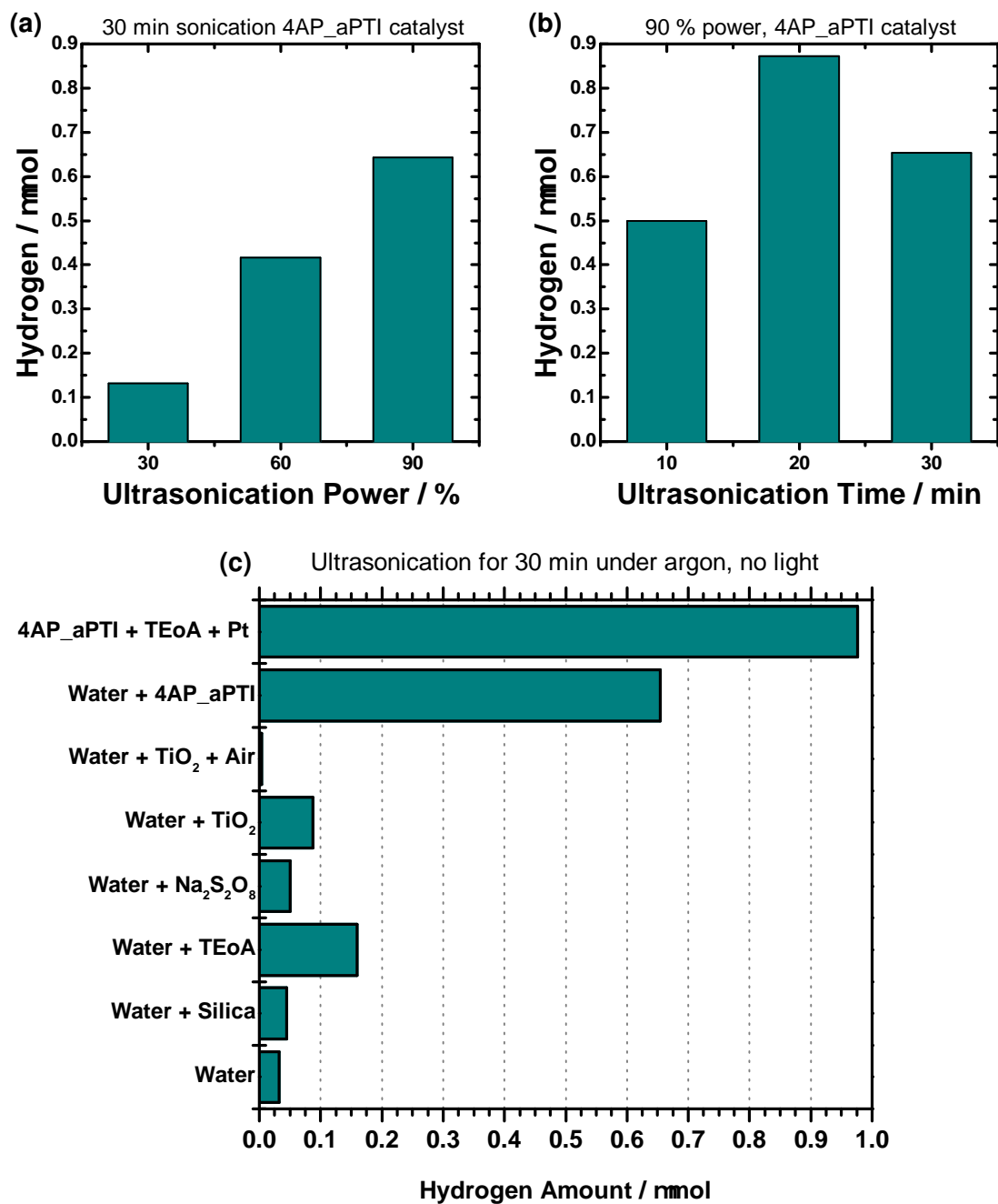
Figure A.7: Sonocatalysis, the effects of ultrasonication on photocatalyst materials. **(a)** Sonication power, **(b)** sonication time and **(c)** different catalyst materials. Argon atmosphere, no light, 150 W ultrasonic bath for 30 min.

## A.7 Metal Oxides for Oxygen Evolution

In the exploration of photocatalytic materials and methods, the well established inorganic metal oxides, should be considered.[120–122] The metal oxide materials screened for photocatalytic activity are: $Ag_3PO_4$, $SnWO_4$, $BiVO_3$, $Zn_3V_2O_8$, $AgNbO_3$, $SrSnO_3$, $BaSnO_3$, $CaSnO_3$, $LiVO_3$, $CaGeO_3$ and $CsNbO_3$.
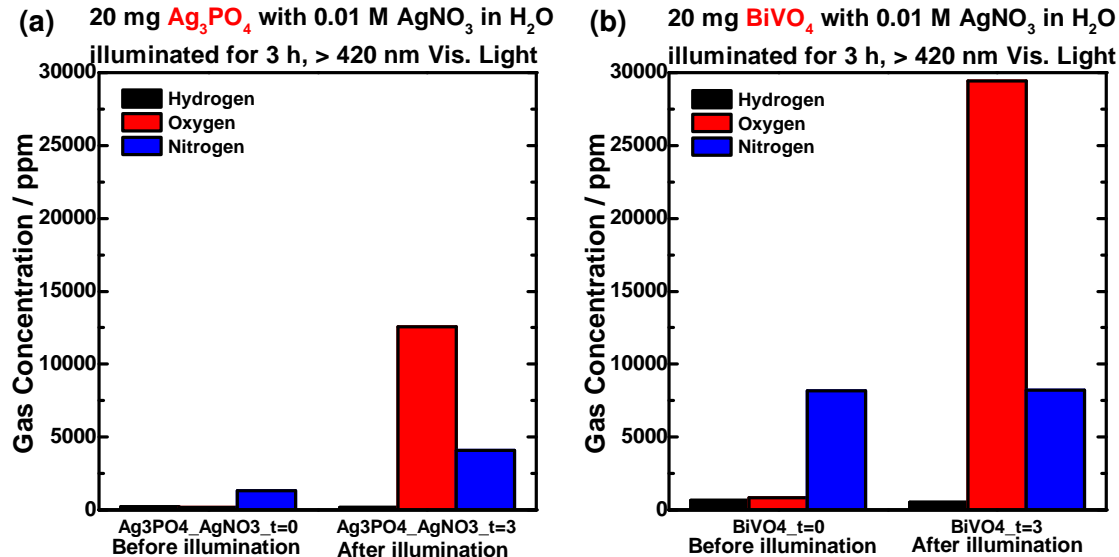


Figure A.8: $BiVO_4$ and $Ag_3PO_4$ for photocatalytic $O_2$ evolution.

Table A.4: Comparison of photocatalysts for visible light $O_2$ evolution. 20 mg of catalyst, $AgNO_3$ electron acceptor, visible light > 420 nm, 10 min sonication and argon purged reactor.

| Photocatalyst | $O_2$ Evolution µmol $h^{-1}$ $g^{-1}$ | Photonic Efficiency % |
|---|---|---|
| $Ag_3PO_4$ | 116.1 | 0.32 |
| $CuWO_4$ | 0.0 | 0.00 |
| $SnWO_4$ | 0.0 | 0.00 |
| $Zn_3V_2O_8$ | 16.0 | 0.04 |
| $BiVO_4$ | 270.2 | 0.87 |

Oxygen evolution experiments were initially challenging because the quantification of $O_2$ was unreliable due to air contamination. Also, the electron acceptor $AgNO_3$ deposited silver contamination on the reactor walls. An interesting coincidence occurred with $AgNO_3$ which side-tracked progress. When attempting to buffer the pH of reactions, the phosphate buffer ($PO_4$) reacted with $AgNO_3$ to form $Ag_3PO_4$ in-situ, one of the best oxygen evolving photocatalysts.[123] Eventually, more reliable $O_2$ evolution data was measured, although the evolution rates remained low, as can be seen in Table A.4.

## A.8    Hiden MS Gas Evolution Supplementary
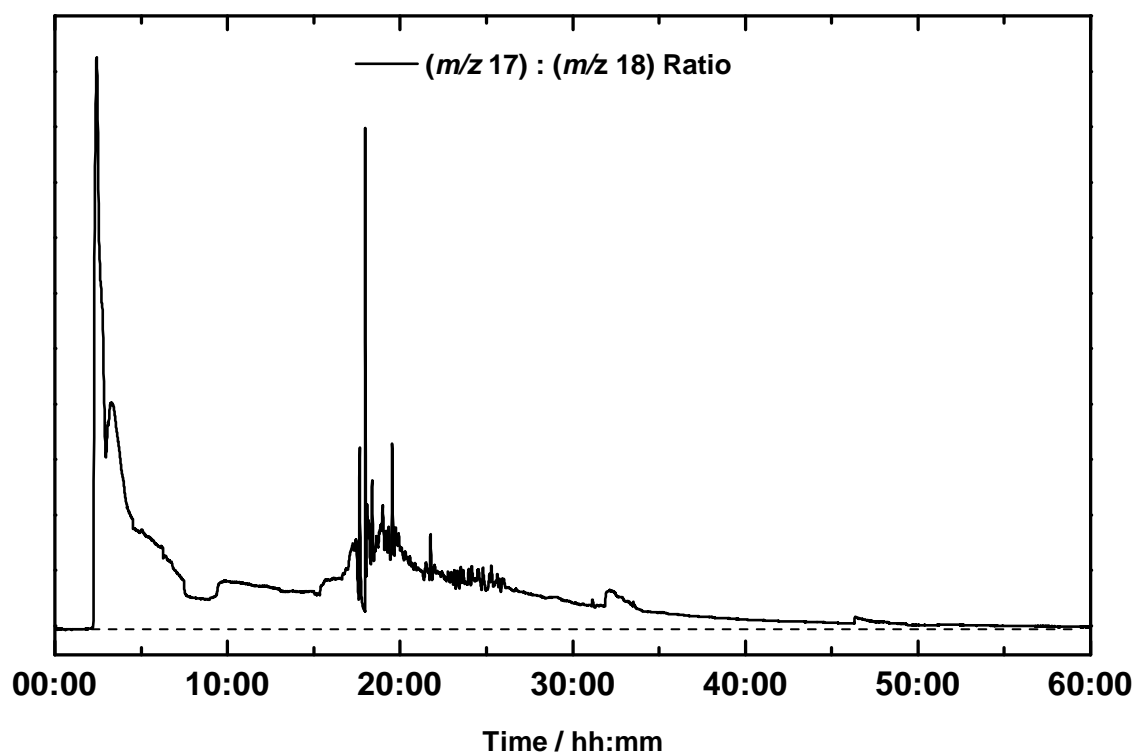


Figure A.9: Division of the $m/z = 17$ (ammonia) and $m/z = 18$ (water) signals during the MS analysis. See Figure 5.4. The ammonia signal is dominated by the water signal due to $OH^+$ species. This graph attempts to show how the signal ratios deviate, proving that another species besides $OH^+$ contributes to the signal. In other words, the ammonia signal in Figure 5.4 could be replaced with the plot above.
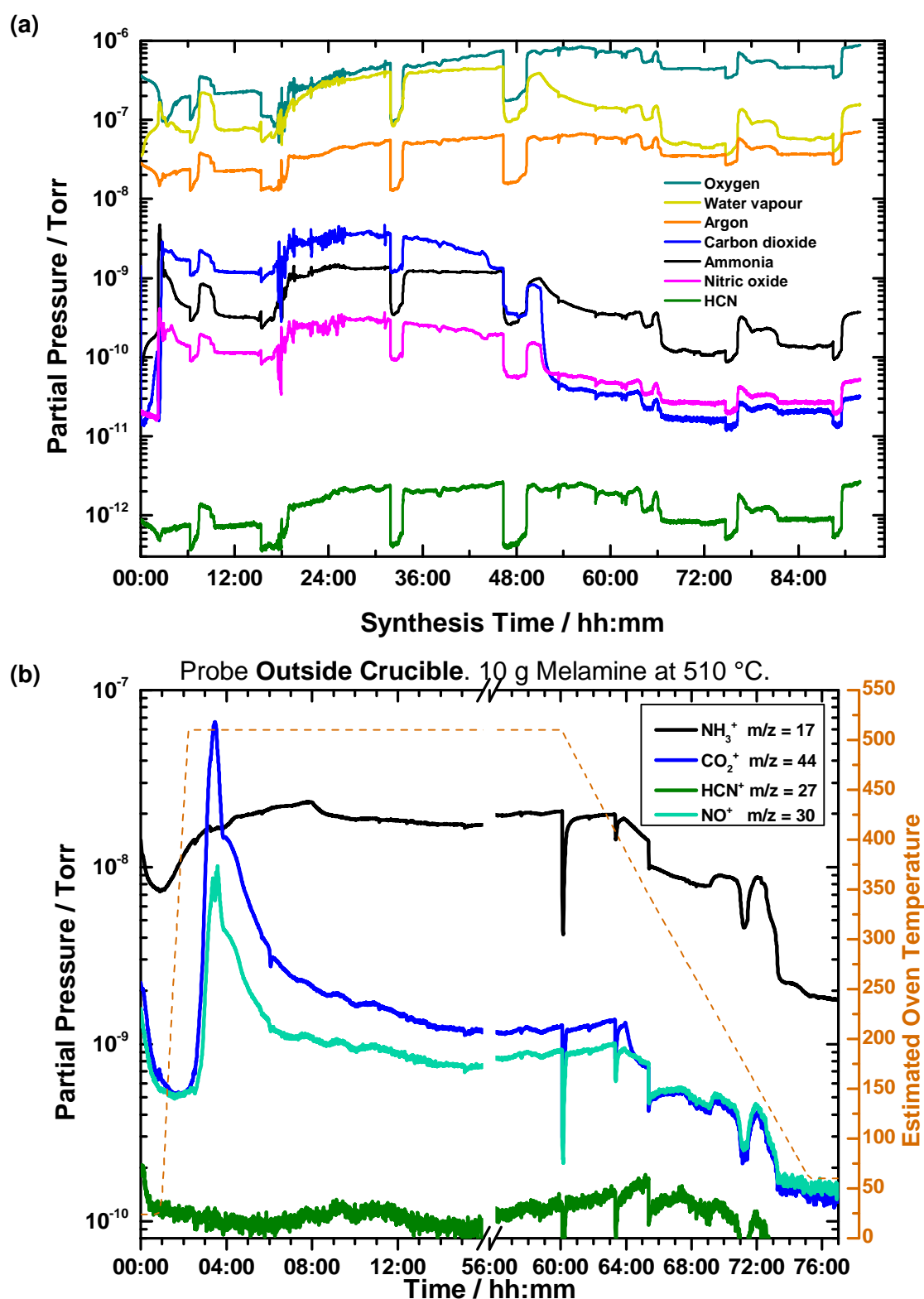
Figure A.10: DEI+ MS time profile of evolved gases during the calcination of melamine. 70 V source, Faraday detector. **(a)** Raw data of Figure 5.4. **(b)** Full profile *Outside Crucible*: 10 g melamine for 60 h, see Figure 5.1 for photo of product.

Table A.5: Permeability coefficient of common gases in PDMS silicone membrane at room temperature and 1 atm.[124] The Barrer unit is a measure of gas permeability. 1 Barrer = $3.348 \times 10^{-19}$ kmol m m$^{-2}$ s$^{-1}$ Pa$^{-1}$. The 'm' represents the thickness of the material whose permeability is being evaluated, and m$^{-2}$ is the reciprocal surface area of that material.

| Gas | Formula | Permeability Coefficient (Barrer) |
|---|---|---|
| Nitrogen | $N_2$ | 280 |
| Carbon monoxide | CO | 340 |
| Oxygen | $O_2$ | 600 |
| Nitric oxide | NO | 600 |
| Argon | Ar | 600 |
| Hydrogen | $H_2$ | 650 |
| Helium | He | 350 |
| Methane | $CH_4$ | 950 |
| Ethylene | $C_2H_4$ | 1350 |
| Ethane | $C_2H_6$ | 2500 |
| Carbon dioxide | $CO_2$ | 3250 |
| Propane | $C_3H_8$ | 4100 |
| Nitrous oxide | $N_2O$ | 4350 |
| Acetone | $C_3H_6O$ | 5860 |
| Ammonia | $NH_3$ | 5900 |
| Nitrogen dioxide | $NO_2$ | 7500 |
| Octane | n-$C_8H_{18}$ | 8600 |
| Butane | n-$C_4H_{10}$ | 9000 |
| Toluene | $C_7H_8$ | 9130 |
| Hexane | n-$C_6H_{14}$ | 9400 |
| Hydrogen sulfide | $H_2S$ | 10000 |
| Benzene | $C_6H_6$ | 10800 |
| Methanol | $CH_3OH$ | 13900 |
| Sulfur dioxide | $SO_2$ | 15000 |
| Pentane | n-$C_5H_{12}$ | 20000 |
| Water | $H_2O$ | 36000 |
| Carbon disulfide | $CS_2$ | 90000 |

## A.9 XPS Area Fittings and Valence Band Data

Figure A.11 shows a high resolution XPS analysis of the nitrogen signals in the 500 h white melon sample. It is certain that heptazine-based melon has a central nitrogen $(N-(C)_3)$ surrounded by six outer ring nitrogens $(C=N-C)$. Thus, the peak area is forced to the ratio of 6:1. Similarly, the NH and $NH_2$ groups are in the same ratio as shown in the structure inset. Valence band maximum agrees with reference[125].
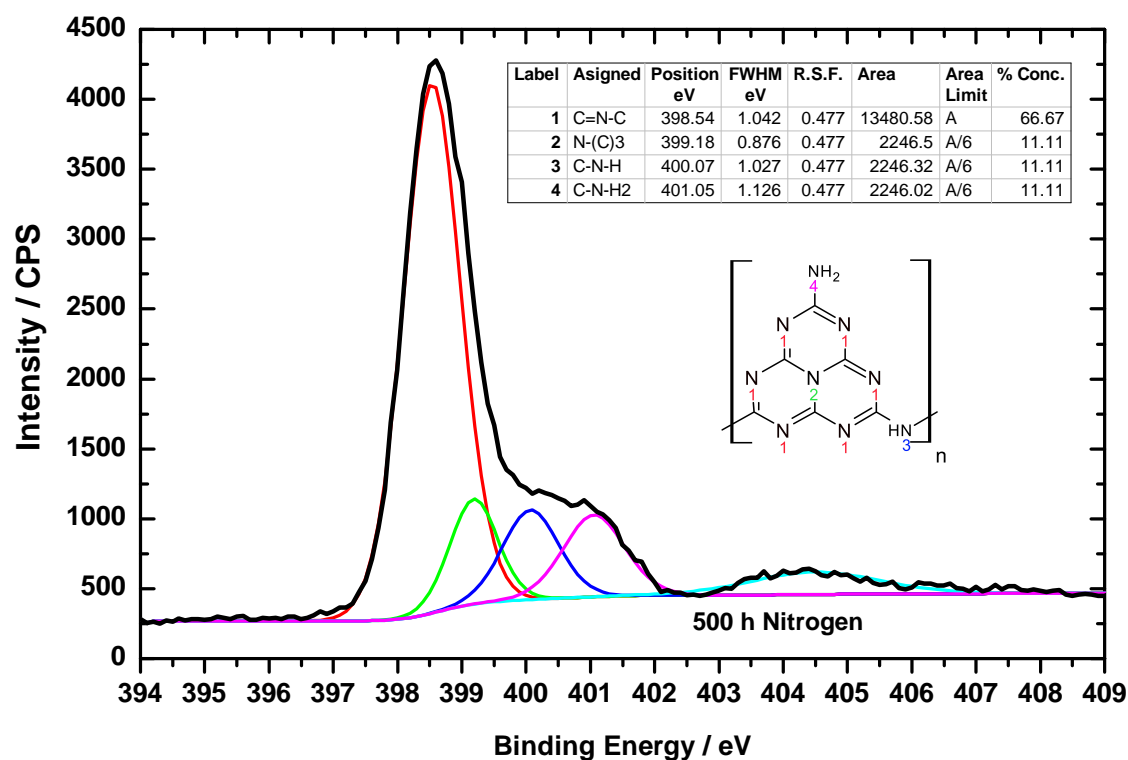


Figure A.11: XPS fittings for 500 h melon with fitting peak areas forced to the ratio 6:1:1:1 as is expected for heptazine melon with NH and $NH_2$ groups.
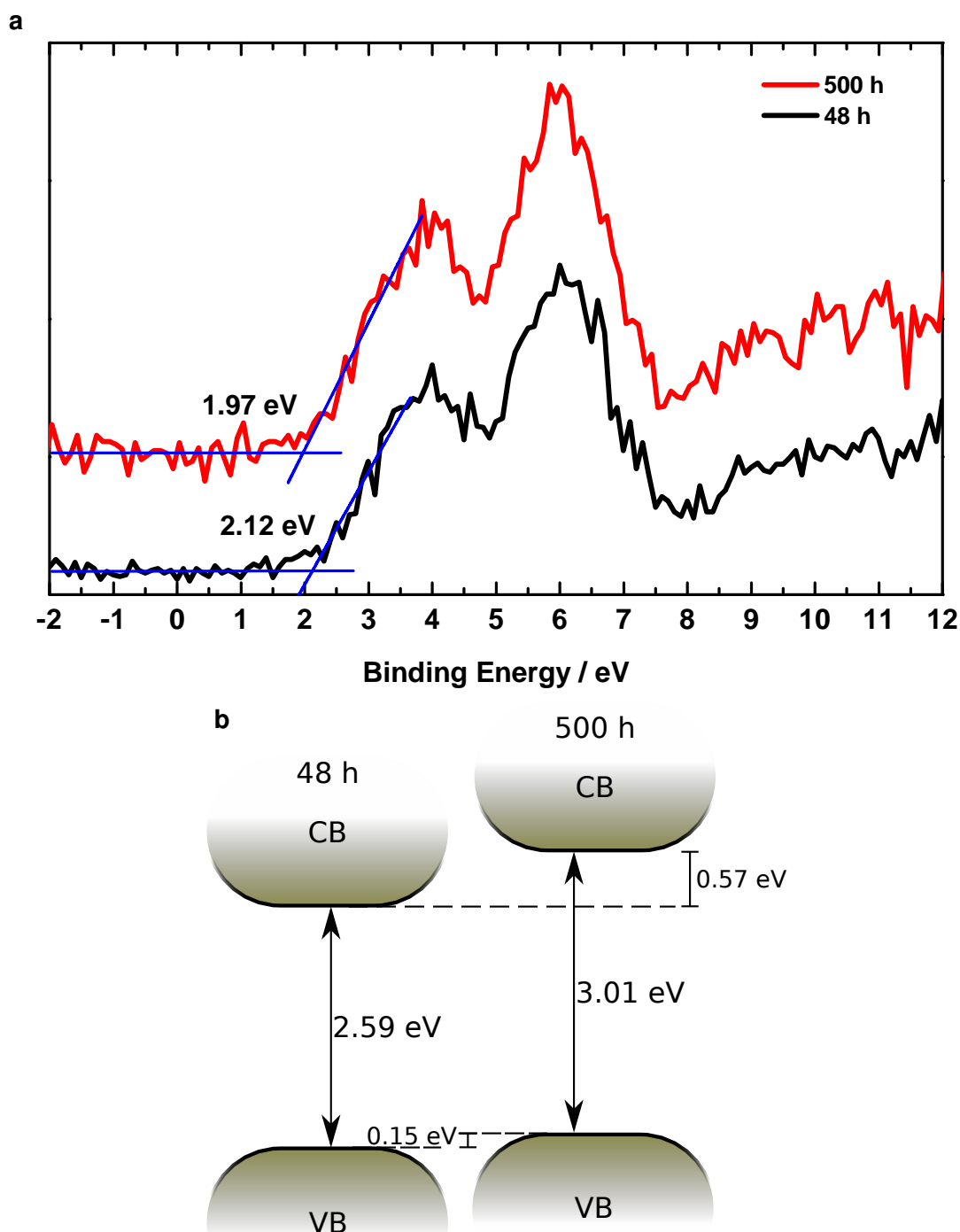
Figure A.12: **(a)** High resolution valence band XPS spectra for the 48 h and 500 h samples. Difference in valence band top is estimated at 0.15 eV. **(b)** Estimated band structure from band gaps and valence top difference of 0.15 eV. The absolute positions relative to vacuum or hydrogen electrodes are not determined with this method, only the relative positions.

## A.10   Programming Code for the Lamp Timers

Below is the C++ programming code for the xenon lamp timers which was written. Comments in the code explain each part. Generally, the program links serial port communication functions with timing functions to allow programmed control of the xenon lamp. This includes starting the lamp at a specified time, stopping the lamp after the desired illumination time and an optional delay to start the lamp. Error codes are read from the power unit for use in troubleshooting. Baud rate 9600, 8 data bits, 1 stop bit and no parity. The program was created with DevC++ software and is free without limitation under the MIT license. The program's executables, source files and logs are located at the networked address:

`\\lotserv\lotgc\Auto␣Lamp␣Timer\`

```
1
2  ////////////////////////////////////////////////////////////////////////////
3  //   Copyright (c) <2015> <Brian Tuffy>                                    //
4  //                                                                         //
5  //   Permission is hereby granted, free of charge, to any person          //
6  //   obtaining a copy of this software and associated documentation       //
7  //   files (the "Software"), to deal in the Software without              //
8  //   restriction, including without limitation the rights to use, copy,   //
9  //   modify, merge, publish, distribute, sublicense, and/or sell copies   //
10 //   of the Software, and to permit persons to whom the Software is       //
11 //   furnished to do so, subject to the following conditions:             //
12 //                                                                         //
13 //   The above copyright notice and this permission notice shall be       //
14 //   included in all copies or substantial portions of the Software.      //
15 //                                                                         //
16 //   THE SOFTWARE IS PROVIDED "AS IS", WITHOUT WARRANTY OF ANY KIND,      //
17 //   EXPRESS OR IMPLIED, INCLUDING BUT NOT LIMITED TO THE WARRANTIES      //
18 //   OF MERCHANTABILITY, FITNESS FOR A PARTICULAR PURPOSE AND             //
19 //   NONINFRINGEMENT. IN NO EVENT SHALL THE AUTHORS OR COPYRIGHT          //
20 //   HOLDERS BE LIABLE FOR ANY CLAIM, DAMAGES OR OTHER LIABILITY,         //
21 //   WHETHER IN AN ACTION OF CONTRACT, TORT OR OTHERWISE, ARISING         //
22 //   FROM, OUT OF OR IN CONNECTION WITH THE SOFTWARE OR THE USE OR        //
23 //   OTHER DEALINGS IN THE SOFTWARE.                                       //
24 ////////////////////////////////////////////////////////////////////////////
25
26 #include <cstdlib>
27 #include <iostream>
28 #include <vector>
29 #include <string>
30 #include <windows.h>
31 #include <stdio.h>
32 #include "SFile.h"
33 #include <fstream>
34 #include "ctime"
35
36 using namespace std;
37 vector<short int> buffer;
38 DWORD start = 0;
39 DWORD res = 0;
40
```

```
41  //Windows functions for pressing keyboard buttons
42  bool Keypress(char &Key)
43  {
44       INPUT_RECORD Event;
45       DWORD NumberOfEvents, EventsRead, EventCounter;
46
47       GetNumberOfConsoleInputEvents
48       (GetStdHandle(STD_INPUT_HANDLE), &NumberOfEvents);
49
50       if (NumberOfEvents == 0)
51           return false;
52
53       for (EventCounter = 0; EventCounter < NumberOfEvents; EventCounter++)
54       {
55           PeekConsoleInput(GetStdHandle
56           (STD_INPUT_HANDLE), &Event, 1, &EventsRead);
57
58           if ((Event.EventType == KEY_EVENT) && ((Event.Event.KeyEvent.bKeyDown)))
59           {
60               ReadConsoleInput
61               (GetStdHandle(STD_INPUT_HANDLE), &Event, 1, &EventsRead);
62
63               Key = Event.Event.KeyEvent.wVirtualKeyCode;
64               if (!(FlushConsoleInputBuffer(GetStdHandle(STD_INPUT_HANDLE))))
65                   exit(0);
66               return true;
67           }
68           else
69               ReadConsoleInput
70               (GetStdHandle(STD_INPUT_HANDLE), &Event, 1, &EventsRead);
71       }
72
73       return false;
74  }
75  /////////////////////////////////////////////////////////////////////////
76  /////////////////////////////////////////////////////////////////////////
77
78  int main() {
79
80      int ComPort=3;          //Communications port. Lamp1=8,Lamp2=6.PC=3
81      SFile sf;
82      fstream of( "output.txt", fstream::out );
83      ofstream log;
84      //Temperary .txt files to read bytes (called output.txt) and Log file.
85
86          if (!sf.Open(ComPort, 9600))        //Open COM port with 9600 bitrate
87              {
88              cerr << "Failed to open COM port. \nSerial COM port "<<ComPort<<
89              " should be connected to the Lamp."
90              " Error code = " << GetLastError() << endl;
91              system("pause");
92              return 1;
93              }
94
95  /////////////////////////////////////////////////////////////////////////
96  /////////////////////////////////////////////////////////////////////////
97    while(1==1)                              //Repeat program indefinitely.
98    {
99          int LampRunMin=180;                //3 h default run time
```

```cpp
100          cout<<"Tuffy Timer 2000. Automatically start and stop xenon lamp 2."
101          "\n \nEnter minutes to run lamp?"<<endl; cin>>LampRunMin;
102          int LampRunSec=LampRunMin*60;
103
104          int DelayMin=660;              //11 h default delay (18:00 to 05:00)
105          cout<<"Enter minutes to delay start of lamp?"<<endl; cin>>DelayMin;
106          int DelaySec=DelayMin*60;
107          system("pause");
108
109          for(time_t DelayEndTime = time(NULL)+DelaySec;time(NULL)<DelayEndTime;)
110              {
111                  time_t MinRemain = DelayEndTime - time(NULL);
112                  tm *ltm3 = localtime(&MinRemain);
113                  system("CLS");
114                  cout<<"waiting "<<ltm3->tm_hour-1<<":"<<ltm3->tm_min <<
115                  ":"<<ltm3->tm_sec << " to start lamp"<< endl;
116
117                  char key = 0;
118                   if (Keypress(key))
119                      {                   //If you press Esc, the program quits.
120                          if (key == VK_ESCAPE)
121                              {
122                                  PostQuitMessage(0);
123                                  Sleep(0);
124                                  return 1;
125                              }
126                      }
127                  Sleep(1000);
128
129          } //End of FOR loop for delay timer before lamp start.
130
131 ////////////////////////////////////////////////////////////////////////////////
132 ////////////////////////////////////////////////////////////////////////////////
133     sf.SetReadTimeOut(2000);
134         //If no byte to read from the port, the program times out (msec).
135
136     char cmd1[] = "START\r";               //Lamp ignition
137     char cmd2[] = "AMPS?\r";               //Current of lamp (Not implemented)
138     char cmd3[] = "VOLTS?\r";              //Voltage of lamp (Not implemented)
139     char cmd4[] = "WATTS?\r";              //Power of lamp (Not implemented)
140     char cmd5[] = "LAMP HRS?\r";           //Lamp running hours (Not implemented)
141     char cmd6[] = "RSTHRS\r";              //Reset lamp running hours (Not implemented)
142
143     DWORD written;
144     sf.Write(cmd1, 6, written);
145         //Lamp START command with # of characters of command (6 for START\r).
146
147     time_t StartTime = time(NULL);
148         //Timer Start time in seconds since 1970.
149
150     BYTE b; //Bytes sent from the xenon lamp e.g. error codes
151
152                  log.open ("Xenon_Log.txt", ios::out | ios::app);  //Open Log file
153                  log<<"Start Code: \n";
154                  Sleep(4100);
155                   while (sf.ReadByte(b))
156                      {
157                          log << b;      // Write error codes to log as Start code
158                      }
```

```
159                              log<<" \n";
160 ////////////////////////////////////////////////////////////////////////////
161 ////////////////////////////////////////////////////////////////////////////
162
163     for (time_t EndTime = StartTime + LampRunSec; time(NULL) < EndTime; )
164     {
165       time_t Difference=EndTime-time(NULL);
166       tm *ltm = localtime(&Difference);
167       system("CLS");
168       {cout<<ltm->tm_hour-1<< ":";                //Hours
169       cout<<ltm->tm_min << ":";                   //Mins
170       cout<<ltm->tm_sec<<" remaining"<<endl;}     //Seconds
171
172       char key = 0;
173       if (Keypress(key))
174       {
175         if (key == VK_BACK)
176                 // If you press the Backspace key during the timer, ...
177                 //... it skips the timer and runs the command.
178         {
179           break;
180         }
181
182         if (key == VK_ESCAPE)
183                 //If you press the Esc key, ...
184                 //... the program quits without running the command.
185         {
186           PostQuitMessage(0);
187           Sleep(0);
188           return 1;
189         }
190
191                 //Printing the timer countdown:
192                 tm *ltm2 = localtime(&StartTime);
193
194                 //Pressing any other key pauses the timer readout.
195                 cout<<"The timer is still running but the program must "
196                 "be in countdown mode to turn off the lamp. "<<endl;
197
198                 //Countdown started at hh:mm:ss.
199                 cout<<"Timer started at "<<ltm2->tm_hour<< ":";
200                 cout<<ltm2->tm_min << ":";
201                 cout<<ltm2->tm_sec<<":\nReading messages from the Lamp... ";
202
203                 //Reading bytes from lamp power supply.
204                 //e.g. "ESR01" = operation successful.
205         while (sf.ReadByte(b))
206         { cout << b;}
207         cout<<"\n";
208
209         system("pause");
210       }
211       Sleep(1000);
212     }
213
214     //Sends the stop command to turn off the lamp.
215     char cmd0[] = "STOP\r";
216     sf.Write(cmd0, 5, written);             //Sending Lamp Stop Command
217
```

**171**

```
218    time_t StopTime = time(NULL);           //Real Lamp Running ON time
219    time_t LampOnTime = StopTime-StartTime;
220
221        log<<" Stop Code:";                  //Lamp off error code sent to Log
222        Sleep(4500);
223
224    char key = 0;
225    while (sf.ReadByte(b))
226    {
227      if (Keypress(key))
228      {
229        if (key == VK_ESCAPE)
230        {
231          PostQuitMessage(0);
232          Sleep(0);
233          return 1;
234        }
235            system("pause");
236      }
237
238        cout << b;            //Bytes sent from the power supply
239        log<< b;
240    }
241    cout<<"\n";
242    log<<"' \n";
243
244        //Countdown started at hh:mm:ss.
245        tm *ltm2 = localtime(&StartTime);
246        cout<<"Timer started at "<<ltm2->tm_hour<< ":";
247        cout<<ltm2->tm_min << ":";
248        cout<<ltm2->tm_sec<<": \n" ;
249
250        //Log output of parameters
251        log <<"Lamp2 Start: "<<ltm2->tm_mday << "/";
252        log <<ltm2->tm_mon+1 << "/";
253        log <<ltm2->tm_year +1900<< "_";
254        log <<ltm2->tm_hour<< ":";
255        //Writing Lamp Start Date to Log
256
257        log <<ltm2->tm_min << ":";
258        log <<ltm2->tm_sec<<" " ;
259        //Writing Lamp Start Time to Log
260
261        tm *ltm4 = localtime(&StopTime);
262        //Here I define ltm4 and output to program and log
263        log <<"Lamp2  Stop: "<<ltm4->tm_mday << "/";
264
265        log <<ltm4->tm_mon+1 << "/";
266        log <<ltm4->tm_year +1900<< "_";
267        log <<ltm4->tm_hour<< ":";
268        log <<ltm4->tm_min << ":";
269        log <<ltm4->tm_sec<<" ";
270        //Writing Lamp Start Date and Time to Log
271
272        tm *ltm3 = localtime(&LampOnTime);
273        //Here I define ltm3 and output to program and log
274        cout<<"Lamp was on for "<<ltm3->tm_hour-1<< ":";
275        cout<<ltm3->tm_min << ":";
276        cout<<ltm3->tm_sec<<": \n";
```

```
277
278          log<<"Lamp on for "<<ltm3->tm_hour-1<< ":";
279          log<<ltm3->tm_min << ":";
280          log<<ltm3->tm_sec<<" \n";
281          log<<"=================================================== \n";
282          log.close();          //Close Scan_file "Xenon Log . txt"
283
284          cout<<"=================================================== \n";
285
286     }   //End of main program
287
288   sf.Close();                    //Close Scan_file "output.txt"
289      system("pause");
290      PostQuitMessage(EXIT_SUCCESS);
291      Sleep(0);
292      return(EXIT_SUCCESS);
293 }
```

# Copyright

Parts of this work have been and are subject to the following copyrights. They have been reproduced with permission of the corresponding publisher and have only been adapted with respect to the format of this thesis.

**Triazine-based carbon nitrides for visible-light-driven hydrogen evolution**

# Abbreviations

**1D** one-dimensional

**2D** two-dimensional

**4AP** 4-amino-2,6-dihydroxypyrimidine (6-aminouracil)

**AC** Alternating current

**AFM** Atomic force microscopy

**AM#** Air Mass

**aPTI** Amorphous poly triazine imide

**ATR** Attenuated total reflection

**BE** Binding energy

**BET** Brunauer-Emmett-Teller

**CB** Conduction band

**CN** Carbon nitride

**CP** Cross-polarisation

**CPPI** Cross-polarisation with polarisation inversion

**DC** Direct current

**DCD** Dicyandiamide

**DEI** Direct electron ionisation

**DFT** Density functional theory

**DLS** Dynamic light scattering

**DMSO** Dimethyl sulfoxide

**DQ-SQ** Double quantum single quantum

**DRA** Diffuse reflectance accessory

**DRS** Diffuse reflectance spectroscopy

## Abbreviations and Symbols

| | |
|---:|:---|
| **DSC** | Differential scanning calorimetry |
| **EI** | Electron ionisation/impact |
| **EJ** | Exa joules (unit) |
| **EtOH** | Ethanol |
| **EA** | Elemental analysis |
| **FFT** | Fast Fourier transform |
| **FID** | Flame ionisation detector, Free induction decay |
| **FTIR** | Fourier transform infrared |
| **FWHM** | Full width at half maximum |
| **GC** | Gas chromatography |
| **HER** | Hydrogen evolution reaction |
| **HMQC** | Heteronuclear multiple-quantum correlation |
| **HOMO** | Highest occupied molecular orbital |
| **HRTEM** | High resolution transmission electron microscopy |
| **IR** | Infrared |
| **IUPAC** | International union of pure and applied chemistry |
| **LMU** | Ludwig Maximilians Universität |
| **LUMO** | Lowest unoccupied molecular orbital |
| **MAS** | Magic angle spinning |
| **MeOH** | Methanol |
| **MPI** | Max Planck Institute |
| **MS** | Mass spectrometry |
| **NHE** | Normal hydrogen electrode |
| **NMR** | Nuclear magnetic resonance |
| **OER** | Oxygen evolution reaction |
| **PC** | Photocatalysis |
| **PDI** | Polydispersity index |
| **PDMS** | Polydimethylsiloxane |

**PXRD** Powder X-ray diffraction

**PE** Photonic efficiency

**PEC** Photoelectrochemistry

**PL** Photoluminescence

**PMT** Photo multiplier tube

**PSD** Position sensitive detector, Particle size distribution

**PTFE** Polytetrafluoroethylene i.e. Teflon®

**PTI** Poly triazine imide

**QGA** Quantitative gas analysis

**QSDFT** Quenched solid density functional theory

**RF** Radio frequency

**RGA** Residual gas analysis

**RMS** Root mean square

**SA** Surface area

**SAED** Selected area electron diffraction

**SEM** Scanning electron microscopy

**TCD** Thermal conductivity detector

**TEA** Triethylamine

**TEoA** Triethanolamine

**TGA** Thermogravimetric analysis

**THF** Tetrahydrofuran

**TMS** Tetramethylsilane

**ULT** Ultra long time

**UV** Ultraviolet

**UV-Vis** Ultraviolet-visible (absorption spectrometer)

**VB** Valence band

**XRD** X-ray diffraction

**XPS** X-ray photoelectron spectroscopy

# Symbols and Constants

| | | | |
|---|---|---|---|
| $\approx$ | Approximately equal to | $t_R$ | Peak retention time |
| $I$ | Light intensity | $w_h$ | Peak width at half height |
| $Abs$ | Absorbance | $L$ | Column length (GC) |
| $A$ | Absorption | $N$ | Theoretical plate number (GC) |
| $F(R)$ | Kubelka-Munk function | $h_p$ | Height equivalent to a theoretical plate |
| $h$ | Planck constant | | |
| $\lambda$ | Photon wavelength | $e^-$ | Electron |
| $c$ | Speed of light | $h^+$ | Positive hole |
| $\nu$ | Photon frequency | $M$ | Molecule |
| $\alpha$ | Absorption coefficient | $m/z$ | Mass-charge ratio |
| $E_g$ | Band gap | $\xi$ | Photonic efficiency |
| $R$ | Reflectance | $n$ | Chemical amount |
| $R_\infty$ | Absolute reflectance | $q_p$ | Photon flux |
| $R_g$ | Ideal gas constant | $P(\lambda)$ | Radiant power |
| $T$ | Transmittance | $P$ | Total power |
| $\epsilon$ | Molar absorptivity coefficient | $A_i$ | Illumination area |
| $c$ | Solution concentration | $t_i$ | Illumination time |
| $l$ | Optical path length | $V$ | Volume |
| $k$ | Absorption coefficient (Kubelka-Munk) | $W$ | Radiant energy |
| | | $C_{H_2}$ | Concentration of hydrogen |
| $s$ | Scattering coefficient | $N_a$ | Avogadro constant |
| $n$ | Tauc exponent | $x$ | Scattering size parameter |

# Non-SI Units

**Torr** 1 Torr = $\frac{101325}{760}$ Pa

**amu** atomic mass unit (amu) = unified atomic mass unit (u) = dalton (Da)

**Barrer** 1 barrer = $1 \times 10^{-10}$ cm$^2$ s$^{-1}$ Torr$^{-1}$ = $7.5005 \times 10^{-18}$ m$^2$ s$^{-1}$ Pa$^{-1}$

# Bibliography

[1] Ceballos, G.; Ehrlich, P. R.; Barnosky, A. D.; Garcia, A.; Pringle, R. M.; Palmer, T. M. *Sci. Adv.* **2015**, *1*, 1–5.

[2] Blakers, A.; Devine-Wright, P.; Gazzoni, D. L.; Hestnes, A. G.; Kituyi, E.; Kretzschmar, J.; Luther, J.; Manwell, J.; Mununda, H.; Rolz, C.; Seka, J.; Volkov, E.; Zhifeng, W.; Yamaguchi, M. *Research and Development on Renewable Energies A Global Report on Photovoltaic and Wind Energy*; 2009; pp 1–23.

[3] Zervos, A. *Renewable Energy Scenario to 2040: Half of the Global Energy Supply from Renewables in 2040*; 2006; p 15.

[4] Bates, J.; Hill, N. *The Role of Physics in Renewable Energy RD & D*; 2005.

[5] Chapman, G. A. *Encyclopedia of Planetary Science*; Springer Netherlands: Dordrecht, 1997; Chapter Solar luminosity, pp 748–748.

[6] ASTM E490-00a(2014) Standard Solar Constant and Zero Air Mass Solar Spectral Irradiance Tables. 2014; http://www.astm.org/Standards/E490.htm.

[7] ASTM G173-03(2012), Standard Tables for Reference Solar Spectral Irradiances: Direct Normal and Hemispherical on 37° Tilted Surface. 2012; http://www.astm.org/Standards/G173.htm.

[8] Jacobson, M. Z.; Delucchi, M. a. *Energy Policy* **2011**, *39*, 1154–1169.

[9] Clerici, A.; Assayag, M. *World Energy Resources: 2013 Survey*; 2013.

[10] WEC, *Sustainable Energy for All 2013-2014: Global Tracking Framework Report*; 2014.

[11] Dincer, I.; Joshi, A. S. *Solar Based Hydrogen Production Systems*; Springer Briefs in Energy; Springer: New York, 2013.

[12] Malato, S.; Fernández-Ibáñez, P.; Maldonado, M.; Blanco, J.; Gernjak, W. *Catal. Today* **2009**, *147*, 1–59.

[13] De Richter, R.; Caillol, S. *J. Photochem. Photobiol. C Photochem. Rev.* **2011**, *12*, 1–19.

[14] Habisreutinger, S. N.; Schmidt-Mende, L.; Stolarczyk, J. K. *Angew. Chem. Int. Ed. Engl.* **2013**, *52*, 7372–408.

[15] Wilderman, M. *Proc. R. Soc. A Math. Phys. Eng. Sci.* **1906**, *77*, 274–276.

[16] Plotnikow, J. *Textbook of Photochemistry*; Verlag von Willhelm Knapp: Berlin, 1910; p 72.

[17] Serpone, N.; Emeline, a. V.; Horikoshi, S.; Kuznetsov, V. N.; Ryabchuk, V. K. *Photochem. Photobiol. Sci.* **2012**, *11*, 1121–50.

[18] Fuijshima, A.; Honda, K. *Nature* **1972**, *238*, 37–38.

[19] Liebig, J. *Ann. der Pharm.* **1834**, *10*, 1–47.

[20] Liu, A. Y.; Cohen, M. L. *Science* **1989**, *245*, 841–842.

[21] Gillan, E. G. *Chem. Mater.* **2000**, *12*, 3906–3912.

[22] Lotsch, B. V.; Döblinger, M.; Sehnert, J.; Seyfarth, L.; Senker, J.; Oeckler, O.; Schnick, W. *Chem.–Eur. J.* **2007**, *13*, 4969–80.

[23] McNaught, A. D.; Wilkinson, A. *IUPAC Compendium of Chemical Terminology 2005*; IUPAC, 2005; p 2315.

[24] Jürgens, B.; Irran, E.; Senker, J.; Kroll, P.; Müller, H.; Schnick, W. *J. Am. Chem. Soc.* **2003**, *125*, 10288–300.

[25] Mitoraj, D.; Kisch, H. *Chem.–Eur. J.* **2010**, *16*, 261–269.

[26] Chingin, K.; Perry, R. H.; Chambreau, S. D.; Vaghjiani, G. L.; Zare, R. N. *Angew. Chemie Int. Ed.* **2011**, *50*, 8634–8637.

[27] Bojdys, M. J.; Wohlgemuth, S. a.; Thomas, A.; Antonietti, M. *Macromolecules* **2010**, *43*, 6639–6645.

[28] Sattler, A.; Pagano, S.; Zeuner, M.; Zurawski, A.; Gunzelmann, D.; Senker, J.; Müller-Buschbaum, K.; Schnick, W. *Chem. - A Eur. J.* **2009**, *15*, 13161–13170.

[29] Zheng, Y.; Liu, J.; Liang, J.; Jaroniec, M.; Qiao, S. Z. *Energy Environ. Sci.* **2012**, *5*, 6717.

[30] Zhu, J.; Xiao, P.; Li, H.; Carabineiro, S. A. C. *ACS Appl. Mater. Interfaces* **2014**, *6*, 16449–65.

[31] Kaneko, M.; Okura, I. *Photocatalysis : Science and Technology*; Kodansha Springer, 2002.

[32] Nocera, D. G. *Acc. Chem. Res.* **2012**, *45*, 767–76.

[33] Pichat, P. In *Photocatalysis and Water Purification: From Fundamentals to Recent Applications*; Pichat, P. D. P., Ed.; John Wiley & Sons, 2013.

[34] Rajeshwar, K.; Osugi, M.; Chanmanee, W.; Chenthamarakshan, C.; Zanoni, M.; Kajitvichyanukul, P.; Krishnan-Ayer, R. *J. Photochem. Photobiol. C Photochem. Rev.* **2008**, *9*, 171–192.

[35] Harada, H. *Ultrason. Sonochem.* **2001**, *8*, 55–58.

[36] Wang, X.; Maeda, K.; Thomas, A.; Takanabe, K.; Xin, G.; Carlsson, J. M.; Domen, K.; Antonietti, M. *Nat. Mater.* **2008**, *8*, 76–80.

[37] Cao, S.; Low, J.; Yu, J.; Jaroniec, M. *Adv. Mater.* **2015**, *27*, 2150–2176.

[38] Braslavsky, S. E.; Braun, A. M.; Cassano, A. E.; Emeline, A. V.; Litter, M. I.; Palmisano, L.; Parmon, V. N.; Serpone, N. *Pure Appl. Chem.* **2011**, *83*, 931–1014.

[39] Peschka, W. *Liquid Hydrogen - Fuel of the Future*; Springer Science & Business Media, 1992; p 303.

[40] Buriak, J. M.; Kamat, P. V.; Schanze, K. S. *ACS Appl. Mater. Interfaces* **2014**, *6*, 11815–11816.

[41] Serpone, N.; Terzian, R.; Lawless, D. *J. Photochem. Photobiol. A Chem.* **1993**, *73*, 11 – 16.

[42] Nick, S. *J. Photochem. Photobiol. A Chem.* **1997**, *104*, 1–12.

[43] Serpone, N.; Sauv, G.; Koch, R.; Tahiri, H.; Piccinini, P.; Pelizzetti, E.; Hidaka, H. *J. Photochem. Photobiol. A Chem.* **1996**, *94*, 191 – 203.

[44] Haynes, W. *CRC Handbook of Chemistry and Physics, 95th Edition*; CRC Press, 2014.

[45] Mohr, P.; Taylor, B.; Newell, D. *Rev. Mod. Phys.* **2012**, *84*, 1527–1605.

[46] Cary, H. H.; Beckman, A. O. *J. Opt. Soc. Am.* **1941**, *31*, 682.

[47] McNaught, A. D.; Wilkinson, A. *IUPAC Compend. Chem. Terminol.*, 2nd ed.; IUPAC: Research Triangle Park, NC, 1997; Chapter Green Book, p 32.

[48] Kortüm, G. *Reflectance Spectroscopy, Principles, Methods, Applications*; Springer, 1969; p 366.

[49] Lambert, J. H.; DiLaura, D. L. *Photometry, or, On the measure and gradations of light, colors, and shade:*; Illuminating Engineering Society of North America, 2001.

[50] Poggendorff, J. C. *Annalen der Physik*; J.A. Barth, 1852.

[51] Kubelka, P. *J. Opt. Soc. Am.* **1948**, *38*, 448–457.

[52] Davis, E. A.; Mott, N. F. *Philos. Mag.* **1970**, *22*, 903–922.

[53] Wood, D. L.; Tauc, J. *Phys. Rev. B* **1972**, *5*, 3144–3151.

[54] Wang, X.; Blechert, S.; Antonietti, M. *ACS Catal.* **2012**, *2*, 1596–1606.

[55] Tauc, J. *Mater. Res. Bull.* **1968**, *3*, 37–46.

[56] Murphy, A. *Sol. Energy Mater. Sol. Cells* **2007**, *91*, 1326–1337.

[57] Mie, G. *Ann. Phys.* **1908**, *330*, 377–445.

[58] Young, A. T. *Appl. Opt.* **1981**, *20*, 533.

[59] Tyndall, J. *Six Lectures on Light*; UCL Library Services, 1872; p 296.

[60] Scott, R. P. W. *Gas Chromatography*; Buttersworth: London, 1960; p 466.

[61] Scott, R. P. W. *Principles and Practice of Chromatography*; Libraryforscience, LLC, 2003.

[62] Kauffman, G. B. *Science* **1968**, *162*, 110–111.

[63] Ettre, L. S. *Pure Appl. Chem.* **1993**, *65*, 819–872.

[64] Young, H. D.; Sears, F. W. *University Physsics*, 7th ed.; Addison-Wesley Longman, 1992; Chapter 15, p 255.

[65] Knewstubb, P. F. *Mass spectrometry and ion-molecule reactions*; Cambridge Universtiy Press, 1969.

[66] Linge, K. L.; Jarvis, K. E. *Quadrupole ICP-MS: Introduction to instrumentation, measurement techniques and analytical capabilities*; Blackwell Publishing Ltd, 2009; Vol. 33; pp 445–467.

[67] Gong, D.; Highfield, J. G.; Ng, S. Z. E.; Tang, Y.; Ho, W. C. J.; Tay, Q.; Chen, Z. *ACS Sustain. Chem. Eng.* **2014**, *2*, 149–157.

[68] Zhang, Y.; Antonietti, M. *Chem. Asian J.* **2010**, *5*, 1307–11.

[69] Bojdys, M. J. Über neue Allotrope und Nanostrukturen von Karbonitriden On new allotropes and nanostructures of carbon nitrides. Ph.D. thesis, Universität Potsdam, 2009.

[70] Lau, V. W.; Mesch, M. B.; Duppel, V.; Blum, V.; Senker, J.; Lotsch, B. V. *J. Am. Chem. Soc.* **2015**, *137*, 1064–1072.

[71] Martin, D. J.; Qiu, K.; Shevlin, S. A.; Handoko, A. D.; Chen, X.; Guo, Z.; Tang, J. *Angew. Chem. Int. Ed. Engl.* **2014**, *53*, 9240–5.

[72] Wang, H. Investigations into Carbon Nitrides and Carbon Nitride Derivatives. Ph.D. thesis, LMU, 2013.

[73] Alvaro, M.; Carbonell, E.; Fornés, V.; García, H. *ChemPhysChem* **2006**, *7*, 200–5.

[74] Sastre, F.; Bouizi, Y.; Fornés, V.; Garcia, H. *J. Colloid Interface Sci.* **2010**, *346*, 172–7.

[75] Tian, J.; Liu, Q.; Ge, C.; Xing, Z.; Asiri, A. M.; Al-Youbi, A. O.; Sun, X. *Nanoscale* **2013**, *5*, 8921–4.

[76] Hong, J.; Yin, S.; Pan, Y.-x.; Han, J.; Zhou, T.; Xu, R. *Nanoscale* **2014**, *6*, 14984–90.

[77] Schwinghammer, K.; Mesch, M. B.; Duppel, V.; Ziegler, C.; Senker, J.; Lotsch, B. V. *J. Am. Chem. Soc.* **2014**, *136*, 1730–3.

[78] Niu, P.; Zhang, L.; Liu, G.; Cheng, H.-M. *Adv. Funct. Mater.* **2012**, *22*, 4763–4770.

[79] Zhang, J.; Chen, Y.; Wang, X. *Energy Environ. Sci.* **2015**, *8*, 3092–3108.

[80] Wirnhier, E. A. Solvothermal and Ionothermal Approaches to Carbon Nitride Chemistry. Ph.D. thesis, LMU, 2013.

[81] Sattler, A.; Schnick, W. *Eur. J. Inorg. Chem.* **2009**, *7*, 4972–4981.

[82] Ju, S.-S.; Han, C.-C.; Wu, C.-J.; Mebel, A. M.; Chen, Y.-T. *J. Phys. Chem. B* **1999**, *103*, 582–596.

[83] Hasenberg, D. *J. Catal.* **1987**, *104*, 441–453.

[84] Komatsu, T. *Macromol. Chem. Phys.* **2001**, *202*, 19–25.

[85] Hagemam, H.; Snyder, R. G.; Peacock, A.; Et.al., *Macromolecules* **1989**, *22*, 3600–3606.

[86] Ong, W.-J.; Tan, L.-L.; Chai, S.-P.; Yong, S.-T. *Dalton Trans.* **2015**, *44*, 1249–57.

[87] Dante, R. C.; Martín-Ramos, P.; Navas-Gracia, L. M.; Sánchez-Arévalo, F. M.; Martín-Gil, J. *J. Macromol. Sci. Part B* **2013**, *52*, 623–631.

[88] Sun, H.; Zhou, G.; Wang, Y.; Suvorova, A.; Wang, S. *ACS Appl. Mater. Interfaces* **2014**, *6*, 16745–54.

[89] Xiang, Q.; Yu, J.; Jaroniec, M. *J. Phys. Chem. C* **2011**, *115*, 7355–7363.

[90] Ding, Z.; Chen, X.; Antonietti, M.; Wang, X. *ChemSusChem* **2011**, *4*, 274–81.

[91] Yuan, B.; Chu, Z.; Li, G.; Jiang, Z.; Hu, T.; Wang, Q.; Wang, C. *J. Mater. Chem. C* **2014**, *2*, 8212–8215.

[92] Fang, J.; Fan, H.; Li, M.; Long, C. *Mater. Chem. Phys.* **2015**, *3*, 13819–13826.

[93] Yang, S.; Gong, Y.; Zhang, J.; Zhan, L.; Ma, L.; Fang, Z.; Vajtai, R.; Wang, X.; Ajayan, P. M. *Adv. Mater.* **2013**, *25*, 2452–6.

[94] Wei, W.; Jacob, T. *Phys. Rev. B* **2013**, *87*, 085202.

[95] Zhang, J.; Wang, X. *Angew. Chem. Int. Ed.* **2015**, *54*, 7230–7232.

[96] Wu, H. Z.; Liu, L. M.; Zhao, S. J. *Phys Chem Chem Phys* **2014**, *16*, 3299–3304.

[97] Gauglitz, G.; Vo-Dinh, T. *Handbook of Spectroscopy*; Wiley, 2003; p 78.

[98] Bohren, C. E.; Wiley, D. R. H. *Absorption and Scattering of Light by Small Particles* .; John Wiley & Sons, 1984; pp 1983–1984.

[99] Sing, K. S. W. *Pure Appl. Chem.* **1985**, *57*, 603–619.

[100] Flanigen, E. M., Sand, L. B., Eds. *Molecular Sieve Zeolites-I*; Advances in Chemistry; American Chemical Society: Washington, D. C., 1974; Vol. 101.

[101] Panasiuk, Y.; Raevskaya, A.; Stroyuk, O. L.; Lytvyn, P.; Kuchmiy, S. Y. *RSC Adv.* **2015**, *5*, 46843–46849.

[102] Asmatulu, R. *Nanotechnology Safety*; Elsevier Science, 2013.

[103] Sattler, A.; Schnick, W. *Zeitschrift für Anorg. und Allg. Chemie* **2006**, *632*, 1518–1523.

[104] Kisch, H. *Angew. Chemie* **2010**, *122*, 9782–9783.

[105] Schwinghammer, K.; Tuffy, B.; Mesch, M. B.; Wirnhier, E.; Martineau, C.; Taulelle, F.; Schnick, W.; Senker, J.; Lotsch, B. V. *Angew. Chem. Int. Ed. Engl.* **2013**, *52*, 2435–9.

[106] Chen, Y.; Wang, B.; Lin, S.; Zhang, Y.; Wang, X. *j. Phys. Chem. C* **2014**, *118*, 29981–29989.

[107] Pal, U.; Ghosh, S.; Chatterjee, D. *Transit. Met. Chem.* **2011**, *37*, 93–96.

[108] Sada, E.; Kumazawa, H.; Ikehara, Y.; Han, Z. *Chem. Eng. J.* **1989**, *40*, 7–12.

[109] Shi, T.; He, J.; Ding, T.; Wang, A. *Int. J. Chem. Kinet.* **1991**, *23*, 815–823.

[110] Vyas, V. S.; Lotsch, B. V. *Nature* **2015**, *521*, 41–42.

[111] Vyas, V. S.; Haase, F.; Stegbauer, L.; Savasci, G.; Podjaski, F.; Ochsenfeld, C.; Lotsch, B. V. *Nat. Commun.* **2015**, *6*, 8508.

[112] Stegbauer, L.; Schwinghammer, K.; Lotsch, B. V. *Chem. Sci.* **2014**, *5*, 2789–2793.

[113] Schwinghammer, K.; Hug, S.; Mesch, M. B.; Senker, J.; Lotsch, B. V. *Energy Environ. Sci.* **2015**, *8*, 3345–3353.

[114] Algara-Siller, G.; Severin, N.; Chong, S. Y.; Björkman, T.; Palgrave, R. G.; Laybourn, A.; Antonietti, M.; Khimyak, Y. Z.; Krasheninnikov, A. V.; Rabe, J. P.; Kaiser, U.; Cooper, A. I.; Thomas, A.; Bojdys, M. J. *Angew. Chemie Int. Ed.* **2014**, *53*, 7450–7455.

[115] Ham, Y.; Maeda, K.; Cha, D.; Takanabe, K.; Domen, K. *Chem. Asian J.* **2013**, *8*, 218–24.

[116] McDermott, E. J.; Wirnhier, E.; Schnick, W.; Virdi, K. S.; Scheu, C.; Kauffmann, Y.; Kaplan, W. D.; Kurmaev, E. Z.; Moewes, A. *J. Phys. Chem. C* **2013**, *117*, 8806–8812.

[117] Mills, A.; Wang, J. *J. Photochem. Photobiol. A Chem.* **1999**, *127*, 123–134.

[118] Xiong, L.; Sun, W.; Yang, Y.; Chen, C.; Ni, J. *J. Colloid Interface Sci.* **2011**, *356*, 211–6.

[119] Penconi, M.; Rossi, F.; Ortica, F.; Elisei, F.; Gentili, P. *Sustainability* **2015**, *7*, 9310–9325.

[120] Jose, R.; Thavasi, V.; Ramakrishna, S. *J. Am. Ceram. Soc.* **2009**, *92*, 289–301.

## Bibliography

[121] Castelli, I. E.; Olsen, T.; Datta, S.; Landis, D. D.; Dahl, S. r.; Thygesen, K. S.; Jacobsen, K. W. *Energy Environ. Sci.* **2012**, *5*, 5814.

[122] Tong, H.; Ouyang, S.; Bi, Y.; Umezawa, N.; Oshikiri, M.; Ye, J. *Adv. Mater.* **2012**, *24*, 229–51.

[123] Yi, Z.; Ye, J.; Kikugawa, N.; Kako, T.; Ouyang, S.; Stuart-Williams, H.; Yang, H.; Cao, J.; Luo, W.; Li, Z.; Liu, Y.; Withers, R. L. *Nat. Mater.* **2010**, *9*, 559–64.

[124] Robb, W. L. *Ann. N. Y. Acad. Sci.* **1968**, *146*, 119–137.

[125] Niu, P.; Yin, L.-C.; Yang, Y.-Q.; Liu, G.; Cheng, H.-M. *Adv. Mater.* **2014**, *26*, 8046–52.

# Curriculum Vitæ

**Personal Information**

Brian Tuffy
Irish
Castlebar, Ireland

**Education:**

**2012 − 2016** PhD continued: Max Planck Institute for Solid State Research (MPI-FKF), Stuttgart, Germany with Prof. Bettina Lotsch

**2010 − 2012** PhD: Ludwig-Maximilians-Universität (LMU), Munich, Germany with Prof. Bettina Lotsch

**2008 − 2010** Master's thesis: "Porphyrin Materials for Organic Light-emitting Diodes" Trinity College Dublin (TCD), Dublin, Ireland with Prof. Werner Blau

**2004 − 2008** B.Sc. in Applied Physics, awarded: First Class Honours
Dublin City University (DCU), Dublin, Ireland

**1998 − 2004** St Geralds College, Castlebar, Co. Mayo, Ireland

**Publications:**

1. Katharina Schwinghammer, Brian Tuffy, Maria B. Mesch, Eva Wirnhier, Charlotte Martineau, Francis Taulelle, Wolfgang Schnick, Jürgen Senker, Bettina V. Lotsch, (**2013**), "Triazine-based Carbon Nitrides for Visible-Light-Driven Hydrogen Evolution", *Angew. Chem. Int. Ed.*, 52: 2435–2439.
doi: 10.1002/anie.201206817

2. Aoife Ryan, Brian Tuffy, Sabine Horn, Werner J. Blau, Mathias O. Senge (**2011**), "Carbazole-linked porphyrin dimers for organic light emitting diodes: synthesis and initial photophysical studies", *Tetrahedron*, 67, 43: 8248–8254
doi: 10.1016/j.tet.2011.08.096

3. Brian Tuffy, (2011) "Porphyrin Materials for Organic Light Emitting Diodes", ISBN: 384652669X, 9783846526699

**Presentations and Posters:**

**25.09.2012** Joint Workshop on Materials Chemistry, Stuttgart, Germany

**07.09.2012** *Talk:* Water – A manifold challenge, Rachel Carson Center for Environment and Society, Munich, Germany

**01.07.2012** *Poster:* 15th International Congress on Catalysis (ICC), Munich, Germany

**20.02.2012** *Talk:* Joint Science Exchange Meeting, Schloss Ringberg, Kreuth, Germany

**08.02.2012** *Poster:* Final Symposium of the Internationales Doktorandenkolleg NanoBioTechnology (IDK-NBT), Herrsching, Germany

**19.09.2011** *Poster:* CeNS Summer Workshop: Nanosciences – From Molecular Systems to Functional Materials, Venice, Italy

**12.09.2011** *Talk:* European Congress and Exhibition on Advanced Materials and Processes (Euromat), Montpellier, France

**02.08.2011** CeNS Summer School, Aiterbach am Chiemsee, Munich, Germany

**21.07.2011** *Poster:* Advances in Photovoltaics and Photocatalysis, Technische Universität, Munich, Germany

**11.04.2011** Energy and Innovation Workshop, Center for Advanced Studies (CAS), LMU, Munich, Germany

**03.09.2009** *Poster:* 9th International Symposium on Advanced Organic Photonics (ISAOP), Japanese-Europe Joint Workshop, Bunratty, Ireland